

Chemical Geology

THE COMPOSITION OF FLUIDS STORED IN THE CENTRAL MEXICAN LITHOSPHERIC MANTLE: INFERENCES FROM NOBLE GASES AND CO₂ IN MANTLE XENOLITHS

--Manuscript Draft--

Manuscript Number:	CHEMGE13694R1
Article Type:	VSI Barry(Hilton)
Keywords:	Mexican mantle xenoliths; Fluid Inclusions; noble gases; CO ₂ ; mantle refertilization; carbonate recycling.
Corresponding Author:	Andres Libardo Sandoval Velasquez Universita degli Studi di Palermo Palermo, Sicily ITALY
First Author:	Andres Libardo Sandoval Velasquez
Order of Authors:	Andres Libardo Sandoval Velasquez Andrea Luca Rizzo Maria Luce Frezzotti Ricardo Saucedo Alessandro Aiuppa
Abstract:	<p>We present the first isotopic (noble gases and CO₂) characterization of fluid inclusions coupled to Raman microspectroscopy analyses in mantle xenoliths from Central Mexico, a geodynamically complex area where the Basin and Range extension was superimposed on the Farallon subduction (terminated at 28 Ma). To characterize the isotopic signature of the Central Mexican lithospheric mantle, we focus on fluid inclusions entrapped in mantle xenoliths found in deposits of the Joya Honda maar (JH), a Quaternary monogenetic volcano belonging to the Ventura Espiritu Santo Volcanic Field (VESVF) in the state of San Luis Potosí (central Mexico). Thirteen ultramafic plagioclase-free xenoliths were selected, all exhibiting a paragenesis $Ol > Opx > Cpx \gg Sp$, and being classified as spinel-lherzolites and harzburgites. All xenoliths bring textural evidence of interstitial glass veins bearing dendritic trails of secondary melt and fluid inclusions (composed of silicate glass \pm CO₂ \pm Mg-Ca carbonates \pm pyrite). These are related to pervasive mantle metasomatism driven by carbonate-rich silicate melt. The Ar and Ne systematics reflect mixing between MORB-like upper mantle and atmospheric fluids, the latter interpreted as reflecting a recycled air component possibly inherited from the Farallon plate subduction. The ³He/⁴He ratios vary between 7.13 and 7.68 Ra, within the MORB range (7-9 Ra), and the ⁴He/⁴⁰Ar* ratios (0.4 - 3.11) are similarly close to the expected range of the fertile mantle (1-5). Taken together, these pieces of evidence suggest that (i) either the mantle He budget was scarcely modified by the Farallon plate subduction, and/or (ii) that any (large) crustal contribution was masked by a later metasomatism/refertilization episode, possibly during the subsequent Basin and Range extension. A silicate melt-driven metasomatism/refertilization (revealed by the association between glass veins and fluid inclusions) is consistent with calculated helium residence time for the Mexican lithospheric mantle (20 to 60Ma) that overlaps the timing of the above geodynamic events. We propose that, after the refertilization event (e.g., over the last ~20Ma), the lithospheric mantle has evolved in a steady-state, becoming slightly more radiogenic. We also estimated ³He fluxes (0.027 - 0.080 mol/g), ⁴He production rates (340 - 1000 mol/yr), and mantle CO₂ fluxes (3.93 x 10⁷ mol/yr to 1.18x10⁸ mol/yr) using the helium isotopic values measured in JH mantle xenoliths. Finally, the JH xenoliths exhibit CO₂/³He ratios comparable to those of the upper mantle (from 3.38 x 10⁸ to 3.82x10⁹) but more positive $\delta^{13}C$ values (between -1.0 and -2.7‰), supporting the involvement of a crustal carbonate component. We propose that the metasomatic silicate melts recycled a crustal carbonate component, inherited by the Farallon plate subduction.</p>



UNIVERSITÀ DEGLI STUDI DI PALERMO

Dipartimento di Scienze della Terra e del Mare (DiSTeM)

COD. FISC. 80023730825 ~ P.IVA 00605880822

Don Porcelli
Editor-in-Chief
Chemical Geology

Saemundur Ari Halldórsson,
Special issue - Guest editor
Chemical Geology

VSI Barry(Hilton)>>>>Submission Deadline mss 1 April 2021: Earth's Volatile Cycles within the Crust-Mantle System: A volume in memory of Dave Hilton; Peter Barry (WHOI, USA), Saemi Halldorson (University of Iceland), Evelyn Furi (CRPG, France), Justin Kulongoski (USGS, USA), Gray Bebout (Lehigh, USA)

Palermo, 25 March 2021

Dears,


We wish to submit the revised manuscript (CHEMGE13694) entitled "THE COMPOSITION OF FLUIDS STORED IN THE CENTRAL MEXICAN LITHOSPHERIC MANTLE: INFERENCES FROM NOBLE GASES AND CO₂ IN MANTLE XENOLITHS" for consideration by *Chemical Geology*. Our paper will be a contribution to the special issue in memory of Dave Hilton ("Earth's Volatile Cycles within the Crust-Mantle System"). This is the result of a collaborative effort between the University of Palermo, the *Istituto Nazionale di Geofisica e Vulcanologia* (INGV), the University of Milano-Bicocca and the *Universidad Autonoma de San Luis Potosí* (Mexico).

The manuscript was modified and improved following the valuable suggestions and comments of the Reviewers. Please find attached the corresponding files.

Thank you for your consideration of this manuscript.

Sincerely,

Corresponding author.


Andrés Libardo Sandoval Velásquez

THE COMPOSITION OF FLUIDS STORED IN THE CENTRAL MEXICAN LITHOSPHERIC MANTLE: INFERENCES FROM NOBLE GASES AND CO₂ IN MANTLE XENOLITHS

Manuscript number: CHEMGE13694

Guest Editor (Saemundur Ari Halldórsson):

First, I thank you for submitting this interesting manuscript to this special issue of Chemical Geology honoring the memory of David Hilton. Two reviewers have now returned their evaluation of your manuscript and both provide detailed review comments. You will see that while they are overall supportive of your work, they have also raised a number of critical comments that you will need to address.

For example, one reviewer (R1) points out that some available literature on this subject is left uncited, including several key references. This same reviewer also points out that fluid-melt partitioning is not discussed as means of explaining the range of values 4/40* observed in your xenoliths.

The other reviewer (R2) expresses concern related to the structure of the manuscript and suggests some condensing of the text. Further, he suggests some rewriting of a section addressing the presence of atmospheric components as he fails to see how the dataset presented support the story presented.

We are grateful for the valuable comments and suggestions of the Reviewers. In general, we have included several key references dealing with the study of noble gases in mantle xenoliths, eg., Matsumoto et al. (1998, 2000), Hopp et al. (2004, 2007a, 2007b), Buikin et al. (2005), and Czuppon et al. (2009). We have included a discussion on the possible influence of fluid-melt partitioning on the He/Ar* measured in the mantle xenoliths.

We also revised the section “*Evidence for a recycled air component: Ne and Ar*”, here we included key diagrams such as ³He vs ³⁶Ar and ²⁰Ne/²²Ne vs ⁴⁰Ar/³⁶Ar that support the existence of a recycled atmospheric component in the Mexican lithospheric mantle, likely inherited from subduction events. We also revised the subsection “No mantle plume component in the JH mantle source” since (²¹Ne/²²Ne)_{Ext} suggests a contribution of plume-derived Neon (<10%).

Finally, analytical uncertainties were added and the structure of the discussion was improved, by moving in the supplementary information part of the secondary processes previously discussed and additional elaboration following the Reviewers suggestions. This allowed to condense the content of the manuscript, as recommended by Rev. 2.

Point-to-point reply to Reviewers' comments

Reviewer #1:

General remarks:

This contribution reports new and actually the first, noble gas compositions and carbon isotope compositions, of mantle xenoliths from Joya Honda, Mexico. These data are complemented by petrologic information and Raman analyses.

Basically, the presented data are of good quality, the sample descriptions are excellent and the authors also explain the geological background in a sound way. Nothing to complain about that part.

I have mainly issues with their discussion of the noble gas results, whereas all other parts are fine. There are several points that deserve a significant change. Since these changes surely will affect the discussion, and maybe the conclusions, I need to recommend a major revision, unfortunately. Otherwise, the topic and quality of data is worth of publication in Chemical Geology.

Major issues:

1) The referencing of the authors seems strange. Besides the citation of Broadley et al. 2020, which deals with extraterrestrial material (ureilites) and hardly with lithospheric mantle, the authors neglect a large body of existing literature. This would be no problem if the cited papers are i) fitting their discussed point and ii) are the "best available on the market". In case of i), for example, it is not clear what the authors want to support with their references: If you discuss infiltration of fluids from a slab into the lithosphere above, it makes not much sense to cite papers that are related to potentially plume-induced rifting processes. And if you want to check for interaction with plume-related fluids it makes no sense to use papers dealing majorily with subduction or closed-system evolution... In case of ii): The authors cite Gautheron et al. 2005 ChemGeol to use their data of European Volcanics. Note, that in the same year Buikin et al. 2005 EPSL also presented stepwise crushing data of the Eifel and the Pannonian Basin with higher precision and higher gas amounts (not surprising, because our lab, which measured these data, performed a preselection with Ar of many more xenoliths to find the most gas-rich ones). Other high quality data of samples from lithospheric mantle are presented in Matsumoto et al. 1998 (Australia); 2000 (Australia); Hopp et al. 2004 EPSL (Saudi-Arabia); 2007a ChemGeol (Saudi-Arabia); 2007b EPSL (Kenya); Czuppon et al. 2009 (Australia).

R: We agree that the reference Broadley et al. (2020) is not appropriate for this paper, therefore this was removed from the main text.

References were modified according to the discussed points in the manuscript. For instance, when discussing noble gas derived or influenced from subduction, we cite papers such as Matsumoto et al. (2001), Hopp et al. (2007a), Hopp and Ionov (2011) and Broadley et al. (2016) and when discussing the relationship between noble gas and mantle plumes we cite Hopp et al. (2004, 2007a, 2007b), Buikin et al. (2005) and Halldórsson et al. (2014). See section 1 (L. 91 of the revised manuscript).

We also added the references suggested by the reviewer. See sections 1 - 5.4 - 6.4.1 - 6.4.2 and Figures 6, 7, 8 and 10.

2) The impact of subduction-related atmospheric noble gases in samples of the continental lithosphere was also discussed by Matsumoto et al. 2001, who reported a correlation between ^3He and ^{36}Ar in samples of the Horoman ophiolite. Maybe you can check this for your samples with highest $^{40}\text{Ar}/^{36}\text{Ar}$ as well. This was interpreted as a co-variation of mantle gases and (subduction-related) atmospheric gases. Hopp et al. (2007a ChemGeol) also discussed a potential subduction-related contribution of atmospheric fluids to the subcontinental mantle lithosphere on the basis of observed element-fractionated atmospheric compositions (i.e. elevated $^{36}\text{Ar}/^{22}\text{Ne}$ -ratios of the atmospheric endmember). The existence of such elevated subduction-related $^{36}\text{Ar}/^{22}\text{Ne}$ -ratios was demonstrated for mantle xenoliths from the Kamchatkan mantle wedge, with nearly atmospheric Ar and Ne, but MORB-like He compositions (Hopp and Ionov, 2011 EPSL). This point is also mentioned in below in 3) in more detail.

R: A fully reply to this comment is provided in the specific point below, in which we address the issue of atmospheric gas interactions more fully. As suggested by the reviewer, we examined a possible correlation between ^{36}Ar and ^3He contents to properly evaluate the impact of subduction-related atmospheric fluids in our mantle xenoliths. We identified a positive correlation between ^3He and ^{36}Ar (samples with $^{40}\text{Ar}/^{36}\text{Ar} > 500$), which supports the existence of an atmospheric component recycled in the local lithospheric mantle (see new Figure 9)

3) Subsection 6.1.1 Atmospheric contamination:

First, I would not speak of "contamination", but "interaction with atmospheric fluids".

Secondly, your remark in L.369 "We find that most of the samples exhibit low air contamination..." is misleading (I assume, you mean interaction with atmospheric gases, not "air"). Looking at your Ne-isotopes most of your data have $^{20}\text{Ne}/^{22}\text{Ne} < 10.5$ (28 out of 33), and 10 out 33 even below a $^{20}\text{Ne}/^{22}\text{Ne}$ of 10. A $^{20}\text{Ne}/^{22}\text{Ne}$ of 10.5 would correspond to about 74% atmospheric Ne, which is not my impression of "low"... Judging from your $^{36}\text{Ar}/^{22}\text{Ne}$ -ratios most of your samples fall in a range below the air-value (18.7) with values down to 1.7, only few are higher, with maximum values of up to 64. Low Ar/Ne were reported in clays, but most studies do not show these ratios.

So, there are two explanations for it: First, your sample suite is unique and an unknown fractionation process affected your xenoliths, or secondly, your calibration gas amounts are slightly offset. No matter what's the reason, commonly subduction-related atmospheric fluids would tend to show elevated $^{36}\text{Ar}/^{22}\text{Ne}$ -ratios relative to air, simply because Ne is more prone to early loss during the subduction process. I observed in fact high atmospheric $^{36}\text{Ar}/^{22}\text{Ne}$ in Kamchatkan xenoliths (Hopp and Ionov, 2011 EPSL). In another study we detected an elevated atmospheric $^{36}\text{Ar}/^{22}\text{Ne}$ ratio admixed with mantle fluids prior to interaction with late-stage local atmospheric gases in mantle xenoliths from Saudi-Arabia and peridotites from Zabargad Island, Red Sea, that evidence subduction-related admixing of atmospheric gases (Hopp et al., 2007 ChemGeol). This is mainly based on isotope ratio considerations $^{40}\text{Ar}/^{36}\text{Ar}$ vs $^{20}\text{Ne}/^{22}\text{Ne}$. I would recommend to include the latter diagram.

R: We thank the reviewer for his insightful comments. This part of the manuscript was extensively restructured following his suggestions:

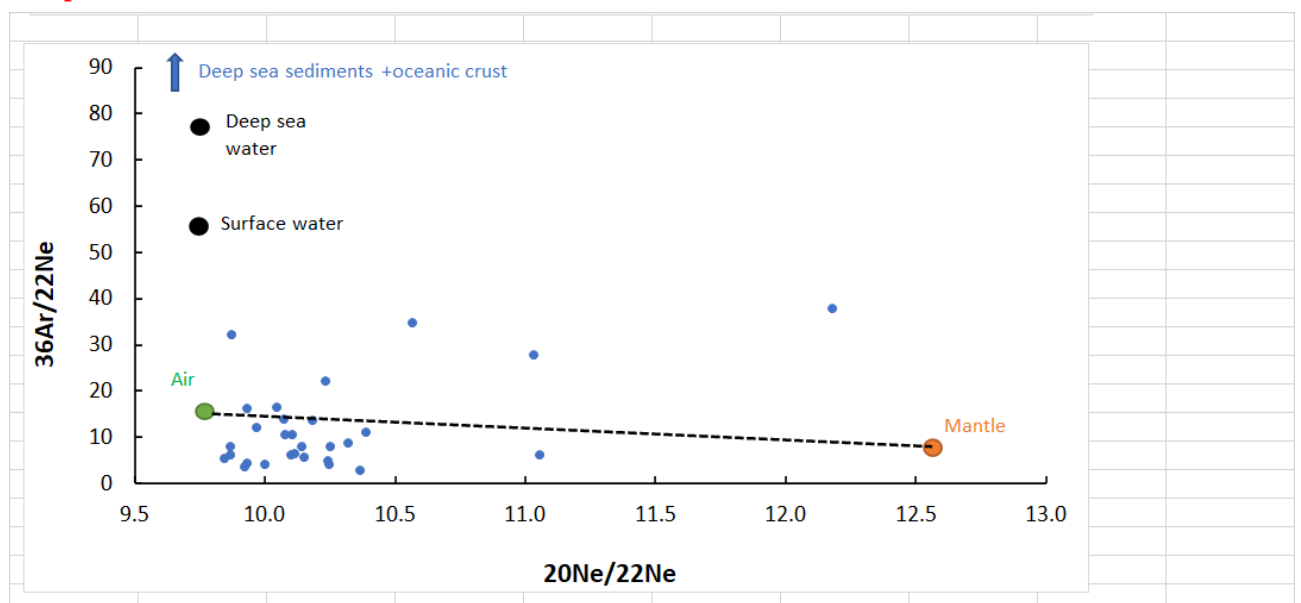
- 1) The title of section 6.1.1 was modified as follows: *“Interaction with atmospheric fluids and evidence for a recycled atmospheric component ”*
- 2) We agree that the statement *“low atmospheric contamination”* was misleading since most samples exhibit $^{20}\text{Ne}/^{22}\text{Ne}$ and $^{36}\text{Ar}/^{22}\text{Ne}$ ratios close to the air values; therefore, this sentence was removed, and the text was edited as follows (see L. 362-377 of the revised manuscript):

“He, Ne and Ar systematics suggest the existence of an atmospheric component in our samples (especially in nodule V-I). In general, the measured R/R_a and $^4\text{He}/^{20}\text{Ne}$ values fall along an air-MORB mixing curve, and overlap with those measured in mantle xenoliths from the European SCLM, the West Antarctic Rift System (WARS), Eastern Australia, Red sea region and N/S Kenya rifts (Figure 7A). The existence of such an atmospheric component is corroborated by $^{40}\text{Ar}/^{36}\text{Ar}$ and $^{20}\text{Ne}/^{22}\text{Ne}$ ratios significantly below the expected MORB values (44,000 and 12.5, respectively; Burnard, 1997; Moreira, 1998; Sarda, 2004). As shown in Figure 7B, $^{40}\text{Ar}/^{36}\text{Ar}$ and $^3\text{He}/^{36}\text{Ar}$ values also fall along a two-component mixing between a MORB-like upper mantle and atmosphere (He/Ar^ ratios of 0.14 to 3.5 explain the whole data variability; see also Figure 9B). Likewise, samples fit the binary mixing air-MORB when using the three-isotope neon plot (Figure 7C), confirming the existence of atmospheric fluids in our inclusions. The atmospheric component is especially notable in nodule V-I that exhibits an isotopic signature close to that of air with $^4\text{He}/^{20}\text{Ne}$ ratios below 10 (for Opx and Cpx) and $^{40}\text{Ar}/^{36}\text{Ar}$ values below 392. These compositions confirm that this nodule likely suffered secondary processes that modified its pristine mantle signature. This sample is therefore not considered representative of the local SCLM (and omitted from the following discussion).”*

3) As suggested by the reviewer, we examined a possible correlation between ^{36}Ar and ^3He contents to properly evaluate the impact of subduction-related atmospheric fluids in our mantle xenoliths. We identified a positive correlation between ^3He and ^{36}Ar (samples with $^{40}\text{Ar}/^{36}\text{Ar} > 500$), which supports the existence of an atmospheric component recycled in the local lithospheric mantle (see new Figure 9).

Likewise, as the reviewer suggests, we included in the paper the diagram $^{20}\text{Ne}/^{22}\text{Ne}$ vs $^{40}\text{Ar}/^{36}\text{Ar}$ (new Figure 9B). Following Langmuir et al. (1978) and Hopp et al. (2007a), and considering the variability of He, Ne and Ar in our dataset, we calculated a $^{40}\text{Ar}/^{36}\text{Ar}$ signature of about 10,500 for the local upper mantle (see Figure 9B and Table 3). This further supports our interpretation that the Mexican lithospheric mantle has been contaminated by atmospheric fluids (likely derived from the mentioned subduction). We highlight that the conditions assumed for the above calculation are the same assumed for the mixing curves plotted in Figure 7. Accordingly, in Figures 7A and 7B we now report the corresponding values of $^4\text{He}/^{20}\text{Ne}$ (11,000) and $^{40}\text{Ar}/^{36}\text{Ar}$ (10,500) expected for the local mantle.

4) Regarding the $^{36}\text{Ar}/^{22}\text{Ne}$, when $^{36}\text{Ar}/^{22}\text{Ne}$ is plotted vs $^{20}\text{Ne}/^{22}\text{Ne}$, as proposed by e.g. Hopp et al. (2007), only a few samples have $^{36}\text{Ar}/^{22}\text{Ne}$ above air ratio (see below). So we find little evidence of Ar/Ne fractionation due to the fact that Ne is more prone to early loss during the subduction process. Instead, the majority of the samples fall along or slightly below the AIR-mantle line, suggesting that an unfractionated behaviour (see plot below). We thus feel information coming from the $^{20}\text{Ne}/^{22}\text{Ne}$ vs $^{40}\text{Ar}/^{36}\text{Ar}$ plot (suggested by the Reviewer as well) more useful and straightforward, also considering we are able to calculate a $^{40}\text{Ar}/^{36}\text{Ar}$ value of the local mantle lower than MORB, supporting our inference of a recycled atmospheric component.



In summary, the diagrams ^{36}Ar vs ^3He and $^{20}\text{Ne}/^{22}\text{Ne}$ vs $^{40}\text{Ar}/^{36}\text{Ar}$ were added to the text as Figure 9; the corresponding table (Table 3) was also included. This information is presented in subsection 6.1.1: “6.1.1 Interaction with atmospheric fluids and evidence for a recycled atmospheric component”.

4) Diffusive fractionation and $4\text{He}/40\text{Ar}^*$ -ratios:

If you state that the ^4He diffusion coefficient is considerably higher than that of ^{40}Ar ($D_{\text{He}}/D_{\text{Ar}} = 3.16$ in solid mantle...) you should be aware - and actually mention it in the manuscript - that this value is a calculated value assuming only atomic mass is governing the difference in diffusion coefficients. Burnard itself stated in his text "...assuming Eq 1 is true..." (Eq 1 is the relation between D and m). I have doubt, that this the case, because He is small enough to allow for interlattice diffusion, which is not likely for Ar. No matter, you should at least specify basic assumptions in your text.

R: We point out that our statement concerning the higher diffusion of He relative to Ar is based on previous studies (opportunedly cited in the same sentence). Therefore, any assumption behind (i.e., the atomic mass is governing the difference in diffusion coefficients) is not ours. However, we agree with the reviewer that this aspect must be explicit. The text was edited as follows (See lines 56 – 61, in supplementary material):

“Previous studies suggest that the ^4He diffusion coefficient is considerably higher than that of ^{40}Ar ($D_{4\text{He}}/D_{40\text{Ar}} = 3.16$ in solid mantle; Burnard, 2004; Yamamoto et al., 2009); this is fundamentally based on the assumption that the difference in the atomic masses of the two elements are the key controls of their different diffusion coefficients. Likewise, the difference in mass between ^3He and ^4He implies important differences in their diffusivities ($D_{3\text{He}}/D_{4\text{He}} = 1.15$; Trull and Kurz, 1993; Burnard, 2004; Yamamoto et al., 2009).

5) Subsection 6.2 The effect of partial melting:

Nobody really knows precisely any partition coefficients, in spite of many efforts. For example, if you look at Heber et al. 2007 (which you cite), the error bars in distribution coefficients are large and mostly 100%. We only know that noble gases are incompatible, though even this was questioned in a study about Ar partitioning coefficients by Thomas et al 2008. Hence, I would not rely on those values. I also would not rely on the assumption that He is more incompatible than Ne, Ar. The studies which you cite do not support this unequivocally, due to the large uncertainties. I may also cite a paper that reported results for He suggestive of a more compatible behaviour as U,Th and, nominally, also as Ne,Ar (Parman et al. 2005). Therefore, you should not write (L. 445ff) "...it has been verified that He is more incompatible than Ar..." You may assume that, but that's not proven...

My major issue here is, that you ignore the far more important process of fluid-melt partitioning, which is nicely displayed in your xenoliths: You talk about the association of glass veins (= former melt) and fluid inclusions. Note, that this not means formation from host magma, because the melt veins and fluid inclusions probably formed earlier (as you also state, I agree with that). In this case, one would expect element fractionation according to the solubilities of the noble gases. Common fractionation factors are 2-4 (He/Ne) and 7-10 (He/Ar) (Lux, 1986; Jambon et al. 1986/87). In case that you observe $4\text{He}/40\text{Ar}^* = 1$ in your fluids means, that your melt composition must already had about 7-10 times higher $4\text{He}/40\text{Ar}^*$ -ratios... (in case of equilibrium fractionation). Though we may argue about details, the large picture is, that your higher $4\text{He}/40\text{Ar}^*$ -ratios do not represent "unfractionated" mantle ratios but are already the most processed one... Quite the opposite, isn't it. From a rough estimate we would expect $4\text{He}/40\text{Ar}^*$ -ratios of about 0.1-0.5 in the xenoliths to be derived from a ca. unfractionated initial melt composition.

Even worse, as I found in my stepwise crushing experiments, not all xenoliths show one element composition. Both the air-corrected $3\text{He}/22\text{Ne}$ and $4\text{He}/40\text{Ar}^*$ ratios may systematically vary during crushing, that means different generations of fluid inclusions seem present, incorporated at different times.

Regarding the lithophile tracers (L. 451ff): If the noble gases form by dissolution from a melt, and if this melt is progressively (by and large) losing fluids on its way through the mantle or crust, we would not expect any correlation with lithophile elements.

R: We understand the point of view of the Reviewer and appreciate his suggestions to consider the melt/fluid partitioning process. Regarding the partition coefficients, we disagree on the fact that we cannot rely on the crystal/melt partition coefficients proposed by Heber et al. (2007), as this study is published in a top geochemistry journal and is widely cited by a number of following studies (142 citations). Although it is true that Heber et al. (2007) report error bars of almost 100% for the partition coefficients, it must be also considered that the Authors suggest that argon has a partition coefficient of about one order of magnitude higher than that of helium ($D_{\text{He}} = 0.00017$ and $D_{\text{Ar}} = 0.0011$), being well outside the respective error bars. Furthermore, we point out that $4\text{He}/40\text{Ar}^*$ ratios systematically much lower (at least one order of magnitude) than the typical mantle production ratio (1-5) have been measured in mantle xenoliths from several localities that, based on a careful petrological observation, have been inferred to be representative of very refractory mantle lithologies (e.g., Lower Silesia, Europe, Rizzo et al., 2018; Greene Point, Antarctica, Correale et al., 2019; Eifel and Siebengebirge, Europe, Rizzo et al., 2019, 2020; Yangtze craton, China, Correale et al., 2016). However, we agree with the Reviewer that the history of fluid inclusions trapped in our mantle xenoliths may have been ultimately influenced by the fluid/melt partitioning of metasomatizing melt(s), as we do not have evidence from mineral chemistry to constrain our

inferences on partial melting and the evidences from texture of xenoliths indicate the occurrence of secondary trails of fluid inclusions related to the metasomatizing melt.

Thus, regarding the fluid-melt partitioning, we agree with the Reviewer that this process could play an important role in determining the composition of fluid inclusions, partially or totally overprinting the signature due to partial melting. We only have some concerns on the counts indicated by the Reviewer, where ${}^4\text{He}/{}^{40}\text{Ar}^* = 1$ would result from an already degassed melt. In fact, starting for simplicity from a mantle with ${}^4\text{He}/{}^{40}\text{Ar}^* = 1$ commonly considered the lower range of production ratio of upper mantle (e.g., Marty, 2012), and considering the olivine/melt partition coefficient proposed by Heber et al. (2007) ($D_{\text{He}} = 0.00017$ and $D_{\text{Ar}} = 0.0011$), the first melt should have ${}^4\text{He}/{}^{40}\text{Ar}^* = 6.5$ while the first gas exsolved from the melt should have ${}^4\text{He}/{}^{40}\text{Ar}^* = 0.92$ (assuming a solubility ratio $S_{\text{He}}/S_{\text{Ar}} = 7$). Therefore, measuring in our samples ${}^4\text{He}/{}^{40}\text{Ar}^*$ around 1 would not necessarily imply high degrees of degassing. To conclude, we completely modified the title and section of partial melting, by shortening this history and adding the fluid/melt partitioning effect, and moving this section in Supplementary information as suggested by reviewer#2 of restructuring the Discussion by immediately focusing on the inferences on the mantle composition beneath the study area.

We agree with the Reviewer that different crushing steps can lead to the release of different families of inclusions; however, we are aware that the information we deduce from crushing is anyway an average a number of inclusions hosted in many crystals. Another important aspect in our study is that we are using the single-step crushing technique at 250 bar, which should ensure comparable experimental conditions.

Regarding the comment by the Reviewer that we should not expect a correlation between lithophile elements and noble gases, we partially disagree because a metasomatizing melt is expected to induce a partial recrystallization of the mantle thus influencing its mineral chemistry. However, to avoid any possible misunderstanding, the sentence "*In fact, the calculated noble gas-based partial melting degrees do not match (are sensibly lower than) those obtained from lithophile elements-based models*" was deleted. (see L. 77 – 106, in supplementary material).

6) Subsection 6.3.1 Evidences for a recycled air component: Ne and Ar

L. 470: "Instead..." I can't follow you here: A ratio cannot be enriched... Do you mean "elevated" ? As a note, "...a primordial component in the local mantle..." is rather pointless. Most Ne in Earths mantle is primordial, no matter which mantle reservoir you look at. Only ${}^{21}\text{Ne}$ is significantly affected by ingrowth of nucleogenic ${}^{21}\text{Ne}$ with time (about 50% in MORB mantle). By the way, atmospheric neon is nearly purely primordial... You need to specify what you mean. Probably you

mean "solar" in the widest sense (there is still a debate about the true mantle $^{20}\text{Ne}/^{22}\text{Ne}$). Furthermore, the EAR represents no uniform reservoir. You will find "hotspot" sources with elevated $^3\text{He}/^4\text{He}$ and lower $^{21}\text{Ne}/^{22}\text{Ne}$, MORB-like signatures (e.g. Turkana depression) and finally compositions characteristic of subcontinental lithosphere. Though the latter is difficult for neon to distinguish, because of admixing of plume-type neon (in my Kenyan samples, Hopp et al. 2007 EPSL, I could identify a plume-contribution which we would now ascribe to the Rungwe hotspot detected shortly after). Nonetheless, He is not affected demonstrating a lithospheric dominance in southern Kenya. To summarize this, you should not use EAR as an acronym for one mantle region. It is diverse.

R: In order to avoid misunderstandings, the phrase *"Instead, samples from EAR exhibit an enrichment in $^{20}\text{Ne}/^{22}\text{Ne}$ relatively to $^{21}\text{Ne}/^{22}\text{Ne}$, due to the presence of a primordial component in the local mantle (Halldorson et al., 2014)"* was removed from the main text.

We agree that the EAR is not a uniform reservoir, therefore we subdivided the noble gas data in three different regions: the Ethiopia (Afar) region, where relatively high $^3\text{He}/^4\text{He}$ ratios ($>10\text{Ra}$) have been reported in ultramafic xenoliths (Halldorson et al., 2014), the Red Sea region (Hopp et al., 2004; Hopp et al., 2007a; Halldorson et al., 2014) and the N/S Kenya rifts (Hopp et al., 2007b and Halldorson et al., 2014). Figures 6, 7, 8 and 10 were updated accordingly.

L. 479: As mentioned above, there exist more references showing the influence of metasomatizing slab fluids that contain atmospheric gases.

R: As discussed above, diagrams ^{36}Ar vs ^3He and $^{20}\text{Ne}/^{22}\text{Ne}$ vs $^{40}\text{Ar}/^{36}\text{Ar}$ were included to discuss the existence of subduction-related atmospheric fluids in our samples. The references Matsumoto et al. (2001) and Hopp et al. (2007a) were added in the main text. See L. 386 and L. 388 of the revised manuscript.

L. 489-491: Again, nothing new under the Sun... Add references.

R: As mentioned above, references were added. However, the phrase *"Moreover, since Ne isotopes of JH overlap the fields of data from WARS and European SCLM mantle xenoliths, the recycling of an atmospheric component in the lithospheric mantle may be common to many other geodynamic contexts"* was deleted. Further details are provided in the comment: section 6.3.1 (Reviewer #2)

7) Subsection 6.3.2: No mantle plume component in the JH mantle source

Regarding the $^{21}\text{Ne}/^{22}\text{Ne}$ (Mantle) values: You need the error bars first, in order to make sense out of your data. You may also apply an error cut, i.e. $<10\%$ error is used for display (or $<20\%$ if not

otherwise possible). I would also recommend to calculate an average air-corrected $^{21}\text{Ne}/^{22}\text{Ne}$ -value for your samples (error weighted) and check, if this value is significantly offset from MORB or not (you may use $^{20}\text{Ne}/^{22}\text{Ne} = 12.5$ for calculation purposes). Your statement, that these air-corrected ratios do not favor a plume-contribution is not correct, if I look at your given values in the Table: Only one sample has a higher than MORB value (V-F opx, 0.0629 compared with MORB = 0.0595). However, since no errors are reported, a statistical relevance is difficult to judge, and perhaps all your data agree with MORB-values within error.

Again regarding the EAR: To my knowledge, the high $^3\text{He}/^4\text{He}$ -values are from basalts, not xenoliths. But again, the EAR is not an entity. You have hotspots (Rungwe, Afar) and MORB-type signatures (Turkana) and SCLM (many others), and mixtures... The diagram $^{21}\text{Ne}/^{22}\text{Ne}$ vs $^4\text{He}/^3\text{He}$ gives an overview of the various possible endmembers, and in its form presented as Fig 9D was the first time shown by Hopp et al. 2004 (with SCLM endmember). A plume-contribution would be visible as a shift along a mixing trajectory towards (e.g.) the Loihi-composition representing deep-mantle. Your data seem to show exactly this behaviour, but not significant regarding the error, I presume. I agree, that your radiogenic mantle endmember is more MORB-like. But the change along the mixing trajectory with a plume component (if significant) is at odds with your section title.

To summarize this: You probably need to change the whole discussion here, but this depends on your error bars...

R: Error bars were added in Figures 7C and 10A. In the latter figure, we reported data by using an error cut $< 10\%$ (2σ uncertainties). We agree that it is not possible to discard the contribution of deep-mantle Neon in our samples; even with error bars, some samples fall along the MORB-Plume mixing line ($^{21}\text{Ne}/^{22}\text{Ne}$ ext < 0.05). Using the binary mixing trend, we have calculated a plume contribution $< 10\%$ in our samples. On the other hand, the homogeneity of $^4\text{He}/^3\text{He}$ ratios and the fact that the samples less contaminated by the atmospheric component fall along the AIR-MORB line (Figure 7C), leads us to propend for a dominating MORB-like composition of the upper mantle. However, a new title for this section is proposed (“6.1.2 Noble gas signature of the JH mantle source”) and the text was improved accordingly (see L. 426 – 440 of the revised manuscript).

Regarding the high $^3\text{He}/^4\text{He}$ values reported in the EAR, these are from both lavas and xenoliths (see Table S1 in Halldorson et al., 2014). In our study we only plotted values from xenoliths.

In subsection 6.4, L. 587ff it sounds as if you have detected for the first time $^3\text{He}/^4\text{He}$ -ratios $> 7R_a$ for SCLM samples... This was already found by Matsumoto et al. 1998... Please, rewrite.

R: In order to avoid misunderstandings, the text was modified as follows (see L. 508 – 510 of the revised manuscript):

“However, some studies on noble gas systematics (including our results) support a more fertile signature ($^3\text{He}/^4\text{He} > 7.0 \text{ Ra}$) for some portions of the SCLM on Earth (e.g., Southern Australia and West Antarctic Rift; Matsumoto et al., 1998; Broadley et al., 2016; Correale et al., 2019)”

Figure 8: Your arrow designated with "radiogenic ^4He addition" is wrong. Both axes are affected by such addition. Please, correct.

R: The arrow and the phrase “radiogenic ^4He addition” were removed from the figure 8 to avoid misunderstandings.

Figures 6-9: Please, extend the literature fields, i.e. include the data of Buikin et al. (2005) for the European SCLM, and Hopp et al. (2007) EPSL for the EAR (Kenya data). If you are really want to give a thorough overview you also need to add data from Hopp et al. (2004) and Hopp et al. (2007) (ChemGeol) for Saudi-Arabia / Zabargad Island, and Matsumoto et al. 1998; 2000; as well as Czuppon et al. 2009 ChemGeol, for the Australian SCLM. But this I leave to the authors.

R: As suggested by the Reviewer, data from Matsumoto et al. (1998, 2000), Hopp et al. (2004, 2007a, 2007b), Buikin et al. (2005), and Czuppon et al. (2009), are now included in Figs. 6, 7, 8 and 10.

References:

There is one duplicate reference given (Rizzo et al 2018a and b, but it's the same...). But in the manuscript it is only 2018, seems correct there...

R: Rizzo et al. (2018a) and Rizzo et al. (2018b) are the same. The right reference is Rizzo et al. (2018). The text was fixed accordingly.

The reference of Broadley et al 2020 "Noble gas variations in ureilites..." is not fitting the topic. Please, remove (or correct, if erroneously cited).

R: The Broadley et al. (2020) reference was deleted from the main text. We agree that this reference is not appropriate.

Table 2:

Please, check your concentrations of sample V-I. ^3He is wrong for Opx, ^{36}Ar is wrong for cpx. And I also doubt the Ne in cpx.

R: You are right. Concentrations of sample V-I were accordingly changed since table cells were displaced.

Furthermore, be consistent in formatting (use either exponential or number style, but not both, in isotope data). Use absolute values instead % errors for all. Now, Ar isotope errors are given as % errors, the others as is (but % is shown in header). Add $^{21}\text{Ne}/^{22}\text{Ne}$ (ex to 12.5) in table header in order to make clear what you did. And add if errors are 1sigma or 2sigma uncertainties!

R: In order to be consistent in formatting, isotopic ratios are now reported using a number style except for $\text{CO}_2/{}^3\text{He}$ ratios due to the large number of decimal places.

Errors are now presented as absolute values. Errors are 1σ uncertainties except for the $^{21}\text{Ne}/^{22}\text{Ne}$ (ex to 12.5) ratio whose errors are 2σ uncertainties. See Table 2.

The $^{21}\text{Ne}/^{22}\text{Ne}$ (EX to 12.5) was added in the table header.

Minor points (typos etc.):

L. 57: Insert "of" after "north..."

R: The text has been modified accordingly.

L. 84: Delete the Broadley et al. 2020 reference. It deals with ureilites, not really appropriate here. Maybe you meant a different reference (see also my issue 1 above).

R: The Broadley et al. (2020) reference was deleted from the main text. We agree that this work is not appropriate for this paper.

L. 140: Should be "phlogopite".

R: Corrected

L. 141: Abbreviation of spinel is "sp".

R: Corrected.

L. 213: Delete the closing bracket after "performed". There is no opener.

R: The closing bracket was deleted.

L. 216ff: The air correction of He by application of Ne requires knowledge of the atmospheric He/Ne ratio in your samples. This might not be warranted, because you can fractionate air He and Ne from another by e.g. differences in low temperature solubility in water or simply by preferred loss of He, if introduced by weathering or adsorption.

R: We respectfully consider that the above consideration made by the reviewer does not apply to our study. ${}^3\text{He}/{}^4\text{He}$ ratios were corrected using the ${}^4\text{He}/{}^{20}\text{Ne}$ ratio as well as in many other noble

gas studies of fluid inclusions. Of course, this correction is valid assuming that there is no fractionation between He and Ne, which is true for most of the dataset except for the samples V-I Opx, V-I Cpx, V-H Opx and V-A Opx (see Figure 7A). Nevertheless, the cases of helium loss above reported probably do not affect the correction of their $^3\text{He}/^4\text{He}$ ratios, since $^4\text{He}/^{20}\text{Ne}$ ratios are relatively high. Anyway, samples V-I Opx, V-I Cpx, V-H Opx and V-A Opx were excluded from the discussion. In conclusion, we do not understand why the Reviewer is mentioning a fractionation of air He and Ne invoking differences of solubility in water, since we are dealing with mantle xenoliths in which fluid inclusions are dominated by CO_2 .

L. 222: You may add a reference to your air value (Steiger and Jäger 1977). More recently, most workers rely on the air ratio of Lee et al. 2006, but that won't change much here.

R: Two references for air values were added: Steiger and Jäger (1977) and Ozima and Podosek (2002). See L. 216 of the revised manuscript.

L. 235: In my copy the delta-sign disappeared. Probably only a display problem, but check your article carefully later on.

R: Delta-sign was added.

L. 256: What do you mean with "areas" ? Surface?

R: "areas" refer to specific parts of the thin sections. To avoid misunderstandings, "in specific areas" was deleted (see L. 249 of the revised manuscript).

L. 259: Add closing bracket after "present".

R: A closing bracket was added.

Section 5.4 (and actually everywhere): Please specify, if your reported errors are 1sigma or 2sigma uncertainties.

R: Reported errors are 1σ uncertainties. Conversely, $^{21}\text{Ne}/^{22}\text{Ne}_{\text{Ex}}$ errors are 2σ uncertainties which is specified in Figure 10 and Table 2. This information was added at the beginning of section 5.4 (see L. 297-298 of the revised manuscript) and in Table 2.

L. 311: A positive correlation between $^{40}\text{Ar}^*$ and ^4He is trivial if you have only mantle gases.

R: The phrase "are positively correlated" was deleted and the text was edited accordingly (see L. 302 of the revised manuscript).

L. 316: Maybe I missed that: Can you explain the meaning of " N_2^* "?

R: N_2^* means nitrogen corrected for atmospheric contamination. We erroneously included this term in the main text. N_2^* was deleted.

L. 331ff: Add errors to your values.

R: Errors were added (see L. 317 and L. 323 of the revised manuscript)

L. 332/333: Write simply "expressed as d13C(V-PDB)".

R: The text has been modified accordingly. L. 325 of the revised manuscript.

L. 488: "Therefore, we consider it possible..."

R: The text has been modified accordingly.

L. 588: "noble gas systematics"

R: The text has been edited as follow: "*However, some studies on noble gas systematics (including our results) ...*" (see L. 508 of the revised manuscript).

L. 622: "...a process, which..."

R: The text has been modified accordingly

Reviewer #2: Review of "The composition of fluids stored in the central Mexican lithospheric mantle: inferences from noble gases and CO₂ in mantle xenoliths" by Sandoval-Velasquez et al.,

This manuscript from Sandoval-Velasquez and co-authors presents new noble gas and carbon isotopes, together with Raman spectrometry of fluid inclusions in mantle xenoliths from Central Mexico. The authors find that the noble gas signature of the fluid inclusions is consistent with mixing between an upper mantle (MORB) source and atmosphere, with a potentially subducted origin. The authors conclude that the upper mantle like noble gas signatures indicate that episodes of subduction have had little effect on the composition of the SCLM, or that a subsequent metasomatic event resulting from the Basin and Range extension overprinted the original subducted signature.

The data in the manuscript appear to be of high quality and the conclusions drawn by the authors are for the most part consistent with the data presented. One major criticism of the paper is that it is overly long and the structure could be improved to make it easier for readers to follow the author's arguments. The other major point is that the discussion concerning the recycled atmospheric component in the samples is not fully backed up by the data and the authors should revise this section (see comments below).

In principle I am therefore of opinion that this manuscript should be accepted following moderate revisions. I have set out below sections of the manuscript that I think could be improved.

As below detailed, we shortened the manuscript, modified the structure of the Discussions and integrated the discussion concerning the recycled atmospheric component.

Minor Comments

Highlights:

Line 13 - Try not to use abbreviation in the highlights. These are meant to show the reader the major points without having to read the paper but that is impossible to do if you use abbreviations.

R: Abbreviations such as FI (fluid inclusions) and JH (Joya Honda maar) were removed from the highlights.

Line 18 - Is "subduction retreating" a common term? Perhaps the "retreat of the Farallon slab" is better.

R: "subduction retreating" was replaced by "retreat of the Farallon slab".

Line 22 - Replace "by" with "from" and change to "the subducting Farallon plate"

R: Done

Main Text:

Line 18 - Is it really necessary to abbreviate "fluid inclusions"? In fact the excessive use of abbreviations throughout the manuscript makes it very difficult to follow at times.

R: In order to make the text easier to read, the abbreviation FI was removed.

Line 20 - Change "over-imposed" to "superimposed"

R: Corrected

Line 37 - Delete "by" in the sentence "is consistent by with...."

R: "by" was deleted

Line 51 - Change "consumption" to "subduction"

R: "subduction" was added.

Line 61 - Change to "now allow the composition of the local lithospheric mantle to be probed."

R: The text has been modified accordingly

Line 80 - No need to abbreviate "melt inclusions"

R: The abbreviation for melt inclusions was removed.

Line 84 - I appreciate the citation but I think the authors may have the wrong paper here. Broadley et al., 2020 is about the noble gas signature of Ureilite meteorites. Perhaps a better paper to cite here would be Broadley et al., 2018 End-Permian extinction amplified by plume-induced release of recycled lithospheric volatiles, Nature Geoscience.

R: The Broadley et al. (2020) reference was deleted from the main text. We agree that this reference is not appropriate for this paper.

Line 88 - If the authors insist on abbreviating all the localities then at least use it consistently. Here you use Joya Honda maar even though you have used the abbreviation JH earlier in the paper.

R: “Joya Honda maar” was replaced by “JH”.

Line 100 - What does physiographic province actually mean?

R: In North America, a physiographic province is defined as a geographic region with a characteristic geomorphology that differs significantly from that of adjacent regions (see Atwood, 1940 for more details). In the case of Mexico, La Mesa Central was previously defined as a physiographic province by Raisz (1959) and Nieto-Samaniego et al. (2005) to describe ““a basin surrounded by higher mountains which is higher and flatter than the Basin and Range province (located to the north). Instead of elongated mountains, this has low elevation areas, mainly dissecting ancient volcanic rocks”. However, we removed this term from the text to avoid further details increasing the length of the manuscript.

Line 111 - Try and be consistent with your units. You use metres here but kilometres earlier in the paragraph.

R: The units were changed from meters (m) to kilometers (km) to be consistent.

Line 114/115 - Inconsistent use of abbreviations.

R: The name “Joya Honda maar” was replaced by the abbreviation “JH”.

Line 118 - Try and avoid superlatives and opinions such as "most spectacular". If this has common usage for this are then maybe provide a citation of who said it first.

R: In fact, the superlative “most spectacular” was used by Saucedo et al. (2017). This reference was included in the text (see L. 120 of the revised manuscript).

Figure 1 - The map is very small and difficult to read. Consider making the map and its text larger and the photo smaller as it is not as important to the paper.

R: The figure was modified accordingly. The map and the text have been enlarged and the figure caption was edited accordingly.

Line 145 - 174 - This section is overly long especially since the majority of it comes from one previous publication (Liang and Elthon, 1990). This whole section could be condensed by 50% by only focussing on the most important points and then referring the readers to Liang and Elthon, 1990 if they require further insights in to these samples.

R: As suggested by the Reviewer, Section 3 was condensed focussing on the main petrological characteristics reported by Liang and Elthon (1990), especially in mineral chemistry results and subsequent interpretations.

Line 202 - Not necessary to cite every publication that has used the same analytical procedure. Focus on the first or any further publication that improved upon the method.

R: The main text was edited accordingly. We focused on the publication of Rizzo et al (2018) and Faccini et al. (2020) for noble gas analysis and Gennaro et al. (2017) and Rizzo et al. (2018) for CO₂ isotopic determinations.

Line 209 - How was the gas "purified"?

R: After removing CO₂, the residual gas mixture was purified under Zr-Al getter pumps in a UHV stainless-steel preparation line. Then, Ar, Kr and Xe were removed in a "cold finger" with active charcoal immersed in liquid nitrogen. Finally, He and Ne were adsorbed in a cold head with active charcoal cooled at 10K and then moved at 40 and 80K to release first He and then Ne, respectively.

This section was added, and the text was modified accordingly. See section 4 (L. 202 – 205 of the revised manuscript).

Line 211 - Admitted may be better than injected since it is a static mass spectrometer.

R: "injected" was changed by "admitted"

Line 212 - How was the CO₂ concentration determined?

R: The moles of CO₂ were quantified by measuring the total pressure of gas (CO₂ + N₂ + O₂ + noble gases) released during crushing, using an IONIVAC Transmitters ITR90, in a known volume of the system, then subtracting the residual pressure of N₂ + O₂ + noble gases after freezing CO₂ in a "cold finger" immersed in liquid nitrogen.

This section was added to the main text. L. 199 – 202 of the revised manuscript.

Line 240 - The same paragenesis as what?

R: “*The same paragenesis*” refers to the same mineralogy observed in the samples. In order to avoid misunderstandings, the word “paragenesis” was replaced by “mineralogy” and the text was edited as follows (L. 235 of the revised manuscript):

“The suite of xenoliths exhibits the same mineralogy”

Section 5.1 - A lot of this is repetition of what has been reported earlier in section 3. Try and condense these sections such that there is as little overlap as possible. For example if you find the exact same texture, size, shape etc as has been previously reported then it is fine to just state this. There is no need to repeat it.

R: As mentioned above, section 3 was condensed to avoid overlapping. As suggested by the reviewer, petrographic characteristics of mantle xenoliths were removed from section 4 (now section 3) and are only presented in section 5.4.

Line 284 - Should be "... among which there is an opaque phase."

R: The text has been modified accordingly

Line 292 - Do you have an explanation as to why the dolomite vibrations are "unexpectedly weak"?

R: weak vibrations could be associated with strong Raman scattering because of disorder (see Frezzotti et al., 2012a). This information is now provided in the main text (see L. 284 of the revised manuscript).

Line 295 - Consider adding a citation here.

R: The references Peccerillo and Frezzotti (2007), Carter et al. (2009) and Frezzotti et al. (2012a) were added. L. 288 of the revised manuscript.

Line 296 - Can you link these analyses to the photomicrographs (figure 4)? For example is the olivine that was analysed shown in figure 4?

R: Yes. In fact, spectra presented in Figures 5A, 5B and 5C correspond to inclusions analysed in Figures 4C, 4D and 4B, respectively. Details are now provided in Figure 5 (see the figure caption).

Line 304 - Change "chemical" to "elemental" since this is the title of this section.

R: “chemical” was changed by “elemental”.

Line 306-321 - Usually it is sufficient to report the concentrations of only the most abundant isotopes. If the reader needs the concentration of the less abundant isotopes we can go to the table or use the ratios to calculate. It just makes it easier for the reader to follow as they are not saturated with values.

R: As suggested by the reviewer, concentrations of the less abundant isotopes such as ^3He and ^{36}Ar were removed from the text.

Line 323 - Is this positive correlation shown in figure 8? If so maybe reference this figure here. Also looking at figure 8 it is hard to see any evidence of a positive correlation. Now this may be down to the use of a log scale on the x-axis but if you are claiming they are correlated then you should show that clearly to the reader.

R: We agree that a positive correlation between $^4\text{He}/^{40}\text{Ar}^*$ and Rc/Ra values is hard to see. The statement “are positively correlated with Rc/Ra” was removed and the text was modified as follows (see L. 315 of the revised manuscript):

“The $^4\text{He}/^{40}\text{Ar}^$ ratios vary between 0.14 and 3.11 (Figure 8), which overlaps in part the typical production ratio of the mantle”*

Line 327 - I am confused by this statement. In the previous sentence you state that the highest 4/20 is 10483 but then you state that the CPX (which have the highest 4/20) max out at 2223. Are these averages? Either way state what these values represent (average, medium, max etc.)

R: Yes, these are averages. The text was modified accordingly (L. 318 – 320 of the revised manuscript):

“ $^4\text{He}/^{20}\text{Ne}$ values range from 2.4 to 10483; the highest values are recorded in Cpx and Ol (on average 2223.2 ± 3196.8 and 1498.6 ± 1306.1 , respectively), while Opx exhibits considerably lower ratios (< 639)”

Line 332 - Delta symbol appears to be missing.

R: Delta symbol was added.

Figure 6 - Again figure are hard to read and interpret. Try and make them bigger for the published version.

R: As suggested, the figure was made bigger for the published version.

Line 355 - What do you mean by we "stand on the above"?

R: With “stand on the above” we mean “based on”. With this sentence we want to emphasize the importance of using both tools (petrography and isotopes) to properly discuss the characteristics of the local mantle. In order to avoid misunderstandings, the text was modified as follows (see L. 346 – 348 of the revised manuscript):

“In the discussion below, we combined the above petrographic evidence and the isotopic signatures (noble gases and CO_2) of the JH fluid inclusions to constrain volatile origin and mantle characteristics.”

Section 6 - I would suggest you reorder the discussion a little. Personally I think it would be better if you discuss your new data in relation to the different mantle signatures and what this means for the different potential processes and then discuss the possible secondary processes. At the moment discussing secondary processes before you even identify the primary signature is bizarre.

R: We appreciate the reviewer suggestion. We reordered the discussion. First, the title “Secondary processes” was removed because we consider it ambiguous; second, the subsection 6.1.1 “*Atmospheric contamination*” is no longer considered as a secondary process since it is an intrinsic characteristic of the local mantle (see subsections 6.2 and 6.4.1, now merged in a unique section); the title of this subsection was replaced by “*Interaction with atmospheric fluids*” as suggested by Reviewer 1; third, Section 6.1.2 “Diffusive Fractionation”, section 6.1.3 “*Exposure to cosmic rays*” and Section 6.2 “The effect of partial melting” were deleted from the main text and moved in supplementary information.

In summary, the discussion was reordered as follows:

6. Discussion

6.1 Inferences on the noble gas signature of the JH source mantle

6.1.1 Interaction with atmospheric fluids and evidence for a recycled atmospheric component 6.1.2
Noble gas signature of the JH mantle source.

6.2 ^3He fluxes, ^4He production and the helium residence time for the Mexican lithospheric mantle.

6.2.1 Mantle CO₂ fluxes

6.3 Inferences on CO₂ origin

Figure 7 - Again could be made bigger.

R: As suggested, the figure was made bigger for the published version.

Line 389 - Where is this CO₂ depletion shown. In a figure or table? Make reference to where the reader can find evidence for this depletion.

R: A reference was added, and the text was edited as follows: “*Some CO₂ depletion is also evident in sample V-I (Figure 6C)*”. See L. 43 – 44, in supplementary material.

Line 424 - This section is irrelevant to your study. There is no evidence of cosmogenic noble gases in your study so there is no need for this section. Can be deleted.

R: We agree that section 6.1.3 is irrelevant, therefore this was removed from the main text and moved to supplementary information.

Line 452 - What do you mean by "sensibly lower than"?

R: We realize that this sentence is not clear. Our statement commented by the Reviewer was made by Rizzo et al. (2018), following the partial melting modeling discussed in e.g. Correale et al. (2016). The batch and fractional melting modeling is based on the crystal-melt partition coefficients of noble gases and $^4\text{He}/^{40}\text{Ar}^*$ ratios measured in mantle xenoliths from the Yangtze Craton (China) and Lower Silesia (Poland). Following this approach, the degree of partial melting calculated from our $^4\text{He}/^{40}\text{Ar}^*$ ratios would be considerably lower than that proposed by petrological studies (10-20%, Liang and Elthon, 1990). Nevertheless, since in this paper we are not dealing with these models, the phrase "*In fact, the calculated noble gas-based partial melting degrees do not match (are sensibly lower than) those obtained from lithophile elements-based models*" was deleted to avoid misunderstandings.

Line 465 - It has taken 465 lines to finally discuss the primary mantle origin of these samples. This section should be discussed earlier in the paper.

R: As mentioned above, the discussion was modified and the paper shortened.

Section 6.3.1 - Firstly, petrographic data cannot be used as evidence for a recycled origin for the atmospheric component. I do not think you have clearly distinguished between air contamination and recycling. There are methods to do this see Matsumoto et al., 2001 and Broadley et al., 2016 which both showed that the atmospheric Ar component was likely recycled due to the correlation between ^3He and ^{36}Ar .

Furthermore, Ne is not generally considered to be efficiently subducted so just by saying your Ne data look similar to Ne data from other localities that have been shown to contain a recycled component is not sufficient to conclude that your samples contain a recycled component. This section needs to be revised.

R: We agree with the Reviewer. As suggested, section 6.3.1 was modified (see section 6.1.1). We included the new diagrams ^{36}Ar vs ^3He and $^{20}\text{Ne}/^{22}\text{Ne}$ vs $^{40}\text{Ar}/^{36}\text{Ar}$ to properly evaluate the impact of subduction-related atmospheric fluids in our mantle xenoliths. We realized that a positive correlation between ^3He and ^{36}Ar exists (in samples with $^{40}\text{Ar}/^{36}\text{Ar} > 500$), as already observed in the papers suggested by the Reviewer#1 and #2. The variability of $^{20}\text{Ne}/^{22}\text{Ne}$ and $^{40}\text{Ar}/^{36}\text{Ar}$ ratios support the existence of an atmospheric component recycled in the local lithospheric mantle. Further details on the above considerations and on the modelling that led us to now estimate a

possible $^{40}\text{Ar}/^{36}\text{Ar}$ of the local mantle, are provided in the response to the comment 6 of Reviewer #1 and in the main text (see L. 383 – 400 of the revised manuscript).

Besides, the sentence “Moreover, since Ne isotopes of JH overlap the fields of data from WARS and European SCLM mantle xenoliths, the recycling of an atmospheric component in the lithospheric mantle may be common to many other geodynamic contexts” was deleted to avoid misunderstandings.

Section 6.3.3 - This should be combined with the previous section as a general section on the mantle origin of the samples.

R: As suggested by the Reviewer, section 6.3.3 and section 6.3.2 were combined. The new section (6.1.2) was entitled “Noble gas signature of the JH mantle source”

Line 524 - Broadley et al., 2016 also reported average $^3\text{He}/^4\text{He}$ values of 8.7 ± 0.3 for WARS xenoliths.

R: According to the study of Correale et al. (2019), which followed that of Broadley et al. (2016), we added the average estimated by Broadley et al. (2016) for those values not affected by the release of cosmogenic helium (Baker Rocks and Browning Pass samples; 7.5 ± 0.45 Ra). We also updated Figures 7, 8 and 10 with this information. The text was edited as follows (L. 443 – 444 of the revised manuscript):

“This $^3\text{He}/^4\text{He}$ signature is similar to that measured at the WARS (7.5 ± 0.45 Ra and 7.1 ± 0.4 Ra; Broadley et al., 2016; Correale et al., 2019) ...”

Line 533 - I see no evidence for a recycled Ne signature.

R: As mentioned above, the existence of an atmospheric component recycled in the local mantle is supported by the correlation between ^3He - ^{36}Ar contents and $^{20}\text{Ne}/^{22}\text{Ne}$ - $^{40}\text{Ar}/^{36}\text{Ar}$ ratios. However, to avoid misunderstandings the text was modified as follows (L. 454 – 456 of the revised manuscript):

“If this interpretation is correct, then past subduction events would only have added a recycled atmospheric component into the mantle (cfr 6.1.1).”

Line 534 - Doesn't require the addition of crustal material. You can add recycled air in fluids without any need for crustal material.

R: The word “crustal” was removed to avoid misunderstandings. L. 457 of the revised manuscript.

Line 560 - What do you mean by "Independently on..."?

R: We mean that, even if our hypothesis about the influence of subduction in the local mantle is erroneous, the petrographic evidence does demonstrate a metasomatic event affecting our mantle

xenoliths. However, we replaced “Independently on” with “Irrespective of”, with the hope to have clarified the meaning of this sentence.

Line 597 - Is there plans to publish this data ? I am not sure what the journals rules are concerning unpublished data but maybe the editor can advice whether this is appropriate.

R: Yes, we plan to publish this data soon. According to the Guide for Authors “Unpublished results and personal communications are not recommended in the reference list, but may be mentioned in the text”.

Line 606 - It is not immediately clear to me how these fluxes are calculated. More detail on how these calculations were done should be provided.

R: More details on the subcontinental mantle mass as well as the total mass of ^3He considered in the calculations are now provided in subsection 6.2 (see L. 508 – 536 of the revised manuscript). The formulas used to estimate ^3He flux, ^4He production and the helium residence time (Rt) were included and described in the text.

Figure 10 - It might be useful to scale the flux to the area in another box. That way you can show how efficient degassing is at each site.

R: Fluxes were scaled to the area and plotted in Figures 11B and 11D. The text and the figure caption were edited accordingly.

1 **THE COMPOSITION OF FLUIDS STORED IN THE CENTRAL MEXICAN LITHOSPHERIC MANTLE:**
2 **INFERENCES FROM NOBLE GASES AND CO₂ IN MANTLE XENOLITHS**

3 A. Sandoval-Velasquez¹, A.L. Rizzo², M. Frezzotti³, R. Saucedo⁴ and A. Aiuppa^{1,2}.

4

5 **Highlights**

6 • Fluid inclusions are used to study the chemical signature of the Mexican subcontinental
7 mantle

8

9 • Inclusions identified in the xenoliths are composed of glass ± CO₂ ± carbonates ± pyrite

10

11 • Isotopes reveal a mixing of atmospheric, MORB-like and carbonate-rich fluids

12

13 • Mantle refertilization would occur after the retreat of the Farallon slab

14

15 • Carbonates and atmospheric fluids are inherited from the subducting Farallon plate.

16

17

1 **THE COMPOSITION OF FLUIDS STORED IN THE CENTRAL MEXICAN**
 2 **LITHOSPHERIC MANTLE: INFERENCES FROM NOBLE GASES AND CO₂ IN MANTLE**
 3 **XENOLITHS**

4 A. Sandoval-Velasquez¹, A.L. Rizzo², M. Frezzotti³, R. Saucedo⁴ and A. Aiuppa^{1,2}.

5

6 **Author's affiliations**

7 ¹*DiSTeM, Università di Palermo, Via Archirafi 36, 90123 Palermo, Italy.*

8 ²*Istituto Nazionale di Geofisica e Vulcanologia (INGV), Sezione di Palermo, Via Ugo La Malfa 153,*
 9 *90146 Palermo, Italy,*

10 ³*Dipartimento di Scienze dell'Ambiente e della Terra, Università di Milano Bicocca, Piazza della*
 11 *Scienza 4, 20126 Milano, Italy,*

12 ⁴*Instituto de Geología, Universidad Autónoma de San Luis Potosí, Dr M. Nava no. 5, Zona*
 13 *Universitaria, 78240 San Luis Potosí, México*

14

15 **Corresponding author e-mail:** andreslibardo.sandovalvelasquez@unipa.it

16

17 **ABSTRACT**

18 We present the first isotopic (noble gases and CO₂) characterization of fluid inclusions (~~FI~~-ecoupled
 19 to Raman microspectroscopy analyses in mantle xenoliths from Central Mexico, a geodynamically
 20 complex area where the Basin and Range extension was ~~over imposed~~superimposed on the Farallon
 21 subduction (terminated at 28 Ma). To characterize the isotopic signature of the Central Mexican
 22 lithospheric mantle, we focus on ~~FI~~fluid inclusions entrapped in mantle xenoliths found in deposits
 23 of the Joya Honda maar (JH), a Quaternary monogenetic volcano belonging to the Ventura Espiritu
 24 Santo Volcanic Field (VESVF) in the state of San Luis Potosí (central Mexico). Thirteen ultramafic
 25 plagioclase-free xenoliths were selected, all exhibiting a paragenesis Ol> Opx> Cpx >> Sp, and being
 26 classified as spinel-lherzolites and harzburgites. All xenoliths bring textural evidence of interstitial
 27 glass veins bearing dendritic trails of secondary melt and fluid inclusions (composed of silicate glass
 28 ± CO₂ ± Mg-Ca carbonates ± pyrite). These are related to pervasive mantle metasomatism driven by
 29 carbonate-rich silicate melt. The Ar and Ne systematics reflect mixing between MORB-like upper
 30 mantle and atmospheric fluids, the latter interpreted as reflecting a recycled air component possibly
 31 inherited from the Farallon plate subduction. The ³He/⁴He ratios vary between 7.13 and 7.68 Ra,
 32 within the MORB range (7-9 Ra), and the ⁴He/⁴⁰Ar* ratios (0.4- 3.11) are similarly close to the
 33 expected range of the fertile mantle (1-5). Taken together, these pieces of evidence suggest that (i)
 34 either the mantle He budget was scarcely modified by the Farallon plate subduction, and/or (ii) that
 35 any (large) crustal contribution was masked by a later metasomatism/refertilization episode, possibly
 36 during the subsequent Basin and Range extension. A silicate melt-driven
 37 metasomatism/refertilization (revealed by the association between glass veins and ~~FI~~fluid inclusions)
 38 is consistent ~~by~~with calculated helium residence time for the Mexican lithospheric mantle (20 to

39 60Ma) that overlaps the timing of the above geodynamic events. We propose that, after the
40 refertilization event (e.g., over the last ~20Ma), the lithospheric mantle has evolved in a steady-state,
41 becoming slightly more radiogenic. We also estimated ^3He fluxes (0.027 - 0.080 mol/g), ^4He
42 production rates (340 - 1000 mol/yr), and mantle CO_2 fluxes (3.93×10^7 mol/yr to 1.18×10^8 mol/yr)
43 using the helium isotopic values measured in JH mantle xenoliths. Finally, the JH xenoliths exhibit
44 $\text{CO}_2/{}^3\text{He}$ ratios comparable to those of the upper mantle (from 3.38×10^8 to 3.82×10^9) but more
45 positive $\delta^{13}\text{C}$ values (between -1.0 and -2.7‰), supporting the involvement of a crustal carbonate
46 component. We propose that the metasomatic silicate melts recycled a crustal carbonate component,
47 inherited by the Farallon plate subduction.

48 **Keywords:** Mexican mantle xenoliths; fluid inclusions; noble gases; CO_2 ; mantle refertilization; carbonate
49 recycling.

50

51 1. INTRODUCTION

52 The ~~consumption-subduction~~ of the Farallon oceanic slab under the North American plate, during the
53 late Oligocene and Middle Miocene, has given rise to enormous changes in the tectonic configuration
54 of the northwestern coast of Mexico. These include the transition from a compressive to a transform
55 margin, and the beginning of a regional extension that produced the Basin and Range Province
56 (Atwater, 1989; Ferrari et al., 2012; Henry and Aranda-Gomez, 1992; Sedlock, 2003).

57 The Basin and Range extension started about 30Ma and was accompanied by intraplate magmatism,
58 which generated several volcanic fields north of the Transmexican Volcanic Belt (TMVB; Aranda-
59 Gómez and Ortega-Gutiérrez, 1987; Luhr and Aranda-Gómez, 1997; Henry and Aranda-Gomez,
60 1992). These fields are typically monogenetic complexes associated with the eruption of alkaline
61 basalts and basanites that have brought to the surface significant amounts of ultramafic xenoliths that
62 now allow ~~the composition of the local lithospheric mantle to be probed~~ ~~probing the composition of~~
63 ~~the local lithospheric mantle~~.

64 The Ventura Espiritu Santo Volcanic Field (VESVF), located in the San Luis Potosí state (central
65 Mexico), is one of the best-known examples of this volcanism, and is characterized by spectacular
66 volcanic structures like the Joya Honda maar (JH), and by frequent ultramafic nodules found in its
67 deposits. Other mantle xenoliths-bearing alkali basalt localities are the Santo Domingo Volcanic
68 Field (SDVF) also located in the San Luis Potosí state, the Pinacate Volcanic Field (PiVF), Las
69 Palomas Volcanic Field (PaVF), the Potrillo maar (Po), the Camargo Volcanic Field (CVF), the
70 Durango Volcanic Field (DVF), the San Quintin Volcanic Field (SQVF) and Isla Isabel (II; Figure
71 1; Basu, 1977; Gutmann, 1986; Aranda-Gómez and Ortega-Gutiérrez, 1987; Luhr et al., 1989; Pier
72 et al., 1992; Luhr and Aranda-Gómez, 1997; Housh et al., 2010).

73 These volcanic structures in the central and NW portion of Mexico, and the textural and petrological
74 characteristics of their ultramafic xenoliths, have already been discussed elsewhere (Aranda-Gómez
75 and Ortega-Gutiérrez, 1987; Luhr and Aranda-Gómez, 1997; Henry and Aranda-Gomez, 1992).
76 These previous studies have revealed a complex (multi-stage) history of deformation, melting and
77 metasomatism, and opened new questions on the evolution of the Mexican lithospheric mantle.
78 Debate exists, however, on the provenance of the metasomatic fluids, and if and to what extent
79 subduction of the Farallon plate has modified mantle composition during the recent Mexican

80 geological history (Pier et al., 1989; Luhr and Aranda-Gómez, 1997; Dávalos-Elizondo et al., 2016).
81 Addressing these questions requires information on the chemical features of metasomatic fluids
82 present in the lithospheric mantle. Fluid- and melt inclusions (~~FI and MI~~) preserved in mantle
83 xenoliths are well known for being valuable sources of information to study the evolution of volatile
84 species trapped in ultramafic mantle rocks, and to derive inferences about the local lithospheric
85 mantle dynamics (Roedder, 1984; Andersen and Neumann, 2001; ~~Gautheron and Moreira, 2002;~~
86 ~~Deines, 2002; Frezzotti et al., 2002a; Buikin et al., 2005; Gautheron et al., 2005a; Martelli et al.,~~
87 ~~2011; Day et al., 2015; Broadley et al., 2016; Rizzo et al., 2018; Correale et al., 2019; Faccini et al.,~~
88 ~~2020).~~

Field Code Changed

89 Here, we aim at filling this gap of knowledge on the volatile composition of the Mexican lithospheric
90 mantle, by reporting on the chemical and isotopic composition (He, Ne, Ar and CO₂) of ~~FI-fluid~~
91 ~~inclusions~~ entrapped in mantle xenoliths found in the ~~Joya Honda maar~~JH. Noble gases are sensitive
92 tracers that provide insights on fluid origin, the composition and evolution of the mantle, and their
93 relationship with different tectonic processes such as subduction (~~Matsumoto et al., 2001; Hopp et~~
94 ~~al., 2007a; Hopp and Ionov, 2011; Martelli et al., 2014; Broadley et al., 2016; Faccini et al., 2020)~~
95 ~~or mantle plumes (Farley and Neroda, 1998; Graham, 2002; Gautheron and Moreira, 2002; Hopp et~~
96 ~~al., 2004, 2007a, 2007b; Gautheron et al., 2005a; Martelli et al., 2011; Correale et al., 2012, 2016,~~
97 ~~2019; Buikin et al., 2005; Halldórsson et al., 2014; Boudoire et al., 2018, 2020; Day et al., 2015;~~
98 ~~Broadley et al., 2016; Rizzo et al., 2018; Faccini et al., 2020).~~ In addition, studying CO₂ abundance
99 and isotopic composition contribute to assessing composition and provenance of metasomatic fluids
100 that may have interacted with these xenoliths (Sano and Marty, 1995; Correale et al., 2015; Gennaro
101 et al., 2017; Rizzo et al., 2018), for example revealing any addition to the mantle of carbonate-rich
102 fluids delivered by sediments and altered oceanic crust in the subducted slab (Plank and Manning,
103 2019).

Formatted: Line spacing: Multiple 1.08 li

Formatted: English (United States)

104

105 2. GEOLOGICAL SETTING

106 The VESVF is located in the southern portion of the ~~physiographic~~ province known as the Mesa
107 Central (Raisz, 1959; Nieto-Samaniego et al., 2005); very close to the Sierra Madre Oriental province
108 (Figure 1). The Mesa Central, located north of the TMVB, comprises a portion of continental crust
109 that has a thickness of 32 km and is delimited by regional faults (Fix, 1975; Nieto-Samaniego et al.,
110 2005). The oldest rocks found in this province are muscovite schists from the Paleozoic (252 Ma),
111 superimposed by turbiditic sequences of the Triassic and volcano-sedimentary sequences of
112 continental origin formed during the mid-late Jurassic (Barboza-Gudiño et al., 1999; Morán-Zenteno
113 et al., 2005; Nieto-Samaniego et al., 2005). The most abundant outcrops correspond to sequences of
114 calcareous rocks of marine origin, formed during a transgression episode during the end of the late
115 Jurassic and the Cretaceous (Carrillo-Bravo, 1971; López-Doncel, 2003; Nieto-Samaniego et al.,
116 2005); these rocks make up the so-called Valles-San Luis Potosí Platform (PVSLP) and the Mesozoic
117 Basin of Central Mexico whose thickness can reach ~~5000-5~~ km and ~~6~~ km, respectively. Cenozoic
118 rocks are mainly volcanic and sedimentary (of continental origin), the most recent being the alkaline
119 basalts of the VESVF, SDVF and DVF whose origin is related to a melting zone located 34 km deep
120 under the Mesa Central (Fix, 1975).

Formatted: English (United States)

121 The VESVF is formed by some isolated scoria cones and three maars among which is the ~~Joya Honda~~
122 ~~maar~~JH (Aranda-Gómez et al., 2007; Saucedo et al., 2017). The JH is located at the intersection

Formatted: Line spacing: Multiple 1.08 li

123 between the PVSLP and the Mesozoic Basin of central Mexico (22 ° 25'4.97 "N and 100 ° 47'15.62"
 124 W), and is thought to have formed at about 311 ± 19 ka (Saucedo et al., 2017). This volcano is
 125 recognized as one of the most spectacular volcanic structure of the VESVF Mexico (Saucedo et al.,
 126 2017), with its elliptical crater having vertical walls defining a 150 – 300 m deep depression (Figure
 127 1). The maar formed through a series of mixed magmatic and phreatomagmatic eruptions that
 128 emplaced a sequence of pyroclastic falls and base surge deposits (having a maximum thickness of
 129 ~100 m). Magma–groundwater interaction is thought to have occurred during magma ascent through
 130 of a NE-SW normal fault system cutting folded limestones, calcareous mudstones, chert lenses and
 131 shales which are part of the Cuesta del Cura (Albian-Cenomanian) and Tamaulipas (Aptian)
 132 Formations (Aranda-Gómez and Luhr, 1996; Aranda Gómez et al., 2000; Saucedo et al., 2017).
 133 Saucedo et al. (2017) identified 5 eruptive phases, the last two of which generated deposits rich in
 134 mantle xenoliths. The erupted magmas are alkaline and mafic in composition (olivine-nepheline
 135 basanites and olivine basalts), and their origin is thought to be associated with decompressional
 136 melting of the asthenosphere and lithospheric mantle under la Mesa Central, as proposed for other
 137 volcanic fields associated to the Basin and Range extension (Aranda-Gómez and Ortega-Gutiérrez,
 138 1987; Luhr et al., 1989; Lee, 2005; Aranda-Gómez et al., 2007).

139

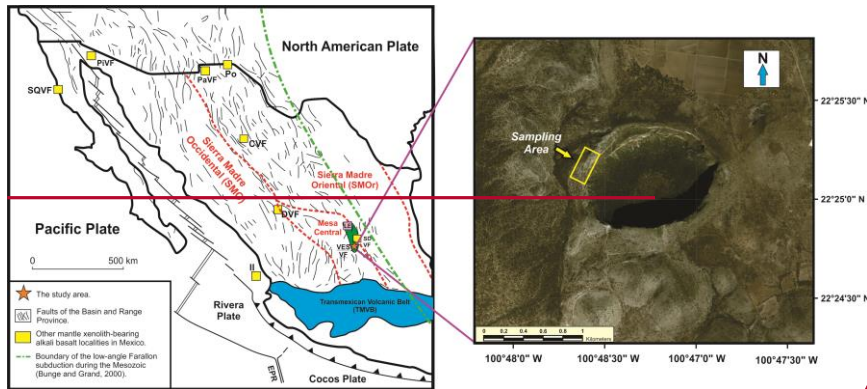


Figure 1. Location of the Joya Honda maar (JH) and geodynamic setting. The left image shows the Mexican part of the Basin and Range Province which has an extension of $9.4 \times 10^4 \text{ km}^2$ (Henry and Aranda Gómez, 1992); the image was adapted from Aranda-Gómez et al. (2000). The green area is the area used to estimate the ^3He production, the helium residence time and ^3He CO_2 fluxes for the lithospheric mantle located under San Luis Potosí state (see sections 6.2.3 and 6.2.4). The pink square represents the location of the Los Encinos Volcanic Field (LE); although this is a monogenetic volcanic field associated with the Basin and Range extension, this lacks mantle xenoliths. Contours of Sierra Madre Occidental, Sierra Madre Oriental, the Transmexican Volcanic Belt and Mesa Central provinces were build based on Gómez Tuena et al. (2007). VESVF: Ventura-Espiritu Santo Volcanic Field, SDVF: Santo Domingo Volcanic Field, PiVF: Pinateate Volcanic Field, PaVF: Las Palomas Volcanic Field, Po: Potrillo maar, CVF: the Camargo Volcanic Field, DVF: Durango Volcanic Field, SQVF: San Quintín Volcanic Field, II: Isla Isabel. Right Image: Google Earth image (February 20th, 2020) showing the Joya Honda maar morphology and sampling area.

140

141 3. PETROLOGICAL BACKGROUND

142 The JH mantle xenoliths have been previously studied and described as spinel lherzolites and
 143 harzburgites (Aranda-Gómez and Ortega-Gutiérrez, 1987; Liang and Elthon, 1990; Luhr and Aranda-
 144 Gómez, 1997). Petrographically, these authors have recognized a protogranular to equigranular

Formatted: Font: Times New Roman, Font color: Black, English (United States)

Field Code Changed

Formatted: Spanish (Latin America)

Formatted: Spanish (Latin America)

Field Code Changed

Field Code Changed

Field Code Changed

Formatted: Spanish (Latin America)

Formatted: Spanish (Latin America)

Field Code Changed

Formatted: Spanish (Latin America)

Formatted: Spanish (Latin America)

Formatted: Font: Not Bold, Spanish (Latin America)

Formatted: Spanish (Latin America)

Formatted: Spanish (Latin America)

Formatted: Spanish (Latin America)

Field Code Changed

Formatted: Font: Not Bold, Spanish (Latin America)

Formatted: Spanish (Latin America)

Formatted: Spanish (Latin America)

145 ~~texture with olivines (Ol), orthopyroxenes (Opx) and clinopyroxenes (Cpx) crystals with size > 2~~
146 ~~mm.~~ The modal composition indicates a relatively constant paragenesis: Ol is the most abundant
147 phase (55-88%), followed by Opx (17-32%), Cpx (1-17%) and Spinel (Sp; 0.3 - 5%); in very few
148 cases, the presence of ~~ph~~phlogopite is also reported with percentages below 1% (Lühr and Aranda-
149 Gómez, 1997). Compositionally, Ol has a Mg# ($Mg\# = 100 \times Mg / (Mg + \sum Fe)$) ranging from 87.5 to
150 91, Opx from 88.6 to 91.2, Cpx from 87.7 to 91.4 and ~~Sp~~in from 75.5 to 82.5 (Liang and Elthon,
151 1990). These authors also report the development of Na-Al poor spongy rims on Opx, Cpx and spinel,
152 explained as due to variable degrees of partial melting that have affected the local upper mantle.

153 Liang and Elthon (1990) classified the xenoliths into two groups based on their modal and
154 geochemical compositions (groups Ia and Ib). In group Ia peridotites, olivines have Mg# ($Mg\#$
155 $= Mg / (Mg + Fe) * 100$) ranging from 89.40 to 90.41, $\sum FeO$ values from 9.42 to 10.38 wt%, and NiO
156 from 0.38 to 0.43 wt%. Mg# in orthopyroxenes vary between 89.86 and 91.21, $\sum FeO$ values range
157 from 5.69 to 6.57 wt%, Na_2O values from 0.08 to 0.15 wt%, and CaO from 0.67 to 0.90 wt%. Cores
158 of Ia clinopyroxenes have high Mg# (89.7 – 91.4), elevated CaO contents (19.27 – 21.43 wt%), Na_2O ,
159 and Al_2O_3 (0.88 – 1.79 wt% and 6.04 – 7.01 wt%, respectively) and LREE (Light Rare Earth
160 Element) depleted patterns ($(La/Yb)_N < 0.8$). Chromian spinels were reported in both groups of
161 peridotites: spinels of group Ia exhibit Cr# values ($Cr\# = 100 \times Cr / (Cr + Al)$) between 79.66 and
162 82.56 which are negatively correlated with Ol Mg# values. Mantle xenoliths from group Ia are
163 interpreted as mantle residues generated by different degrees of partial melting and extraction of
164 picritic melts in the upper mantle; these authors calculated a degree of partial melting between 7%
165 and 22% for Ia xenoliths, using melting models based on bulk-rock MgO, Ni and Sc abundances.
166 Group Ib peridotites exhibit similar degrees of partial melting (1-20%) followed by metasomatic
167 enrichment (Liang and Elthon, 1990). One of the most important characteristic of Ib xenoliths is the
168 extreme core-to-rim chemical zoning (and LREE-enriched patterns; $(La/Yb)_N > 0.8$) in
169 clinopyroxene, revealed by a decrease of Al_2O_3 and Na_2O towards the rim, while Mg#, CaO, TiO_2
170 and Cr_2O_3 tend to increase (Liang and Elthon, 1990). According to these authors, high FeO- Na_2O
171 contents in the cores of Ib minerals and LREE enrichment in Cpx crystals suggest interaction between
172 silicate melts (basaltic in composition) and a residual mantle similar to group Ia xenoliths.
173 Additionally, they explain the extreme core-to-rim chemical zoning, and reaction rims in Cpx, by the
174 reaction with H_2O -rich fluids depleting Cpx rims in Na_2O and Al_2O_3 (also increasing TiO_2 contents).

175

176 Generally, Ib olivines have lower Mg# values ranging from 87.76 to 89.32, ($\sum FeO$ from 10.37 to
177 11.89 wt%), and NiO contents from 0.38 to 0.40 wt%. Ib orthopyroxenes also exhibit lower Mg# and
178 higher Na_2O and $\sum FeO$ contents if compared with group Ia peridotites; Mg# values vary from 88.61
179 to 89.75, $\sum FeO$ from 6.56 to 7.26 wt%, Na_2O values from 0.19 to 0.22 wt% and CaO from 0.72 to
180 0.80 wt%. Ib clinopyroxenes core analysis reveal low Mg# (87.78 – 88.99), low CaO (17.41 – 18.58
181 wt%), high Na_2O (2.40 – 2.74 wt%) and high Al_2O_3 contents (7.21 – 7.67 wt%) if compared with Ib
182 clinopyroxenes. Finally, chromian spinels have relatively low Cr# (75.59 – 79.87) and are positively
183 correlated with Mg# values measured in olivines. One of the most important characteristic of Ib
184 xenoliths is the extreme core to rim chemical zoning (and LREE enriched patterns; $(La/Yb)_N > 0.8$)
185 in clinopyroxene, revealed by a decrease of Al_2O_3 and Na_2O towards the rim, while Mg#, CaO,
186 TiO_2 and Cr_2O_3 tend to increase (Liang and Elthon, 1990). Group Ib peridotites exhibit similar
187 degrees of partial melting (1-20%) followed by metasomatic enrichment (Liang and Elthon, 1990).

188 ~~According to these authors, high FeO-Na₂O contents in the cores of Ib minerals and LREE~~
189 ~~enrichment in Cpx crystals suggest interaction between silicate melts (basanitic in composition) and~~
190 ~~a residual mantle similar to group Ia xenoliths. Additionally, they explain the extreme core to rim~~
191 ~~chemical zoning, and reaction rims in Cpx, by the reaction with H₂O rich fluids depleting Cpx rims~~
192 ~~in Na₂O and Al₂O₃ (also increasing TiO₂ contents).~~

194 195 4. SAMPLES AND METHODS

196 Samples were collected from the eastern part of the JH (Figure 1), where units IV and V emerge
197 according to the stratigraphy described by Saucedo et al. (2017). These units are composed of
198 pyroclastic fall and flow deposits where the highest concentration of mantle xenoliths is found. The
199 nodules are usually dispersed within or hosted in basanitic lavas. Thirteen fresh nodules were selected
200 with diameters between 5 and 10 cm; additionally, a pyroxenite sample was studied (sample V-C)
201 and was only used for noble gas analysis due to its small diameter (<5 cm). Eight nodules were
202 selected for petrographic analysis on thin and polished sections. Petrographic analysis was performed
203 at the petrography laboratory of the University of Milano-Bicocca based on the textural classification
204 proposed by Mercier and Nicolas (1975); the modal composition was carried out by point counting
205 (from 4000 to 7000 points per section).

206 Two double-polished rock sections of about 130 μm thickness were selected for the Raman of fluid
207 inclusions. Analyzed ~~fluid inclusions~~ are located at 10 to 20 μm depth below the sample surface.
208 Analyses were performed using a Labram Evolution (Horiba Scientific, Japan) at the Dipartimento
209 di Scienze dell'Ambiente e della Terra, Università Milano Bicocca. The polarized Raman spectra
210 were excited using a green Ar-ion laser operating at 532 nm, with 50-70 mW emission power. Spectra
211 acquisition was performed with a backscattered geometry and a 600 g/mm diffraction grating. A
212 transmitted light Olympus B40 microscope with a 100 × objective (Numerical aperture, N.A., = 0.90)
213 was used for all the acquisitions (spatial resolution < = 1 μm). Confocality was maintained with a
214 pinhole of 100 μm. Spectra were collected with variable acquisition times (from 20 to 30 sec). The
215 spectrometer was calibrated using a Silicon standard. To increase band attribution accuracy better
216 than 0.2 cm⁻¹, spectra were baseline corrected and processed by statistical analysis (Fityk software;
217 Wojdyr, 2010) using a Voigt Pseudo-function, a convolution of a Lorentzian with a Gaussian line
218 shape. Mineral and fluid identification has been based on our reference spectra database (Frezza et
219 al., 2012a).

220 Noble gas and CO₂ isotopic determinations were performed at the noble gas and stable isotopes
221 laboratories of INGV, Sezione di Palermo, following the preparation methods and analytical
222 procedures described in ~~Nuccio et al. (2008), Gennaro et al. (2017), and Rizzo et al. (2018) and~~
223 ~~Faccini et al. (2020), Correale et al. (2015, 2019), Gennaro et al. (2017), Rizzo et al. (2018), and~~
224 ~~Faccini et al. (2020)~~. All xenoliths were crushed and sieved with the aim of hand-picking crystals
225 with diameters >0.5 mm. Thirty-five aliquots (13 Ol, 11 Opx and 13 Cpx) of crystals (weights of
226 0.05 to 2 g) were selected for noble gas isotopic analysis. Before analysis, samples were cleaned
227 ultrasonically in 6.5% HNO₃ (for CO₂ analysis samples were cleaned in HCl), deionized water and
228 high-purity acetone. ~~After drying, samples were accurately weighed and loaded into an ultra-high-~~
229 ~~vacuum (UHV) crusher for noble gas analyses that was pumped and backed for 48h at 120°C. As~~

Formatted: Italian (Italy)

Formatted: Line spacing: Multiple 1.08 li

Formatted: Font: Times New Roman, Italian (Italy)

Formatted: Italian (Italy)

Formatted: Font: Times New Roman, Italian (Italy)

Field Code Changed

Formatted: Italian (Italy)

Formatted: English (United States)

230 soon as the ultra-high-vacuum was reached, fluid inclusions were released by single-step crushing at
 231 about 200 bar and room temperature (21°C). After drying, samples were accurately weighed and
 232 loaded into an ultra-high vacuum crusher for noble gas analyses; FI were released by single-step
 233 crushing at about 200 bar and room temperature (21°C). Single step technique was used to minimize
 234 the addition of secondary helium (cosmogenic ³He and radiogenic ⁴He) accumulated in the crystal
 235 lattice (Kurz, 1986; Graham, 2002; Rizzo et al., 2018; Correale et al., 2019-); this is supported by
 236 the homogeneity of the dataset (more details about the effect of secondary helium in our samples are
 237 provided in supplementary material). The moles of CO₂ were quantified by measuring the total
 238 pressure of gas (generally CO₂+N₂+O₂+noble gases) released during crushing (by an IONIVAC
 239 Transmitters ITR90) in a known volume of the system, then subtracting the residual pressure of
 240 N₂+O₂+noble gases after removing CO₂ in a “cold finger” immersed in liquid nitrogen. For noble
 241 gas analysis, the residual gas mixture was purified under Zr-Al getter pumps in a UHV stainless-steel
 242 preparation line. After then, Ar (and Kr and Xe) was removed in a “cold finger” with active charcoal
 243 immersed in liquid nitrogen. Finally, He and Ne were adsorbed in a cold head with active charcoal
 244 cooled at 10K and then moved at 40 and 80K in order to release first He and then Ne, respectively.
 245 ~~For noble gas analysis, the gas mixture extracted from crystals was purified in a stainless steel
 246 preparation line to separate He, Ne, and Ar from other species (N₂, H₂, H₂O, CO₂). He, Ne, and Ar
 247 were separated using cryogenic and active carbon traps and then injected into mass spectrometers.
 248 At the time of crushing, a first estimate of the concentration of CO₂ in FI was performed.~~ He and
 249 Ne isotopes were analyzed using two different split-flight-tube mass spectrometers (Helix SFT-
 250 Thermo), while Ar isotopes were analyzed by a multi-collector mass spectrometer (Argus, GVI). The
 251 measured ³He/⁴He ratios are expressed as R/R_a (where R is the ratio of the sample and R_a the He
 252 isotopic ratio of air = 1.39×10⁻⁶); this ratio was corrected for atmospheric contamination based on
 253 the measured ⁴He/²⁰Ne ratio and the values are expressed as R_c/R_a (eq.1);

Formatted: Superscript

Formatted: Superscript

$$254 \quad R_c/R_a = ((R_M/R_a)(He/Ne)_M - (He/Ne)_A) / ((He/Ne)_M - (He/Ne)_A) \quad \text{eq.1}$$

255 where R_M/R_a and (He/Ne)_M are the measured values and (He/Ne)_A refers to the atmospheric
 256 theoretical value (0.318). ⁴⁰Ar values were also corrected for atmospheric contamination:

$$257 \quad {}^{40}\text{Ar}^* = {}^{40}\text{Ar}_{\text{sample}} - ({}^{36}\text{Ar}_{\text{sample}} \cdot ({}^{40}\text{Ar}/{}^{36}\text{Ar})_{\text{air}}) \quad \text{eq.2}$$

258 where ⁴⁰Ar* is the corrected ⁴⁰Ar, ⁴⁰Ar/³⁶Ar_{air} = 295.5 and ²¹Ne/²²Ne_{air} = 0.029 (Steiger and Jäger,
 259 1977; Ozima and Podosek, 2002). Values of ²⁰Ne, ²¹Ne, ²²Ne, ³⁶Ar, and ³⁸Ar are also reported.
 260 Analytical uncertainties (1σ) for ³He/⁴He, ²⁰Ne/²²Ne, ²¹Ne/²²Ne, ⁴⁰Ar/³⁶Ar, and ³⁸Ar/³⁶Ar ratios are
 261 <2.7%, <6.3%, <7.5%, <2.0%, and <1.7%, respectively. The ²⁰Ne/²²Ne and ²¹Ne/²²Ne ratios are
 262 corrected for isobaric interferences at m/z values of 20 (⁴⁰Ar²⁺) and 22 (⁴⁴CO₂⁺²) (Rizzo et al., 2018;
 263 Faccini et al., 2020).

Formatted: Font: Calibri

Formatted: English (United Kingdom)

264 Based on the results of the initial CO₂ measurements, twelve aliquots with the highest concentrations
 265 were selected for isotopic CO₂ analysis. After crushing, the gas released was cleaned using a
 266 purification line composed by two cryogenic traps and by a 626B Baratron® Absolute Capacitance
 267 Manometer MKS (measuring range 10⁻³–10 mbar) to remove H₂O and any atmospheric component,
 268 and to quantify the gas released (Gennaro et al., 2017; Rizzo et al., 2018). The purified CO₂ was
 269 condensed in a glass sampler (adjusted to atmospheric pressure by adding pure helium), and this was
 270 transferred to the mass spectrometer. The ¹³C/¹²C isotope ratio was determined using a Thermo
 271 (Finnigan) Delta Plus XP CF-IRMS connected to a Trace GC gas chromatograph and a Thermo

272 (Finnigan) GC/C III interface. The $^{13}\text{C}/^{12}\text{C}$ is expressed using the delta notation ($\delta^{13}\text{C}$) in per mil
273 (‰) relative to the V-PDB international standard.

274

275 5. RESULTS

276 5.1 Petrography

277 The suite ~~of~~ xenoliths ~~is formed by~~ exhibits the same ~~paragenesis~~ mineralogy: Ol > Opx > Cpx >>
278 Sp. All samples are plagioclase-free and are classified as spinel lherzolites and harzburgites (Figure
279 2). Peridotites show protogranular to porphyroclastic textures, in which two generations of Ol, Opx
280 and Cpx crystals are observed (Figure 3); the first generation corresponds to large, elongated and
281 deformed crystals of sizes greater than 3 mm (porphyroclasts); the second generation corresponds to
282 smaller crystals with polygonal shapes (neoblasts $\leq 3\text{mm}$), which occur in the rock as a consequence
283 of an intense recrystallization process.

284 Olivines are present as translucent crystals without alteration. Ol porphyroclasts exhibit anhedral
285 forms (size $< 4.5\text{ mm}$) with curved grain boundaries, kink bands and numerous fractures due to
286 deformation (Figure 3A); some crystals have Opx and Cpx inclusions ($< 1\text{mm}$) with rounded shapes.
287 Most of the neoblasts are less than 2 mm long and are characterized by straight borders and subhedral
288 forms. Orthopyroxenes exhibit light brown colours without alteration; opx porphyroclasts are
289 characterized by anhedral and elongated forms with curved grain boundaries and diameters $\leq 4.5\text{ mm}$
290 (Figure 3B, 3C and 3D). Neoblasts exhibit euhedral forms with well-developed straight boundaries
291 and sizes less than 2 mm; Opx tends to concentrate forming clusters of three or more crystals ~~in~~
292 ~~specific areas~~, where vermicular spinel is commonly observed (Figure 3E and 3F); some Opx may
293 contain small Cpx inclusions ($< 0.2\text{mm}$). Opx may exhibit a rough areas (especially over the rims)
294 that resembles spongy rims, which may expand over the entire crystal (Figure 3B, 3C and 3F). Cpx
295 crystals are light green, with subhedral to anhedral forms, sizes $\leq 2\text{ mm}$ (rare crystals with diameters
296 greater than 4 mm are present). Spongy textures along crystal rims in Cpx are very common and
297 varies in thickness, this texture sometimes develops as bands or affecting the entire crystal surface
298 (Figure 3C and 3G). Finally, spinel occurs as dark brown crystals with irregular shapes (anhedral
299 forms with curved grain borders), sizes $\leq 2\text{ mm}$ and develop as vermicular intergrowths in pyroxene
300 clusters (Figure 3E and 3F).

301 Peridotites cut by glass veins that develop along the crystal borders, extending into single crystals as
302 micro-fractures. Veins have variable thicknesses, the largest being 0.3 mm thick (Figure 3D, 3F and
303 3H). Veins do not show a genetic relation with the host lava and are mainly formed by glass and may
304 contain relatively large ($\leq 0.25\text{ mm}$) crystals of Cpx, tiny crystals with high birefringence, identified
305 as carbonates; and rare opaque minerals.

306

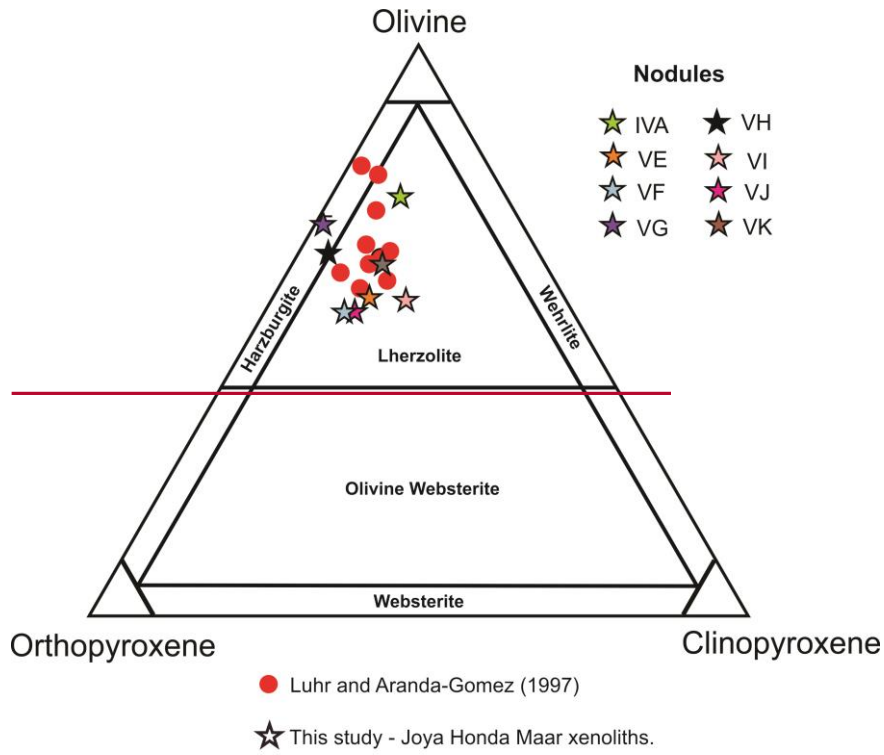


Figure 2. Ternary classification for ultramafic and mafic rocks, from Streckeisen (1976).

307

308

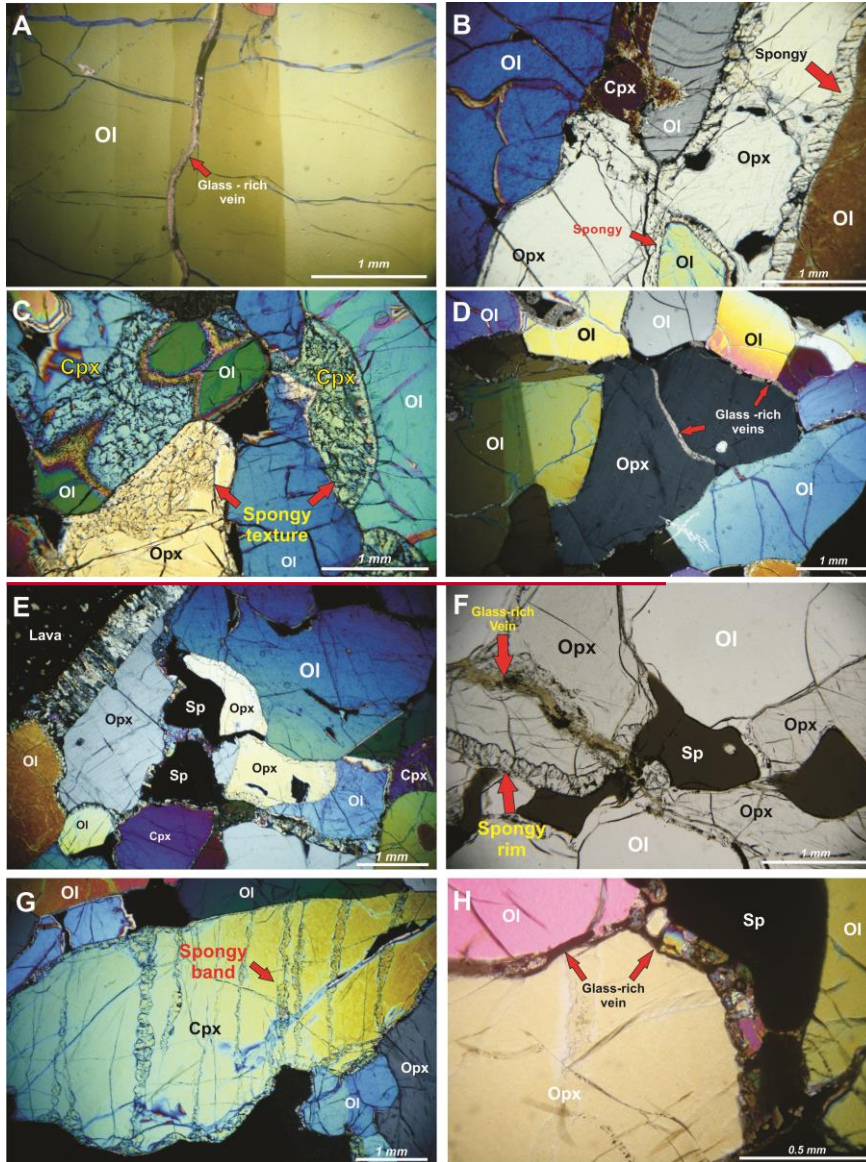


Figure 3. Microphotographs of the JH mantle xenoliths in cross-polarized light (A, B, C, D, E, G, H) and transmitted plane-polarized light (F). Ol: olivine, Opx: orthopyroxene, Cpx: clinopyroxene, Sp: spinel. A) Ol porphyroclast with well-developed kink bands and glass-rich veins. B) Spongy rims developed in Opx crystals. C) Cpx and Opx crystals are almost and totally replaced by the spongy rim. D) Porphyroclastic texture: Opx crystal being cut by a glass-rich vein. E) Opx cluster. F) Opx cluster cut by a vein composed of light brown glass and some opaque minerals, note the presence of spongy rims in Opx. G) Cpx porphyroclast with development of spongy bands. H) Glass-rich veins around Opx porphyroclast.

309 **5.2 Fluid and melt inclusions**

310 Olivine crystals contain abundant dendritic trails of secondary inclusions consisting of glass, mineral
311 phases, and a fluid phase. Dendritic inclusion trails are intragranular and typically originate from the
312 glass/carbonate microveins permeating the rocks (Figure 4A). Figure 4 shows this peculiar texture
313 resulting from the association of large (15-30 μm) irregularly-shaped inclusions containing silicate
314 glass (melt) with subordinate crystals and a fluid phase in variable proportions, along with smaller
315 (<20 μm) inclusions dominated by glass (melt) or fluid, \pm crystals. Similar inclusion textures are
316 also observed in orthopyroxene and clinopyroxene, while fluid inclusions in the absence of glass,
317 generally observed in peridotites (Andersen and Neumann, 2001; Frezzotti and Touret, 2014), are
318 extremely rare. In inclusions, the silicate glass is colorless, isotropic, and does not show any
319 devitrification (Figure 4B). Mineral phases (< 30 μm) are high birefringent and texturally associated
320 with the glass (Figure 4C). The fluid is CO_2 -rich, one or two phases (L, or L+V). Fluid-dominated
321 inclusions may contain tiny mineral grains, among which there is an opaque phase (Figure 4D).

322

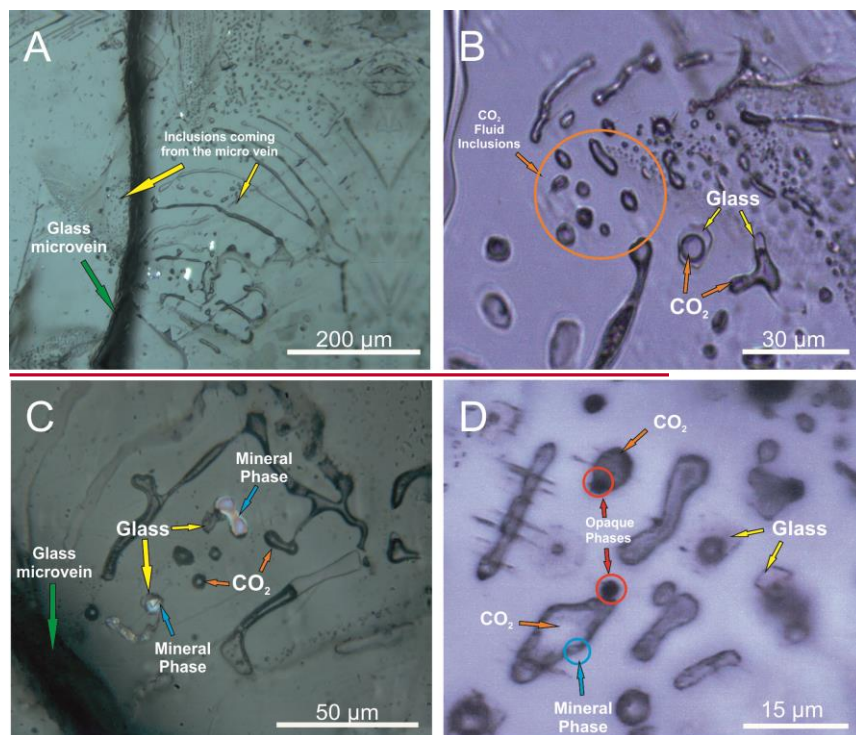


Figure 4. Microphotographs of inclusions identified in olivine. A) Melt and fluid inclusions originating from microveins. B) Intragranular trail of dendritic inclusions. C) Inclusions composed by glass and high birefringent mineral phases (cross polarized light illumination). D) Opaque phases associated to fluid inclusions.

323

324 **5.3 Raman microspectroscopy**

325 Raman microspectroscopy analyses of dendritic inclusions reveal that mineral phases texturally
326 associated with silicate glass are Mg-calcite (Figure 5A; vibrations at 1088, 714, 284, 158 cm⁻¹). The
327 fluid is pure CO₂ (Figure 5B; Fermi doublet at about 1282 -1387 cm⁻¹). Interestingly, in most CO₂
328 inclusions, Raman spectra also reveal the presence of dolomite (Figure 5C; vibrations at 1094-1096,
329 722-723, 299-300 cm⁻¹). Dolomite vibrations, however, are unexpectedly weak ([likely linked to](#)
330 [disorder: Frezzotti et al., 2012a](#)) and broad (full width at half maximum up to 15 cm⁻¹) (Figure 5C).
331 Also, the main vibration at 1098 cm⁻¹ is downshifted from 2 to 4 cm⁻¹. These spectral characteristics
332 indicate a relevant order decrease in the crystalline structure as it occurs in decomposing carbonates
333 ([Frezzotti and Peccerillo, 2007; Carteret et al., 2009; Frezzotti et al., 2012a](#)).

334 The tiny mineral grains observed in a few CO₂ inclusions are magnesite (Figure 5D; vibrations at
335 1094, 723, 322, 202 cm⁻¹). An opaque mineral has been identified as pyrite (Figure 5D; vibrations at
336 342 and 377 cm⁻¹). The association of Mg-carbonate ± pyrite in CO₂-rich inclusions is suggestive of
337 fluid inclusion-host olivine reactions at low temperatures (Frezzotti et al., 2012b), probably during
338 host lava cooling at the surface.

339

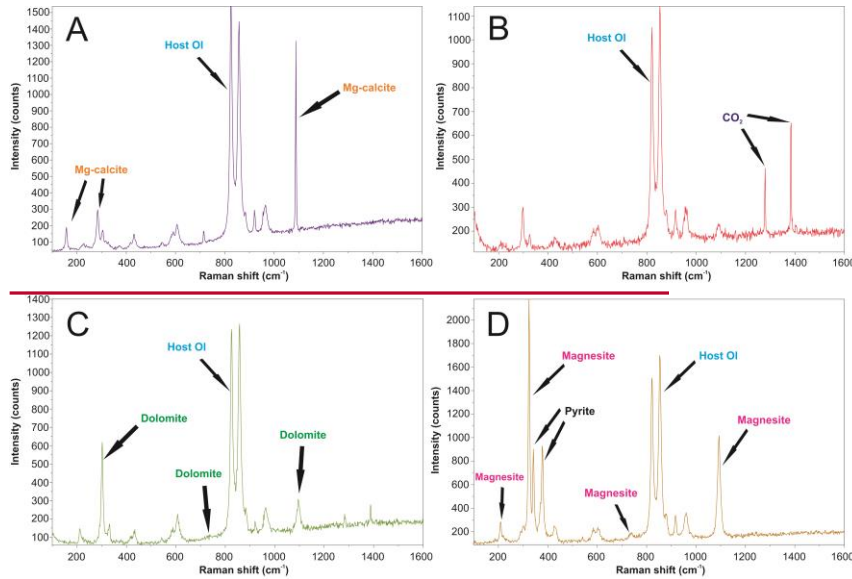


Figure 5: Raman spectroscopy applied in olivine inclusions. Further details are discussed in section 5.2.

340

341 **5.4 Elemental and Isotopic composition**

342 The [chemical elemental](#) and isotopic composition of the crystal-hosted [FI-fluid inclusions](#) in the JH
343 mantle xenoliths are reported in Table 2; [reported errors are 1σ uncertainties, except for ²¹Ne/²²Ne_{ext}](#)
344 [ratios whose errors are 2σ uncertainties](#). ⁴He concentrations range between 8.56 x 10⁻¹⁴ and 1.29 x

Formatted: Line spacing: Multiple 1.08 li

Formatted: Font: Times New Roman, Italian (Italy)

Field Code Changed

Formatted: Font: Times New Roman, Italian (Italy)

Formatted: Italian (Italy)

Formatted: Font: Calibri, Italian (Italy)

Formatted: Line spacing: Multiple 1.08 li

Formatted: Superscript

Formatted: Superscript

Formatted: Subscript

345 10^{-11} mol/g where the highest concentrations are observed in Cpx ($\sim 4.28 \times 10^{-12}$ mol/g) followed by
346 Ol ($\sim 2.21 \times 10^{-12}$ mol/g) and Opx ($\sim 2.06 \times 10^{-12}$ mol/g). ~~^3He contents vary from 7.37×10^{-19} to 1.29~~
347 ~~$\times 10^{-16}$ mol/g, with the highest values also recorded in Cpx (4.04×10^{-17} mol/g), followed by Ol (2.28~~
348 ~~$\times 10^{-17}$ mol/g) and Opx (2.11×10^{-17} mol/g).~~ ^3He and ^4He concentrations for the V-I crystals are
349 significantly lower than those measured in other nodules. $^{40}\text{Ar}^*$ content ranges from 5.37×10^{-14} to
350 1.08×10^{-11} mol/g; in general, both $^{40}\text{Ar}^*$ and ^4He values ~~are positively correlated and~~ are similar to
351 those previously reported in mantle xenoliths from the European Subcontinental Lithospheric Mantle
352 (European SCLM); ~~Gautheron et al., 2005; Martelli et al., 2011; Rizzo et al., 2018; Faccini et al., 2020,~~
353 ~~East African Rift (EAR; Halldórsson et al., 2014), and the West Antarctic Rift System (WARS-~~
354 ~~SCLM; Corrales et al., 2019), the Eastern Australia SCLM and some regions belonging the East~~
355 ~~African Rift (Northern/Southern Kenya rifts and the Ethiopia-Afar region; Figure 6A; Matsumoto et~~
356 ~~al., 1998, 2000; Hopp et al., 2004, 2007a, 2007b; Buikin et al., 2005; Gautheron et al., 2005a;~~
357 ~~Czuppon et al., 2009; Martelli et al., 2011; Halldórsson et al., 2014; Broadley et al., 2016; Rizzo et~~
358 ~~al., 2018; Corrales et al., 2019; Faccini et al., 2020; Figure 6A).~~ The ^{36}Ar contents vary from $3.38 \times$
359 ~~10^{-16} to 4.14×10^{-14} mol/g. The highest concentrations of $^{40}\text{Ar}^*$, ^{36}Ar and N_2^* are also found in Cpx.~~
360 ^{20}Ne , ^{21}Ne and ^{22}Ne values tend to be high in Cpx and Opx; ^{20}Ne ranges from 1.42×10^{-16} to $5.08 \times$
361 10^{-14} mol/g, ^{21}Ne from 5.22×10^{-19} to 1.21×10^{-16} mol/g and ^{22}Ne from 1.34×10^{-17} to 4.90×10^{-15}
362 mol/g. CO_2 is the most abundant gas, on average its contents are higher in Cpx and Opx (1.02×10^{-7}
363 and 3.18×10^{-8} mol/g, respectively) than in Ol (3.43×10^{-9} mol/g); CO_2 contents are positively
364 correlated with ^3He , ^4He , $^{40}\text{Ar}^*$, ^{20}Ne , ^{21}Ne and ^{22}Ne , but are lower than those observed in European
365 SCLM xenoliths (Figure 6B and 6C).

366 In detail, the Rc/Ra values vary as follows: Ol from 7.13 to 7.68 Ra, Opx from 6.15 to 7.54 Ra, and
367 Cpx from 5.40 to 7.59 Ra. The $^4\text{He}/^{40}\text{Ar}^*$ ratios ~~are positively correlated with Rc/Ra and~~ vary
368 between 0.14 and 3.11 (Figure 8), which overlaps in part the typical production ratio of the mantle
369 ($^4\text{He}/^{40}\text{Ar}^* = 1 - 5$; Yamamoto et al., 2009; Marty, 2012); on average the highest values belong to Ol
370 crystals (1.51 ± 0.76), compared to Opx (0.72 ± 0.25) and Cpx (0.78 ± 0.40). $^4\text{He}/^{20}\text{Ne}$ values range
371 from 2.4 to 10483; the highest values are recorded in Cpx (~~-2223.2~~) and Ol (on average $2223.2 \pm$
372 3196.8 and -1498.6 ± 1306.1 , respectively), while Opx exhibits considerably lower ratios (<639).
373 This tendency is also observed for $^{40}\text{Ar}/^{36}\text{Ar}$ ratios that vary from 303 to 8231 in Cpx, from 392 to
374 2518 in Ol, and from 340 to 1436 in Opx. It should be noted that those samples with the lowest values
375 of Rc/Ra, also are depleted in $^4\text{He}/\text{Ar}^*$, $^{40}\text{Ar}/^{36}\text{Ar}$ and $^4\text{He}/^{20}\text{Ne}$. On average $^{20}\text{Ne}/^{22}\text{Ne}$ and $^{21}\text{Ne}/^{22}\text{Ne}$
376 ratios vary from 10.2 ± 0.50 and 9.8 to 12.1 and from 0.0288 0.332 ± 0.0058 to 0.0553 , respectively;
377 in both cases, the values are slightly higher in Cpx compared to Ol and Opx. Finally, the isotope
378 composition of CO_2 expressed as $\delta^{13}\text{C}$ values (in per mil vs V-PDB) varies between -0.97 and $-$
379 2.86% and does not exhibit a systematic variation between Ol, Opx and Cpx. The most negative
380 value (-2.86%) was reported in IV-A Opx while the most positive values belong to two aliquots of
381 the same nodule: V-K Ol (-1.10) and V-K Opx (-0.97).

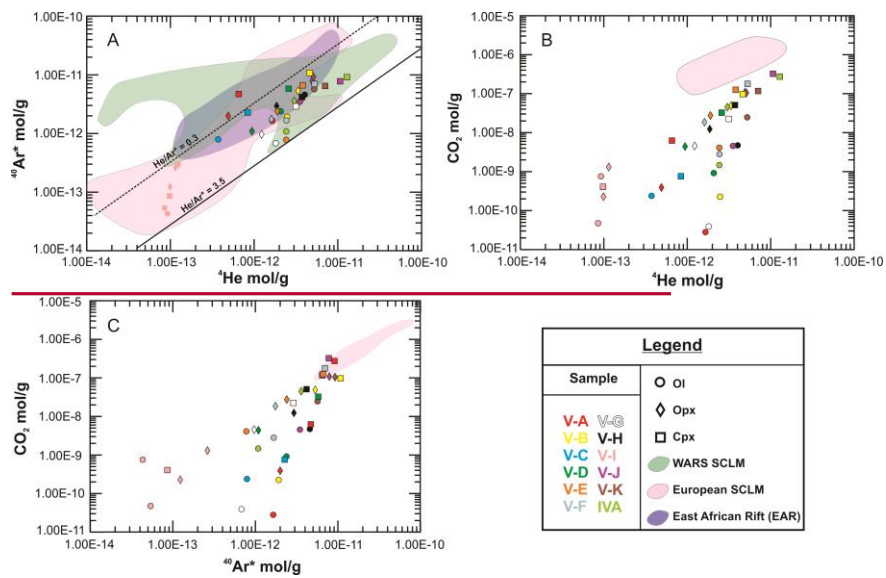
382
383
384
385
386

Field Code Changed

Field Code Changed

Formatted: Font: Calibri

Formatted: No underline



Formatted Table

Figure 6. ^{40}Ar , $^{40}\text{Ar}^2$ and CO_2 contents measured in FI hosted in JH mantle xenoliths. SCLM: Subcontinental Lithospheric Mantle. The West Antarctic Rift System (WARS) SCLM compositional range was built using FI data measured by Correale et al. (2010). European SCLM range includes FI values measured in mantle xenoliths from the Rhenish Massif (Germany), Pannonian basin, Massif Central (Central France), Tallante – Calatrava (Spain), and Lower Silesia (Poland); data was taken from Gautheron et al. (2005); Marvelli et al. (2011); Rizzo et al. (2018). East African Rift (EAR) data was taken from Halldórsson et al. (2014).

387

388

Formatted: Font: (Default) Calibri, Not Bold, Italic

Formatted: Normal, Left, Line spacing: single

389 **6. Discussion**

390 Present textural and Raman spectroscopy observations indicate that the JH ~~FI~~ fluid inclusions are
391 CO₂-dominated (Figure 5) and, even more importantly, that they are strictly associated with the
392 pervasive infiltration of glass veins (Figures 3, 4). The inclusions typically exhibit the coexistence of
393 glass, mineral phases, and a fluid phase, and form dendritic trails of ~~FI~~ fluid inclusions originating
394 from the glass/carbonate microveins permeating the rocks (Figure 4A). The close association
395 between glass and ~~FI~~ fluid inclusions, and their originating from the glass microveins, are strongly
396 suggestive of trapping of fluids delivered by degassing of a carbonate-rich silicate melt at mantle
397 depth. Textural observations and preliminary compositional information (indicating that glass veins
398 contain 59±3 wt % SiO₂) clearly exclude that the glass veins are related to the basanitic to basaltic
399 host magma.

400 In view of the above, and in line with previous work (Liang and Elthon, 1990; Luhr and Aranda-
401 Gómez, 1997), we relate the ~~FI~~ fluid inclusions trapped in JH xenoliths to a melt-related metasomatic
402 event deep in the source mantle. The overprinted textures in Cpx along crystal rims (named as spongy
403 rims by Luhr and Aranda-Gómez, 1997) (see Figure 3) have also been associated to this metasomatic
404 event (Liang and Elthon, 1990).

405 In the discussion below, we ~~combined stand on~~ the above petrographic evidence ~~while we use and~~
406 ~~the~~ isotopic signatures (noble gases and CO₂) of the JH ~~FI~~ fluid inclusions to constrain volatile origin
407 and mantle characteristics. However, ~~before the origin of noble gases and carbon can be explored,~~
408 ~~an initial an initial~~ screening of the dataset ~~is was necessary required~~ to filter out ~~any samples that~~
409 ~~have suffered from effect related~~ to secondary processes affecting the ~~xenoliths~~ fluid inclusion
410 compositions (see ~~The details on the above screening are reported in~~ Supplementary information);
411 ~~while the processes are reported in the main figures, when recalled.~~ The filtered dataset is used below
412 to infer volatile sources and processes deep in the mantle.

413

414 **6.1 Diffusive Fractionation**

415 ~~As shown in Figure 6, the lowest noble gas concentrations (especially helium) were measured in V-~~
416 ~~I crystals and, to a minor extent, in V A and V C (He < 10⁻¹² mol/g). Some CO₂ depletion is also~~
417 ~~evident in sample V I (Figure 6C). When plotting ³He, ⁴He, ⁴⁰Ar*, and ⁴He/⁴⁰Ar* vs. R_c/R_a (Figures~~
418 ~~8 and 10A-10C), we find that in sample V I the He and Ar depletion is also accompanied by ³He/⁴He~~
419 ~~(< 6.15 R_a) sensibly lower than the dataset average (7.39 ± 0.14 R_a). In samples V A and V C, the~~
420 ~~³He/⁴He decrease is less important. It is worth noting that the lower R_c/R_a values mostly correspond~~
421 ~~to pyroxenes (Opx and Cpx) from the same nodule, while Ol crystals are less or not modified. Indeed,~~
422 ~~Ol from V I show ³He/⁴He values (7.25 – 7.37 R_a) that are comparable to the rest of the dataset (7.21~~
423 ~~– 7.36 R_a).~~

424 ~~Following Burnard et al. (1998), Burnard (2004), and Yamamoto et al. (2009), this data variability~~
425 ~~can be interpreted as due to preferential loss of He (relative to Ar and CO₂) due to diffusive~~
426 ~~fractionation. In fact, in case of radiogenic ⁴He in growth or addition to fluid inclusions, an increase~~
427 ~~of ⁴He concentration with decreasing ³He/⁴He values should be expected, without any relative~~
428 ~~decrease of ³He, ⁴⁰Ar*, and ⁴He/⁴⁰Ar*. We highlight that He diffusion into the fast flowing melt-~~
429 ~~filled dissolution channels cutting the mantle is commonly invoked during partial melting (Burnard,~~
430 ~~2004; Yamamoto et al., 2009; Faccini et al., 2020) and/or metasomatism of solid mantle that~~

Formatted: Font: Bold, Not Italic

Formatted: Font: Bold, Not Italic

Formatted: Font: Bold, Not Italic

431 prevalently affects pyroxene crystals. Some studies conclude that the ⁴He diffusion coefficient is
432 considerably higher than that of ⁴⁰Ar ($D_{4He}/D_{40Ar} = 3.16$ in solid mantle; Burnard, 2004; Yamamoto
433 et al., 2009); this is especially true assuming that only the relative atomic mass controls the difference
434 in diffusion coefficients. Likewise, the difference in mass between ³He and ⁴He implies important
435 differences in their diffusivities ($D_{3He}/D_{4He} = 1.15$; Trull and Kurz, 1993; Burnard, 2004; Yamamoto
436 et al., 2009). Hence, in case of diffusive loss of He, a decrease in ³He/⁴He and ⁴He/⁴⁰Ar* is expected,
437 as observed in V-A and V-I pyroxenes. Because the clearest evidence of diffusive fractionation are
438 observed in pyroxenes, we exclude V-C because OI from this sample show ³He/⁴He values (7.13 Ra)
439 comparable to Opx (7.33 Ra) from the same nodule (although OI have lower He concentrations). In
440 any case, in order to properly interpret the origin of the He in the following sections of the discussion,
441 pyroxenes from V-I and V-A nodules will not be discussed further.

Formatted: Font: (Default) Times New Roman

442 To support the hypothesis of a diffusive fractionation, in Figures 8 and 10A-B-C we model this
443 process based on the approach proposed by Burnard et al. (1998), Burnard (2004), Yamamoto et al.
444 (2009), and already applied in Boudoire et al. (2020) and Faccini et al. (2020). We consider a starting
445 mantle composition of ³He = 1.56×10^{-17} mol/g, ⁴He = 1.5×10^{-12} mol/g, and ⁴⁰Ar* = 6×10^{-13} mol/g,
446 which corresponds to the lowest concentrations of these species in nodules not evidently modified
447 by diffusion. We additionally use a starting ⁴He/⁴⁰Ar* = 2.5 (the average mantle production ratio),
448 and a ³He/⁴He = 7.5 Ra, which is within the Re/Ra variability of the dataset. According to our
449 modeling, diffusive fractionation is able to justify the data variability observed in pyroxene from V-
450 A and V-I samples, which will not be discussed anymore.

Formatted: Font: Not Italic

452 **6.1 Secondary processes**

453 **6.1.1.6.2 Atmospheric Contamination Interaction with atmospheric fluids**

Formatted: Font: Bold, Not Italic

454 **6.1 Inferences on the noble gas signature of the JH source mantle**

Formatted: Font: Bold, Not Italic

455 *6.1.1 Interaction with atmospheric fluids and Evidence for a recycled atmospheric component*

456 In order to correctly interpret the noble gas data obtained in FI-fluid inclusions from the JH mantle
457 xenoliths, it is necessary to evaluate the atmospheric contamination in our samples interaction with
458 atmospheric fluids. It is well known that Ar and Ne are more susceptible (relative to He) to
459 contamination, due to their higher abundances in atmosphere relative to the mantle fluids. For this
460 reason, tracers such as ⁴⁰Ar and ³⁶Ar, ⁴He/²⁰Ne, ²⁰Ne/²²Ne, ²¹Ne/²²Ne, and ⁴⁰Ar/³⁶Ar are normally used
461 to investigate the isotopic contribution from the atmosphere (Matsumoto et al., 2001; Gurenko et al.,
462 2006; Hopp et al., 2004, 2007a, 2007b; Nuccio et al., 2008; Martelli et al., 2014; Oppenheimer et al.,
463 2014; Rizzo et al., 2018) (Gurenko et al., 2006; Nuccio et al., 2008; Martelli et al., 2014;
464 Oppenheimer et al., 2014; Rizzo et al., 2018).

Field Code Changed

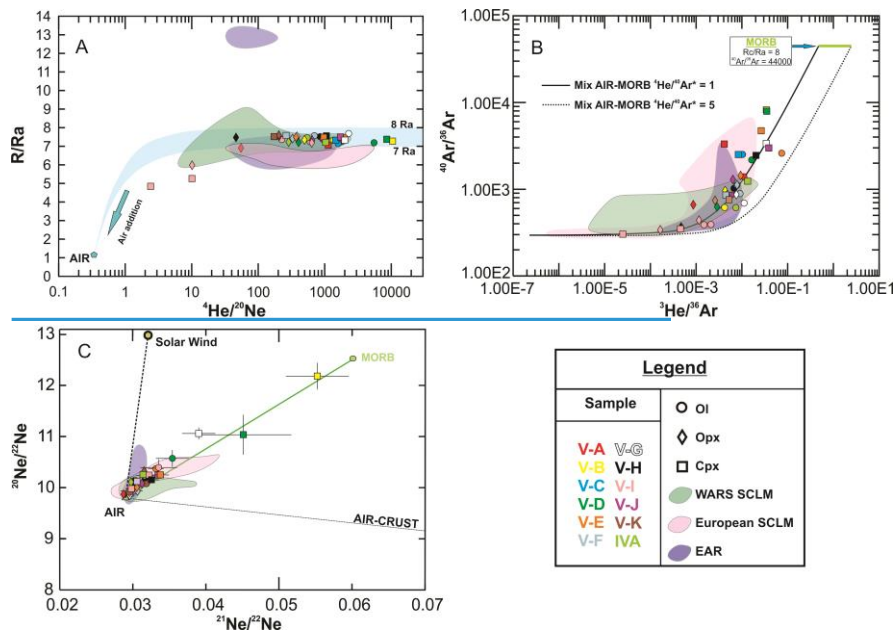
465 He, Ne and Ar systematics suggest the existence of an atmospheric component in our samples We
466 find that most of the samples exhibit low air contamination (except specially especially for in nodule
467 V-I). Indeed, the differences between R/Ra and Re/Ra are negligible, except for V-I pyroxenes that
468 also show the lowest ⁴He/²⁰Ne values of the dataset (≤ 10). In general, the measured R/Ra and
469 ⁴He/²⁰Ne values fall along an binary mixing air-MORB mixing curve, and overlap with those
470 measured in mantle xenoliths from the European SCLM, the East African Rift (EAR), the West

Formatted: English (United Kingdom)

Formatted: Line spacing: Multiple 1.08 li

471 Antarctic Rift System (WARS), Eastern Australia, Red sea region and N/S Kenya rifts and WARS, except for a few samples that show among the highest ever measured $^4\text{He}/^{20}\text{Ne}$ ratios for the SCLM (up to 10483) (Figure 7A)(Figure 7A). This evidenceThe existence of such an atmospheric component of a limited atmospheric contribution is corroborated by low the high $^{40}\text{Ar}/^{36}\text{Ar}$ and $^3\text{He}/^{36}\text{Ar}$ values (up to 8231 and 0.07, respectively; Figure 7B), which in turn support the robustness of the ^{40}Ar correction (e.g. Martelli et al., 2014; Rizzo et al., 2015, 2018). However, our $^{40}\text{Ar}/^{36}\text{Ar}$ and $^{20}\text{Ne}/^{22}\text{Ne}$ ratios which are significantly below the expected MORB values (44,000 and 12.5, respectively; Burnard, 1997; Moreira, 1998; Sarda, 2004) Burnard, 1997; Moreira et al., 1998). As shown in Figure 7B, $^{40}\text{Ar}/^{36}\text{Ar}$ correlate with and $^3\text{He}/^{36}\text{Ar}$ values, and also fall along a two-component mixing between a MORB-like upper mantle and atmosphere well fits the Ar-He dataset, (whereas He/Ar^* ratios between of 0.14 and to 3.5 are able to explain the whole data variability; see also Figure 9B; see Fig. 4) (with the exception of a few samples that exhibit $^4\text{He}/^{40}\text{Ar}^*$ ratios affected by other processes; see Section 6.3). Likewise, samples fit the binary mixing air-MORB when using the three-isotope neon plot (Figure 7C), confirming the existence of atmospheric fluids in our inclusions. The atmospheric component Atmospheric contamination is especially notable only in nodule V-I that exhibits an isotopic signature close to that of air with $^4\text{He}/^{20}\text{Ne}$ ratios below 10 (for Opx and Cpx) and $^{40}\text{Ar}/^{36}\text{Ar}$ values below 392. These compositions confirm that this nodule likely suffered secondary processes that modified its pristine mantle signature. This sample is therefore not considered not anymore representative of the local SCLM (and omitted from the following discussion).

491
492



- Formatted: Superscript
- Formatted: Superscript
- Formatted: Font: Times New Roman, Portuguese (Brazil)
- Formatted: Portuguese (Brazil)
- Field Code Changed
- Field Code Changed
- Formatted: Portuguese (Brazil)
- Formatted: Portuguese (Brazil)
- Formatted: Not Highlight
- Formatted: Portuguese (Brazil)
- Formatted: Font: Calibri

Figure 7. A) $^4\text{He}/^{20}\text{Ne}$ vs R/Ra diagram, the blue shaded area represents the binary mixing between air and an upper mantle source with R/Ra values between 7 and 8; B) $^3\text{He}/^{40}\text{Ar}$ vs $^{40}\text{Ar}/^{26}\text{Ar}$ diagram; the solid and dotted lines describe the binary mixing air-MORB with $^4\text{He}/^{40}\text{Ar}^*$ values of 1 and 5, respectively; C) $^{21}\text{Ne}/^{20}\text{Ne}$ vs. $^{20}\text{Ne}/^{22}\text{Ne}$ diagram in which the green line represents the binary mixing air-MORB mantle as defined by Sarda et al. (1988) and Moreira et al. (1998) at $^{21}\text{Ne}/^{22}\text{Ne}_{\text{air}} = 0.029$ and $^{20}\text{Ne}/^{22}\text{Ne}_{\text{air}} = 9.8$ and $^{21}\text{Ne}/^{22}\text{Ne} = 0.06$ and $^{20}\text{Ne}/^{22}\text{Ne} = 12.5$; the primordial neon composition is reported as Solar wind at $^{21}\text{Ne}/^{22}\text{Ne} = 0.0328$ and $^{20}\text{Ne}/^{22}\text{Ne} = 13.8$ (Heber et al., 2009); the crust endmember was plotted at $^{21}\text{Ne}/^{22}\text{Ne} = 0.6145$ and $^{20}\text{Ne}/^{22}\text{Ne} = 0.3$ (Kennedy et al., 1990). The WARS SCLM, European SCLM and EAR compositional ranges were built using FI data cited in Figure 6.

493

494 6.1.2 Diffusive Fractionation

495 As shown in Figure 6, the lowest noble gas concentrations (especially helium) were measured in V-
 496 I crystals and, to a minor extent, in V-A and V-C ($\text{He} < 10^{-12}$ mol/g). Some CO_2 depletion is also
 497 evident in sample V-I. When plotting ^3He , ^4He , $^{40}\text{Ar}^*$, and $^4\text{He}/^{40}\text{Ar}^*$ vs. R/Ra (Figures 8 and 9A-
 498 9C), we find that in sample V-I the He and Ar depletion is also accompanied by $^3\text{He}/^4\text{He}$ (< 6.15
 499 Ra) sensibly lower than the dataset average (7.39 ± 0.14 Ra). In samples V-A and V-C, the $^3\text{He}/^4\text{He}$
 500 decrease is less important. It is worth noting that the lower R/Ra values mostly correspond to
 501 pyroxenes (Opx and Cpx) from the same nodule, while Ol crystals are less or not modified. Indeed,
 502 Ol from V-I show $^3\text{He}/^4\text{He}$ values ($7.25 - 7.37$ Ra) that are comparable to the rest of the dataset
 503 ($7.21 - 7.36$ Ra).

504 Following Burnard et al. (1998), Burnard (2004), and Yamamoto et al. (2009), this data variability
 505 can be interpreted as due to preferential loss of He (relative to Ar and CO_2) due to diffusive
 506 fractionation. In fact, in case of radiogenic ^4He in-growth or addition to FI, an increase of ^4He
 507 concentration with decreasing $^3\text{He}/^4\text{He}$ values should be expected, without any relative decrease of
 508 ^3He , $^{40}\text{Ar}^*$, and $^4\text{He}/^{40}\text{Ar}^*$. We highlight that He diffusion into the fast flowing melt filled
 509 dissolution channels cutting the mantle is commonly invoked during partial melting (Burnard,
 510 2004; Yamamoto et al., 2009; Faccini et al., 2020) and/or metasomatism of solid mantle that
 511 prevalently affects pyroxene crystals. The ^4He diffusion coefficient is considerably higher than that
 512 of ^{40}Ar ($D_{^4\text{He}}/D_{^{40}\text{Ar}} = 3.16$ in solid mantle; Burnard, 2004; Yamamoto et al., 2009). Likewise, the
 513 difference in mass between ^3He and ^4He implies important differences in their diffusivities
 514 ($D_{^3\text{He}}/D_{^4\text{He}} = 1.15$; Trull and Kurz, 1993; Burnard, 2004; Yamamoto et al., 2009). Hence, in case of
 515 diffusive loss of He, a decrease in $^3\text{He}/^4\text{He}$ and $^4\text{He}/^{40}\text{Ar}^*$ is expected, as observed in V-A and V-I
 516 pyroxenes. Because the clearest evidences of diffusive fractionation are observed in pyroxenes, we
 517 exclude V-C because Ol from this sample show $^3\text{He}/^4\text{He}$ values (7.13 Ra) comparable to Opx (7.33
 518 Ra) from the same nodule (although Ol have lower He concentrations). In any case, in order to
 519 properly interpret the origin of the He in the following sections of the discussion, pyroxenes from
 520 V-I and V-A nodules will not be discussed further.

521 To support the hypothesis of a diffusive fractionation, in Figures 8 and 9A-B-C we model this
 522 process based on the approach proposed by Burnard et al. (1998), Burnard (2004), Yamamoto et al.
 523 (2009), and already applied in Boudoire et al. (2020) and Faccini et al. (2020). We consider a
 524 starting mantle composition of $^3\text{He} = 1.56 \times 10^{-17}$ mol/g, $^4\text{He} = 1.5 \times 10^{-12}$ mol/g, and $^{40}\text{Ar}^* = 6 \times 10^{-13}$
 525 mol/g, which corresponds to the lowest concentrations of these species in nodules not evidently
 526 modified by diffusion. We additionally use a starting $^4\text{He}/^{40}\text{Ar}^* = 2.5$ (the average mantle
 527 production ratio), and a $^3\text{He}/^4\text{He} = 7.5$ Ra, which is within the R/Ra variability of the dataset.

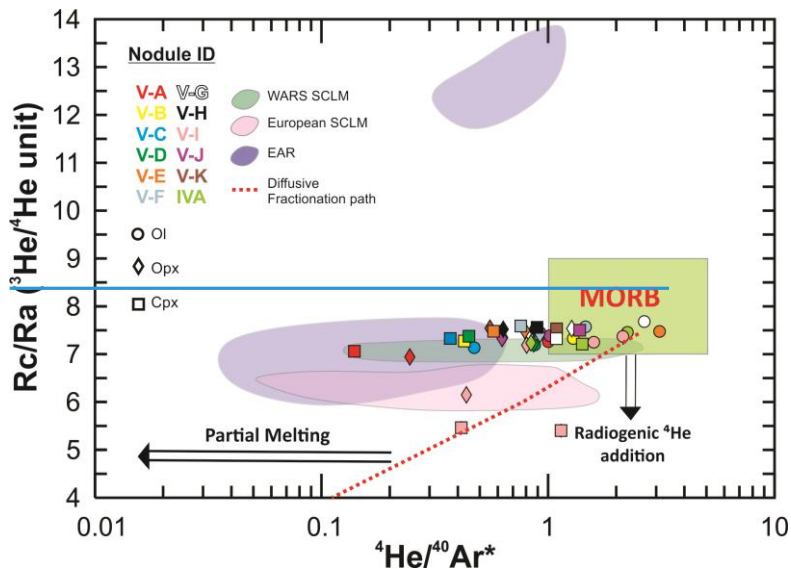
528 According to our modeling, diffusive fractionation is able to justify the data variability observed in
 529 pyroxene from V-A and V-I samples, which will not be discussed anymore.

530

531 *6.1.3 Exposure to cosmic rays*

532 Several studies have shown that rocks exposed to cosmic rays (i.e. after eruption) favor the
 533 accumulation of ^3He in the crystal lattices shifting the original $^3\text{He}/^4\text{He}$ ratios to higher values
 534 (Kurz, 1986; Lal, 1987; Dunai and Baur, 1995; Dunai, 2010; Broadley et al., 2016; Nesterenok and
 535 Yakubovich, 2016; Correale et al., 2019). According to e.g. Dunai and Baur (1995) and Correale et
 536 al. (2019 and references therein), crystals with low He concentrations are more prone to changes
 537 due to the diffusion of ^3He from lattices into the FI. However, in the case of the JH mantle
 538 xenoliths, the aliquots with the lowest He contents ($^3\text{He} < 10^{-17}$ and $^4\text{He} < 10^{-12}$; Figure 9A, 9B)
 539 generally show an opposite effect, that is a decrease in $^3\text{He}/^4\text{He}$ compared to the samples with the
 540 highest helium concentrations that we interpreted as the result of diffusive fractionation. The
 541 eruption time of JH xenoliths (311 ± 19 ka; Saucedo et al., 2017) limits the exposure time to
 542 cosmic rays. Finally, the single step crushing method prevents the contribution of secondary He
 543 accumulated in the crystal lattice (cosmogenic ^3He and radiogenic ^4He), as evidenced by other
 544 authors (Kurz, 1986; Graham, 2002; Gautheron et al., 2005; Rizzo et al., 2018; Correale et al.,
 545 2019; Faccini et al., 2020). We therefore conclude that the effect of cosmogenic ^3He in our samples
 546 is negligible.

547



Formatted: English (United Kingdom)

Formatted: English (United Kingdom)

Formatted Table

Figure 8. $^4\text{He}/^{40}\text{Ar}^*$ vs. $^2\text{He}/\text{He}$ corrected for air contamination (Re/Ra) ratios of FI from JH mantle xenoliths. MORB range is reported at $\text{Re/Ra} = 8 \pm 1$ (Graham, 2002) and $^4\text{He}/^{40}\text{Ar}^*$ from 1 to 5 (Yamamoto et al., 2009). The WARS-SCLM, European-SCLM and EAR compositional ranges were built using FI data cited in Figure 6. The diffusive fractionation path was modeled using the diffusion coefficient (D) of ^2He , ^4He , and $^{40}\text{Ar}^*$ ($D_{\text{He}^2}/D_{\text{He}^4} = 1.15$ and $D_{\text{He}^4}/D_{\text{Ar}^*} = 3.16$ in solid mantle; Burnard, 2004; Yamamoto et al., 2009).

548

6.2.3 The effect of partial melting

It has previously shown (Graham, 2002; Burnard, 2004; Yamamoto et al., 2009; Correale et al., 2012, 2016, 2019; Rizzo et al., 2018; Faccini et al., 2020) that the noble gas signature of mantle xenoliths depends to some extent on the melting history of the mantle source, and that the $^4\text{He}/^{40}\text{Ar}^*$ ratio is a useful tracer to understand partial melting degree in mantle xenoliths. The method stands on the different mineral/melt partition coefficients of the two elements (Heber et al., 2007). In detail, it has been verified that He is more incompatible than Ar, thus escaping the mantle more effectively during partial melting, and ultimately causing a $^4\text{He}/^{40}\text{Ar}^*$ decrease in the mantle residuum (Burnard, 2004; Heber et al., 2007; Yamamoto et al., 2009), as observed in Figure 8. However, Rizzo et al. (2018) first argued that estimating partial melting degrees based $^4\text{He}/^{40}\text{Ar}^*$ in FI fluid inclusions is tricky, because noble gases are not directly measured in crystals (i.e., dissolved in the solid matrix) but rather in the FI fluid inclusions hosted in crystals. In fact, the calculated noble gas based partial melting degrees do not match (are sensibly lower than) those obtained from lithophile elements-based models. On the other hand, the relative $^4\text{He}/^{40}\text{Ar}^*$ variations observed in FI fluid inclusions are qualitatively consistent with those indicated by lithophile elements-based models, suggesting that an equilibrium between the noble gas in FI fluid inclusions and those dissolved in the crystals must exist (Rizzo et al., 2018; Faccini et al., 2020).

As noted in Figure 8, the variability of $^4\text{He}/^{40}\text{Ar}^*$ ratios in the JH nodules reflects processes that have mainly affected the pyroxenes. Indeed, the majority of Ol crystals have $^4\text{He}/^{40}\text{Ar}^*$ values within the typical production ratio of a fertile mantle ($^4\text{He}/^{40}\text{Ar}^* = 1.5$; Marty, 2012), while Opx and Cpx crystals exhibit slightly lower $^4\text{He}/^{40}\text{Ar}^*$ ratios, from 0.4 to 1.4. In general, the $^4\text{He}/^{40}\text{Ar}^*$ population of our samples implies that source mantle melting may have to some extent impacted the Opx and Cpx noble gas signature, but not that of Ol, ultimately suggesting a low degree of partial melting. We stress that the degrees of partial melting are not well constrained on petrological basis for the JH spinel lherzolites, as a wide range (7–22%) has been proposed in previous work (Liang and Elthon, 1990).

575

6.3.4 Inferences on the noble gas signature of the JH source mantle

6.3.4.1 Evidences for a recycled air atmospheric component: Ne and Ar: Ne and Ar

As stated in section 6.1.12, the Ne and Ar isotopic systematics strongly support the presence of an atmospheric component in the JH FI fluid inclusions. This air-derived component is mixed with fluids having a MORB-like signature (Figure 7B, C). A similar behavior is observed in mantle xenoliths from the European SCLM, the West Antarctic Rift System (WARS), Eastern Australia SCLM, Red sea region, N/S Kenya rifts, WARS and Ethiopia (Afar), and European SCLM mantle xenoliths, as well as in other portions of SCLM on Earth (e.g., Gurenko et al., 2006). Instead, samples from EAR

583

Formatted: Font: Not Bold

Field Code Changed

Formatted: Italian (Italy)

Field Code Changed

Field Code Changed

Field Code Changed

Field Code Changed

Field Code Changed

Field Code Changed

Formatted: Font: Not Bold

Formatted: English (United States)

584 exhibit an enrichment in $^{20}\text{Ne}/^{22}\text{Ne}$ relatively to $^{21}\text{Ne}/^{22}\text{Ne}$, due to the presence of a primordial
585 component in the local mantle (Halldórsson et al., 2014).

586 The atmospheric component identified in the FI fluid inclusions may derive from two main possible
587 processes, as summarized by Nuccio et al. (2008), Martelli et al. (2011), Correale et al. (2012), and
588 Rizzo et al. (2018), and Faccini et al. (2020): a) air entrapment in crystal fractures during or after
589 eruption of transporting lava, and b) the interaction with subducted atmospheric fluids recycled in
590 the upper mantle.

591 Although air entrapment in crystals microcracks cannot be totally discarded due to surface exposure
592 of the xenoliths over the last 300 ky, ~~the positive correlation between ^3He and ^{36}Ar suggests our~~
593 ~~petrographic evidence of a close association between FI and glass veins (Figure 4) support a deep~~
594 ~~origin (Figure 9aA), i.e.g., a recycled air-atmospheric component in the local-lithospheric mantle~~
595 ~~likely inherited from subduction (Matsumoto et al., 2001). - Indeed, there is petrological evidence~~
596 ~~that supports the interaction of the local upper mantle with metasomatic fluids possibly coming from~~
597 ~~the subducted oceanic crust (Pier et al., 1989; Luhr and Aranda-Gómez, 1997; Dávalos-Elizondo et~~
598 ~~al., 2016). - In view of the above, and with the aim of constraining the $^{40}\text{Ar}/^{36}\text{Ar}$ signature expected~~
599 ~~for the local mantle, we also evaluated the relationship between $^{20}\text{Ne}/^{22}\text{Ne}$ and $^{40}\text{Ar}/^{36}\text{Ar}$ ratios (Fig-~~
600 ~~ure 9b Figure 9BS4), using - We based on the approach used by Langmuir et al. (1978) and Hopp et~~
601 ~~al. (2007a) according to the variability of our dataset. Considering an upper mantle $^{20}\text{Ne}/^{22}\text{Ne}$ ratio~~
602 ~~equal to 12.5 (Sarda et al., 1988; Moreira et al., 1998), $^{36}\text{Ar}/^{22}\text{Ne}$ ratios between 4.21 and 93.5, a~~
603 ~~maximum $^4\text{He}/^{20}\text{Ne}$ ratio of 11,000 and $^4\text{He}/^{40}\text{Ar}^*$ ratios between 0.14 and 3.11 (as observed in our~~
604 ~~samples; see Figures 7A and 8), we recalculated that a local upper mantle with $^{40}\text{Ar}/^{36}\text{Ar}$~~
605 ~~ratios signature equal to of about 10,500 for the local upper mantle can justify the variability of our~~
606 ~~xenoliths (see Figure 9B and Table 3). Assuming a MORB-like $^{40}\text{Ar}/^{36}\text{Ar}$ signature of This approach~~
607 ~~suggests that the original $^{40}\text{Ar}/^{36}\text{Ar}$ of the upper-pristine upper mantle (~44,000; (Moreira et al., 1998),~~
608 ~~our evidence these calculations further support has decreased significantly and supports the existence~~
609 ~~of an atmospheric component in the Mexican lithospheric mantle, likely recycled during subduction~~
610 ~~events. Similar indications were observed in SCLM xenoliths from European localities, West~~
611 ~~Antarctic Rift System (WARS), Eastern Australia, Red sea region, N/S Kenya rifts and Ethiopia~~
612 ~~(Afar) (Matsumoto et al., 1998, 2000; Hopp et al., 2004, 2007a, 2007b; Buikin et al., 2005;~~
613 ~~Gautheron et al., 2005a; Czuppon et al., 2009; Martelli et al., 2011; Halldórsson et al., 2014; Broadley~~
614 ~~et al., 2016; Rizzo et al., 2018; Correale et al., 2019; Faccini et al., 2020).~~

615 Petrological evidence also ~~supports~~ highlights the interaction of the local upper mantle with
616 ~~metasomatic fluids possibly coming from the subducted oceanic crust (Pier et al., 1989; Luhr and~~
617 ~~Aranda-Gómez, 1997; Dávalos-Elizondo et al., 2016). Subduction may have favored recycling of air-~~
618 ~~rich components in the interested portion of the SCLM. Even though the present-day plate geometry~~
619 ~~in central and southern Mexico implies ~~then and at the~~ oceanic crust subduction terminates beneath~~
620 ~~the TMVB (Figure 1; Pardo and Suárez, 1995; Ferrari et al., 2012) i.e. 200 km south JH, subduction~~
621 ~~of the Farallon plate beneath the western part of North America during the Mesozoic and Paleogene~~
622 ~~could have potentially modified the Mexican lithospheric mantle directly below la Mesa Central (Pier~~
623 ~~et al., 1989; Bunge and Grand, 2000). ~~We consider~~ Therefore, we consider ~~it possible~~ realistic that~~
624 ~~the presence of an atmospheric component in FI fluid inclusions from JH is mostly attributable to a~~
625 ~~local SCLM feature. Moreover, since Ne isotopes of JH overlap the fields of data from WARS and~~
626 ~~European SCLM mantle xenoliths, the recycling of an atmospheric component in the lithospheric~~
627 ~~mantle may be common to many other geodynamic contexts.~~

Formatted: English (United States)

Formatted: Line spacing: Multiple 1.15 li

Formatted: Superscript

Formatted: Superscript

Formatted: Superscript

Formatted: Superscript

Formatted: Superscript

Formatted: Superscript

Formatted: Superscript

Formatted: Superscript

Formatted: Superscript

Formatted: Superscript

Formatted: Superscript

Formatted: Superscript

Formatted: Superscript

Formatted: Superscript

Formatted: Line spacing: Multiple 1.08 li

Field Code Changed

Formatted: Spanish (Spain)

Formatted: Spanish (Spain)

Formatted: Font: Calibri

628

629

630 6.4.1.3.2 *Noble gas signature of the JH mantle source*
631 *No mantle plume component in the JH mantle source.*

632 Ne isotopes can additionally be used, in combination with He isotopes, to resolve any potential
633 influence of a mantle plume on the isotopic signature of the JH mantle xenoliths. To this aim, the
634 relationship between the extrapolated neon isotope ratio (i.e. the air-free mantle $^{21}\text{Ne}/^{22}\text{Ne}$ ratio
635 expressed as $^{21}\text{Ne}/^{22}\text{Ne}_{\text{EX}}$) and the $^3\text{He}/^4\text{He}$ values was evaluated (e.g., Hopp et al., 2004, 2007b;
636 Halldórsson et al., 2014). The $^{21}\text{Ne}/^{22}\text{Ne}_{\text{EX}}$ values were calculated by extrapolating the measured
637 $^{21}\text{Ne}/^{22}\text{Ne}$ ratios to Neon-B ($^{20}\text{Ne}/^{22}\text{Ne}=12.5$) using the methodology proposed by Graham (2002)
638 and Halldórsson et al. (2014). Only those samples with $^{40}\text{Ar}/^{36}\text{Ar}$ ratios $> 300-500$ and $^{20}\text{Ne}/^{22}\text{Ne}$
639 ratios distinguishable from air were selected. For comparison, the same calculation was made using
640 the Ne isotopes previously reported for the European SCLM (Buikin et al., 2005; Gautheron et al.,
641 2005a; Martelli et al., 2011; Rizzo et al., 2018; Faccini et al., 2020) (Gautheron et al. 2005; Martelli
642 et al. 2011; Rizzo et al. 2018), the WARS SCLM (Broadley et al., 2016; Correale et al.,
643 2019) (Correale et al., 2019), Eastern Australia SCLM (Matsumoto et al., 1998, 2000), Red sea region
644 (Hopp et al., 2004; Halldórsson et al., 2014) and the EAREthiopia (Afar) region (Halldórsson et al.,
645 2014) and N/S Kenya rifts (Hopp et al., 2007b; Halldórsson et al., 2014); as a result, the graph
646 reported in the Figure 9D-10A was obtained.

647 As evidenced in Figure 9D-10A, samples V-K/VF Ol, VF Opx and V-E/V-H Cpx exhibit our mantle
648 xenoliths have $(^{21}\text{Ne}/^{22}\text{Ne})_{\text{EX}}$ and $^4\text{He}/^3\text{He}$ ratios close to the theoretical value for a MORB-like upper
649 mantle (as observed for some mantle xenoliths from the Easter Australia SCLM and the Red sea
650 region), the remaining values fall along the binary mixing MORB-Plume mixing line.
651 Concerning When comparing our samples with other portions of SCLM on Earth, and are higher
652 compared to typical plume related values. Concerning the WARS, and the European SCLM
653 values and the N/S Kenya rifts, we notice that JH nodules have similar $(^{21}\text{Ne}/^{22}\text{Ne})_{\text{EX}}$ and but lower
654 $^4\text{He}/^3\text{He}$ values, -confirming the presence of a common dominating MORB component for the three
655 these localities and the less radiogenic nature of the Mexican lithospheric mantle. On the other hand,
656 the Instead, the EAR-Ethiopian xenoliths more clearly exhibit both $(^{21}\text{Ne}/^{22}\text{Ne})_{\text{EX}}$ and $^4\text{He}/^3\text{He}$ two
657 groups of values, one group with $(^{21}\text{Ne}/^{22}\text{Ne})_{\text{EX}}$ similar to the European SCLM and another group
658 with ratios similar close to the a Plume endmember component.

659 Halldórsson et al. (2014) interpreted this variability by a binary mixing between these two end-
660 members (SCLM and Plume), confirming the influence of a single mantle plume source In the case
661 of JH mantle xenoliths, $(^{21}\text{Ne}/^{22}\text{Ne})_{\text{EX}}$ ratios < 0.05 would suggest a deep-mantle contribution of
662 plume derived Neon ($< 10\%$). However, it must be taken into account that the samples less
663 contaminated by the atmospheric component fall within the AIR-MORB line when considering their
664 error bars (Figure 7C). In addition, this component does not affect the $^3\text{He}/^4\text{He}$ ratios helium ratios
665 which reflect a homogeneous MORB-like upper mantle signature. Based on noble gas
666 signatures these evidences, we conclude that the upper mantle beneath JH is predominantly MORB-
667 like with a minimum contamination by a recycled crustal component, although we cannot totally
668 discard a deep-mantle neon isotopic ratios from JH xenoliths do not totally exclude a plume
669 contribution, the local upper mantle is predominantly MORB with a minimum contamination by a
670 recycled crust. This conclusion support the idea. The helium and neon isotopic ratios from JH

Formatted: Font: Italic

Formatted: Font: Italic

Formatted: Line spacing: Multiple 1.08 li

Field Code Changed

Formatted: Font: Times New Roman, English (United States)

Field Code Changed

Formatted: Font: Times New Roman, Italian (Italy)

Formatted: Italian (Italy)

Field Code Changed

Field Code Changed

Formatted: Font: Times New Roman, English (United States)

Field Code Changed

Formatted: Font: Times New Roman, Spanish (Spain)

Formatted: Spanish (Spain)

Formatted: Font: Times New Roman, Spanish (Spain)

Formatted: Spanish (Spain)

Field Code Changed

Formatted: Spanish (Spain)

Field Code Changed

Formatted: Spanish (Spain)

Formatted: Spanish (Spain)

Formatted: Font: Calibri, Spanish (Spain)

Formatted: Line spacing: Multiple 1.08 li

Formatted: Danish

Field Code Changed

Formatted: Danish

Formatted: Danish

Formatted: Not Superscript/ Subscript

671 ~~xenoliths thus exclude a lower mantle contribution to the local SCLM. Rather, they point to a MORB-~~
672 ~~like source with a minimum contamination by a recycled crust, confirming that the VESVF is rather~~
673 ~~due to originates from~~ extension and melting of the lithospheric mantle under the Mesa Central
674 province.

675

676 6.3.3 A MORB-like $^3\text{He}/^4\text{He}$ He ratio signature

677 As discussed above, the $^3\text{He}/^4\text{He}$ ratios measured in the xenoliths indicate a MORB-like signature
678 (8.1 Ra , Graham, 2002; Figure 910) for the JH mantle. The relative invariance of the Rc/Ra values
679 suggests that the upper mantle under this portion of La Mesa Central is relatively homogeneous in
680 terms of noble gases ($\text{Rc/Ra} = 7.39 \pm 0.14$; Figure 10B - D). This $^3\text{He}/^4\text{He}$ signature is similar to
681 that measured at the WARS ($7.5 \pm 0.5 \text{ Ra}$ and $7.1 \pm 0.4 \text{ Ra}$; Broadley et al., 2016; Correale et al.,
682 2019) and at the upper range of that inferred at the WARS/N/S Kenya rifts and Red Sea region (6.6
683 $\pm 0.7 \text{ Ra}$ and $7.0 \pm 0.9 \text{ Ra}$, respectively; Hopp et al., 2004, 2007b; Halldórsson et al., 2014), ($7.1 \pm$
684 0.4 ; Correale et al., 2019), but manifestly less radiogenic than the European SCLM (6.1 ± 0.9 ;
685 Gautheron and Moreira, 2002; Buikin et al., 2005; Gautheron et al., 2005a; Martelli et al., 2011;
686 Rizzo et al., 2018; Faccini et al., 2020), Gautheron and Moreira, 2002; Gautheron et al., 2005; Martelli
687 et al., 2011; Rizzo et al., 2018).

688

689 The MORB-type $^3\text{He}/^4\text{He}$ He signature at JH deserves some consideration in relation to the past
690 geodynamic history of the area. We envisage two possible scenarios.

691 In scenario 1, the relatively homogeneous (MORB-like) $^3\text{He}/^4\text{He}$ ratios for the JH mantle xenoliths
692 might be taken as indicative of a low-to-negligible recycling of crustal materials during the
693 subduction of Farallon plate (20-40 Ma). A limited input of U-Th-bearing crustal materials would in
694 fact explain well the low contribution of radiogenic ^4He in the local mantle. If this interpretation is
695 correct, then past subduction events would only have added only have altered the Ne and Ar isotopic
696 budgets via the addition of a recycled air-atmospheric component into the mantle (cfr 6.31.1).
697 Alternatively, one may consider a scenario (scenario 2) in which any addition of (subduction-related)
698 crustal materials during subduction of the Farallon plate was later (during the <20 Ma Basin and
699 Range extensional phase) overprinted by an influx of MORB-like materials, rising from deeper
700 (asthenospheric to deep SCL) mantle domains. This latter scenario is supported by the geodynamic
701 reconstructions that indicate a metasomatism/refertilization of the lithospheric mantle during the
702 Basin and Range extensional phase. Paleo-subduction reconstructions indicate that the Farallon plate
703 subducted horizontally underneath Western North-America and Northern-Central Mexico between
704 74 - 40Ma, producing the Laramide orogeny in the United States and the mountain range known as
705 the Sierra Madre Oriental (SMOr) east of the JH (Figure 1; Atwater, 1989; Cserna, 1989;
706 Severinghaus and Atwater, 1990; Bunge and Grand, 2000; Eguiluz de Antuñano et al., 2000; Lee,
707 2005). This tectonic configuration would have changed at ~40-20Ma, however, when the retreating
708 subduction of the Farallon slab occurred, a commonly invoked cause for initiation of the Basin and
709 Range extension (Leeman and Harry, 1993; Nieto-Samaniego et al., 1999, 2005; Lee, 2005; Sedlock,
710 2003), (Leeman and Harry, 1993; Nieto-Samaniego et al., 1999; Lee, 2005; Nieto-Samaniego et al.,
711 2005; Sedlock, 2003). According to Nieto-Samaniego et al. (1999), retreating of the oceanic slab
712 favored the influx of younger and hotter asthenospheric material that ultimately led to melt generation
713 and extension at the base of the Mesa Central. Evidence of this process comes from the intense

Formatted: Font: (Default) Times New Roman, 11 pt, English (United States)

Formatted: Font: (Default) Times New Roman, 11 pt, English (United States)

Formatted: Font: (Default) Times New Roman, 11 pt

Formatted: Font: (Default) Times New Roman, 11 pt

Formatted: Font: (Default) Times New Roman, 11 pt

Field Code Changed

Formatted: Font: Times New Roman, French (France)

Formatted: French (France)

Formatted: Font: Times New Roman, French (France)

Formatted: Font: Times New Roman, French (France)

Field Code Changed

Formatted: Font: Calibri, French (France)

Formatted: Line spacing: Multiple 1.08 li

Field Code Changed

Formatted: Font: Times New Roman, English (United States)

Formatted: English (United Kingdom)

Formatted: English (United Kingdom)

Field Code Changed

Formatted: English (United Kingdom)

714 normal faulting in the Mesa Central registered 30Ma, 23-24Ma 12-13Ma ago, and from the transition
 715 from calc-alkaline volcanism (in the so-called Sierra Madre Occidental; SMO; Figure 1) to intraplate
 716 alkaline volcanism (Henry and Aranda-Gomez, 1992; Nieto-Samaniego et al., 1999; Aranda Gómez
 717 et al., 2000). Injection of ³He-rich (MORB-like) asthenospheric melts during the mid-Cenozoic could
 718 well have caused re-fertilization/re-juvenation of the Mexican lithospheric mantle in a model similar
 719 to that proposed for the lithospheric mantle beneath the Yangtze craton and the WARS (Correale et
 720 al., 2016, 2019; Faccini et al., 2020). This scenario is possible if we assume that almost all ³He comes
 721 from asthenospheric melts, as proposed by [Gautheron and Moreira \(2002\)](#) and [Gautheron et al.](#)
 722 [\(2005a\)](#) ~~Gautheron and Moreira (2002) and Gautheron et al. (2005)~~ to explain the noble gases
 723 systematics of the European SCLM (a steady-state model).

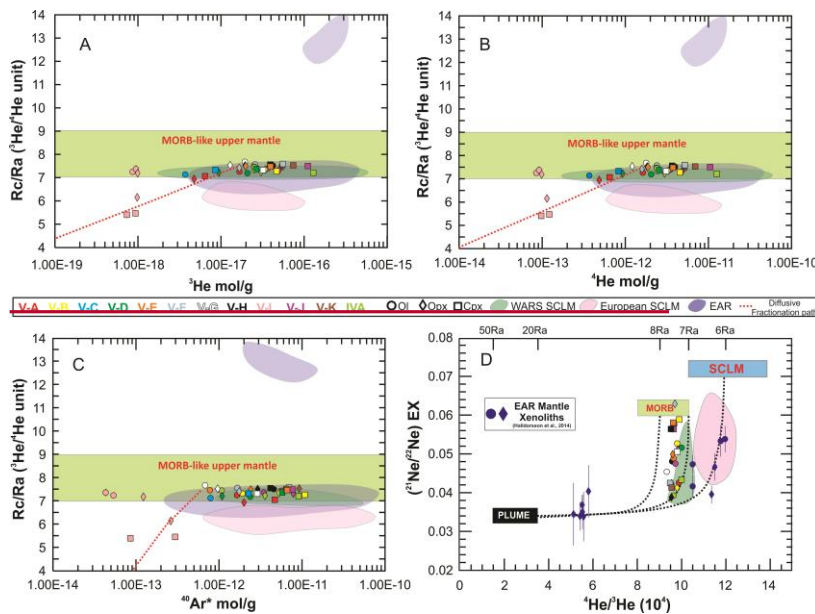


Figure 9. A) ³He, B) ⁴He and C) ⁴⁰Ar* vs ³He/⁴He corrected for air contamination (R_c/R_a). MORB range is reported at R_c/R_a = 8 ± 1 (Graham, 2002). D) ²¹Ne/²²Ne_{EX} ratios vs ⁴He/⁴He ratios, adapted from Halldórsson et al. (2014). Dotted lines are binary mixing between three endmembers: 1) Plume, at 20Ra and ²¹Ne/²²Ne_{EX} = 0.034 ± 0.001, 2) MORB-like upper mantle at 8 ± 1 Ra and ²¹Ne/²²Ne_{EX} = 0.06 ± 0.001 and SCLM at 6.1 ± 0.9 Ra and ²¹Ne/²²Ne_{EX} = 0.07 ± 0.001.

724 ~~Independently on~~ [respective if](#) of subduction is considered to have (scenario 2) or have not (scenario
 725 1) impacted the He mantle budget, there is unquestionable petrographic evidence (this study; Liang
 726 and Elthon, 1990; Luhr and Aranda-Gómez, 1997) for a melt-related metasomatic event affecting the
 727 JH, potentially during Basin and Range extensional phase (Nieto-Samaniego et al., 1999).

728

Field Code Changed

Formatted: Font: Times New Roman, English (United States)

Formatted: Font: Calibri

Formatted Table

729 **6.2.4.5 ³He fluxes, ⁴He production and the helium residence time for the Mexican lithospheric**
730 **mantle**

731 The MORB-type He signature of JH xenoliths can quantitatively be interpreted in light of the SCLM
732 model of Gautheron and Moreira, (2002). According to the authors (see ~~also~~ ~~(Griffin et al.,~~
733 ~~1999, 2009), Griffin et al., 1999, 2009),~~ the geochemical and isotopic characteristics of the SCLM
734 are the ultimate result of any past interaction with fluids and melts coming from (i) deeper mantle
735 sources and/or (2) recycled slab components that have alternated over geological time (Griffin et al.,
736 1999). In terms of helium isotopes, Gautheron and Moreira (2002) argued that the SCLM is globally
737 homogeneous (6.1 ± 0.9 Ra). They based this inference on the study of suites of ultramafic xenoliths
738 and alkali basalts collected from different continental settings (Europe, USA, Antarctic, Australia,
739 and West Africa).

740 In order to explain its helium isotopic homogeneity, Gautheron and Moreira (2002) proposed the
741 global lithospheric mantle is in steady state for helium. In their model, the global SCLM is
742 continuously metasomatized by melts and fluids with a MORB-like helium signature coming from
743 the asthenosphere (affecting the entire reservoir); eventually, this signature becomes more radiogenic
744 due to U and Th decay resulting in lower ³He/⁴He ratios (e.g. 6.1 ± 0.9 Ra). Thus, the steady-state
745 model is based on the balance between the He flux from the asthenosphere and the in-situ production
746 in the lithosphere of radiogenic ⁴He. From this model, it is possible to estimate the helium residence
747 time in the lithospheric mantle (Rt), the ³He flux (F) and the ⁴He production (P*). The model uses
748 the dimensions of the SCLM (thickness, surface and density) assuming a constant U + Th
749 concentration. These authors reported a Rt = ~200 Ma, F= 270 mol/yr and P* = 6.8x10⁶ mol/yr for
750 the global SCLM, while Gautheron et al. (2005) obtained a Rt = 5-150 Ma, F= 3.5 x10⁴ at/m²/s (~ 1
751 mol/yr) and P* ~ 3 x 10⁴ mol/yr for the European SCLM.

752 However, ~~some studies on noble gas systematics (including our results) our data and a recent study~~
753 ~~on West Antarctic Rift (Correale et al., 2019)~~ support a more fertile signature (³He/⁴He > 7.0 Ra) for
754 some portions of the SCLM on Earth (e.g., Southern Australia and West Antarctic Rift; ~~Matsumoto~~
755 ~~et al., 1998; Broadley et al., 2016; Correale et al., 2019).~~ Therefore, we argue that the steady state
756 model proposed by Gautheron and Moreira (2002) should be applied in local portions of SCLM to
757 eventually detail their interactions with the asthenosphere. Using this steady-state model, and
758 considering the ³He/⁴He signature of the JH mantle xenoliths, we estimated the helium residence
759 time, the ³He flux and the ⁴He production for the lithospheric mantle located under the San Luis
760 Potosí state (central Mexico) ~~following Gautheron and Moreira (2002).~~

761
$$F = \frac{P^*}{\left(\frac{^3\text{He}}{^4\text{He}}\right)_{\text{SCLM}} - \left(\frac{^3\text{He}}{^4\text{He}}\right)_{\text{MORB}}} \quad \text{eq.3}$$

762 In eq. 3, F is the ³He flux (cc STP/yr) and P* is the ⁴He production (P* = 2.8 * 10⁻¹⁴ * (4.35 + Th/U) *
763 U * M). U is the concentration of uranium in ppm and M is the mass of the subcontinental mantle.
764 The helium residence time Rt is defined as:

765
$$Rt = \frac{\text{Total } ^3\text{He in the SCLM (cc STP)}}{F} \quad \text{eq.4}$$

766 –The parameters used in the calculation are as follows: 1) the average of the ³He/⁴He ratios
767 measured in JH mantle xenoliths equal to ~~97.500 (7.387.38~~ Ra) and a MORB endmember equal to
768 ~~84.600 (8.5 Ra)~~. The latter value is higher than that assumed by Gautheron and Moreira (2002) (8.0

Formatted: Font: Not Italic

Formatted: Font: Not Italic

Formatted: Line spacing: Multiple 1.08 li

Field Code Changed

Formatted: Font: Times New Roman, English (United States)

Formatted: Font: Calibri

Formatted: Line spacing: Multiple 1.08 li

Field Code Changed

Formatted: Font: Times New Roman, English (United States)

Formatted: Font: Calibri

Formatted: Font: 12 pt

Formatted: Font: 12 pt

Formatted: Font: 12 pt

Formatted: Font: 12 pt, Raised by 2 pt

Formatted: Font: 12 pt

Formatted: Font: 12 pt, Raised by 2 pt

Formatted: Font: 12 pt

Formatted: Font: 12 pt

Formatted: Font: 12 pt

Formatted: Font: 12 pt, Raised by 2 pt

Formatted: Font: 12 pt

Formatted: Font: 12 pt, Raised by 2 pt

Formatted: Font: 12 pt

Formatted: Font: 12 pt

Formatted: Font: 12 pt

Formatted: Raised by 2 pt

Formatted: Line spacing: Multiple 1.08 li

769 Ra) because preliminary results for mantle xenoliths from other localities in central Mexico yield
770 Rc/Ra values of ≤ 8.35 (unpublished data); 2) U contents between 0.01 and 0.03 ppm as previously
771 reported for mantle xenoliths from central Mexico (Dávalos-Elizondo et al., 2016) and a Th/U = 3
772 as assumed by Gautheron and Moreira (2002); 3) A subcontinental mantle mass equal to 3.66×10^{21}
773 g. This mass was estimated assuming a thickness of the local lithospheric mantle ~~of~~ ~ 150 km
774 (density of 3.3×10^6 g/m³; Gautheron and Moreira, 2002) and a ~~4~~ surface of 7.4×10^9 m² that
775 includes all the Cenozoic intraplate monogenetic volcanic fields located in the San Luis Potosí state
776 (VESVF, SDVF and Los Encinos volcanic field; see Figure 1; Aranda-Gómez et al., 2007); 5) A
777 upper mantle ⁴He concentration ~~equal to~~ 1×10^{-6} ccSTP/g (4.5×10^{-11} mol/g), which corresponds
778 to the maximum value identified for continental mantle xenoliths (Gautheron and Moreira, 2002);
779 this value is equivalent to a ³He concentration $= 1.0 \times 10^{-11}$ ccSTP/g (4.5×10^{-16} mol/g) assuming a
780 Rc/Ra = 7.38; thus the total ³He estimated for the local SCLM is 1.64×10^6 mol (3.66×10^{10} cc STP).
781 ~~The results obtained are reported in Table 34.~~

782 The calculated ³He fluxes for the Mexican lithospheric mantle vary from 0.027 to 0.080 mol/g
783 (Figure ~~10A11A~~). These fluxes are very low if compared with the values reported for the global
784 SCLM, the European SCLM or MORB values (800-1300 mol/g; Marty and Jambon, 1987; Javoy et
785 al., 1989; Michael and Graham, 2015; Tucker et al., 2018). When scaled to the surface area (7.4×10^9
786 m²) of volcanism in the San Luis Potosí state, our specific fluxes vary between 6.9 and 20.7 at/s/cm²
787 (Figure 11B) which are well above the MORB and the global SCLM values (4.8 at/s/cm² and 3.5
788 at/s/cm², respectively; Craig et al., 1975; Gautheron and Moreira, 2002) confirming a high ³He
789 contribution from the asthenosphere under central Mexico.

790 The associated Rt values range from 20 to 60 Ma. These estimates are lower if compared to the global
791 SCLM and would explain the less radiogenic character of the Mexican lithospheric mantle. In this
792 model, the Rt values do not depend on the area but have a close relationship with the average of the
793 ³He/⁴He ratios measured in the mantle xenoliths. It is reasonable to think that the smaller the ³He/⁴He
794 ratio measured in the xenoliths (7.38 Ra for JH xenoliths and 6.1Ra for the SCLM), the longer the
795 helium residence time in the lithospheric mantle should be. Therefore, low Rt values implies low ⁴He
796 production and high ³He/⁴He ratios, as observed in JH mantle xenoliths. Moreover, our estimated Rt
797 range overlaps with the inferred age range for the retreating subduction of the Farallon slab (40-20
798 Ma ago); a processes, which may have triggered the injection of asthenospheric melts in the
799 lithospheric mantle and the generation of the Basin and Range province (Nieto-Samaniego et al.,
800 1999; Lee, 2005). If correct, our results would independently indicate that the last major geodynamic
801 modification in the lithospheric mantle underneath the JH occurred during the lower and mid-
802 Cenozoic. We argue that the refertilization event was able to increase the ³He/⁴He signature within
803 the MORB-like range, overprinting the pre-Cenozoic signature recorded by the Mexican lithospheric
804 mantle. Since then, the latter would have evolved in a similar way to that proposed by Gautheron and
805 Moreira (2002), ~~i.e.~~, in a steady state becoming slightly more radiogenic during the last ~ 20 Ma
806 down to the measured ³He/⁴He values.

807 In conclusion, both the low production of ⁴He and the relative lower Rt (compared to other areas)
808 could explain the high ³He/⁴He ratios measured in JH mantle xenoliths. However, we caution these
809 are local estimates; therefore, in order to minimize the effect generated by the area and possible
810 mantle heterogeneities, future work will target obtaining isotopic data for mantle xenoliths from other

Formatted: Superscript

Formatted: Superscript

Formatted: Superscript

Formatted: Superscript

Formatted: Superscript

Formatted: Superscript

Formatted: Font: Calibri

811 localities of the Basin and Range extension in Mexico. This will allow a more realistic reconstruction
812 of the evolution of the Mexican lithosphere in terms of noble gases.

813

814 *6.254.1 Mantle CO₂ fluxes*

815 We combine the ³He flux estimated above with the CO₂/³He ratios measured in the JH xenoliths (e.g.
816 Marty and Jambon, 1987; Tucker et al., 2018) to calculate the mantle-derived CO₂ fluxes in the area.
817 Taking U concentrations between 0.01 ppm and 0.03 ppm and a CO₂/³He_(avg) ~1.47 x 10⁹, the
818 calculated CO₂ fluxes range from 3.93 x 10⁷ mol/yr (~~1.02 x 10¹⁰ at/s/cm²~~) to 1.18 x 10⁸ mol/yr
819 (~~3.05 x 10¹⁰ at/s/cm²~~; ~~Figure 11C-110BD~~). Our estimated fluxes are lower than previously estimated
820 for other continental rift localities (such as the EAR), consistent with the small area of the San Luis
821 Potosí volcanic field (considered in the model), and correspond to <0.1% of the MORB CO₂ fluxes;
822 similarly, our fluxes are lower than estimated for hot spot settings such as Hawaii or Canary Islands
823 (Hauri et al., 2019). Additional studies on noble gas and CO₂ isotopic data from other mantle
824 xenolith locations in central and northwestern Mexico are required to further validate our results.

825

Formatted: Superscript

Formatted: Superscript

Formatted: Superscript

Formatted: Superscript

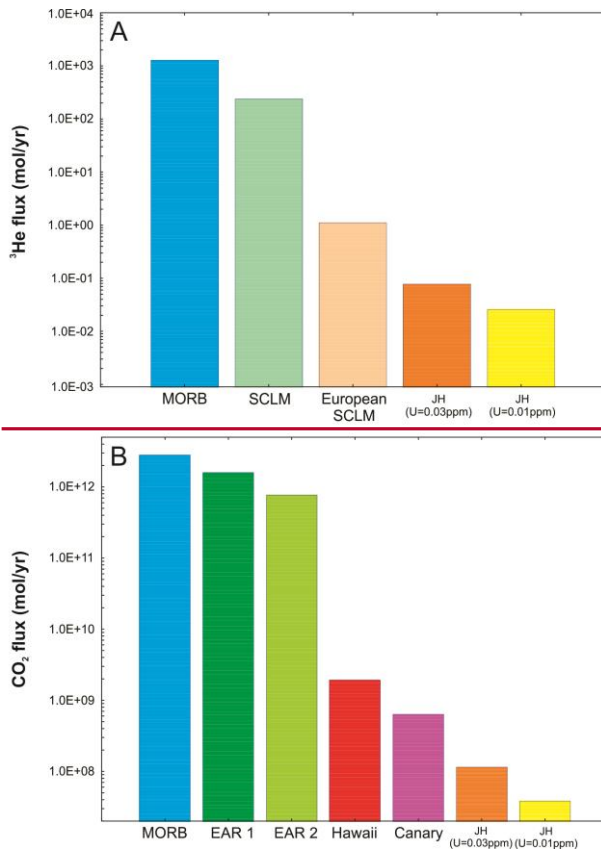


Figure 10. A) Comparison between ³He fluxes measured in central Mexico based on JH mantle xenoliths analysis (at U=0.01 and 0.03 ppm) and other localities; MORB value was built using data from Michael and Graham (2015) using a CO₂/He ratio = 2.2 × 10⁶ (Marty and Tolstikhin, 1998); SCLM value was taken from Gautheron and Moreira (2002); the European SCLM flux was calculated based on Gautheron et al. (2005). B) Associated CO₂ fluxes (mol/yr) for central Mexico compared with other tectonic localities. MORB CO₂ flux was calculated after Michael and Graham (2015); EAR1 and EAR2 values were taken from Lee et al. (2016) and Foley and Fischer (2017), respectively; Hawaii and Canary fluxes were obtained from Hawri et al. (2019).

826

827

828

829 **6.5.36 Inferences on CO₂ origin.**

830 In JH peridotites, fluids are dominated by CO₂ (Figure 6), as typically recorded by other worldwide
 831 mantle xenoliths (Andersen and Neumann, 2001; Deines, 2002; Frezzotti and Touret, 2014). (Deines,
 832 2002; Andersen and Neumann, 2001, Frezzotti and Touret, 2014). Thus, the CO₂ isotopic
 833 composition can be used to constrain carbon origin. Our samples exhibit δ¹³C ratios between -0.97
 834 and -2.86‰ (Figure 4+12A); they are therefore isotopically more positive (¹³C-rich) than found in

Formatted Table

Formatted: Line spacing: Multiple 1.08 li

Formatted: Font: Times New Roman, English (United States)

Field Code Changed

835 European mantle xenoliths in alkaline intra-plate and extensional contexts, such as in the Hyblean
836 plateau (southeast Sicily, Italy; ranging from -4 to -2‰; Correale et al., 2015) and Lower Silesia
837 (southwest Poland; ranging from -4.7 to -3.1‰; Rizzo et al., 2018).

Formatted: Font: Calibri

838

839 The CO₂ isotopic composition in the JH peridotites is also well above the δ¹³C MORB mantle range
840 (-8‰ < δ¹³C < -4‰; Sano and Marty, 1995). When δ¹³C values are plotted against Rc/Ra and
841 CO₂/He ratios (Figure 4B, 4C), our samples fall along a MORB-Limestone mixing line,
842 suggesting source mantle Carbon contamination by C-rich fluids with a crustal carbonate signature.

843 The crustal carbon component found in fluid inclusions of JH xenoliths may in principle derive
844 from two main distinct processes: (i) infiltration of CO₂ rich fluids derived by assimilation of
845 carbonates by host magmas during ascent through the continental crust, and (ii) mantle
846 metasomatism by CO₂-rich fluids and melts derived from subducted oceanic crust and sediments.

847 Infiltration of CO₂ fluids in mantle xenoliths outgassed during assimilation of carbonates in basanitic
848 magmas in the continental crust should be considered since JH maar formed on carbonate deposits
849 (the Valles-San Luis Potosí calcareous platform (PVSLP) and the Mesozoic Basin of central
850 Mexico). However, the relatively fast ascent rates of the host magma through the continental crust
851 (Luhr et al., 1989; Pier et al., 1989), and the lack of carbonate xenoliths in the host lava, argue against
852 a crustal component inherited during sin-eruptive magma ascent. Conversely, petrographic and
853 Raman evidence indicates pervasive infiltration of carbonate-bearing silicate melts and CO₂-fluids
854 in peridotites (Figure 4), strongly supporting deep carbon mobility during a metasomatic event in the
855 lithospheric mantle. We, therefore, conclude that the carbonate component identified in JH CO₂
856 fluids was trapped under mantle conditions and is related to CO₂ degassing of metasomatic
857 carbonate-rich silicate melts on reaction with mantle minerals. Metasomatic processes occurred well
858 before entrainment by the host magma and eruption (as proposed by Liang and Elthon, 1990).

859 As mentioned in the previous sections, northwestern Mexico's current tectonic configuration
860 indicates that the Cocos and Rivera plates do not directly affect the mantle under the Mesa Central,
861 making it difficult to consider involvement of present subduction (Figure 1). Moreover, some studies
862 suggest that the contribution of carbonate sediments from the subducting slab is minimal. The CO₂-
863 rich plume gases released by arc volcanoes (e.g., Popocatepetl) come from the assimilation of
864 limestone deposits, as evidenced by trace element analysis performed in mafic rocks and the presence
865 of carbonate xenoliths in volcanic deposits (Goff et al., 1998, 2001; Aiuppa et al., 2017). A low
866 contribution of subducted Carbon in fluids has also been proposed for other volcanic fields belonging
867 to the TMVB, such as the Sierra Chichinautzin Volcanic Field (SCVF; Verma, 2000) and the
868 Michoacan-Guanajuato Volcanic Field (MGVF; Verma and Hasenaka, 2004).

869 In contrast to present-day subduction being an unlikely driver, we emphasize a possible major role
870 played by older subduction of the Farallon underneath the northwestern margin of North America
871 during the Mesozoic and early Cenozoic (Atwater, 1989; Ferrari et al., 2012; Henry and Aranda-
872 Gomez, 1992; Sedlock, 2003). Several authors claim that the North American lithospheric mantle
873 could have been hydrated by fluids or melts released by flat subduction of the Farallon plate, as
874 evidenced by petrological studies of mantle xenoliths from the Sierra Nevada and the Colorado
875 Plateau (Smith et al., 1999; Lee, 2005; Li et al., 2008). "Farallon hydration" (Lee, 2005) is suggested
876 to have occurred during the late Cretaceous and early Cenozoic, and to have affected the lithospheric

877 mantle up to 800 km inboard of the trench (Li et al., 2008). This metasomatic event is also well
 878 documented in Mexican xenoliths (Liang and Elthon, 1990; Dávalos-Elizondo et al., 2016; Levrèsse
 879 et al., 2016). For example, Luhr and Aranda-Gómez (1997) interpreted the systematic east to west
 880 oxygen fugacity increase in Cenozoic mantle xenoliths from central and northern Mexico as induced
 881 by the progressive oxidation of the lithospheric mantle by fluids released by the Farallon oceanic
 882 slab.

883 In light of the above, the interaction between subducted fluids delivered by the Farallon plate and the
 884 Mexican lithospheric mantle could represent a feasible mechanism to explain the heavy $\delta^{13}\text{C}$
 885 signatures of JH mantle fluids. We argue that the crustal carbon component identified in the **FI-fluid**
 886 **inclusions** would reflect a mantle feature induced by an old subduction-related carbonate component
 887 inherited during the mid-Cenozoic before the Basin and Range extension (Middle Miocene; Henry
 888 and Aranda-Gomez, 1992; Sedlock, 2003) and recycled in the local mantle.

889

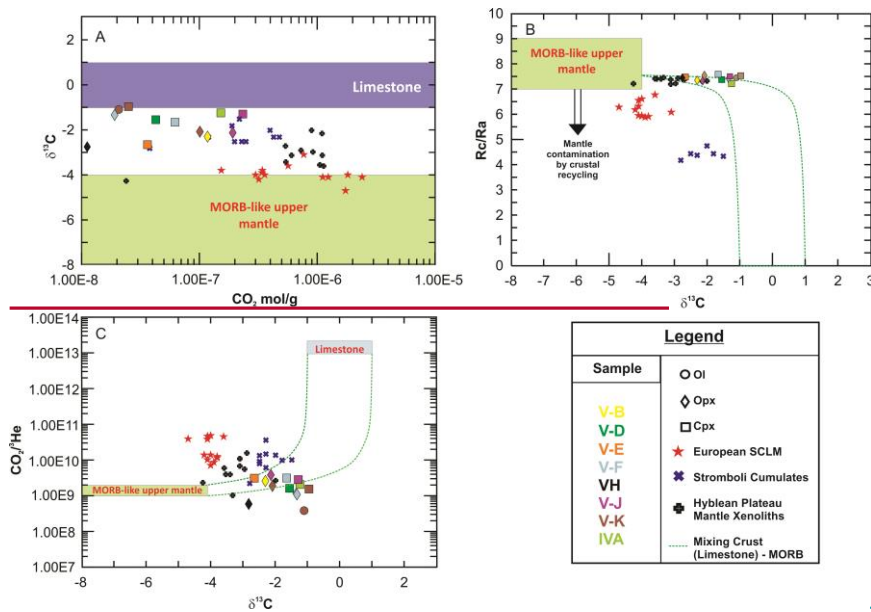


Figure 11. A) CO_2 vs $\delta^{13}\text{C}$. Hyblean, Stromboli and European SCLM data from Correale et al. (2015), Gennaro et al. (2017) and Rizzo et al. (2018), respectively. B) $\delta^{13}\text{C}$ vs He^2/He^4 corrected for air contamination (Re/Ra). Dotted lines are binary mixing between two endmembers: 1) Limestone at $\delta^{13}\text{C} = -1$, 1 and $\text{Re/Ra} = 0.01$ and 2) MORB-like upper mantle at $\delta^{13}\text{C} = -4$ and $\text{Re/Ra} = 7.38$. C) $\delta^{13}\text{C}$ vs CO_2/He . Dotted lines are binary mixing between two endmembers: 1) Limestone at $\delta^{13}\text{C} = -1$, 1 and $\text{CO}_2/\text{He} = 10^{12}$ and 2) MORB-like upper mantle at $\delta^{13}\text{C} = -4$ and $\text{CO}_2/\text{He} = 1.00 \times 10^8, 2.00 \times 10^8$.

890 **7. CONCLUSIONS**

891 We investigate the petrography and noble gas- CO_2 composition of **FI-fluid inclusions** in ultramafic
 892 mantle xenoliths collected from JH, in central Mexico. Peridotites are classified as spinel-lherzolites

Formatted: English (United States)

Formatted: English (United States)

893 and harzburgites. Petrographic observations and Raman microspectroscopy analyses of fluid and
894 melt inclusions reveal the coexistence of glass/carbonate microveins and a CO₂ fluid phase
895 permeating the rocks, suggesting interaction between peridotites and degassing carbonate-rich
896 silicate melts at mantle depth.

897 The ⁴He/⁴⁰Ar* range (0.14 - 3.11) partially overlaps that of fertile mantle (1-5), ~~which could and~~
898 indicate ~~either~~ a low degree of partial melting ~~and~~ or the occurrence of a
899 metasomatism/refertilization process by melts degassing fluids ultimately entrapped in the mantle as
900 secondary fluid inclusions.

901 Ne and Ar systematics reveal a mixing between atmospheric and MORB-like fluids, strongly
902 supporting the presence of an atmospheric component eventually recycled from the Farallon plate
903 subduction. ~~Although, (²¹Ne/²²Ne)_{ex} ratios suggest the existence of plume-derived Neon in our fluid~~
904 inclusions. JH mantle xenoliths exhibit homogeneous ³He/⁴He signature (7.394 ± 0.214 Ra) that is
905 comparable to that of the MORB-like mantle and ~~higher similar to than~~ other worldwide SCLM
906 localities (eg., Eastern Australia, N/S Kenya rifts and WARS). This isotopic signature results from a
907 low recycling of crustal components in the local mantle possibly overprinted by a
908 metasomatism/refertilization episode reasonably occurred after the ~~subduction retreating retreat~~
909 of the Farallon slab during the early and mid-Cenozoic.

910 Based on the “Steady-state” model proposed by Gautheron and Moreira (2002), we estimated a
911 helium residence time in the local SCLM between 20-60Ma, which overlaps the geodynamic
912 evolution of the area and the metasomatism/refertilization event. Since then, the lithospheric mantle
913 would have evolved in a steady state for helium (from a MORB signature ~8.5 Ra) becoming slightly
914 more radiogenic during the last ~20Ma. We also calculated ³He fluxes between 0.027 - 0.080 mol/g,
915 ⁴He production rates from 340 to 1000 mol/yr and mantle CO₂ fluxes from 3.93 x 10⁷ mol/yr to
916 1.18x10⁸ mol/yr represent less than the 0.1% of the MORB CO₂ fluxes.

917 ~~He and Ne isotopic signatures argue against the presence of a mantle plume under central Mexico.~~

918 The δ¹³C values measured in JH ~~fluid inclusions~~ reveal a binary mixing between a MORB-like
919 upper mantle and a crustal carbonate component (limestone). We propose that the crustal
920 CO₂/carbonate component identified in JH xenoliths was trapped under mantle conditions through
921 metasomatic reactions between peridotites and C-bearing silicate melts. These would have acted as
922 carriers in the local mantle of a recycled carbon component inherited from the Mesozoic to early
923 Cenozoic Farallon subduction.

924

925 **ACKNOWLEDGMENTS**

926 This work is part of the PhD (XXXIV cycle) of Andres Libardo Sandoval Velasquez at the University
927 of Palermo. This research was funded by the Italian Miur (Grant N. 2017LMNLAW) and from Deep
928 Carbon Observatory. We thank Mariagrazia Misseri and Mariano Tantillo for helping in sample
929 preparation and in the isotope analysis of noble gases carried out in the noble gas laboratory of INGV-
930 Palermo. We also thank Ygor Oliveri and Giorgio Capasso for their effort in the INGV-Palermo
931 stable-isotopes laboratory. Raman facilities were provided by DISAT at Università Milano Bicocca
932 within the frame of MIUR Progetti di Eccellenza 2018-2022. We are grateful to Dr. Jens Hopp and
933 Dr Michael Ward Broadley for their valuable comments that improved our manuscript.

Formatted: Superscript

Formatted: Superscript

Formatted: Subscript

Formatted: Justified, Indent: First line: 0"

Formatted: Font: Times New Roman, Font color: Auto, English (United States), Pattern: Clear

REFERENCES

Aiuppa, A., Fischer, T.P., Plank, T., Robidoux, P., Di Napoli, R., 2017. Along-arc, inter-arc and arc-to-arc variations in volcanic gas CO₂/S T ratios reveal dual source of carbon in arc volcanism. *Earth Science Reviews* 168, 24–47. <https://doi.org/10.1016/j.earscirev.2017.03.005>

Andersen, T., Neumann, E. R., 2001. Fluid inclusions in mantle xenoliths. *Lithos* 55, 301–320. [https://doi.org/10.1016/S0024-4937\(00\)00049-9](https://doi.org/10.1016/S0024-4937(00)00049-9)

Aranda-Gómez, J.J., Henry, C.D., F. Luhr, J., 2000. Evolución tectonomagmática post-paleocénica de la Sierra Madre Occidental y de la porción meridional de la provincia tectónica de Cuencas y Sierras, México. *BSGM* 53, 59–71. <https://doi.org/10.18268/BSGM2000v53n1a3>

Aranda-Gómez, J.J., Luhr, J.F., 1996. Origin of the Joya Honda maar, San Luis Potosí, México. *Journal of Volcanology and Geothermal Research* 74, 1–18. [https://doi.org/10.1016/S0377-0273\(96\)00044-3](https://doi.org/10.1016/S0377-0273(96)00044-3)

Aranda-Gómez, J.J., Luhr, J.F., Housh, T.B., Valdez-Moreno, G., Chávez-Cabello, G., 2007. Late Cenozoic intraplate-type volcanism in central and northern México: A review, in: *Geology of México: Celebrating the Centenary of the Geological Society of México*. Geological Society of America. [https://doi.org/10.1130/2007.2422\(04\)](https://doi.org/10.1130/2007.2422(04))

Aranda-Gómez, J.J., Ortega-Gutiérrez, F., 1987. Mantle xenoliths in México, in: *Mantle Xenoliths*. John Wiley, New York, pp. 75–84.

Atwater, T., 1989. Plate tectonic history of the northeast Pacific and western North America, in: Winterer, E.L., Hussong, D.M., Decker, R.W. (Eds.), *The Eastern Pacific Ocean and Hawaii*. Geological Society of America, North America, pp. 21–72. <https://doi.org/10.1130/DNAG-GNA-N.21>

Barboza-Gudino, J.R., Tristán-González, M., Torres-Hernández, J.R., 1999. Tectonic setting of pre-Oxfordian units from central and northeastern Mexico: A review, in: *Special Paper 340: Mesozoic Sedimentary and Tectonic History of North-Central Mexico*. Geological Society of America, pp. 197–210. <https://doi.org/10.1130/0-8137-2340-X.197>

Basu, A.R., 1976. Textures, microstructures and deformation of ultramafic xenoliths from San Quintín, Baja California. *Tectonophysics* 43, 213–246. [https://doi.org/10.1016/0040-1951\(77\)90118-4](https://doi.org/10.1016/0040-1951(77)90118-4)

Boudoire, G., Rizzo, A.L., Arienzo, I., Di Muro, A., 2020. Paroxysmal eruptions tracked by variations of helium isotopes: inferences from Piton de la Fournaise (La Réunion island). *Sci Rep* 10, 9809. <https://doi.org/10.1038/s41598-020-66260-x>

Broadley, M.W., Ballentine, C.J., Chavrit, D., Dallai, L., Burgess, R., 2016. Sedimentary halogens and noble gases within Western Antarctic xenoliths: Implications of extensive volatile recycling to the sub-continental lithospheric mantle. *Geochimica et Cosmochimica Acta* 176, 139–156. <https://doi.org/10.1016/j.gca.2015.12.013>

Bunge, H. P., Grand, S.P., 2000. Mesozoic plate motion history below the northeast Pacific Ocean from seismic images of the subducted Farallon slab. *Nature* 405, 337–340. <https://doi.org/10.1038/35012586>

Burnard, P., 2004. Diffusive fractionation of noble gases and helium isotopes during mantle melting. *Earth and Planetary Science Letters* 220, 287–295. [https://doi.org/10.1016/S0012-821X\(04\)00060-3](https://doi.org/10.1016/S0012-821X(04)00060-3)

980 Burnard, P., 1997. Vesicle-Specific Noble Gas Analyses of "Popping Rock": Implications for
981 Primordial Noble Gases in Earth. *Science* 276, 568–571.
982 <https://doi.org/10.1126/science.276.5312.568>

983 Burnard, P.G., Farley, K.A., Turner, G., 1998. Multiple fluid pulses in a Samoan harzburgite. *Chemical*
984 *Geology* 147, 99–114. [https://doi.org/10.1016/S0009-2541\(97\)00175-7](https://doi.org/10.1016/S0009-2541(97)00175-7)

985 Carrillo-Bravo, J., 1971. La plataforma de Valles San Luis Potosí. *Boletín de la Asociación Mexicana*
986 *de Geólogos Petroleros* 23, 100.

987 Correale, A., Martelli, M., Paonita, A., Rizzo, A., Brusca, L., Scribano, V., 2012. New evidence of
988 mantle heterogeneity beneath the Hyblean Plateau (southeast Sicily, Italy) as inferred from
989 noble gases and geochemistry of ultramafic xenoliths. *Lithos* 132–133, 70–81.
990 <https://doi.org/10.1016/j.lithos.2011.11.007>

991 Correale, A., Paonita, A., Rizzo, A., Grassa, F., Martelli, M., 2015. The carbon isotope signature of
992 ultramafic xenoliths from the Hyblean Plateau (southeast Sicily, Italy): Evidence of mantle
993 heterogeneity. *Geochem. Geophys. Geosyst.* 16, 600–611.
994 <https://doi.org/10.1002/2014GC005656>

995 Correale, A., Pelorosso, B., Rizzo, A.L., Coltorti, M., Italiano, F., Bonadiman, C., Giacomoni, P.P.,
996 2019. The nature of the West Antarctic Rift System as revealed by noble gases in mantle
997 minerals. *Chemical Geology* 524, 104–118.
998 <https://doi.org/10.1016/j.chemgeo.2019.06.020>

999 Correale, A., Rizzo, A.L., Barry, P.H., Lu, J., Zheng, J., 2016. Refertilization of lithospheric mantle
1000 beneath the Yangtze craton in south-east China: Evidence from noble gases geochemistry.
1001 *Gondwana Research* 38, 289–303. <https://doi.org/10.1016/j.jgr.2016.01.003>

1002 Craig, H., Clarke, W.B., Beg, M.A., 1975. Excess ^3He in deep water on the East Pacific Rise. *Earth and*
1003 *Planetary Science Letters* 26, 125–132. [https://doi.org/10.1016/0012-821X\(75\)90079-5](https://doi.org/10.1016/0012-821X(75)90079-5)

1004 Cserna, Z. de, 1989. An outline of the geology of Mexico, in: Bally, A.W., Palmer, A.R. (Eds.), *The*
1005 *Geology of North America—An Overview*. Geological Society of America, pp. 233–264.
1006 <https://doi.org/10.1130/DNAG-GNA-A.233>

1007 Dávalos-Elizondo, M.G., Aranda-Gómez, J.J., Levresse, G., Cervantes de la Cruz, K.E., 2016. Química
1008 mineral y geoquímica de xenolitos del manto del campo volcánico Santo Domingo, San Luis
1009 Potosí: evidencias de procesos metasomáticos del manto bajo porciones de la Mesa
1010 Central, México. *Revista Mexicana de Ciencias Geológicas* 33, 81–104.

1011 Deines, P., 2002. The carbon isotope geochemistry of mantle xenoliths. *Earth Science Reviews* 58,
1012 247–278. [https://doi.org/10.1016/S0012-8252\(02\)00064-8](https://doi.org/10.1016/S0012-8252(02)00064-8)

1013 Dunai, T.J., 2010. *Cosmogenic Nuclides: Principles, Concepts and Applications in the Earth Surface*
1014 *Sciences*. Cambridge University Press, Cambridge.
1015 <https://doi.org/10.1017/CBO9780511804519>

1016 Dunai, T.J., Baur, H., 1995. Helium, neon, and argon systematics of the European subcontinental
1017 mantle: Implications for its geochemical evolution. *Geochimica et Cosmochimica Acta* 59,
1018 2767–2783. [https://doi.org/10.1016/0016-7037\(95\)00172-V](https://doi.org/10.1016/0016-7037(95)00172-V)

1019 Eguiluz de Antuñano, S., Aranda García, M., Marrett, R., 2000. Tectónica de la Sierra Madre Oriental,
1020 México. *BSGM* 53, 1–26. <https://doi.org/10.18268/BSGM2000v53n1a1>

1021 Faccini, B., Rizzo, A.L., Bonadiman, C., Ntaflou, T., Seghedi, I., Grégoire, M., Ferretti, G., Coltorti, M.,
1022 2020. Subduction-related melt refertilisation and alkaline metasomatism in the Eastern
1023 Transylvanian Basin lithospheric mantle: Evidence from mineral chemistry and noble gases
1024 in fluid inclusions. *Lithos* 364–365, 105516. <https://doi.org/10.1016/j.lithos.2020.105516>

1025 Ferrari, L., Orozco-Esquivel, T., Manea, V., Manea, M., 2012. The dynamic history of the Trans-
1026 Mexican Volcanic Belt and the Mexico subduction zone. *Tectonophysics* 522–523, 122–149.
1027 <https://doi.org/10.1016/j.tecto.2011.09.018>

1028 Fix, J.E., 1975. The Crust and Upper Mantle of Central Mexico. *Geophysical Journal International* 43,
1029 453–499. <https://doi.org/10.1111/j.1365-246X.1975.tb00643.x>
1030 Foley, S.F., Fischer, T.P., 2017. An essential role for continental rifts and lithosphere in the deep
1031 carbon cycle. *Nature Geosci* 10, 897–902. <https://doi.org/10.1038/s41561-017-0002-7>
1032 Frezzotti, M.L., Ferrando, S., Tecce, F., Castelli, D., 2012b. Water content and nature of solutes in
1033 shallow mantle fluids from fluid inclusions. *Earth and Planetary Science Letters* 351–352,
1034 70–83. <https://doi.org/10.1016/j.epsl.2012.07.023>
1035 Frezzotti, M.L., Tecce, F., Casagli, A., 2012a. Raman spectroscopy for fluid inclusion analysis. *Journal*
1036 *of Geochemical Exploration* 112, 1–20. <https://doi.org/10.1016/j.gexplo.2011.09.009>
1037 Frezzotti, M. L., Touret, J.L.R., 2014. CO₂, carbonate rich melts, and brines in the mantle.
1038 *Geoscience Frontiers* 5, 697–710. <https://doi.org/10.1016/j.gsf.2014.03.014>
1039 Gautheron, C., Cartigny, P., Moreira, M., Harris, J., Allegre, C., 2005. Evidence for a mantle
1040 component shown by rare gases, C and N isotopes in polycrystalline diamonds from Orapa
1041 (Botswana). *Earth and Planetary Science Letters* 240, 559–572.
1042 <https://doi.org/10.1016/j.epsl.2005.09.060>
1043 Gautheron, C., Moreira, M., 2002. Helium signature of the subcontinental lithospheric mantle. *Earth*
1044 *and Planetary Science Letters* 199, 39–47. [https://doi.org/10.1016/S0012-821X\(02\)00563-](https://doi.org/10.1016/S0012-821X(02)00563-0)
1045 [0](https://doi.org/10.1016/S0012-821X(02)00563-0)
1046 Gautheron, Cecile, Moreira, M., Allègre, C., 2005. He, Ne and Ar composition of the European
1047 lithospheric mantle. *Chemical Geology* 217, 97–112.
1048 <https://doi.org/10.1016/j.chemgeo.2004.12.009>
1049 Gennaro, M.E., Grassa, F., Martelli, M., Renzulli, A., Rizzo, A.L., 2017. Carbon isotope composition
1050 of CO₂ rich inclusions in cumulate forming mantle minerals from Stromboli volcano (Italy).
1051 *Journal of Volcanology and Geothermal Research* 346, 95–103.
1052 <https://doi.org/10.1016/j.jvolgeores.2017.04.001>
1053 Goff, F., Janik, C.J., Werner, C., Counce, D., Stimac, J.A., Siebe, C., Love, S.P., Williams, S.N., Fischer,
1054 T., Johnson, L., 1998. Geochemical surveillance of magmatic volatiles at Popocatepetl
1055 volcano, Mexico. *GSA Bulletin* 110, 695–710. [https://doi.org/10.1130/0016-](https://doi.org/10.1130/0016-7606(1998)110<0695:GSOMVA>2.3.CO;2)
1056 [7606\(1998\)110<0695:GSOMVA>2.3.CO;2](https://doi.org/10.1130/0016-7606(1998)110<0695:GSOMVA>2.3.CO;2)
1057 Goff, F., Love, S.P., Warren, R.G., Counce, D., Obenholzner, J., Siebe, C., Schmidt, S.C., 2001. Passive
1058 infrared remote sensing evidence for large, intermittent CO₂ emissions at Popocatepetl
1059 volcano, Mexico. *Chemical Geology* 177, 133–156. [https://doi.org/10.1016/S0009-](https://doi.org/10.1016/S0009-2541(00)00387-9)
1060 [2541\(00\)00387-9](https://doi.org/10.1016/S0009-2541(00)00387-9)
1061 Gómez Tuena, A., Orozco-Esquivel, M.A., Ferrari, L., 2007. Igneous petrogenesis of the Trans-
1062 Mexican Volcanic Belt, in: *Geology of Mexico: Celebrating the Centenary of the Geological*
1063 *Society of Mexico*. Geological Society of America. [https://doi.org/10.1130/2007.2422\(05\)](https://doi.org/10.1130/2007.2422(05))
1064 Graham, D.W., 2002. Noble Gas Isotope Geochemistry of Mid-Ocean Ridge and Ocean Island
1065 Basalts: Characterization of Mantle Source Reservoirs. *Reviews in Mineralogy and*
1066 *Geochemistry* 47, 247–317. <https://doi.org/10.2138/rmg.2002.47.8>
1067 Gurenko, A.A., Hoernle, K.A., Hauff, F., Schmincke, H. U., Han, D., Miura, Y.N., Kaneoka, I., 2006.
1068 Major, trace element and Nd–Sr–Pb–O–He–Ar isotope signatures of shield stage lavas from
1069 the central and western Canary Islands: Insights into mantle and crustal processes.
1070 *Chemical Geology* 233, 75–112. <https://doi.org/10.1016/j.chemgeo.2006.02.016>
1071 Gutmann, James.T., 1986. Origin of four and five phase ultramafic xenoliths from Sonora, Mexico.
1072 *American Mineralogist* 71, 1076–1084.
1073 Halldórsson, S.A., Hilton, D.R., Scarsi, P., Abebe, T., Hopp, J., 2014. A common mantle plume source
1074 beneath the entire East African Rift System revealed by coupled helium–neon systematics:

Formatted: Italian (Italy)

Formatted: Italian (Italy)

Formatted: Italian (Italy)

Formatted: Italian (Italy)

1075 HELIUM-NEON ISOTOPES IN THE EARS. *Geophys. Res. Lett.* 41, 2304–2311.
1076 <https://doi.org/10.1002/2014GL059424>

1077 Hauri, E.H., Cottrell, E., Kelley, K.A., Tucker, J.M., Shimizu, K., Voyer, M.L., Marske, J., Saal, A.E.,
1078 2019. Carbon in the Convecting Mantle, in: Orcutt, B.N., Daniel, I., Dasgupta, R. (Eds.), *Deep*
1079 *Carbon*. Cambridge University Press, pp. 237–275.
1080 <https://doi.org/10.1017/9781108677950.009>

1081 Heber, V.S., Brooker, R.A., Kelley, S.P., Wood, B.J., 2007. Crystal-melt partitioning of noble gases
1082 (helium, neon, argon, krypton, and xenon) for olivine and clinopyroxene. *Geochimica et*
1083 *Cosmochimica Acta* 71, 1041–1061. <https://doi.org/10.1016/j.gca.2006.11.010>

1084 Heber, V.S., Wieler, R., Baur, H., Olinger, C., Friedmann, T.A., Burnett, D.S., 2009. Noble gas
1085 composition of the solar wind as collected by the Genesis mission. *Geochimica et*
1086 *Cosmochimica Acta* 73, 7414–7432. <https://doi.org/10.1016/j.gca.2009.09.013>

1087 Henry, C.D., Aranda-Gomez, J.J., 1992. The real southern Basin and Range: Mid- to late Cenozoic
1088 extension in Mexico. *Geology* 20, 701–704. [https://doi.org/10.1130/0091-7613\(1992\)020<0701:TRSBAR>2.3.CO;2](https://doi.org/10.1130/0091-7613(1992)020<0701:TRSBAR>2.3.CO;2)

1089 Housh, T.B., Aranda-Gómez, J.J., Luhr, J.F., 2010. Isla Isabel (Nayarit, México): Quaternary alkalic
1090 basalts with mantle xenoliths erupted in the mouth of the Gulf of California. *Journal of*
1091 *Volcanology and Geothermal Research* 197, 85–107.
1092 <https://doi.org/10.1016/j.jvolgeores.2009.06.011>

1094 Javoy, M., Pineau, F., Agrinier, P., 1989. Volatiles and Stable Isotopes in Recycling, in: Hart, S.R.,
1095 Gülen, L. (Eds.), *Crust/Mantle Recycling at Convergence Zones*. Springer Netherlands,
1096 Dordrecht, pp. 121–138. https://doi.org/10.1007/978-94-009-0895-6_13

1097 Kennedy, B.M., Hiyagon, H., Reynolds, J.H., 1990. Crustal neon: a striking uniformity. *Earth and*
1098 *Planetary Science Letters* 98, 277–286. [https://doi.org/10.1016/0012-821X\(90\)90030-2](https://doi.org/10.1016/0012-821X(90)90030-2)

1099 Kurz, M.D., 1986. Cosmogenic helium in a terrestrial igneous rock. *Nature* 320, 435–439.
1100 <https://doi.org/10.1038/320435a0>

1101 Lal, D., 1987. Production of ³He in terrestrial rocks. *Chemical Geology: Isotope Geoscience section*
1102 66, 89–98. [https://doi.org/10.1016/0168-9622\(87\)90031-5](https://doi.org/10.1016/0168-9622(87)90031-5)

1103 Lee, C.A., 2005. Trace Element Evidence for Hydrous Metasomatism at the Base of the North
1104 American Lithosphere and Possible Association with Laramide Low Angle Subduction. *The*
1105 *Journal of Geology* 113, 673–685. <https://doi.org/10.1086/449327>

1106 Lee, H., Muirhead, J.D., Fischer, T.P., Ebinger, C.J., Kattenhorn, S.A., Sharp, Z.D., Kianji, G., 2016.
1107 Massive and prolonged deep carbon emissions associated with continental rifting. *Nature*
1108 *Geosci* 9, 145–149. <https://doi.org/10.1038/ngeo2622>

1109 Leeman, W.P., Harry, D.L., 1993. A Binary Source Model for Extension-Related Magmatism in the
1110 Great Basin, Western North America. *Science* 262, 1550–1554.
1111 <https://doi.org/10.1126/science.262.5139.1550>

1112 Levresse, G., Cervantes-de la Cruz, K.E., Aranda-Gómez, J.J., Dávalos-Elizondo, M.G., Jiménez-
1113 Sandoval, S., Rodríguez-Melgarejo, F., Alba Aldave, L.A., 2016. CO₂ fluid inclusion
1114 barometry in mantle xenoliths from central Mexico: A detailed record of magma ascent.
1115 *Journal of Volcanology and Geothermal Research* 310, 72–88.
1116 <https://doi.org/10.1016/j.jvolgeores.2015.11.012>

1117 Li, Z.-X.A., Lee, C. T.A., Peslier, A.H., Lenardic, A., Mackwell, S.J., 2008. Water contents in mantle
1118 xenoliths from the Colorado Plateau and vicinity: Implications for the mantle rheology and
1119 hydration-induced thinning of continental lithosphere. *J. Geophys. Res.* 113, B09210.
1120 <https://doi.org/10.1029/2007JB005540>

Formatted: Italian (Italy)

Formatted: Italian (Italy)

Formatted: Italian (Italy)

Formatted: Italian (Italy)

Formatted: Italian (Italy)

Formatted: Italian (Italy)

Formatted: Italian (Italy)

Formatted: Italian (Italy)

Formatted: Italian (Italy)

Formatted: Italian (Italy)

Formatted: Italian (Italy)

Formatted: Italian (Italy)

Formatted: Italian (Italy)

Formatted: Italian (Italy)

Formatted: Italian (Italy)

Formatted: Italian (Italy)

Formatted: Italian (Italy)

Formatted: Italian (Italy)

Formatted: Italian (Italy)

Formatted: Italian (Italy)

Formatted: Italian (Italy)

Formatted: Italian (Italy)

Formatted: Italian (Italy)

Formatted: Italian (Italy)

Formatted: Italian (Italy)

Formatted: Italian (Italy)

Formatted: Italian (Italy)

Formatted: Italian (Italy)

Formatted: Italian (Italy)

1121 Liang, Y., Elthon, D., 1990. Geochemistry and petrology of spinel lherzolite xenoliths from Xalapasco
1122 de La Joya, San Luis Potosi, Mexico: Partial melting and mantle metasomatism. *J. Geophys.*
1123 *Res.* 95, 15859. <https://doi.org/10.1029/JB095iB10p15859>

1124 López-Doncel, R., 2003. La Formación Tamabra del Cretácico medio en la porción central del margen
1125 occidental de la Plataforma Valles. *Revista Mexicana de Ciencias Geológicas* 20, 1–19.

1126 Luhr, J.F., Aranda-Gómez, J.J., 1997. Mexican Peridotite Xenoliths and Tectonic Terranes:
1127 Correlations among Vent Location, Texture, Temperature, Pressure, and Oxygen Fugacity.
1128 *Journal of Petrology* 38, 1075–1112. <https://doi.org/10.1093/ptro/38.8.1075>

1129 Luhr, J.F., Aranda-Gomez, J.J., Pier, J.G., 1989. Spinel lherzolite bearing quaternary volcanic centers
1130 in San Luis Potosi, Mexico: 1. Geology, mineralogy, and petrology. *J. Geophys. Res.* 94,
1131 7916. <https://doi.org/10.1029/JB094iB06p07916>

1132 Martelli, M., Bianchini, G., Beccalua, L., Rizzo, A., 2011. Helium and argon isotopic compositions of
1133 mantle xenoliths from Tallante and Calatrava, Spain. *Journal of Volcanology and*
1134 *Geothermal Research* 200, 18–26. <https://doi.org/10.1016/j.jvolgeores.2010.11.015>

1135 Martelli, M., Rizzo, A.L., Renzulli, A., Ridolfi, F., Arienzo, I., Rosciglione, A., 2014. Noble gas signature
1136 of magmas from a heterogeneous mantle wedge: The case of Stromboli volcano (Aeolian
1137 Islands, Italy). *Chemical Geology* 368, 39–53.
1138 <https://doi.org/10.1016/j.chemgeo.2014.01.003>

1139 Marty, B., 2012. The origins and concentrations of water, carbon, nitrogen and noble gases on
1140 Earth. *Earth and Planetary Science Letters* 313–314, 56–66.
1141 <https://doi.org/10.1016/j.epsl.2011.10.040>

1142 Marty, B., Jambon, A., 1987. C3He in volatile fluxes from the solid Earth: implications for carbon
1143 geodynamics. *Earth and Planetary Science Letters* 83, 16–26.
1144 [https://doi.org/10.1016/0012-821X\(87\)90047-1](https://doi.org/10.1016/0012-821X(87)90047-1)

1145 Marty, B., Tolstikhin, I.N., 1998. CO2 fluxes from mid-ocean ridges, arcs and plumes. *Chemical*
1146 *Geology* 145, 233–248. [https://doi.org/10.1016/S0009-2541\(97\)00145-9](https://doi.org/10.1016/S0009-2541(97)00145-9)

1147 Mercier, J.-C.C., Nicolas, A., 1975. Textures and Fabrics of Upper Mantle Peridotites as Illustrated
1148 by Xenoliths from Basalts. *Journal of Petrology* 16, 454–487.
1149 <https://doi.org/10.1093/petrology/16.1.454>

1150 Michael, P.J., Graham, D.W., 2015. The behavior and concentration of CO2 in the suboceanic
1151 mantle: Inferences from undegassed ocean ridge and ocean island basalts. *Lithos* 236–237,
1152 338–351. <https://doi.org/10.1016/j.lithos.2015.08.020>

1153 Morán-Zenteno, D.J., Cerca, M., Keppie, J.D., 2005. La evolución tectónica y magmática cenozoica
1154 del suroeste de México: avances y problemas de interpretación. *BSGM* 57, 319–341.
1155 <https://doi.org/10.18268/BSGM2005v57n3a4>

1156 Moreira, M., Kunz, J., Allègre, C., 1998. Rare Gas Systematics in Popping Rock: Isotopic and
1157 Elemental Compositions in the Upper Mantle. *Science* 279, 1178–1181.
1158 <https://doi.org/10.1126/science.279.5354.1178>

1159 Nesterenok, A.V., Yakubovich, O.V., 2016. Production of 3He in rocks by reactions induced by
1160 particles of the nuclear active and muon components of cosmic rays: Geological and
1161 petrological implications. *Petrology* 24, 21–34.
1162 <https://doi.org/10.1134/S0869591116010057>

1163 Nieto-Samaniego, Á.F., Alaniz-Álvarez, S.A., Camprubí Cano, A., 2005. La Mesa Central de México:
1164 estratigrafía, estructura y evolución tectónica cenozoica. *BSGM* 57, 285–318.
1165 <https://doi.org/10.18268/BSGM2005v57n3a3>

1166 Nieto-Samaniego, Á.F., Ferrari, L., Alaniz-Álvarez, S.A., Labarthe-Hernández, G., Rosas-Elguera, J.,
1167 1999. Variation of Cenozoic extension and volcanism across the southern Sierra Madre

Formatted: Italian (Italy)

Formatted: Italian (Italy)

Formatted: Italian (Italy)

Formatted: Italian (Italy)

Formatted: Italian (Italy)

Formatted: Italian (Italy)

Formatted: Italian (Italy)

Formatted: Italian (Italy)

Formatted: Italian (Italy)

Formatted: Italian (Italy)

Formatted: Italian (Italy)

Formatted: Italian (Italy)

Formatted: Italian (Italy)

Formatted: Italian (Italy)

Formatted: Italian (Italy)

Formatted: Italian (Italy)

Formatted: Italian (Italy)

Formatted: Italian (Italy)

Formatted: Italian (Italy)

Formatted: Italian (Italy)

1168 Occidental volcanic province, Mexico. *GSA Bulletin* 111, 347–363.
 1169 [https://doi.org/10.1130/0016-7606\(1999\)111<0347:VOCEAV>2.3.CO;2](https://doi.org/10.1130/0016-7606(1999)111<0347:VOCEAV>2.3.CO;2)

1170 Nuccio, P.M., Paonita, A., Rizzo, A., Rosciglione, A., 2008. Elemental and isotope covariation of noble
 1171 gases in mineral phases from Etnean volcanics erupted during 2001–2005, and genetic
 1172 relation with peripheral gas discharges. *Earth and Planetary Science Letters* 272, 683–690.
 1173 <https://doi.org/10.1016/j.epsl.2008.06.007>

1174 Oppenheimer, C., Fischer, T.P., Scaillet, B., 2014. Volcanic Degassing: Process and Impact, in:
 1175 *Treatise on Geochemistry*. Elsevier, pp. 111–179. <https://doi.org/10.1016/B978-0-08-095975-7.00304-1>

1176 Ozima, M., Podosek, F.A., 2002. Noble Gas Geochemistry. Cambridge University Press.

1177 Pardo, M., Suárez, G., 1995. Shape of the subducted Rivera and Cocos plates in southern Mexico:
 1178 Seismic and tectonic implications. *J. Geophys. Res.* 100, 12357–12373.
 1179 <https://doi.org/10.1029/95JB00919>

1180 Pier, J.G., Luhr, J.F., Podosek, F.A., Aranda-Gómez, J.J., 1992. The La Breña–El Jagüey Maar
 1181 Complex, Durango, Mexico: II. Petrology and geochemistry. *Bull. Volcanol.* 54, 405–428.
 1182 <https://doi.org/10.1007/BF00312322>

1183 Pier, J.G., Podosek, F.A., Luhr, J.F., Brannon, J.C., Aranda-Gomez, J.J., 1989. Spinel lherzolite-bearing
 1184 quaternary volcanic centers in San Luis Potosí, Mexico: 2. SR and ND Isotopic Systematics.
 1185 *J. Geophys. Res.* 94, 7941. <https://doi.org/10.1029/JB094iB06p07941>

1186 Plank, T., Manning, C.E., 2019. Subducting carbon. *Nature* 574, 343–352.
 1187 <https://doi.org/10.1038/s41586-019-1643-z>

1188 Raisz, E., 1959. Landforms of Mexico.

1189 Rizzo, A.L., Barberi, F., Carapezza, M.L., Di Piazza, A., Francalanci, L., Sortino, F., D’Alessandro, W.,
 1190 2015. New mafic magma refilling a quiescent volcano: Evidence from He–Ne–Ar isotopes
 1191 during the 2011–2012 unrest at Santorini, Greece: RESEARCH ARTICLE. *Geochem. Geophys.*
 1192 *Geosyst.* 16, 798–814. <https://doi.org/10.1002/2014GC005653>

1193 Rizzo, A.L., Pelorosso, B., Coltorti, M., Ntaflos, T., Bonadiman, C., Matusiak-Matek, M., Italiano, F.,
 1194 Bergonzoni, G., 2018a. Geochemistry of Noble Gases and CO₂ in Fluid Inclusions From
 1195 Lithospheric Mantle Beneath Wilcza Góra (Lower Silesia, Southwest Poland). *Front. Earth*
 1196 *Sci.* 6, 215. <https://doi.org/10.3389/feart.2018.00215>

1197 Rizzo, A.L., Pelorosso, B., Coltorti, M., Ntaflos, T., Bonadiman, C., Matusiak-Matek, M., Italiano, F.,
 1198 Bergonzoni, G., 2018b. Geochemistry of Noble Gases and CO₂ in Fluid Inclusions From
 1199 Lithospheric Mantle Beneath Wilcza Góra (Lower Silesia, Southwest Poland). *Front. Earth*
 1200 *Sci.* 6, 215. <https://doi.org/10.3389/feart.2018.00215>

1201 Sano, Y., Marty, B., 1995. Origin of carbon in fumarolic gas from island arcs. *Chemical Geology* 119,
 1202 265–274. [https://doi.org/10.1016/0009-2541\(94\)00097-R](https://doi.org/10.1016/0009-2541(94)00097-R)

1203 Sarda, P., Staudacher, T., Allegre, C., 1988. Neon isotopes in submarine basalts. *Earth and Planetary*
 1204 *Science Letters* 91, 73–88. [https://doi.org/10.1016/0012-821X\(88\)90152-5](https://doi.org/10.1016/0012-821X(88)90152-5)

1205 Saucedo, R., Macías, J.L., Ocampo-Díaz, Y.Z.E., Gómez-Villa, W., Rivera-Olguín, E., Castro-Govea, R.,
 1206 Sánchez-Núñez, J.M., Leyer, P.W., Torres-Hernández, J.R., Carrasco-Núñez, G., 2017. Mixed
 1207 magmatic–phreatomagmatic explosions during the formation of the Joya Honda maar, San
 1208 Luis Potosí, Mexico. *Geological Society, London, Special Publications* 446, 255–279.
 1209 <https://doi.org/10.1144/SP446.11>

1210 Sedlock, R.L., 2003. Geology and tectonics of the Baja California Peninsula and adjacent areas, in:
 1211 *Tectonic Evolution of Northwestern Mexico and the Southwestern USA*. Geological Society
 1212 of America. <https://doi.org/10.1130/0-8137-2374-4.1>

Formatted: Italian (Italy)

Formatted: Italian (Italy)

Formatted: Italian (Italy)

Formatted: Italian (Italy)

Formatted: Italian (Italy)

Formatted: Italian (Italy)

Formatted: Italian (Italy)

Formatted: Italian (Italy)

Formatted: Italian (Italy)

Formatted: Italian (Italy)

Formatted: Italian (Italy)

Formatted: Italian (Italy)

Formatted: Italian (Italy)

Formatted: Italian (Italy)

Formatted: Italian (Italy)

Formatted: Italian (Italy)

Formatted: Italian (Italy)

Formatted: Italian (Italy)

Formatted: Italian (Italy)

Formatted: Italian (Italy)

Formatted: Italian (Italy)

Formatted: Italian (Italy)

Formatted: Italian (Italy)

Formatted: Italian (Italy)

Formatted: Italian (Italy)

Formatted: Italian (Italy)

1214 [Severinghaus, J., Atwater, T., 1990. Chapter 1: Cenozoic geometry and thermal state of the](#)
1215 [subducting slabs beneath western North America, in: Geological Society of America](#)
1216 [Memoirs. Geological Society of America, pp. 1–22. <https://doi.org/10.1130/MEM176-p1>](#)
1217 [Smith, D., Alexis Riter, J.C., Mertzman, S.A., 1999. Water, rock interactions, orthopyroxene growth,](#)
1218 [and Si enrichment in the mantle: evidence in xenoliths from the Colorado Plateau,](#)
1219 [southwestern United States. Earth and Planetary Science Letters 165, 45–54.](#)
1220 [https://doi.org/10.1016/S0012-821X\(98\)00251-9](https://doi.org/10.1016/S0012-821X(98)00251-9)
1221 [Steiger, R.H., Jäger, E., 1977. Subcommittee on geochronology: Convention on the use of decay](#)
1222 [constants in geo- and cosmochemistry. Earth and Planetary Science Letters 36, 359–362.](#)
1223 [https://doi.org/10.1016/0012-821X\(77\)90060-7](https://doi.org/10.1016/0012-821X(77)90060-7)
1224 [Streckeisen, A., 1976. To each plutonic rock its proper name. Earth Science Reviews 12, 1–33.](#)
1225 [https://doi.org/10.1016/0012-8252\(76\)90052-0](https://doi.org/10.1016/0012-8252(76)90052-0)
1226 [Trull, T.W., Kurz, M.D., 1993. Experimental measurements of ³He and ⁴He mobility in olivine and](#)
1227 [clinopyroxene at magmatic temperatures. Geochimica et Cosmochimica Acta 57, 1313–](#)
1228 [1324. \[https://doi.org/10.1016/0016-7037\\(93\\)90068-8\]\(https://doi.org/10.1016/0016-7037\(93\)90068-8\)](#)
1229 [Tucker, J.M., Mukhopadhyay, S., Gonnermann, H.M., 2018. Reconstructing mantle carbon and](#)
1230 [noble gas contents from degassed mid-ocean ridge basalts. Earth and Planetary Science](#)
1231 [Letters 496, 108–119. <https://doi.org/10.1016/j.epsl.2018.05.024>](#)
1232 [Verma, S.P., 2000. Geochemistry of the subducting Cocos plate and the origin of subduction-](#)
1233 [unrelated mafic volcanism at the volcanic front of the central Mexican Volcanic Belt, in:](#)
1234 [Cenozoic Tectonics and Volcanism of Mexico. Geological Society of America.](#)
1235 <https://doi.org/10.1130/0-8137-2334-5.195>
1236 [Verma, S.P., Hasenaka, T., 2004. Sr, Nd, and Pb isotopic and trace element geochemical constraints](#)
1237 [for a veined mantle source of magmas in the Michoacan Guanajuato Volcanic Field, west-](#)
1238 [central Mexican Volcanic Belt. Geochem. J. 38, 43–65.](#)
1239 <https://doi.org/10.2343/geochemj.38.43>
1240 [Wojdyr, M., 2010. Fityk: a general purpose peak fitting program. J Appl Crystallogr 43, 1126–1128.](#)
1241 <https://doi.org/10.1107/S0021889810030499>
1242 [Yamamoto, J., Nishimura, K., Sugimoto, T., Takemura, K., Takahata, N., Sano, Y., 2009. Diffusive](#)
1243 [fractionation of noble gases in mantle with magma channels: Origin of low He/Ar in mantle-](#)
1244 [derived rocks. Earth and Planetary Science Letters 280, 167–174.](#)
1245 <https://doi.org/10.1016/j.epsl.2009.01.029>

1247 **TABLES**

1248 *Table 1. Modal composition of JH mantle xenoliths.*

1249

Sample	Rock type	OI (%)	Opx (%)	Cpx (%)	Sp (%)
VE	Lherzolite	54.47	28.96	14.37	2.2
VJ	Lherzolite	52.01	32.31	13.39	2.29
IVA	Lherzolite	72.48	15.86	10.45	1.21
VF	Lherzolite	52.08	33.97	11.93	2.02

Formatted: Italian (Italy)

Formatted: Italian (Italy)

Formatted: Italian (Italy)

Formatted: Italian (Italy)

Formatted: Italian (Italy)

Formatted: Italian (Italy)

Formatted: Italian (Italy)

Formatted: Italian (Italy)

Formatted: Italian (Italy)

Formatted: Italian (Italy)

Formatted: Italian (Italy)

Formatted: Italian (Italy)

Formatted: Italian (Italy)

Formatted: Italian (Italy)

Formatted: Italian (Italy)

Formatted: Italian (Italy)

Formatted: Italian (Italy)

Formatted: Italian (Italy)

Formatted: Italian (Italy)

Formatted: Italian (Italy)

Formatted: Italian (Italy)

Formatted: Italian (Italy)

Formatted: Italian (Italy)

Formatted: Italian (Italy)

Formatted: Italian (Italy)

Formatted: Italian (Italy)

Formatted: Italian (Italy)

Formatted: Italian (Italy)

Formatted Table

VI	Lherzolite	53.41	23.48	19.79	3.32
VG	Harzburgite	68.14	30.04	1.26	0.56
VK	Lherzolite	61.27	24.59	13.69	0.44
VH	Harzburgite	62.08	31.26	4.47	2.18

Table 2. Fluid inclusions compositions from JH mantle xenoliths. Concentrations of noble gases isotopes and CO₂ are reported in mol/g; r² = replica.

Sample (nodule)	Phase	Weight (g)	³ He	⁴ He	²⁰ Ne	²¹ Ne	²² Ne	CO ₂	⁴⁰ Ar	³⁶ Ar	⁴⁰ Ar	⁴ He/ ²⁰ Ne	⁴ He/ ⁴ He _{atm}
V-A	Ol	0.95855	1.67E-17	1.65E-12	9.11E-16	2.72E-18	9.26E-17	2.80E-11	Formatted Table				
V-A	Opk	0.26388	4.74E-18	4.91E-13	8.90E-15	2.59E-17	9.00E-16	3.91E-10	3.61E-12	5.45E-15	2.00E-12	55.2	0.25
V-A	Crk	0.21991	6.45E-18	6.57E-13	5.81E-16	2.62E-18	5.41E-17	6.23E-09	5.16E-12	1.55E-15	4.70E-12	1131.4	0.14
V-B	Ol	0.99706	2.53E-17	2.48E-12	1.84E-15	5.52E-18	1.88E-16	2.26E-10	3.70E-12	6.01E-15	1.92E-12	1349.7	1.29
V-B	Opk	0.47776	3.43E-17	3.36E-12	6.75E-15	1.97E-17	6.61E-16	4.88E-08	7.67E-12	7.95E-15	5.32E-12	497.5	0.63
V-B	Crk	0.48584	4.67E-17	4.62E-12	4.41E-16	2.00E-18	3.61E-17	9.70E-08	1.12E-11	1.36E-15	1.08E-11	10483.3	0.43
V-C	Ol	0.59294	3.71E-18	3.74E-13	2.35E-16	n.a	2.61E-17	2.30E-10	Formatted Table				
V-C	Crk	0.5587	8.55E-18	8.40E-13	5.73E-16	1.82E-18	5.87E-17	7.61E-10	2.57E-12	1.02E-15	2.27E-12	1466.6	0.37
V-D	Ol	1.02241	2.08E-17	2.08E-12	3.76E-16	1.25E-18	3.67E-17	9.18E-10	2.76E-12	1.27E-15	2.38E-12	5534.0	0.87
V-D	Opk	0.49922	9.46E-18	9.43E-13	2.33E-15	7.04E-18	2.39E-16	4.39E-09	2.07E-12	3.30E-15	1.09E-12	404.4	0.86
V-D	Crk	0.47389	2.66E-17	2.59E-12	3.02E-16	1.23E-18	2.73E-17	3.25E-08	6.01E-12	7.58E-16	5.78E-12	8576.0	0.45
V-E	Ol	1.02916	2.51E-17	2.42E-12	1.22E-15	3.90E-18	1.19E-16	4.14E-09	Formatted Table				
V-E	Opk	0.51352	1.98E-17	1.90E-12	5.12E-15	1.56E-17	5.16E-16	2.74E-08	3.03E-12	2.11E-15	2.41E-12	371.6	0.79
V-E	Crk	0.32954	3.96E-17	3.81E-12	3.93E-15	1.27E-17	3.81E-16	1.25E-07	7.06E-12	1.50E-15	6.62E-12	970.0	0.58
V-F	Ol	1.01203	2.57E-17	2.44E-12	3.49E-15	1.05E-17	3.55E-16	2.81E-09	2.50E-12	2.81E-15	1.67E-12	700.6	1.46
V-F	Opk	0.52681	1.66E-17	1.61E-12	4.91E-15	1.51E-17	4.98E-16	1.85E-08	2.37E-12	2.11E-15	1.75E-12	328.5	0.92
V-F	Crk	0.31734	5.58E-17	5.29E-12	2.01E-14	6.07E-17	1.99E-15	1.78E-07	1.06E-11	1.24E-14	6.98E-12	262.9	0.76
V-G	Ol	1.00336	1.94E-17	1.81E-12	7.91E-16	2.44E-18	7.78E-17	3.91E-11	Formatted Table				
V-G	Opk	0.50526	1.29E-17	1.23E-12	3.20E-15	9.62E-18	3.26E-16	4.54E-09	1.47E-12	1.69E-15	9.68E-13	384.5	1.27
V-G	Crk	0.32136	3.21E-17	3.15E-12	1.57E-15	5.55E-18	1.52E-16	2.24E-08	3.17E-12	9.41E-16	2.89E-12	2003.4	1.09
V-H	Ol	1.0181	4.21E-17	4.03E-12	4.72E-15	1.47E-17	4.66E-16	4.73E-09	6.44E-12	6.29E-15	4.58E-12	853.7	0.88
V-H	Opk	0.53853	1.95E-17	1.86E-12	4.01E-14	1.16E-16	3.94E-15	1.23E-08	1.52E-11	4.14E-14	2.93E-12	46.5	0.64
V-H	Crk	0.30754	3.92E-17	3.73E-12	3.52E-15	1.13E-17	3.46E-16	5.09E-08	4.74E-12	1.93E-15	4.17E-12	1062.1	0.90
V-I	Ol	1.0437	8.62E-19	8.56E-14	1.42E-16	5.22E-19	1.39E-17	4.74E-11	2.25E-13	5.78E-16	5.37E-14	604.6	1.59
V-I	Opk	0.5057	5.02E-17	9.93E-14	1.55E-16	6.59E-19	1.34E-17	2.26E-10	3.77E-13	8.58E-16	1.23E-13	639.0	0.8
V-I	Crk	0.49525	9.34E-19	1.23E-13	5.08E-14	1.46E-16	4.90E-15	n.a	3.72E-14	2.97E-13	n.a	2.4	0.41
V-I+r*	Ol	1.01139	9.47E-19	9.25E-14	4.09E-16	1.32E-18	4.07E-17	7.54E-10	1.75E-13	4.48E-16	4.32E-14	226.0	2.14
V-I+r*	Opk	0.50086	9.81E-19	1.15E-13	1.13E-14	3.37E-17	1.14E-15	1.31E-09	2.02E-12	5.94E-15	2.63E-13	10.1	0.44
V-I+r*	Crk	0.57112	7.37E-19	9.81E-14	9.68E-15	2.89E-17	9.72E-16	4.07E-10	5.64E-13	1.62E-15	8.59E-14	10.1	1.14
V-J	Ol	1.0333	3.63E-17	3.53E-12	3.77E-15	1.15E-17	3.76E-16	4.55E-09	5.30E-12	6.20E-15	3.47E-12	937.0	1.02
V-J	Opk	0.5061	5.02E-17	4.93E-12	7.60E-15	2.36E-17	7.58E-16	1.08E-07	1.02E-11	7.88E-15	7.87E-12	649.1	0.63
V-J	Crk	0.30875	1.11E-16	1.07E-11	6.19E-15	2.02E-17	6.07E-16	3.23E-07	8.59E-12	2.87E-15	7.75E-12	1726.7	1.38
V-K	Ol	1.0225	5.42E-17	5.24E-12	4.99E-15	1.58E-17	4.99E-16	2.46E-08	7.72E-12	6.93E-15	5.67E-12	1049.9	0.92
V-K	Opk	0.52687	5.37E-17	5.13E-12	2.48E-14	7.37E-17	2.38E-15	1.05E-07	1.54E-11	2.07E-14	9.25E-12	206.6	0.55
V-K	Crk	0.30567	7.40E-17	7.07E-12	4.08E-14	1.21E-16	4.11E-15	1.16E-07	1.06E-11	1.40E-14	6.47E-12	173.4	1.09
IV-A	Ol	1.03046	2.52E-17	2.43E-12	4.47E-15	1.29E-17	4.34E-16	1.47E-09	2.09E-12	3.40E-15	1.08E-12	543.9	2.24
IV-A	Opk	0.49715	3.04E-17	3.02E-12	1.05E-14	3.07E-17	1.03E-15	4.49E-08	5.48E-12	6.38E-15	3.59E-12	286.9	0.84
IV-A	Crk	0.47966	1.29E-16	1.29E-11	1.25E-14	3.82E-17	1.22E-15	2.73E-07	1.20E-11	9.65E-15	9.11E-12	1033.2	1.42

Table 2. Continued.

1252 [Aiuppa, A., Fischer, T.P., Plank, T., Robidoux, P., Di Napoli, R., 2017. Along-arc, inter-arc and arc-](#)
1253 [to-arc variations in volcanic gas CO₂/ST ratios reveal dual source of carbon in arc volcanism.](#)
1254 [Earth-Science Reviews 168, 24–47. https://doi.org/10.1016/j.earscirev.2017.03.005](#)
1255 [Andersen, T., Neumann, E.-R., 2001. Fluid inclusions in mantle xenoliths. *Lithos* 55, 301–320.](#)
1256 [https://doi.org/10.1016/S0024-4937\(00\)00049-9](#)
1257 [Aranda-Gómez, J., Luhr, J.F., 1996. Origin of the Joya Honda maar, San Luis Potosí, México. *Journal*
1258 \[of Volcanology and Geothermal Research\]\(#\) 74, 1–18. \[https://doi.org/10.1016/S0377-\]\(#\)
1259 \[0273\\(96\\)00044-3\]\(#\)
1260 \[Aranda-Gómez, J.J., Henry, C.D., F. Luhr, J., 2000. Evolución tectonomagmática post-paleocénica\]\(#\)
1261 \[de la Sierra Madre Occidental y de la porción meridional de la provincia tectónica de\]\(#\)
1262 \[Cuencas y Sierras, México. *BSGM* 53, 59–71. https://doi.org/10.18268/BSGM2000v53n1a3\]\(#\)
1263 \[Aranda-Gómez, J.J., Luhr, J.F., Housh, T.B., Valdez-Moreno, G., Chávez-Cabello, G., 2007. Late\]\(#\)
1264 \[Cenozoic intraplate-type volcanism in central and northern México: A review, in: *Geology*\]\(#\)
1265 \[of México: Celebrating the Centenary of the Geological Society of México. Geological\]\(#\)
1266 \[Society of America. https://doi.org/10.1130/2007.2422\\(04\\)\]\(#\)
1267 \[Aranda-Gómez, J.J., Ortega-Gutiérrez, F., 1987. Mantle xenoliths in México, in: *Mantle Xenoliths*.\]\(#\)
1268 \[John Wiley, New York, pp. 75–84.\]\(#\)
1269 \[Atwater, T., 1989. Plate tectonic history of the northeast Pacific and western North America, in:\]\(#\)
1270 \[Winterer, E.L., Husson, D.M., Decker, R.W. \\(Eds.\\), *The Eastern Pacific Ocean and Hawaii*.\]\(#\)
1271 \[Geological Society of America, North America, pp. 21–72. https://doi.org/10.1130/DNAG-\]\(#\)
1272 \[GNA-N.21\]\(#\)
1273 \[Barboza-Gudino, J.R., Tristán-González, M., Torres-Hernández, J.R., 1999. Tectonic setting of pre-\]\(#\)
1274 \[Oxfordian units from central and northeastern Mexico: A review, in: *Special Paper 340:*\]\(#\)
1275 \[Mesozoic Sedimentary and Tectonic History of North-Central Mexico. Geological Society\]\(#\)
1276 \[of America, pp. 197–210. https://doi.org/10.1130/0-8137-2340-X.197\]\(#\)
1277 \[Basu, A.R., 1977. Textures, microstructures and deformation of ultramafic xenoliths from San\]\(#\)
1278 \[Quintín, Baja California. *Tectonophysics* 43, 213–246. https://doi.org/10.1016/0040-\]\(#\)
1279 \[1951\\(77\\)90118-4\]\(#\)
1280 \[Boudoire, G., Rizzo, A.L., Arienzo, I., Di Muro, A., 2020. Paroxysmal eruptions tracked by\]\(#\)
1281 \[variations of helium isotopes: inferences from Piton de la Fournaise \\(La Réunion island\\). *Sci*\]\(#\)
1282 \[Rep\]\(#\) 10, 9809. \[https://doi.org/10.1038/s41598-020-66260-x\]\(#\)
1283 \[Boudoire, G., Rizzo, A.L., Di Muro, A., Grassa, F., Liuzzo, M., 2018. Extensive CO₂ degassing in\]\(#\)
1284 \[the upper mantle beneath oceanic basaltic volcanoes: First insights from Piton de la\]\(#\)
1285 \[Fournaise volcano \\(La Réunion Island\\). *Geochimica et Cosmochimica Acta* 235, 376–401.\]\(#\)
1286 \[https://doi.org/10.1016/j.gca.2018.06.004\]\(#\)
1287 \[Broadley, M.W., Ballentine, C.J., Chavrit, D., Dallai, L., Burgess, R., 2016. Sedimentary halogens\]\(#\)
1288 \[and noble gases within Western Antarctic xenoliths: Implications of extensive volatile\]\(#\)
1289 \[recycling to the sub continental lithospheric mantle. *Geochimica et Cosmochimica Acta* 176,\]\(#\)
1290 \[139–156. https://doi.org/10.1016/j.gca.2015.12.013\]\(#\)
1291 \[Buikin, A., Trieloff, M., Hopp, J., Althaus, T., Korochantseva, E., Schwarz, W.H., Altherr, R., 2005.\]\(#\)
1292 \[Noble gas isotopes suggest deep mantle plume source of late Cenozoic mafic alkaline\]\(#\)
1293 \[volcanism in Europe. *Earth and Planetary Science Letters* 230, 143–162.\]\(#\)
1294 \[https://doi.org/10.1016/j.epsl.2004.11.001\]\(#\)
1295 \[Bunge, H.-P., Grand, S.P., 2000. Mesozoic plate-motion history below the northeast Pacific Ocean\]\(#\)
1296 \[from seismic images of the subducted Farallon slab. *Nature* 405, 337–340.\]\(#\)
1297 \[https://doi.org/10.1038/35012586\]\(#\)
1298 \[Burnard, P., 2004. Diffusive fractionation of noble gases and helium isotopes during mantle melting.\]\(#\)
1299 \[Earth and Planetary Science Letters\]\(#\) 220, 287–295. \[https://doi.org/10.1016/S0012-\]\(#\)
1300 \[821X\\(04\\)00060-3\]\(#\)](#)

1301 [Burnard, P., 1997. Vesicle-Specific Noble Gas Analyses of “Popping Rock”: Implications for](#)
1302 [Primordial Noble Gases in Earth. Science 276, 568–571.](#)
1303 <https://doi.org/10.1126/science.276.5312.568>

1304 [Carrillo-Bravo, J., 1971. La plataforma de Valles-San Luis Potosí. Boletín de la Asociación](#)
1305 [Mexicana de Geólogos Petroleros. Boletín de la Asociación Mexicana de Geólogos](#)
1306 [Petroleros 23, 100.](#)

1307 [Carteret, C., Dandeu, A., Moussaoui, S., Muhr, H., Humbert, B., Plasari, E., 2009. Polymorphism](#)
1308 [Studied by Lattice Phonon Raman Spectroscopy and Statistical Mixture Analysis Method.](#)
1309 [Application to Calcium Carbonate Polymorphs during Batch Crystallization. Crystal Growth](#)
1310 [& Design 9, 807–812. https://doi.org/10.1021/cg800368u](#)

1311 [Correale, A., Martelli, M., Paonita, A., Rizzo, A., Brusca, L., Scribano, V., 2012. New evidence of](#)
1312 [mantle heterogeneity beneath the Hyblean Plateau \(southeast Sicily, Italy\) as inferred from](#)
1313 [noble gases and geochemistry of ultramafic xenoliths. Lithos 132–133, 70–81.](#)
1314 <https://doi.org/10.1016/j.lithos.2011.11.007>

1315 [Correale, A., Paonita, A., Rizzo, A., Grassa, F., Martelli, M., 2015. The carbon-isotope signature of](#)
1316 [ultramafic xenoliths from the Hyblean Plateau \(southeast Sicily, Italy\): Evidence of mantle](#)
1317 [heterogeneity. Geochem. Geophys. Geosyst. 16, 600–611.](#)
1318 <https://doi.org/10.1002/2014GC005656>

1319 [Correale, A., Pelorosso, B., Rizzo, A.L., Coltorti, M., Italiano, F., Bonadiman, C., Giacomoni, P.P.,](#)
1320 [2019. The nature of the West Antarctic Rift System as revealed by noble gases in mantle](#)
1321 [minerals. Chemical Geology 524, 104–118. https://doi.org/10.1016/j.chemgeo.2019.06.020](#)

1322 [Correale, A., Rizzo, A.L., Barry, P.H., Lu, J., Zheng, J., 2016. Refertilization of lithospheric mantle](#)
1323 [beneath the Yangtze craton in south-east China: Evidence from noble gases geochemistry.](#)
1324 [Gondwana Research 38, 289–303. https://doi.org/10.1016/j.gr.2016.01.003](#)

1325 [Craig, H., Clarke, W.B., Beg, M.A., 1975. Excess ³He in deep water on the East Pacific Rise. Earth](#)
1326 [and Planetary Science Letters 26, 125–132. https://doi.org/10.1016/0012-821X\(75\)90079-5](#)

1327 [Cserna, Z. de, 1989. An outline of the geology of Mexico, in: Bally, A.W., Palmer, A.R. \(Eds.\), The](#)
1328 [Geology of North America—An Overview. Geological Society of America, pp. 233–264.](#)
1329 <https://doi.org/10.1130/DNAG-GNA-A.233>

1330 [Czuppon, G., Matsumoto, T., Handler, M.R., Matsuda, J., 2009. Noble gases in spinel peridotite](#)
1331 [xenoliths from Mt Quincan, North Queensland, Australia: Undisturbed MORB-type noble](#)
1332 [gases in the subcontinental lithospheric mantle. Chemical Geology 266, 19–28.](#)
1333 <https://doi.org/10.1016/j.chemgeo.2009.03.029>

1334 [Dávalos-Elizondo, M.G., Aranda Gómez, J.J., Levresse, G., Cervantes-de la Cruz, K.E., 2016.](#)
1335 [Química mineral y geoquímica de xenolitos del manto del campo volcánico Santo Domingo,](#)
1336 [San Luis Potosí: evidencias de procesos metasomáticos del manto bajo porciones de la Mesa](#)
1337 [Central. México. Revista Mexicana de Ciencias Geológicas 33, 81–104.](#)

1338 [Day, J.M.D., Barry, P.H., Hilton, D.R., Burgess, R., Pearson, D.G., Taylor, L.A., 2015. The helium](#)
1339 [flux from the continents and ubiquity of low-³He/⁴He recycled crust and lithosphere.](#)
1340 [Geochimica et Cosmochimica Acta 153, 116–133. https://doi.org/10.1016/j.gca.2015.01.008](#)

1341 [Deines, P., 2002. The carbon isotope geochemistry of mantle xenoliths. Earth-Science Reviews 58,](#)
1342 [247–278. https://doi.org/10.1016/S0012-8252\(02\)00064-8](#)

1343 [Eguiluz de Antuñano, S., Aranda García, M., Marrett, R., 2000. Tectónica de la Sierra Madre](#)
1344 [Oriental, México. BSGM 53, 1–26. https://doi.org/10.18268/BSGM2000v53n1a1](#)

1345 [Faccini, B., Rizzo, A.L., Bonadiman, C., Ntaflou, T., Seghedi, I., Grégoire, M., Ferretti, G., Coltorti,](#)
1346 [M., 2020. Subduction-related melt refertilisation and alkaline metasomatism in the Eastern](#)
1347 [Transylvanian Basin lithospheric mantle: Evidence from mineral chemistry and noble gases](#)
1348 [in fluid inclusions. Lithos 364–365, 105516. https://doi.org/10.1016/j.lithos.2020.105516](#)

1349 [Ferrari, L., Orozco-Esquivel, T., Manea, V., Manea, M., 2012. The dynamic history of the Trans-](#)
1350 [Mexican Volcanic Belt and the Mexico subduction zone. Tectonophysics 522–523, 122–](#)
1351 [149. https://doi.org/10.1016/j.tecto.2011.09.018](#)

1352 [Fix, J.E., 1975. The Crust and Upper Mantle of Central Mexico. *Geophysical Journal International*](#)
1353 [43, 453–499. <https://doi.org/10.1111/j.1365-246X.1975.tb00643.x>](#)

1354 [Foley, S.F., Fischer, T.P., 2017. An essential role for continental rifts and lithosphere in the deep](#)
1355 [carbon cycle. *Nature Geosci* 10, 897–902. <https://doi.org/10.1038/s41561-017-0002-7>](#)

1356 [Frezzotti, M., Peccerillo, A., 2007. Diamond-bearing COHS fluids in the mantle beneath Hawaii.](#)
1357 [Earth and Planetary Science Letters 262, 273–283.](#)
1358 [https://doi.org/10.1016/j.epsl.2007.08.001](#)

1359 [Frezzotti, M.L., Andersen, T., Neumann, E.-R., Simonsen, S.L., 2002a. Carbonatite melt–CO₂ fluid](#)
1360 [inclusions in mantle xenoliths from Tenerife, Canary Islands: a story of trapping,](#)
1361 [immiscibility and fluid–rock interaction in the upper mantle. *Lithos* 64, 77–96.](#)
1362 [https://doi.org/10.1016/S0024-4937\(02\)00178-0](#)

1363 [Frezzotti, M.L., Ferrando, S., Tecce, F., Castelli, D., 2012b. Water content and nature of solutes in](#)
1364 [shallow-mantle fluids from fluid inclusions. *Earth and Planetary Science Letters* 351–352,](#)
1365 [70–83. <https://doi.org/10.1016/j.epsl.2012.07.023>](#)

1366 [Frezzotti, M.L., Tecce, F., Casagli, A., 2012a. Raman spectroscopy for fluid inclusion analysis.](#)
1367 [Journal of Geochemical Exploration 112, 1–20.](#)
1368 [https://doi.org/10.1016/j.gexplo.2011.09.009](#)

1369 [Frezzotti, M.-L., Touret, J.L.R., 2014. CO₂, carbonate-rich melts, and brines in the mantle.](#)
1370 [Geoscience Frontiers 5, 697–710. <https://doi.org/10.1016/j.gsf.2014.03.014>](#)

1371 [Gautheron, C., Moreira, M., 2002. Helium signature of the subcontinental lithospheric mantle. *Earth*
1372 \[and Planetary Science Letters 199, 39–47. \\[https://doi.org/10.1016/S0012-821X\\\(02\\\)00563-0\\]\\(https://doi.org/10.1016/S0012-821X\\(02\\)00563-0\\)\]\(#\)](#)

1373 [Gautheron, C., Moreira, M., Allègre, C., 2005a. He, Ne and Ar composition of the European](#)
1374 [lithospheric mantle. *Chemical Geology* 217, 97–112.](#)
1375 [https://doi.org/10.1016/j.chemgeo.2004.12.009](#)

1376 [Gennaro, M.E., Grassa, F., Martelli, M., Renzulli, A., Rizzo, A.L., 2017. Carbon isotope composition](#)
1377 [of CO₂-rich inclusions in cumulate-forming mantle minerals from Stromboli volcano](#)
1378 [\(Italy\). *Journal of Volcanology and Geothermal Research* 346, 95–103.](#)
1379 [https://doi.org/10.1016/j.jvolgeores.2017.04.001](#)

1380 [Goff, F., Janik, C.J., Werner, C., Counce, D., Stimac, J.A., Siebe, C., Love, S.P., Williams, S.N.,](#)
1381 [Fischer, T.P., Johnson, L., 1998. Geochemical surveillance of magmatic volatiles at](#)
1382 [Popocatepetl volcano, Mexico. *GSA Bulletin* 110, 695–710. \[https://doi.org/10.1130/0016-\]\(https://doi.org/10.1130/0016-7606\(1998\)110<0695:GSOMVA>2.3.CO;2\)](#)
1383 [7606\(1998\)110<0695:GSOMVA>2.3.CO;2](#)

1384 [Goff, F., Love, S.P., Warren, R.G., Counce, D., Obenholzner, J., Siebe, C., Schmidt, S.C., 2001.](#)
1385 [Passive infrared remote sensing evidence for large, intermittent CO₂ emissions at](#)
1386 [Popocatepetl volcano, Mexico. *Chemical Geology* 177, 133–156.](#)
1387 [https://doi.org/10.1016/S0009-2541\(00\)00387-9](#)

1388 [Gómez-Tuena, A., Orozco-Esquivel, M.A.T., Ferrari, L., 2007. Igneous petrogenesis of the Trans-](#)
1389 [Mexican Volcanic Belt, in: *Geology of México: Celebrating the Centenary of the*](#)
1390 [Geological Society of México. Geological Society of America.](#)
1391 [https://doi.org/10.1130/2007.2422\(05\)](#)

1392 [Graham, D.W., 2002. Noble Gas Isotope Geochemistry of Mid-Ocean Ridge and Ocean Island](#)
1393 [Basalts: Characterization of Mantle Source Reservoirs. *Reviews in Mineralogy and*](#)
1394 [Geochemistry 47, 247–317. <https://doi.org/10.2138/rmg.2002.47.8>](#)

1395 [Griffin, W.L., O'Reilly, S., Ryan, C.G., 1999. The composition and origin of sub-continental](#)
1396 [lithospheric mantle, in: *Mantle Petrology: Field Observations and High Pressure*](#)
1397 [Experimentation: A Tribute to Francis F. \(Joe\) Boyd. The Geochemical Society, pp. 13–45.](#)

1398 [Griffin, W.L., O'Reilly, S.Y., Afonso, J.C., Begg, G.C., 2009. The Composition and Evolution of](#)
1399 [Lithospheric Mantle: a Re-evaluation and its Tectonic Implications. *Journal of Petrology* 50,](#)
1400 [1185–1204. <https://doi.org/10.1093/petrology/egn033>](#)

1401 [Gurenko, A.A., Hoernle, K.A., Hauff, F., Schmincke, H.-U., Han, D., Miura, Y.N., Kaneoka, I.,](#)
1402 [2006. Major, trace element and Nd–Sr–Pb–O–He–Ar isotope signatures of shield stage lavas](#)

1403 from the central and western Canary Islands: Insights into mantle and crustal processes.
1404 *Chemical Geology* 233, 75–112. <https://doi.org/10.1016/j.chemgeo.2006.02.016>

1405 Gutmann, J.T., 1986. Origin of four and five-phase ultramafic xenoliths from Sonora, Mexico.
1406 *American Mineralogist* 71, 1079–1084.

1407 Halldórsson, S.A., Hilton, D.R., Scarsi, P., Abebe, T., Hopp, J., 2014. A common mantle plume
1408 source beneath the entire East African Rift System revealed by coupled helium-neon
1409 systematics: HELIUM-NEON ISOTOPES IN THE EARS. *Geophys. Res. Lett.* 41, 2304–
1410 2311. <https://doi.org/10.1002/2014GL059424>

1411 Hauri, E.H., Cottrell, E., Kelley, K.A., Tucker, J.M., Shimizu, K., Voyer, M.L., Marske, J., Saal,
1412 A.E., 2019. Carbon in the Convecting Mantle, in: Orcutt, B.N., Daniel, I., Dasgupta, R.
1413 (Eds.), Deep Carbon. Cambridge University Press, pp. 237–275.
1414 <https://doi.org/10.1017/9781108677950.009>

1415 Heber, V.S., Wieler, R., Baur, H., Olinger, C., Friedmann, T.A., Burnett, D.S., 2009. Noble gas
1416 composition of the solar wind as collected by the Genesis mission. *Geochimica et*
1417 *Cosmochimica Acta* 73, 7414–7432. <https://doi.org/10.1016/j.gca.2009.09.013>

1418 Henry, C.D., Aranda-Gómez, J.J., 1992. The real southern Basin and Range: Mid- to late Cenozoic
1419 extension in Mexico. *Geology* 20, 701–704. [https://doi.org/10.1130/0091-
1420 7613\(1992\)020<0701:TRSBAR>2.3.CO;2](https://doi.org/10.1130/0091-7613(1992)020<0701:TRSBAR>2.3.CO;2)

1421 Hopp, J., Ionov, D.A., 2011. Tracing partial melting and subduction-related metasomatism in the
1422 Kamchatkan mantle wedge using noble gas compositions. *Earth and Planetary Science*
1423 *Letters* 302, 121–131. <https://doi.org/10.1016/j.epsl.2010.12.001>

1424 Hopp, J., Trierloff, M., Altherr, R., 2004. Neon isotopes in mantle rocks from the Red Sea region
1425 reveal large-scale plume–lithosphere interaction. *Earth and Planetary Science Letters* 219,
1426 61–76. [https://doi.org/10.1016/S0012-821X\(03\)00691-5](https://doi.org/10.1016/S0012-821X(03)00691-5)

1427 Hopp, J., Trierloff, M., Altherr, R., 2007b. Noble gas compositions of the lithospheric mantle below
1428 the Chyulu Hills volcanic field, Kenya. *Earth and Planetary Science Letters* 261, 635–648.
1429 <https://doi.org/10.1016/j.epsl.2007.07.027>

1430 Hopp, J., Trierloff, M., Buikin, A., Korochantseva, E., Schwarz, W., Althaus, T., Altherr, R., 2007a.
1431 Heterogeneous mantle argon isotope composition in the subcontinental lithospheric mantle
1432 beneath the Red Sea region. *Chemical Geology* 240, 36–53.
1433 <https://doi.org/10.1016/j.chemgeo.2007.01.004>

1434 Housh, T.B., Aranda-Gómez, J.J., Luhr, J.F., 2010. Isla Isabel (Nayarit, México): Quaternary alkallic
1435 basalts with mantle xenoliths erupted in the mouth of the Gulf of California. *Journal of*
1436 *Volcanology and Geothermal Research* 197, 85–107.
1437 <https://doi.org/10.1016/j.jvolgeores.2009.06.011>

1438 Javoy, M., Pineau, F., Agrinier, P., 1989. Volatiles and Stable Isotopes in Recycling, in: Hart, S.R.,
1439 Gülen, L. (Eds.), Crust/Mantle Recycling at Convergence Zones. Springer Netherlands,
1440 Dordrecht, pp. 121–138. https://doi.org/10.1007/978-94-009-0895-6_13

1441 Kennedy, B.M., Hiyagon, H., Reynolds, J.H., 1990. Crustal neon: a striking uniformity. *Earth and*
1442 *Planetary Science Letters* 98, 277–286. [https://doi.org/10.1016/0012-821X\(90\)90030-2](https://doi.org/10.1016/0012-821X(90)90030-2)

1443 Kurz, M.D., 1986. Cosmogenic helium in a terrestrial igneous rock. *Nature* 320, 435–439.
1444 <https://doi.org/10.1038/320435a0>

1445 Langmuir, C.H., Vocke, R.D., Hanson, G.N., Hart, S.R., 1978. A general mixing equation with
1446 applications to Icelandic basalts. *Earth and Planetary Science Letters* 37, 380–392.
1447 [https://doi.org/10.1016/0012-821X\(78\)90053-5](https://doi.org/10.1016/0012-821X(78)90053-5)

1448 Lee, C.A., 2005. Trace Element Evidence for Hydrous Metasomatism at the Base of the North
1449 American Lithosphere and Possible Association with Laramide Low- Angle Subduction.
1450 *The Journal of Geology* 113, 673–685. <https://doi.org/10.1086/449327>

1451 Lee, H., Muirhead, J.D., Fischer, T.P., Ebinger, C.J., Kattenhorn, S.A., Sharp, Z.D., Kianji, G., 2016.
1452 Massive and prolonged deep carbon emissions associated with continental rifting. *Nature*
1453 *Geosci* 9, 145–149. <https://doi.org/10.1038/ngeo2622>

1454 [Leeman, W.P., Harry, D.L., 1993. A Binary Source Model for Extension-Related Magmatism in the](#)
1455 [Great Basin, Western North America. *Science* 262, 1550–1554.](#)
1456 <https://doi.org/10.1126/science.262.5139.1550>

1457 [Levesse, G., Cervantes-de la Cruz, K.E., Aranda-Gómez, J.J., Dávalos-Elizondo, M.G., Jiménez-](#)
1458 [Sandoval, S., Rodríguez-Melgarejo, F., Alba-Aldave, L.A., 2016. CO₂ fluid inclusion](#)
1459 [barometry in mantle xenoliths from central Mexico: A detailed record of magma ascent.](#)
1460 [Journal of Volcanology and Geothermal Research 310, 72–88.](#)
1461 <https://doi.org/10.1016/j.jvolgeores.2015.11.012>

1462 [Li, Z.-X.A., Lee, C.-T.A., Peslier, A.H., Lenardic, A., Mackwell, S.J., 2008. Water contents in mantle](#)
1463 [xenoliths from the Colorado Plateau and vicinity: Implications for the mantle rheology and](#)
1464 [hydration-induced thinning of continental lithosphere. *J. Geophys. Res.* 113, B09210.](#)
1465 <https://doi.org/10.1029/2007JB005540>

1466 [Liang, Y., Elthon, D., 1990. Geochemistry and petrology of spinel lherzolite xenoliths from](#)
1467 [Xalapasco de La Joya, San Luis Potosi, Mexico: Partial melting and mantle metasomatism.](#)
1468 [J. Geophys. Res. 95, 15859. https://doi.org/10.1029/JB095iB10p15859](#)

1469 [López-Doncel, R., 2003. La Formación Tamabra del Cretácico medio en la porción central del](#)
1470 [margen occidental de la Plataforma Valles. *Revista Mexicana de Ciencias Geológicas* 20, 1–](#)
1471 [19.](#)

1472 [Luhr, J.F., Aranda-Gomez, J.J., 1997. Mexican Peridotite Xenoliths and Tectonic Terranes:](#)
1473 [Correlations among Vent Location, Texture, Temperature, Pressure, and Oxygen Fugacity.](#)
1474 [Journal of Petrology 38, 1075–1112. https://doi.org/10.1093/etroj/38.8.1075](#)

1475 [Luhr, J.F., Aranda-Gomez, J.J., Pier, J.G., 1989. Spinel-lherzolite-bearing quaternary volcanic](#)
1476 [centers in San Luis Potosí, Mexico: 1. Geology, mineralogy, and petrology. *J. Geophys.*](#)
1477 [Res. 94, 7916. https://doi.org/10.1029/JB094iB06p07916](#)

1478 [Martelli, M., Bianchini, G., Beccaluva, L., Rizzo, A., 2011. Helium and argon isotopic compositions](#)
1479 [of mantle xenoliths from Tallante and Calatrava, Spain. *Journal of Volcanology and*](#)
1480 [Geothermal Research 200, 18–26. https://doi.org/10.1016/j.jvolgeores.2010.11.015](#)

1481 [Martelli, M., Rizzo, A.L., Renzulli, A., Ridolfi, F., Arienzo, I., Rosciglione, A., 2014. Noble-gas](#)
1482 [signature of magmas from a heterogeneous mantle wedge: The case of Stromboli volcano](#)
1483 [\(Aeolian Islands, Italy\). *Chemical Geology* 368, 39–53.](#)
1484 <https://doi.org/10.1016/j.chemgeo.2014.01.003>

1485 [Marty, B., 2012. The origins and concentrations of water, carbon, nitrogen and noble gases on Earth.](#)
1486 [Earth and Planetary Science Letters 313–314, 56–66.](#)
1487 <https://doi.org/10.1016/j.epsl.2011.10.040>

1488 [Marty, B., Jambon, A., 1987. C³He in volatile fluxes from the solid Earth: implications for carbon](#)
1489 [geodynamics. *Earth and Planetary Science Letters* 83, 16–26. https://doi.org/10.1016/0012-](#)
1490 [821X\(87\)90047-1](#)

1491 [Marty, B., Tolstikhin, I.N., 1998. CO₂ fluxes from mid-ocean ridges, arcs and plumes. *Chemical*](#)
1492 [Geology 145, 233–248. https://doi.org/10.1016/S0009-2541\(97\)00145-9](#)

1493 [Matsumoto, T., Chen, Y., Matsuda, J.-I., 2001. Concomitant occurrence of primordial and recycled](#)
1494 [noble gases in the Earth's mantle. *Earth and Planetary Science Letters* 185, 35–47.](#)
1495 [https://doi.org/10.1016/S0012-821X\(00\)00375-7](https://doi.org/10.1016/S0012-821X(00)00375-7)

1496 [Matsumoto, T., Honda, M., McDougall, I., O'Reilly, S.Y., 1998. Noble gases in anhydrous lherzolites](#)
1497 [from the newer volcanics, southeastern Australia: a MORB-like reservoir in the](#)
1498 [subcontinental mantle. *Geochimica et Cosmochimica Acta* 62, 2521–2533.](#)
1499 [https://doi.org/10.1016/S0016-7037\(98\)00173-2](https://doi.org/10.1016/S0016-7037(98)00173-2)

1500 [Matsumoto, T., Honda, M., McDougall, I., O'Reilly, S.Y., Norman, M., Yaxley, G., 2000. Noble](#)
1501 [gases in pyroxenites and metasomatised peridotites from the Newer Volcanics, southeastern](#)
1502 [Australia: Implications for mantle metasomatism. *Chemical Geology* 168, 49–73.](#)
1503 [https://doi.org/10.1016/S0009-2541\(00\)00181-9](https://doi.org/10.1016/S0009-2541(00)00181-9)

1504 [Mercier, J.-C.C., Nicolas, A., 1975. Textures and Fabrics of Upper-Mantle Peridotites as Illustrated](#)
1505 [by Xenoliths from Basalts. Journal of Petrology 16, 454–487.](#)
1506 <https://doi.org/10.1093/petrology/16.1.454>

1507 [Michael, P.J., Graham, D.W., 2015. The behavior and concentration of CO₂ in the suboceanic](#)
1508 [mantle: Inferences from undegassed ocean ridge and ocean island basalts. Lithos 236–237,](#)
1509 [338–351. https://doi.org/10.1016/j.lithos.2015.08.020](#)

1510 [Morán-Zenteno, D.J., Cerca, M., Keppie, J.D., 2005. La evolución tectónica y magmática cenozoica](#)
1511 [del suroeste de México: avances y problemas de interpretación. BSGM 57, 319–341.](#)
1512 <https://doi.org/10.18268/BSGM2005v57n3a4>

1513 [Moreira, M., 1998. Rare Gas Systematics in Popping Rock: Isotopic and Elemental Compositions in](#)
1514 [the Upper Mantle. Science 279, 1178–1181. https://doi.org/10.1126/science.279.5354.1178](#)

1515 [Nieto-Samaniego, Á.F., Alaniz-Álvarez, S.A., Camprubí i Cano, A., 2005. La Mesa Central de](#)
1516 [México: estratigrafía, estructura y evolución tectónica cenozoica. BSGM 57, 285–318.](#)
1517 <https://doi.org/10.18268/BSGM2005v57n3a3>

1518 [Nieto-Samaniego, Á.F., Ferrari, L., Alaniz-Álvarez, S.A., Labarthe-Hernández, G., Rosas-Elguera,](#)
1519 [J., 1999. Variation of Cenozoic extension and volcanism across the southern Sierra Madre](#)
1520 [Occidental volcanic province, Mexico. GSA Bulletin 111, 347–363.](#)
1521 [https://doi.org/10.1130/0016-7606\(1999\)111<0347:VOCEAV>2.3.CO;2](https://doi.org/10.1130/0016-7606(1999)111<0347:VOCEAV>2.3.CO;2)

1522 [Nuccio, P.M., Paonita, A., Rizzo, A., Rosciglione, A., 2008. Elemental and isotope covariation of](#)
1523 [noble gases in mineral phases from Etnean volcanics erupted during 2001–2005, and genetic](#)
1524 [relation with peripheral gas discharges. Earth and Planetary Science Letters 272, 683–690.](#)
1525 <https://doi.org/10.1016/j.epsl.2008.06.007>

1526 [Oppenheimer, C., Fischer, T.P., Scaillet, B., 2014. Volcanic Degassing: Process and Impact, in:](#)
1527 [Treatise on Geochemistry. Elsevier, pp. 111–179. https://doi.org/10.1016/B978-0-08-](#)
1528 [095975-7.00304-1](#)

1529 [Ozima, M., Podosek, F.A., 2002. Noble Gas Geochemistry. Cambridge University Press.](#)

1530 [Pardo, M., Suárez, G., 1995. Shape of the subducted Rivera and Cocos plates in southern Mexico:](#)
1531 [Seismic and tectonic implications. J. Geophys. Res. 100, 12357–12373.](#)
1532 <https://doi.org/10.1029/95JB00919>

1533 [Pier, J.G., Luhr, J.F., Podosek, F.A., Aranda-Gómez, J.J., 1992. The La Breña-El Jagüey Maar](#)
1534 [Complex, Durango, Mexico: II. Petrology and geochemistry. Bull Volcanol 54, 405–428.](#)
1535 <https://doi.org/10.1007/BF00312322>

1536 [Pier, J.G., Podosek, F.A., Luhr, J.F., Brannon, J.C., Aranda-Gómez, J.J., 1989. Spinel-lherzolite-](#)
1537 [bearing quaternary volcanic centers in San Luis Potosí, Mexico: 2. SR and ND Isotopic](#)
1538 [Systematics. J. Geophys. Res. 94, 7941. https://doi.org/10.1029/JB094iB06p07941](#)

1539 [Plank, T., Manning, C.E., 2019. Subducting carbon. Nature 574, 343–352.](#)
1540 <https://doi.org/10.1038/s41586-019-1643-z>

1541 [Raisz, E., 1959. Landforms of Mexico.](#)

1542 [Rizzo, A.L., Pelorosso, B., Coltorti, M., Ntaflos, T., Bonadiman, C., Matusiak-Mańek, M., Italiano,](#)
1543 [F., Bergonzoni, G., 2018. Geochemistry of Noble Gases and CO₂ in Fluid Inclusions From](#)
1544 [Lithospheric Mantle Beneath Wilcza Góra \(Lower Silesia, Southwest Poland\). Front. Earth](#)
1545 [Sci. 6, 215. https://doi.org/10.3389/feart.2018.00215](#)

1546 [Roedder, E., 1984. Fluid Inclusions: An Introduction to Studies of All Types of Fluid Inclusions,](#)
1547 [Gas, Liquid, Or Melt, Trapped in Materials from Earth and Space, and Their Application to](#)
1548 [the Understanding of Geologic Processes. Mineralogical Society of America.](#)

1549 [Sano, Y., Marty, B., 1995. Origin of carbon in Fumarolic gas from island arcs. Chemical Geology](#)
1550 [119, 265–274. https://doi.org/10.1016/0009-2541\(94\)00097-R](#)

1551 [Sarda, P., 2004. Surface noble gas recycling to the terrestrial mantle. Earth and Planetary Science](#)
1552 [Letters 228, 49–63. https://doi.org/10.1016/j.epsl.2004.09.026](#)

1553 [Sarda, P., Staudacher, T., Allegre, C., 1988. Neon isotopes in submarine basalts. Earth and Planetary](#)
1554 [Science Letters 91, 73–88. https://doi.org/10.1016/0012-821X\(88\)90152-5](#)

1555 [Saucedo, R., Macías, J.L., Ocampo-Díaz, Y.Z.E., Gómez-Villa, W., Rivera-Olguín, E., Castro-](#)
1556 [Govea, R., Sánchez-Núñez, J.M., Layer, P.W., Torres Hernández, J.R., Carrasco-Núñez, G.,](#)
1557 [2017. Mixed magmatic–phreatomagmatic explosions during the formation of the Joya](#)
1558 [Honda maar, San Luis Potosí, Mexico. Geological Society, London, Special Publications](#)
1559 [446, 255–279. <https://doi.org/10.1144/SP446.11>](#)

1560 [Sedlock, R.L., 2003. Geology and tectonics of the Baja California Peninsula and adjacent areas, in:](#)
1561 [Tectonic Evolution of Northwestern Mexico and the Southwestern USA. Geological Society](#)
1562 [of America. <https://doi.org/10.1130/0-8137-2374-4.1>](#)

1563 [Severinghaus, J., Atwater, T., 1990. Chapter 1: Cenozoic geometry and thermal state of the](#)
1564 [subducting slabs beneath western North America, in: Geological Society of America](#)
1565 [Memoirs. Geological Society of America, pp. 1–22. <https://doi.org/10.1130/MEM176-p1>](#)

1566 [Smith, D., Alexis Riter, J.C., Mertzman, S.A., 1999. Water–rock interactions, orthopyroxene growth,](#)
1567 [and Si-enrichment in the mantle: evidence in xenoliths from the Colorado Plateau,](#)
1568 [southwestern United States. Earth and Planetary Science Letters 165, 45–54.](#)
1569 [\[https://doi.org/10.1016/S0012-821X\\(98\\)00251-9\]\(https://doi.org/10.1016/S0012-821X\(98\)00251-9\)](#)

1570 [Steiger, R.H., Jäger, E., 1977. Subcommission on geochronology: Convention on the use of decay](#)
1571 [constants in geo- and cosmochronology. Earth and Planetary Science Letters 36, 359–362.](#)
1572 [\[https://doi.org/10.1016/0012-821X\\(77\\)90060-7\]\(https://doi.org/10.1016/0012-821X\(77\)90060-7\)](#)

1573 [Streckeisen, A., 1976. To each plutonic rock its proper name. Earth-Science Reviews 12, 1–33.](#)
1574 [\[https://doi.org/10.1016/0012-8252\\(76\\)90052-0\]\(https://doi.org/10.1016/0012-8252\(76\)90052-0\)](#)

1575 [Tucker, J.M., Mukhopadhyay, S., Gonnermann, H.M., 2018. Reconstructing mantle carbon and](#)
1576 [noble gas contents from degassed mid-ocean ridge basalts. Earth and Planetary Science](#)
1577 [Letters 496, 108–119. <https://doi.org/10.1016/j.epsl.2018.05.024>](#)

1578 [Verma, S.P., 2000. Geochemistry of the subducting Cocos plate and the origin of subduction-](#)
1579 [unrelated mafic volcanism at the volcanic front of the central Mexican Volcanic Belt, in:](#)
1580 [Cenozoic Tectonics and Volcanism of Mexico. Geological Society of America.](#)
1581 [<https://doi.org/10.1130/0-8137-2334-5.195>](#)

1582 [Verma, S.P., Hasenaka, T., 2004. Sr, Nd, and Pb isotopic and trace element geochemical constraints](#)
1583 [for a veined-mantle source of magmas in the Michoacan-Guanajuato Volcanic Field, west-](#)
1584 [central Mexican Volcanic Belt. Geochem. J. 38, 43–65.](#)
1585 [<https://doi.org/10.2343/geochemj.38.43>](#)

1586 [Wojdyr, M., 2010. Fityk: a general-purpose peak fitting program. J Appl Cryst 43, 1126–1128.](#)
1587 [<https://doi.org/10.1107/S0021889810030499>](#)

1588 [Yamamoto, J., Nishimura, K., Sugimoto, T., Takemura, K., Takahata, N., Sano, Y., 2009. Diffusive](#)
1589 [fractionation of noble gases in mantle with magma channels: Origin of low He/Ar in mantle-](#)
1590 [derived rocks. Earth and Planetary Science Letters 280, 167–174.](#)
1591 [<https://doi.org/10.1016/j.epsl.2009.01.029>](#)

1593

1594

1595

1596

1597

1598

1599

Formatted: Justified

Sample	Phase	Re/Ra	Total Error +/-	⁴⁰ Ar/ ³⁶ Ar	Error (%)	³⁸ Ar/ ³⁶ Ar	Error (%)	²⁰ Ne/ ²² Ne	Error (%)	²¹ Ne/ ²² Ne	Error (%)	²¹ Ne/ ²² Ne
V.A	Ol	7.26	0.062	1391.46	0.09	0.19251	0.19	9.93	0.06	0.0297	0.00135	Formatted: English (United Kingdom)
V.A	Opx	6.94	0.130	662.11	0.14	0.18892	0.19	9.87	0.04	0.0288	0.00050	Formatted: Font: 10 pt, English (United Kingdom)
V.A	Cpx	7.06	0.126	3320.08	0.30	0.20543	0.21	n-a	n-a	n-a	n-a	Formatted: English (United Kingdom)
V.B	Ol	7.33	0.058	614.85	0.06	0.18772	0.19	9.87	0.04	0.0296	0.00082	Formatted: English (United Kingdom)
V.B	Opx	7.35	0.063	964.58	0.07	0.18291	0.18	9.97	0.03	0.0298	0.00045	Formatted: English (United Kingdom)
V.B	Cpx	7.27	0.058	8231.50	0.17	0.20717	0.21	12.18	0.26	0.0553	0.00431	Formatted: English (United Kingdom)
V.C	Ol	7.13	0.096	2518.41	0.52	0.22231	0.22	n-a	n-a	n-a	n-a	Formatted: English (United Kingdom)
V.C	Cpx	7.33	0.073	2511.64	0.23	0.19747	0.20	n-a	n-a	n-a	n-a	Formatted: English (United Kingdom)
V.D	Ol	7.19	0.058	2177.87	0.12	0.19317	0.19	10.57	0.16	0.0354	0.00222	Formatted: English (United Kingdom)
V.D	Opx	7.22	0.079	626.23	0.10	0.18834	0.19	n-a	n-a	n-a	n-a	Formatted: English (United Kingdom)
V.D	Cpx	7.37	0.066	7026.55	0.21	0.20644	0.21	11.03	0.29	0.0452	0.00659	Formatted: English (United Kingdom)
V.E	Ol	7.47	0.069	2598.15	0.43	0.19010	0.19	10.37	0.07	0.0332	0.00107	Formatted: English (United Kingdom)
V.E	Opx	7.50	0.072	1436.20	0.13	0.18305	0.18	10.00	0.04	0.0306	0.00046	Formatted: English (United Kingdom)
V.E	Cpx	7.48	0.071	4719.85	0.33	0.18136	0.18	10.25	0.05	0.0338	0.00145	Formatted: English (United Kingdom)
V.F	Ol	7.57	0.069	889.63	0.08	0.18730	0.19	9.87	0.04	0.0297	0.00064	Formatted: English (United Kingdom)
V.F	Opx	7.42	0.077	1123.07	0.14	0.19054	0.19	9.93	0.04	0.0307	0.00072	Formatted: English (United Kingdom)
V.F	Cpx	7.59	0.071	856.84	0.06	0.18382	0.18	10.12	0.03	0.0306	0.00045	Formatted: English (United Kingdom)
V.G	Ol	7.68	0.071	690.44	0.10	0.18565	0.18	10.23	0.06	0.0316	0.00117	Formatted: English (United Kingdom)
V.G	Opx	7.53	0.081	866.39	0.17	0.18036	0.18	9.85	0.04	0.0296	0.00067	Formatted: English (United Kingdom)
V.G	Cpx	7.32	0.073	3371.87	0.43	0.18281	0.18	11.06	0.11	0.0390	0.00222	Formatted: English (United Kingdom)
V.H	Ol	7.52	0.079	1023.71	0.06	0.18503	0.18	10.18	0.03	0.0317	0.00044	Formatted: English (United Kingdom)
V.H	Opx	7.52	0.085	366.42	0.00	0.18303	0.18	10.11	0.02	0.0301	0.00027	Formatted: English (United Kingdom)
V.H	Cpx	7.56	0.071	2457.00	0.27	0.19215	0.19	10.15	0.05	0.0326	0.00104	Formatted: English (United Kingdom)
V.I	Ol	7.25	0.127	388.43	0.22	0.19569	0.20	n-a	n-a	n-a	n-a	Formatted: English (United Kingdom)
V.I	Opx	7.19	0.154	439.10	0.34	0.19092	0.19	11.59	0.73	0.0492	0.01944	Formatted: English (United Kingdom)
V.I	Cpx	5.46	0.139	303.48	0.05	0.18009	0.18	10.24	0.01	0.0323	0.00035	Formatted: English (United Kingdom)
V.I*	Ol	7.37	0.172	391.97	0.30	0.19246	0.20	10.39	0.16	0.0336	0.00254	Formatted: English (United Kingdom)
V.I*	Opx	6.15	0.079	339.74	0.08	0.18402	0.19	9.91	0.03	0.0296	0.00024	Formatted: English (United Kingdom)
V.I*	Cpx	5.40	0.144	348.57	0.16	0.18113	0.19	9.98	0.03	0.0298	0.00034	Formatted: English (United Kingdom)
V.J	Ol	7.38	0.074	854.91	0.06	0.18694	0.19	10.05	0.03	0.0307	0.00054	Formatted: English (United Kingdom)
V.J	Opx	7.33	0.077	1294.25	0.07	0.18590	0.19	10.08	0.03	0.0313	0.00056	Formatted: English (United Kingdom)

V-J	C_{pk}	7.50	0.067	2993.26	0.19	0.19053	0.19	10.24	0.03	0.0335	0.00074	Formatted: English (United Kingdom)
V-K	Θ	7.45	0.076	1114.13	0.00	0.18660	0.19	10.07	0.03	0.0319	0.00045	Formatted: English (United Kingdom)
V-K	Θ_{pk}	7.54	0.078	741.96	0.00	0.18186	0.18	10.32	0.02	0.0316	0.00034	Formatted: English (United Kingdom)
V-K	C_{pk}	7.53	0.070	756.34	0.07	0.18796	0.19	9.92	0.02	0.0296	0.00025	Formatted: English (United Kingdom)
W-A	Θ	7.45	0.083	614.05	0.07	0.18144	0.19	10.14	0.04	0.0303	0.00056	Formatted: English (United Kingdom)
W-A	Θ_{pk}	7.23	0.096	858.77	0.06	0.18068	0.19	10.10	0.03	0.0298	0.00045	Formatted: English (United Kingdom)
W-A	C_{pk}	7.21	0.065	1238.93	1.99	0.18113	0.19	10.25	0.03	0.0314	0.00047	Formatted: English (United Kingdom)

1600
1601
1602

Table 3. ^4He production rates, ^3He fluxes, helium residence time and CO_2 fluxes calculated for the lithospheric mantle beneath central Mexico. P^* , F and R_t values were calculated based on mathematical formulations proposed by Gautheron and Moreira (2002).

U (ppm)	P^* (ccSTP/g)	P^* (mol/yr)	F (ccSTP/year)	F (mol/yr)	R_t (Ma)	CO_2	Formatted: English (United Kingdom)
0.01	7.69E+06	3.42E+02	5.99E+02	0.027	61.17	3.93E	Formatted: English (United Kingdom)
0.012	9.23E+06	4.12E+02	7.19E+02	0.032	50.97	4.72E	Formatted: English (United Kingdom)
0.014	1.08E+07	4.81E+02	8.38E+02	0.037	43.69	5.50E	Formatted: English (United Kingdom)
0.016	1.23E+07	5.49E+02	9.58E+02	0.043	38.23	6.29E	Formatted: English (United Kingdom)
0.018	1.38E+07	6.18E+02	1.08E+03	0.048	33.98	7.07E	Formatted: English (United Kingdom)
0.02	1.54E+07	6.87E+02	1.20E+03	0.053	30.58	7.86E	Formatted: English (United Kingdom)
0.022	1.69E+07	7.55E+02	1.32E+03	0.059	27.80	8.65E	Formatted: English (United Kingdom)
0.024	1.85E+07	8.24E+02	1.44E+03	0.064	25.49	9.43E	Formatted: English (United Kingdom)
0.026	2.00E+07	8.93E+02	1.56E+03	0.070	23.53	1.02E	Formatted: English (United Kingdom)
0.028	2.15E+07	9.62E+02	1.68E+03	0.075	21.84	1.10E	Formatted: English (United Kingdom)
0.03	2.31E+07	1.03E+03	1.80E+03	0.080	20.39	1.18E	Formatted: English (United Kingdom)
▲							Formatted: English (United Kingdom)
P^* : ^4He production							Formatted: English (United Kingdom)
F : ^3He flux							Formatted: English (United Kingdom)
R_t : Helium residence time							Formatted: English (United Kingdom)

1603
1604
1605

1606
1607
1608
1609
1610
1611
1612
1613
1614
1615

Figure Captions

1617 **Figure 1.** Location of the Joya Honda maar (JH) and geodynamic setting. The map shows the Mexican part
1618 of the Basin and Range Province which has an extension of 9.4×10^5 km² (Henry and Aranda-Gomez, 1992);
1619 the image was adapted from Aranda-Gómez et al. (2000). The green area is the area used to estimate the ⁴He
1620 production, the helium residence time and ³He-CO₂ fluxes for the lithospheric mantle located under San Luis
1621 Potosí state (see subsections 6.5 and 6.5.1). The pink square represents the location of the Los Encinos Volcanic
1622 Field (LE); although this is a monogenetic volcanic field associated with the Basin and Range extension, this
1623 lacks mantle xenoliths. Contours of Sierra Madre Occidental, Sierra Madre Oriental, the Transmexican
1624 Volcanic Belt and Mesa Central provinces were build based on Gómez-Tuena et al. (2007). VESVF: Ventura
1625 Espiritu Santo Volcanic Field, SDVF: Santo Domingo Volcanic Field, PiVF: Pinacate Volcanic Field, PaVF:
1626 Las Palomas Volcanic Field, Po: Potrillo maar, CVF: the Camargo Volcanic Field, DVF: Durango Volcanic
1627 Field, SQVF: San Quintin Volcanic Field, II: Isla Isabel. Upper right image: Google Earth image (February
1628 20th, 2020) showing the Joya Honda maar morphology and sampling area.

1629 **Figure 2.** Ternary classification for ultramafic and mafic rocks, from Streckeisen (1976).

1630 **Figure 3.** Microphotographs of the JH mantle xenoliths in cross-polarized light (A, B, C, D, E, G, H) and
1631 transmitted plane-polarized light (F). Ol: olivine, Opx: orthopyroxene, Cpx: clinopyroxene, Sp: spinel. A) Ol
1632 porphyroclast with well-developed kink bands and glass-rich veins. B) Spongy rims developed in Opx crystals;
1633 C) Cpx and Opx crystals are almost and totally replaced by the spongy rim. D) Porphyroclastic texture: Opx
1634 crystal being cut by a glass-rich vein. E) Opx cluster. F) Opx cluster cut by a vein composed of light brown
1635 glass and some opaque minerals, note the presence of spongy rims in Opx. G) Cpx porphyroclast with
1636 development of spongy bands. H) Glass-rich veins around Opx porphyroclast.

1637 **Figure 4.** Microphotographs of inclusions identified in olivine. A) Melt and fluid inclusions originating from
1638 microveins. B) Intragranular trail of dendritic inclusions. C) Inclusions composed by glass and high
1639 birefringent mineral phases (cross-polarized light illumination). D) Opaque phases associated to fluid
1640 inclusions.

1641 **Figure 5:** Raman spectroscopy applied in olivine inclusions. A) Raman spectra of birefringent mineral phases
1642 (Mg-calcite) observed in Figure 4C. B) Raman spectra of pure CO₂ fluid inclusions identified in Figure 4D. C)

Formatted: Font: (Default) Times New Roman, 14 pt, Bold

Formatted: Italian (Italy)

1643 Raman spectra of dolomite contained in some inclusions of Figure 4B. D) Raman spectra of magnesite and
1644 pyrite contained in olivine inclusions.

1645 **Figure 6.** ^4He , $^{40}\text{Ar}^*$ and CO_2 contents measured in fluid inclusions hosted in JH mantle xenoliths. SCLM:
1646 Subcontinental Lithospheric Mantle. The West Antarctic Rift System (WARS) SCLM compositional range
1647 was built using fluid inclusions data measured by Broadley et al. (2016) and Correale et al. (2019). European
1648 SCLM range includes fluid inclusions values measured in mantle xenoliths from the Rhenish Massif
1649 (Germany), Pannonian basin, Massif Central (Central France), Tallante - Calatrava (Spain), Lower Silesia
1650 (Poland) and the Eastern Transylvanian Basin; data was taken from Buikin et al. (2005), Gautheron et al.,
1651 (2005a), Martelli et al. (2011), Rizzo et al. (2018) and Faccini et al. (2020). Eastern Australia SCLM data was
1652 taken from Matsumoto et al. (1998, 2000) and Czuppon et al. (2009). Red sea region data from Hopp et al.
1653 (2004), Hopp et al. (2007a) and Halldórsson et al. (2014). Northern/Southern Kenya rifts data was taken from
1654 Hopp et al. (2007b) and Halldórsson et al. (2014). The Ethiopia (afar) field was designed after Halldórsson et
1655 al. (2014).

1656 **Figure 7.** A) $^4\text{He}/^{20}\text{Ne}$ vs R/Ra diagram, the solid lines represent the binary mixing between air and an upper
1657 mantle source with R/Ra values between 7 and 8. B) $^3\text{He}/^{40}\text{Ar}$ vs $^{40}\text{Ar}/^{36}\text{Ar}$ diagram. C) $^{21}\text{Ne}/^{22}\text{Ne}$ vs. $^{20}\text{Ne}/^{22}\text{Ne}$
1658 diagram in which the green line represents the binary mixing air-MORB mantle as defined by Sarda et al.
1659 (1988) and Moreira et al. (1998) at $^{21}\text{Ne}/^{22}\text{Ne}_{\text{air}} = 0.029$ and $^{20}\text{Ne}/^{22}\text{Ne}_{\text{air}} = 9.8$ and $^{21}\text{Ne}/^{22}\text{Ne} = 0.06$ and
1660 $^{20}\text{Ne}/^{22}\text{Ne} = 12.5$; the primordial neon composition is reported as Solar wind at $^{21}\text{Ne}/^{22}\text{Ne} = 0.0328$ and
1661 $^{20}\text{Ne}/^{22}\text{Ne} = 13.8$ (Heber et al., 2009); the crust endmember was plotted at $^{21}\text{Ne}/^{22}\text{Ne} = 0.6145$ and $^{20}\text{Ne}/^{22}\text{Ne} =$
1662 0.3 (Kennedy et al., 1990). The WARS SCLM, European SCLM, Ethiopia (Afar), N/S Kenya rifts, Eastern
1663 Australia SCLM and Red sea compositional ranges were built using fluid inclusions data cited in Figure 6.

1664 **Figure 8.** $^4\text{He}/^{40}\text{Ar}^*$ vs $^3\text{He}/^4\text{He}$ corrected for air contamination (Rc/Ra) ratios of fluid inclusions from JH
1665 mantle xenoliths. MORB range is reported at Rc/Ra = 8 ± 1 (Graham, 2002) and $^4\text{He}/^{40}\text{Ar}^*$ from 1 to 5
1666 (Yamamoto et al., 2009). The WARS SCLM, European SCLM, Ethiopia (Afar), N/S Kenya rifts, Eastern
1667 Australia SCLM and Red sea compositional ranges were built using fluid inclusions data cited in Figure 6. The
1668 diffusive fractionation path is modeled using the diffusion coefficient (D) of ^3He , ^4He , and $^{40}\text{Ar}^*$
1669 ($D^3\text{He}/D^4\text{He}=1.15$ and $D^4\text{He}/D^{40}\text{Ar}=3.16$ in solid mantle; Burnard, 2004; Yamamoto et al., 2009) (see
1670 supplementary material). Partial melting (see arrow) can lead to decreasing $^4\text{He}/^{40}\text{Ar}^*$ (see supplementary
1671 materials).

1672 **Figure 9.** A) ^{36}Ar vs ^3He concentration. Plotted values correspond to samples with $^{40}\text{Ar}/^{36}\text{Ar} > 500$. B)
1673 $^{20}\text{Ne}/^{22}\text{Ne}$ vs $^{40}\text{Ar}/^{36}\text{Ar}$. Mixing curves are the result of mass-balance and isotopic mass balance equations using
1674 the parameters reported in Table 3.

1675 **Figure 10.** A) $^{21}\text{Ne}/^{22}\text{Ne}_{\text{EX}}$ ratios vs $^4\text{He}/^3\text{He}$ ratios, adapted from Hopp et al. (2004) and Halldórsson et al.
1676 (2014). Values with 2σ uncertainties $<10\%$ are plotted. Dotted lines are binary mixing between three
1677 endmembers: 1) Plume, at 20Ra and $^{21}\text{Ne}/^{22}\text{Ne}_{\text{EX}} = 0.034 \pm 0.001$, 2) MORB-like upper mantle at 8Ra , 7Ra
1678 and $^{21}\text{Ne}/^{22}\text{Ne}_{\text{EX}} = 0.06 \pm 0.001$ and SCLM at $6.1 \pm 0.9\text{Ra}$ and $^{21}\text{Ne}/^{22}\text{Ne}_{\text{EX}} = 0.07 \pm 0.001$. B) ^3He , C) ^4He
1679 and D) $^{40}\text{Ar}^*$ vs $^3\text{He}/^4\text{He}$ corrected for air contamination (Rc/Ra). MORB range is reported at Rc/Ra = 8 ± 1
1680 (Graham, 2002).

1681 **Figure 11.** A) Comparison between ^3He fluxes measured in central Mexico based on JH mantle xenoliths
1682 analysis (at U=0.01 and 0.03 ppm) and other localities. MORB value was estimated using data from Michael
1683 and Graham (2015) and based on $\text{CO}_2/^3\text{He}$ ratio = 2.2×10^9 (Marty and Tolstikhin, 1998); SCLM value was
1684 taken from Gautheron and Moreira (2002); the European SCLM flux was calculated based on Gautheron et al.
1685 (2005a). B) ^3He fluxes scaled to the surface area. See the text for more details. C) Associated CO_2 fluxes
1686 (mol/yr) for central Mexico compared with other tectonic localities. MORB CO_2 flux was calculated after
1687 Michael and Graham (2015); EAR1 and EAR2 values were taken from Lee et al. (2016) and Foley and Fischer
1688 (2017), respectively; Hawaii and Canary fluxes were obtained from Hauri et al. (2019). D) CO_2 fluxes scaled
1689 to the surface area.

Formatted: Superscript

Formatted: Superscript

Formatted: Superscript

Formatted: Superscript

Formatted: Superscript

Formatted: Superscript

Formatted: Superscript

Formatted: Superscript

Formatted: Font: Not Italic, Font color: Auto

Formatted: Font: Not Bold

Formatted: Subscript

1690 **Figure 12.** A) CO₂ vs δ¹³C. Hyblean, Stromboli and European SCLM data from Correale et al. (2015), Gennaro
1691 et al. (2017) and Rizzo et al. (2018), respectively. B) δ¹³C vs 3He/4He corrected for air contamination (Rc/Ra).
1692 Dotted lines are binary mixing between two endmembers: 1) Limestone at δ¹³C = -1, 1 and Rc/Ra = 0.01 and 2)
1693 MORB-like upper mantle at δ¹³C = -4 and Rc/Ra = 7.38. C) δ¹³C vs CO₂/βHe. Dotted lines are binary mixing
1694 between two endmembers: 1) Limestone at δ¹³C = -1, 1 and CO₂/βHe = 10⁻¹³ and 2) MORB-like upper mantle
1695 at δ¹³C = -4 and CO₂/βHe = 1.00 x 10⁻⁹, 2.00 x 10⁻⁹.
1696

Formatted: Font: Not Bold

Formatted: Superscript

Table 2. Fluid inclusions compositions from JH mantle xenoliths. Concentrations are reported in mol/g. r*: reply made in sample V-I.

Sample	Phase	Weight (g)	³ He	⁴ He	²⁰ Ne	²¹ Ne	²² Ne	CO ₂ ^a	⁴⁰ Ar	³⁶ Ar	^{40*} Ar	⁴ He/ ²⁰ Ne	⁴ He/ ⁴⁰ Ar*	⁴ He/CO ₂	R/Ra	Rc/Ra	err
V-A	Ol	0.95855	1.67E-17	1.65E-12	9.11E-16	2.72E-18	9.26E-17	2.80E-11	2.09E-12	1.50E-15	1.65E-12	1814.0	1.00	0.05901	7.26	7.26	
V-A	Opx	0.26388	4.74E-18	4.91E-13	8.90E-15	2.59E-17	9.00E-16	3.91E-10	3.61E-12	5.45E-15	2.00E-12	55.2	0.25	0.00126	6.91	6.94	0.13
V-A	Cpx	0.21991	6.45E-18	6.57E-13	5.81E-16	2.62E-18	5.41E-17	6.23E-09	5.16E-12	1.55E-15	4.70E-12	1131.4	0.14	0.00011	7.06	7.06	0.13
V-B	Ol	0.99706	2.53E-17	2.48E-12	1.84E-15	5.52E-18	1.88E-16	2.26E-10	3.70E-12	6.01E-15	1.92E-12	1349.7	1.29	0.01100	7.32	7.33	0.06
V-B	Opx	0.4776	3.43E-17	3.36E-12	6.75E-15	1.97E-17	6.61E-16	4.88E-08	7.67E-12	7.95E-15	5.32E-12	497.5	0.63	0.00007	7.34	7.35	0.06
V-B	Cpx	0.48584	4.67E-17	4.62E-12	4.41E-16	2.00E-18	3.61E-17	9.70E-08	1.12E-11	1.36E-15	1.08E-11	10483.3	0.43	0.00005	7.27	7.27	0.06
V-C	Ol	0.59294	3.71E-18	3.74E-13	2.35E-16	n.a	2.61E-17	2.38E-10	8.96E-13	3.56E-16	7.91E-13	1593.9	0.47	0.00157	7.13	7.13	0.10
V-C	Cpx	0.5587	8.55E-18	8.40E-13	5.73E-16	1.82E-18	5.87E-17	7.61E-10	2.57E-12	1.02E-15	2.27E-12	1466.6	0.37	0.00110	7.32	7.33	0.07
V-D	Ol	1.02241	2.08E-17	2.08E-12	3.76E-16	1.25E-18	3.67E-17	9.18E-10	2.76E-12	1.27E-15	2.38E-12	5534.0	0.87	0.00227	7.19	7.19	0.06
V-D	Opx	0.49922	9.46E-18	9.43E-13	2.33E-15	7.04E-18	2.39E-16	4.39E-09	2.07E-12	3.30E-15	1.09E-12	404.4	0.86	0.00021	7.21	7.22	0.08
V-D	Cpx	0.47389	2.66E-17	2.59E-12	3.02E-16	1.23E-18	2.73E-17	3.25E-08	6.01E-12	7.58E-16	5.78E-12	8576.0	0.45	0.00008	7.37	7.37	0.07
V-E	Ol	1.02916	2.51E-17	2.42E-12	1.22E-15	3.90E-18	1.19E-16	4.11E-09	8.79E-13	3.38E-16	7.79E-13	1982.0	3.11	0.00059	7.47	7.47	0.07
V-E	Opx	0.51352	1.98E-17	1.90E-12	5.12E-15	1.56E-17	5.16E-16	2.74E-08	3.03E-12	2.11E-15	2.41E-12	371.6	0.79	0.00007	7.49	7.50	0.07
V-E	Cpx	0.32954	3.96E-17	3.81E-12	3.93E-15	1.27E-17	3.81E-16	1.25E-07	7.06E-12	1.50E-15	6.62E-12	970.0	0.58	0.00003	7.48	7.48	0.07
V-F	Ol	1.01203	2.57E-17	2.44E-12	3.49E-15	1.05E-17	3.55E-16	2.81E-09	2.50E-12	2.81E-15	1.67E-12	700.6	1.46	0.00087	7.57	7.57	0.07
V-F	Opx	0.52681	1.66E-17	1.61E-12	4.91E-15	1.51E-17	4.98E-16	1.85E-08	2.37E-12	2.11E-15	1.75E-12	328.5	0.92	0.00009	7.41	7.42	0.08
V-F	Cpx	0.31734	5.58E-17	5.29E-12	2.01E-14	6.07E-17	1.99E-15	1.78E-07	1.06E-11	1.24E-14	6.98E-12	262.9	0.76	0.00003	7.58	7.59	0.07
V-G	Ol	1.00336	1.94E-17	1.81E-12	7.91E-16	2.44E-18	7.78E-17	3.91E-11	1.19E-12	1.72E-15	6.81E-13	2292.1	2.66	0.04634	7.68	7.68	0.07
V-G	Opx	0.50526	1.29E-17	1.23E-12	3.20E-15	9.62E-18	3.26E-16	4.54E-09	1.47E-12	1.69E-15	9.68E-13	384.5	1.27	0.00027	7.53	7.53	0.08
V-G	Cpx	0.32136	3.21E-17	3.15E-12	1.57E-15	5.55E-18	1.52E-16	2.24E-08	3.17E-12	9.41E-16	2.89E-12	2003.4	1.09	0.00014	7.32	7.32	0.07
V-H	Ol	1.0181	4.21E-17	4.03E-12	4.72E-15	1.47E-17	4.66E-16	4.72E-09	6.44E-12	6.29E-15	4.58E-12	853.7	0.88	0.00085	7.51	7.52	0.08
V-H	Opx	0.53853	1.95E-17	1.86E-12	4.01E-14	1.16E-16	3.94E-15	1.23E-08	1.52E-11	4.14E-14	2.93E-12	46.5	0.64	0.00015	7.47	7.52	0.08
V-H	Cpx	0.30754	3.92E-17	3.73E-12	3.52E-15	1.13E-17	3.46E-16	5.09E-08	4.74E-12	1.93E-15	4.17E-12	1062.1	0.90	0.00007	7.56	7.56	0.07
V-I	Ol	1.0437	8.62E-19	8.56E-14	1.42E-16	5.22E-19	1.39E-17	4.74E-11	2.25E-13	5.78E-16	5.37E-14	604.6	1.59	0.00181	7.24	7.25	0.13
V-I	Opx	0.5057	9.92E-19	9.93E-14	1.55E-16	6.59E-19	1.34E-17	2.26E-10	3.77E-13	8.58E-16	1.23E-13	639.0	0.8	0.00044	7.18	7.19	0.15
V-I	Cpx	0.49525	9.34E-19	1.23E-13	5.08E-14	1.46E-16	4.90E-15	n.a	1.13E-11	3.72E-14	2.97E-13	2.4	0.41	n.a	4.84	5.46	0.14
V-I r*	Ol	1.01139	9.47E-19	9.25E-14	4.09E-16	1.32E-18	4.07E-17	7.54E-10	1.75E-13	4.48E-16	4.32E-14	226.0	2.14	0.00012	7.36	7.37	0.13
V-I r*	Opx	0.50086	9.81E-19	1.15E-13	1.13E-14	3.37E-17	1.14E-15	1.31E-09	2.02E-12	5.94E-15	2.63E-13	10.1	0.44	0.00009	5.98	6.15	0.08
V-I r*	Cpx	0.57112	7.37E-19	9.81E-14	9.68E-15	2.89E-17	9.72E-16	4.07E-10	5.64E-13	1.62E-15	8.59E-14	10.1	1.14	0.00024	5.26	5.40	0.14
V-J	Ol	1.0333	3.63E-17	3.53E-12	3.77E-15	1.15E-17	3.76E-16	4.55E-09	5.30E-12	6.20E-15	3.47E-12	937.0	1.02	0.00078	7.38	7.38	0.07
V-J	Opx	0.5061	5.02E-17	4.93E-12	7.60E-15	2.36E-17	7.58E-16	1.08E-07	1.02E-11	7.88E-15	7.87E-12	649.1	0.63	0.00005	7.32	7.33	0.08
V-J	Cpx	0.30875	1.11E-16	1.07E-11	6.19E-15	2.02E-17	6.07E-16	3.23E-07	8.59E-12	2.87E-15	7.75E-12	1726.7	1.38	0.00003	7.50	7.50	0.07
V-K	Ol	1.0225	5.42E-17	5.24E-12	4.99E-15	1.58E-17	4.99E-16	2.46E-08	7.72E-12	6.93E-15	5.67E-12	1049.9	0.92	0.00021	7.45	7.45	0.07
V-K	Opx	0.52687	5.37E-17	5.13E-12	2.48E-14	7.37E-17	2.38E-15	1.05E-07	1.54E-11	2.07E-14	9.25E-12	206.6	0.55	0.00005	7.53	7.54	0.08
V-K	Cpx	0.30567	7.40E-17	7.07E-12	4.08E-14	1.21E-16	4.11E-15	1.16E-07	1.06E-11	1.40E-14	6.47E-12	173.4	1.09	0.00006	7.52	7.53	0.07
IV-A	Ol	1.03046	2.52E-17	2.43E-12	4.47E-15	1.29E-17	4.34E-16	1.47E-09	2.09E-12	3.40E-15	1.08E-12	543.9	2.24	0.00165	7.45	7.45	0.08
IV-A	Opx	0.49715	3.04E-17	3.02E-12	1.05E-14	3.07E-17	1.03E-15	4.49E-08	5.48E-12	6.38E-15	3.59E-12	286.9	0.84	0.00007	7.23	7.23	0.10
IV-A	Cpx	0.47966	1.29E-16	1.29E-11	1.25E-14	3.82E-17	1.22E-15	2.73E-07	1.20E-11	9.65E-15	9.11E-12	1033.2	1.42	0.00005	7.21	7.21	0.06

Formatted: Font: 10 pt

Formatted Table

Formatted: Font: 10 pt, Italian (Italy)

Formatted Table

Formatted Table

Table 2. Continued. ^a First estimation of CO₂ during noble gases analysis; ^b CO₂ measured from glass line.

Sample	Phase	⁴⁰ Ar/ ³⁶ Ar	error +/- (1σ)	³⁸ Ar/ ³⁶ Ar	error +/- (1σ)	²⁰ Ne/ ²² Ne	error +/- (1σ)	²¹ Ne/ ²² Ne	error +/- (1σ)	²¹ Ne/ ²² Ne EX to 12.5	error +/- (2σ)	CO ₂ / ³ He	³ He/ ³⁶ Ar	CO ₂ / ³ He	CO ₂ ^b	
V-A	Ol	1391.46	1.24	0.19251	0.00037	9.93	0.06	0.0297	0.00135	0.043	0.003	1.68E+06	0.0111	n.a	n.a	
V-A	Opx	662.11	0.93	0.18892	0.00036	9.87	0.04	0.0288	0.00050	n.a	n.a	8.24E+07	0.0009	n.a	n.a	
V-A	Cpx	3320.08	9.83	0.20543	0.00042	n.a	n.a	n.a	n.a	n.a	n.a	9.66E+08	0.0041	n.a	n.a	
V-B	Ol	614.85	0.37	0.18772	0.00035	9.87	0.04	0.0296	0.00082	0.053	0.003	8.93E+06	0.0042	n.a	n.a	
V-B	Opx	964.58	0.65	0.18291	0.00033	9.97	0.03	0.0298	0.00045	0.041	0.001	1.42E+09	0.0043	2.58E+09	1.17E-07	-2.30
V-B	Cpx	8231.50	13.81	0.20717	0.00043	12.18	0.26	0.0553	0.00431	n.a	n.a	2.07E+09	0.0343	n.a	n.a	n.a
V-C	Ol	2518.41	13.00	0.22231	0.00049	n.a	n.a	n.a	n.a	n.a	n.a	6.43E+07	0.0104	n.a	n.a	n.a
V-C	Cpx	2511.64	5.81	0.19747	0.00039	n.a	n.a	n.a	n.a	n.a	n.a	8.90E+07	0.0084	n.a	n.a	n.a
V-D	Ol	2177.87	2.53	0.19317	0.00037	10.57	0.16	0.0354	0.00227	n.a	n.a	4.41E+07	0.0164	n.a	n.a	n.a
V-D	Opx	626.23	0.62	0.18834	0.00035	n.a	n.a	n.a	n.a	n.a	n.a	4.64E+08	0.0029	n.a	n.a	n.a
V-D	Cpx	7926.55	24.39	0.20644	0.00043	11.03	0.39	0.0452	0.00659	n.a	n.a	1.22E+09	0.0350	1.61E+09	4.27E-08	-1.55
V-E	Ol	2598.15	11.14	0.19010	0.00036	10.37	0.07	0.0332	0.00107	0.049	0.003	1.64E+08	0.0743	n.a	n.a	n.a
V-E	Opx	1436.20	1.91	0.18305	0.00033	10.00	0.04	0.0306	0.00046	0.050	0.002	1.39E+09	0.0094	n.a	n.a	n.a
V-E	Cpx	4719.85	15.56	0.18136	0.00033	10.25	0.05	0.0338	0.00115	0.058	0.004	3.16E+09	0.0265	9.17E+08	3.63E-08	-2.66
V-F	Ol	889.63	0.69	0.18730	0.00035	9.87	0.04	0.0297	0.00064	n.a	0.003	1.09E+08	0.0091	n.a	n.a	n.a
V-F	Opx	1123.07	1.53	0.19054	0.00036	9.93	0.04	0.0307	0.00072	0.063	0.003	1.11E+09	0.0079	1.15E+09	1.91E-08	-1.34
V-F	Cpx	856.84	0.53	0.18382	0.00034	10.12	0.03	0.0306	0.00045	0.042	0.001	3.18E+09	0.0045	1.12E+09	6.22E-08	-1.66
V-G	Ol	690.44	0.68	0.18565	0.00034	10.23	0.06	0.0316	0.00117	0.045	0.003	2.02E+06	0.0112	n.a	n.a	n.a
V-G	Opx	866.39	1.50	0.18036	0.00032	9.85	0.04	0.0296	0.00062	n.a	n.a	3.52E+08	0.0076	n.a	n.a	n.a
V-G	Cpx	3371.87	14.57	0.18281	0.00033	11.06	0.11	0.0390	0.00227	n.a	n.a	6.97E+08	0.0341	n.a	n.a	n.a
V-H	Ol	1023.71	0.63	0.18503	0.00034	10.18	0.03	0.0317	0.00041	0.048	0.001	1.12E+08	0.0067	n.a	n.a	n.a
V-H	Opx	366.42	0.00	0.18303	0.00033	10.11	0.02	0.0301	0.00027	0.039	0.001	6.33E+08	0.0005	n.a	n.a	n.a
V-H	Cpx	2457.00	6.70	0.19215	0.00037	10.15	0.05	0.0326	0.00104	0.056	0.004	1.30E+09	0.0203	n.a	n.a	n.a
V-I	Ol	388.43	0.86	0.19569	0.00038	n.a	n.a	n.a	n.a	n.a	n.a	5.50E+07	0.0015	n.a	n.a	n.a
V-I	Opx	439.10	1.49	0.19092	0.00036	11.59	0.73	0.0492	0.01944	n.a	n.a	2.28E+08	0.0586	n.a	n.a	n.a
V-I	Cpx	303.48	0.16	0.18009	0.00032	10.24	0.01	0.0323	0.00025	n.a	n.a	0.00E+00	0.0000	n.a	n.a	n.a
V-I*	Ol	391.97	1.17	0.19246	0.00038	10.39	0.16	0.0336	0.00251	n.a	n.a	7.95E+08	0.0021	n.a	n.a	n.a
V-I*	Opx	339.74	0.26	0.18402	0.00035	9.91	0.03	0.0296	0.00029	n.a	n.a	1.33E+09	0.0002	n.a	n.a	n.a
V-I*	Cpx	348.57	0.56	0.18113	0.00034	9.98	0.03	0.0298	0.00034	n.a	n.a	5.52E+08	0.0005	n.a	n.a	n.a
V-J	Ol	854.91	0.48	0.18694	0.00035	10.05	0.03	0.0307	0.00053	0.047	0.002	1.25E+08	0.0058	n.a	n.a	n.a
V-J	Opx	1294.25	0.87	0.18590	0.00035	10.08	0.03	0.0313	0.00056	0.051	0.002	2.15E+09	0.0064	3.82E+09	1.92E-07	-2.13
V-J	Cpx	2993.26	5.58	0.19053	0.00036	10.24	0.03	0.0335	0.00071	0.056	0.002	2.90E+09	0.0388	2.10E+09	2.34E-07	-1.30
V-K	Ol	1114.13	0.00	0.18660	0.00035	10.07	0.03	0.0319	0.00049	0.058	0.002	4.54E+08	0.0078	3.82E+08	2.07E-08	n.a
V-K	Opx	741.96	0.00	0.18186	0.00033	10.32	0.02	0.0316	0.00031	0.042	0.001	1.95E+09	0.0026	1.88E+09	1.01E-07	-2.08
V-K	Cpx	756.34	0.50	0.18796	0.00035	9.92	0.02	0.0296	0.00029	0.041	0.001	1.57E+09	0.0053	3.38E+08	2.50E-08	-0.97
IV A	Ol	614.05	0.43	0.18144	0.00034	10.14	0.04	0.0303	0.00050	0.039	0.001	5.84E+07	0.0074	n.a	n.a	n.a
IV A	Opx	858.77	0.49	0.18068	0.00033	10.10	0.03	0.0298	0.00045	n.a	n.a	1.48E+09	0.0048	2.22E+09	6.76E-08	-2.86
IV A	Cpx	1238.93	24.70	0.18113	0.00034	10.25	0.03	0.0314	0.00047	0.043	0.001	2.11E+09	0.0134	1.18E+09	1.52E-07	-1.25

Formatted: Font: 10 pt

Formatted Table

Formatted Table

Formatted Table

1714

1715

1716

Table 3. Expected noble gas isotopic ratios for the Mexican lithospheric mantle. $^{20}\text{Ne}/^{22}\text{Ne}_{\text{air}}$, $^{40}\text{Ar}/^{36}\text{Ar}_{\text{air}}$ ratios after Steiger and Jäger (1977) and Ozima and Podosek (2002).

<u>R/Ra</u>	<u>$^4\text{He}/^{40}\text{Ar}^*$</u>	<u>$^4\text{He}/^{20}\text{Ne}$</u>	<u>$^{36}\text{Ar}/^{22}\text{Ne}$</u>	<u>$^{40}\text{Ar}/^{36}\text{Ar}$</u>	<u>$^{20}\text{Ne}/^{22}\text{Ne}$</u>	<u>$^{20}\text{Ne}/^{22}\text{Ne}_{\text{air}}$</u>	<u>$^{40}\text{Ar}/^{36}\text{Ar}_{\text{air}}$</u>
<u>7.39 ± 0.14</u>	<u>0.14 - 3.11</u>	<u>11000</u>	<u>4.21 - 93.5</u>	<u>10500</u>	<u>12.5</u>	<u>9.8</u>	<u>295.5</u>

1717

1718

1719

1720

Table 4. ^4He production rates, ^3He fluxes, helium residence time and CO_2 fluxes calculated for the lithospheric mantle beneath central Mexico. P*, F and Rt values were calculated based on mathematical formulations proposed by Gautheron and Moreira (2002). P*: ^4He production, F: ^3He flux, Rt: Helium residence time.

<u>U (ppm)</u>	<u>P* (ccSTP/g)</u>	<u>P* (mol/yr)</u>	<u>F (ccSTP/year)</u>	<u>F (mol/yr)</u>	<u>Rt (Ma)</u>	<u>CO_2 flux (mol/yr)</u>	<u>CO_2 flux (g/yr)</u>
<u>0.01</u>	<u>7.69E+06</u>	<u>3.43E+02</u>	<u>5.99E+02</u>	<u>0.027</u>	<u>61.17</u>	<u>3.93E+07</u>	<u>1.73E+09</u>
<u>0.012</u>	<u>9.23E+06</u>	<u>4.12E+02</u>	<u>7.19E+02</u>	<u>0.032</u>	<u>50.97</u>	<u>4.72E+07</u>	<u>2.08E+09</u>
<u>0.014</u>	<u>1.08E+07</u>	<u>4.81E+02</u>	<u>8.38E+02</u>	<u>0.037</u>	<u>43.69</u>	<u>5.50E+07</u>	<u>2.42E+09</u>
<u>0.016</u>	<u>1.23E+07</u>	<u>5.49E+02</u>	<u>9.58E+02</u>	<u>0.043</u>	<u>38.23</u>	<u>6.29E+07</u>	<u>2.77E+09</u>
<u>0.018</u>	<u>1.38E+07</u>	<u>6.18E+02</u>	<u>1.08E+03</u>	<u>0.048</u>	<u>33.98</u>	<u>7.07E+07</u>	<u>3.11E+09</u>
<u>0.02</u>	<u>1.54E+07</u>	<u>6.87E+02</u>	<u>1.20E+03</u>	<u>0.053</u>	<u>30.58</u>	<u>7.86E+07</u>	<u>3.46E+09</u>
<u>0.022</u>	<u>1.69E+07</u>	<u>7.55E+02</u>	<u>1.32E+03</u>	<u>0.059</u>	<u>27.80</u>	<u>8.65E+07</u>	<u>3.80E+09</u>
<u>0.024</u>	<u>1.85E+07</u>	<u>8.24E+02</u>	<u>1.44E+03</u>	<u>0.064</u>	<u>25.49</u>	<u>9.43E+07</u>	<u>4.15E+09</u>
<u>0.026</u>	<u>2.00E+07</u>	<u>8.93E+02</u>	<u>1.56E+03</u>	<u>0.070</u>	<u>23.53</u>	<u>1.02E+08</u>	<u>4.50E+09</u>
<u>0.028</u>	<u>2.15E+07</u>	<u>9.62E+02</u>	<u>1.68E+03</u>	<u>0.075</u>	<u>21.84</u>	<u>1.10E+08</u>	<u>4.84E+09</u>
<u>0.03</u>	<u>2.31E+07</u>	<u>1.03E+03</u>	<u>1.80E+03</u>	<u>0.080</u>	<u>20.39</u>	<u>1.18E+08</u>	<u>5.19E+09</u>

1721

1 **THE COMPOSITION OF FLUIDS STORED IN THE CENTRAL MEXICAN**
2 **LITHOSPHERIC MANTLE: INFERENCES FROM NOBLE GASES AND CO₂ IN MANTLE**
3 **XENOLITHS**

4 A. Sandoval-Velasquez¹, A.L. Rizzo², M. Frezzotti³, R. Saucedo⁴ and A. Aiuppa^{1,2}.

5

6 **Author's affiliations**

7 ¹*DiSTeM, Università di Palermo, Via Archirafi 36, 90123 Palermo, Italy.*

8 ²*Istituto Nazionale di Geofisica e Vulcanologia (INGV), Sezione di Palermo, Via Ugo La Malfa 153,*
9 *90146 Palermo, Italy,*

10 ³*Dipartimento di Scienze dell'Ambiente e della Terra, Università di Milano Bicocca, Piazza della*
11 *Scienza 4, 20126 Milano, Italy,*

12 ⁴*Instituto de Geología, Universidad Autónoma de San Luis Potosí, Dr M. Nava no. 5, Zona*
13 *Universitaria, 78240 San Luis Potosí, México*

14

15 **Corresponding author e-mail:** andreslibardo.sandovalvelasquez@unipa.it

16

17 **ABSTRACT**

18 We present the first isotopic (noble gases and CO₂) characterization of fluid inclusions coupled to
19 Raman microspectroscopy analyses in mantle xenoliths from Central Mexico, a geodynamically
20 complex area where the Basin and Range extension was superimposed on the Farallon subduction
21 (terminated at 28 Ma). To characterize the isotopic signature of the Central Mexican lithospheric
22 mantle, we focus on fluid inclusions entrapped in mantle xenoliths found in deposits of the Joya
23 Honda maar (JH), a Quaternary monogenetic volcano belonging to the Ventura Espiritu Santo
24 Volcanic Field (VESVF) in the state of San Luis Potosí (central Mexico). Thirteen ultramafic
25 plagioclase-free xenoliths were selected, all exhibiting a paragenesis Ol>Opx>Cpx >> Sp, and being
26 classified as spinel-lherzolites and harzburgites. All xenoliths bring textural evidence of interstitial
27 glass veins bearing dendritic trails of secondary melt and fluid inclusions (composed of silicate glass
28 ± CO₂ ± Mg-Ca carbonates ± pyrite). These are related to pervasive mantle metasomatism driven by
29 carbonate-rich silicate melt. The Ar and Ne systematics reflect mixing between MORB-like upper
30 mantle and atmospheric fluids, the latter interpreted as reflecting a recycled air component possibly
31 inherited from the Farallon plate subduction. The ³He/⁴He ratios vary between 7.13 and 7.68 Ra,
32 within the MORB range (7-9 Ra), and the ⁴He/⁴⁰Ar* ratios (0.4 - 3.11) are similarly close to the
33 expected range of the fertile mantle (1-5). Taken together, these pieces of evidence suggest that (i)
34 either the mantle He budget was scarcely modified by the Farallon plate subduction, and/or (ii) that
35 any (large) crustal contribution was masked by a later metasomatism/refertilization episode, possibly
36 during the subsequent Basin and Range extension. A silicate melt-driven
37 metasomatism/refertilization (revealed by the association between glass veins and fluid inclusions)
38 is consistent with calculated helium residence time for the Mexican lithospheric mantle (20 to 60Ma)

39 that overlaps the timing of the above geodynamic events. We propose that, after the refertilization
40 event (e.g., over the last ~20Ma), the lithospheric mantle has evolved in a steady-state, becoming
41 slightly more radiogenic. We also estimated ^3He fluxes (0.027 - 0.080 mol/g), ^4He production rates
42 (340 - 1000 mol/yr), and mantle CO_2 fluxes (3.93×10^7 mol/yr to 1.18×10^8 mol/yr) using the helium
43 isotopic values measured in JH mantle xenoliths. Finally, the JH xenoliths exhibit $\text{CO}_2/{}^3\text{He}$ ratios
44 comparable to those of the upper mantle (from 3.38×10^8 to 3.82×10^9) but more positive $\delta^{13}\text{C}$ values
45 (between -1.0 and -2.7‰), supporting the involvement of a crustal carbonate component. We propose
46 that the metasomatic silicate melts recycled a crustal carbonate component, inherited by the Farallon
47 plate subduction.

48 **Keywords:** *Mexican mantle xenoliths; fluid inclusions; noble gases; CO_2 ; mantle refertilization; carbonate*
49 *recycling.*

50

51 1. INTRODUCTION

52 The subduction of the Farallon oceanic slab under the North American plate, during the late
53 Oligocene and Middle Miocene, has given rise to enormous changes in the tectonic configuration of
54 the northwestern coast of Mexico. These include the transition from a compressive to a transform
55 margin, and the beginning of a regional extension that produced the Basin and Range Province
56 (Atwater, 1989; Ferrari et al., 2012; Henry and Aranda-Gomez, 1992; Sedlock, 2003).

57 The Basin and Range extension started about 30Ma and was accompanied by intraplate magmatism,
58 which generated several volcanic fields north of the Transmexican Volcanic Belt (TMVB; Aranda-
59 Gómez and Ortega-Gutiérrez, 1987; Luhr and Aranda-Gómez, 1997; Henry and Aranda-Gomez,
60 1992). These fields are typically monogenetic complexes associated with the eruption of alkaline
61 basalts and basanites that have brought to the surface significant amounts of ultramafic xenoliths that
62 now allow the composition of the local lithospheric mantle to be probed .

63 The Ventura Espiritu Santo Volcanic Field (VESVF), located in the San Luis Potosí state (central
64 Mexico), is one of the best-known examples of this volcanism, and is characterized by spectacular
65 volcanic structures like the Joya Honda maar (JH), and by frequent ultramafic nodules found in its
66 deposits. Other mantle xenoliths-bearing alkali basalt localities are the Santo Domingo Volcanic
67 Field (SDVF) also located in the San Luis Potosí state, the Pinacate Volcanic Field (PiVF), Las
68 Palomas Volcanic Field (PaVF), the Potrillo maar (Po), the Camargo Volcanic Field (CVF), the
69 Durango Volcanic Field (DVF), the San Quintin Volcanic Field (SQVF) and Isla Isabel (II; Figure
70 1; Basu, 1977; Gutmann, 1986; Aranda-Gómez and Ortega-Gutiérrez, 1987; Luhr et al., 1989; Pier
71 et al., 1992; Luhr and Aranda-Gómez, 1997; Housh et al., 2010).

72 These volcanic structures in the central and NW portion of Mexico, and the textural and petrological
73 characteristics of their ultramafic xenoliths, have already been discussed elsewhere (Aranda-Gómez
74 and Ortega-Gutiérrez, 1987; Luhr and Aranda-Gómez, 1997; Henry and Aranda-Gomez, 1992).
75 These previous studies have revealed a complex (multi-stage) history of deformation, melting and
76 metasomatism, and opened new questions on the evolution of the Mexican lithospheric mantle.
77 Debate exists, however, on the provenance of the metasomatic fluids, and if and to what extent
78 subduction of the Farallon plate has modified mantle composition during the recent Mexican
79 geological history (Pier et al., 1989; Luhr and Aranda-Gómez, 1997; Dávalos-Elizondo et al., 2016).

80 Addressing these questions requires information on the chemical features of metasomatic fluids
81 present in the lithospheric mantle. Fluid and melt inclusions preserved in mantle xenoliths are well
82 known for being valuable sources of information to study the evolution of volatile species trapped in
83 ultramafic mantle rocks, and to derive inferences about the local lithospheric mantle dynamics
84 (Roedder, 1984; Andersen and Neumann, 2001; Deines, 2002; Frezzotti et al., 2002a; Buikin et al.,
85 2005; Gautheron et al., 2005a; Martelli et al., 2011; Day et al., 2015; Broadley et al., 2016; Rizzo
86 et al., 2018; Correale et al., 2019; Faccini et al., 2020).

87 Here, we aim at filling this gap of knowledge on the volatile composition of the Mexican lithospheric
88 mantle, by reporting on the chemical and isotopic composition (He, Ne, Ar and CO₂) of fluid
89 inclusions entrapped in mantle xenoliths found in the JH. Noble gases are sensitive tracers that
90 provide insights on fluid origin, the composition and evolution of the mantle, and their relationship
91 with different tectonic processes such as subduction (Matsumoto et al., 2001; Hopp et al., 2007a;
92 Hopp and Ionov, 2011; Martelli et al., 2014; Broadley et al., 2016; Faccini et al., 2020) or mantle
93 plumes (Hopp et al., 2004, 2007a, 2007b; Buikin et al., 2005; Halldórsson et al., 2014; Boudoire
94 et al., 2018, 2020). In addition, studying CO₂ abundance and isotopic composition contribute to
95 assessing composition and provenance of metasomatic fluids that may have interacted with these
96 xenoliths (Sano and Marty, 1995; Correale et al., 2015; Gennaro et al., 2017; Rizzo et al., 2018), for
97 example revealing any addition to the mantle of carbonate-rich fluids delivered by sediments and
98 altered oceanic crust in the subducted slab (Plank and Manning, 2019).

99

100 **2. GEOLOGICAL SETTING**

101 The VESVF is located in the southern portion of the province known as the Mesa Central (Raisz,
102 1959; Nieto-Samaniego et al., 2005); very close to the Sierra Madre Oriental province (Figure 1).
103 The Mesa Central, located north of the TMVB, comprises a portion of continental crust that has a
104 thickness of 32 km and is delimited by regional faults (Fix, 1975; Nieto-Samaniego et al., 2005). The
105 oldest rocks found in this province are muscovite schists from the Paleozoic (252 Ma), superimposed
106 by turbiditic sequences of the Triassic and volcano-sedimentary sequences of continental origin
107 formed during the mid-late Jurassic (Barboza-Gudiño et al., 1999; Morán-Zenteno et al., 2005; Nieto-
108 Samaniego et al., 2005). The most abundant outcrops correspond to sequences of calcareous rocks
109 of marine origin, formed during a transgression episode during the end of the late Jurassic and the
110 Cretaceous (Carrillo-Bravo, 1971; López-Doncel, 2003; Nieto-Samaniego et al., 2005); these rocks
111 make up the so-called Valles-San Luis Potosí Platform (PVSLP) and the Mesozoic Basin of Central
112 Mexico whose thickness can reach 5 km and 6 km, respectively. Cenozoic rocks are mainly volcanic
113 and sedimentary (of continental origin), the most recent being the alkaline basalts of the VESVF,
114 SDVF and DVF whose origin is related to a melting zone located 34 km deep under the Mesa Central
115 (Fix, 1975).

116 The VESVF is formed by some isolated scoria cones and three maars among which is the JH
117 (Aranda-Gómez et al., 2007; Saucedo et al., 2017). The JH is located at the intersection between the
118 PVSLP and the Mesozoic Basin of central Mexico (22 ° 25'4.97 "N and 100 ° 47'15.62" W), and is
119 thought to have formed at about 311 ± 19 ka (Saucedo et al., 2017). This volcano is recognized as
120 one of the most spectacular volcanic structure of Mexico (Saucedo et al., 2017), with its elliptical
121 crater having vertical walls defining a 150 – 300 m deep depression (Figure 1). The maar formed
122 through a series of mixed magmatic and phreatomagmatic eruptions that emplaced a sequence of

123 pyroclastic falls and base surge deposits (having a maximum thickness of ~100 m). Magma-
124 groundwater interaction is thought to have occurred during magma ascent through of a NE-SW
125 normal fault system cutting folded limestones, calcareous mudstones, chert lenses and shales which
126 are part of the Cuesta del Cura (Albian-Cenomanian) and Tamaulipas (Aptian) Formations (Aranda-
127 Gómez and Luhr, 1996; Aranda Gómez et al., 2000; Saucedo et al., 2017). Saucedo et al. (2017)
128 identified 5 eruptive phases, the last two of which generated deposits rich in mantle xenoliths. The
129 erupted magmas are alkaline and mafic in composition (olivine-nepheline basanites and olivine
130 basalts), and their origin is thought to be associated with decompressional melting of the
131 asthenosphere and lithospheric mantle under la Mesa Central, as proposed for other volcanic fields
132 associated to the Basin and Range extension (Aranda-Gómez and Ortega-Gutiérrez, 1987; Luhr et
133 al., 1989; Lee, 2005; Aranda-Gómez et al., 2007).

134

135 **3. PETROLOGICAL BACKGROUND**

136 The JH mantle xenoliths have been previously studied and described as spinel lherzolites and
137 harzburgites (Aranda-Gómez and Ortega-Gutiérrez, 1987; Liang and Elthon, 1990; Luhr and Aranda-
138 Gómez, 1997). The modal composition indicates a relatively constant paragenesis: Ol is the most
139 abundant phase (55-88%), followed by Opx (17-32%), Cpx (1-17%) and Spinel (Sp; 0.3 - 5%); in
140 very few cases, the presence of phlogopite is also reported with percentages below 1% (Luhr and
141 Aranda-Gómez, 1997). Compositionally, Ol has a Mg# ($Mg\# = 100 \times Mg / (Mg + \sum Fe)$) ranging from
142 87.5 to 91, Opx from 88.6 to 91.2, Cpx from 87.7 to 91.4 and Sp from 75.5 to 82.5 (Liang and Elthon,
143 1990). These authors also report the development of Na-Al poor spongy rims on Opx, Cpx and spinel,
144 explained as due to variable degrees of partial melting that have affected the local upper mantle.

145 Liang and Elthon (1990) classified the xenoliths into two groups based on their modal and
146 geochemical compositions (groups Ia and Ib). Mantle xenoliths from group Ia are interpreted as
147 mantle residues generated by different degrees of partial melting and extraction of picritic melts in
148 the upper mantle; these authors calculated a degree of partial melting between 7% and 22% for Ia
149 xenoliths, using melting models based on bulk-rock MgO, Ni and Sc abundances. Group Ib
150 peridotites exhibit similar degrees of partial melting (1-20%) followed by metasomatic enrichment
151 (Liang and Elthon, 1990). One of the most important characteristic of Ib xenoliths is the extreme
152 core-to-rim chemical zoning (and LREE-enriched patterns; $(La/Yb)_N > 0.8$) in clinopyroxene,
153 revealed by a decrease of Al_2O_3 and Na_2O towards the rim, while Mg#, CaO, TiO_2 and Cr_2O_3 tend
154 to increase (Liang and Elthon, 1990). According to these authors, high FeO- Na_2O contents in the
155 cores of Ib minerals and LREE enrichment in Cpx crystals suggest interaction between silicate melts
156 (basanitic in composition) and a residual mantle similar to group Ia xenoliths. Additionally, they
157 explain the extreme core-to-rim chemical zoning, and reaction rims in Cpx, by the reaction with H_2O -
158 rich fluids depleting Cpx rims in Na_2O and Al_2O_3 (also increasing TiO_2 contents).

159

160 **4. SAMPLES AND METHODS**

161 Samples were collected from the eastern part of the JH (Figure 1), where units IV and V emerge
162 according to the stratigraphy described by Saucedo et al. (2017). These units are composed of
163 pyroclastic fall and flow deposits where the highest concentration of mantle xenoliths is found. The

164 nodules are usually dispersed within or hosted in basanitic lavas. Thirteen fresh nodules were selected
165 with diameters between 5 and 10 cm; additionally, a pyroxenite sample was studied (sample V-C)
166 and was only used for noble gas analysis due to its small diameter (<5 cm). Eight nodules were
167 selected for petrographic analysis on thin and polished sections. Petrographic analysis was performed
168 at the petrography laboratory of the University of Milano-Bicocca based on the textural classification
169 proposed by Mercier and Nicolas (1975); the modal composition was carried out by point counting
170 (from 4000 to 7000 points per section).

171 Two double-polished rock sections of about 130 μm thickness were selected for the Raman of fluid
172 inclusions. Analyzed fluid inclusions are located at 10 to 20 μm depth below the sample surface.
173 Analyses were performed using a Labram Evolution (Horiba Scientific, Japan) at the Dipartimento
174 di Scienze dell'Ambiente e della Terra, Università Milano Bicocca. The polarized Raman spectra
175 were excited using a green Ar-ion laser operating at 532 nm, with 50-70 mW emission power. Spectra
176 acquisition was performed with a backscattered geometry and a 600 g/mm diffraction grating. A
177 transmitted light Olympus B40 microscope with a 100 \times objective (Numerical aperture, N.A., = 0.90)
178 was used for all the acquisitions (spatial resolution $\leq 1\mu\text{m}$). Confocality was maintained with a
179 pinhole of 100 μm . Spectra were collected with variable acquisition times (from 20 to 30 sec). The
180 spectrometer was calibrated using a Silicon standard. To increase band attribution accuracy better
181 than 0.2 cm^{-1} , spectra were baseline corrected and processed by statistical analysis (Fityk software;
182 Wojdyr, 2010) using a Voigt Pseudo-function, a convolution of a Lorentzian with a Gaussian line
183 shape. Mineral and fluid identification has been based on our reference spectra database (Frezzotti et
184 al., 2012a).

185 Noble gas and CO_2 isotopic determinations were performed at the noble gas and stable isotopes
186 laboratories of INGV, Sezione di Palermo, following the preparation methods and analytical
187 procedures described in Gennaro et al. (2017), Rizzo et al. (2018) and Faccini et al. (2020). All
188 xenoliths were crushed and sieved with the aim of hand-picking crystals with diameters $>0.5\text{ mm}$.
189 Thirty-five aliquots (13 Ol, 11 Opx and 13 Cpx) of crystals (weights of 0.05 to 2 g) were selected for
190 noble gas isotopic analysis. Before analysis, samples were cleaned ultrasonically in 6.5% HNO_3 (for
191 CO_2 analysis samples were cleaned in HCl), deionized water and high-purity acetone. After drying,
192 samples were accurately weighed and loaded into an ultra-high-vacuum (UHV) crusher for noble gas
193 analyses that was pumped and backed for 48h at 120°C . As soon as the ultra-high-vacuum was
194 reached, fluid inclusions were released by single-step crushing at about 200 bar and room
195 temperature (21°C). Single step technique was used to minimize the addition of secondary helium
196 (cosmogenic ^3He and radiogenic ^4He) accumulated in the crystal lattice (Kurz, 1986; Graham, 2002,
197 Rizzo et al., 2018; Correale et al., 2019); this is supported by the homogeneity of the dataset (more
198 details about the effect of secondary helium in our samples are provided in supplementary material).
199 The moles of CO_2 were quantified by measuring the total pressure of gas (generally
200 $\text{CO}_2+\text{N}_2+\text{O}_2+\text{noble gases}$) released during crushing (by an IONIVAC Transmitters ITR90) in a
201 known volume of the system, then subtracting the residual pressure of $\text{N}_2+\text{O}_2+\text{noble gases}$ after
202 removing CO_2 in a "cold finger" immersed in liquid nitrogen. For noble gas analysis, the residual
203 gas mixture was purified under Zr-Al getter pumps in a UHV stainless-steel preparation line. After
204 then, Ar (and Kr and Xe) was removed in a "cold finger" with active charcoal immersed in liquid
205 nitrogen. Finally, He and Ne were adsorbed in a cold head with active charcoal cooled at 10K and
206 then moved at 40 and 80K in order to release first He and then Ne, respectively. He and Ne isotopes
207 were analyzed using two different split-flight-tube mass spectrometers (Helix SFT-Thermo), while
208 Ar isotopes were analyzed by a multi-collector mass spectrometer (Argus, GVI). The measured

209 $^3\text{He}/^4\text{He}$ ratios are expressed as R/R_a (where R is the ratio of the sample and R_a the He isotopic ratio
210 of air = 1.39×10^{-6}); this ratio was corrected for atmospheric contamination based on the measured
211 $^4\text{He}/^{20}\text{Ne}$ ratio and the values are expressed as R_c/R_a (eq.1):

$$212 \quad R_c/R_a = ((R_M/R_a)(\text{He/Ne})_M - (\text{He/Ne})_A)/((\text{He/Ne})_M - (\text{He/Ne})_A) \quad \text{eq.1}$$

213 where R_M/R_a and $(\text{He/Ne})_M$ are the measured values and $(\text{He/Ne})_A$ refers to the atmospheric
214 theoretical value (0.318). ^{40}Ar values were also corrected for atmospheric contamination:

$$215 \quad ^{40}\text{Ar}^* = ^{40}\text{Ar}_{\text{sample}} - (^{36}\text{Ar}_{\text{sample}} \cdot (^{40}\text{Ar}/^{36}\text{Ar})_{\text{air}}) \quad \text{eq.2}$$

216 where $^{40}\text{Ar}^*$ is the corrected ^{40}Ar , $^{40}\text{Ar}/^{36}\text{Ar}_{\text{air}} = 295.5$ and $^{21}\text{Ne}/^{22}\text{Ne}_{\text{air}} = 0.029$ (Steiger and Jäger,
217 1977; Ozima and Podosek, 2002). Values of ^{20}Ne , ^{21}Ne , ^{22}Ne , ^{36}Ar , and ^{38}Ar are also reported.
218 Analytical uncertainties (1σ) for $^3\text{He}/^4\text{He}$, $^{20}\text{Ne}/^{22}\text{Ne}$, $^{21}\text{Ne}/^{22}\text{Ne}$, $^{40}\text{Ar}/^{36}\text{Ar}$, and $^{38}\text{Ar}/^{36}\text{Ar}$ ratios are
219 $<2.7\%$, $<6.3\%$, $<7.5\%$, $<2.0\%$, and $<1.7\%$, respectively. The $^{20}\text{Ne}/^{22}\text{Ne}$ and $^{21}\text{Ne}/^{22}\text{Ne}$ ratios are
220 corrected for isobaric interferences at m/z values of 20 ($^{40}\text{Ar}^{2+}$) and 22 ($^{44}\text{CO}_2^{+2}$) (Rizzo et al., 2018;
221 Faccini et al., 2020).

222 Based on the results of the initial CO_2 measurements, twelve aliquots with the highest concentrations
223 were selected for isotopic CO_2 analysis. After crushing, the gas released was cleaned using a
224 purification line composed by two cryogenic traps and by a 626B Baratron® Absolute Capacitance
225 Manometer MKS (measuring range 10^{-3} –10 mbar) to remove H_2O and any atmospheric component,
226 and to quantify the gas released (Gennaro et al., 2017; Rizzo et al., 2018). The purified CO_2 was
227 condensed in a glass sampler (adjusted to atmospheric pressure by adding pure helium), and this was
228 transferred to the mass spectrometer. The $^{13}\text{C}/^{12}\text{C}$ isotope ratio was determined using a Thermo
229 (Finnigan) Delta Plus XP CF-IRMS connected to a Trace GC gas chromatograph and a Thermo
230 (Finnigan) GC/C III interface. The $^{13}\text{C}/^{12}\text{C}$ is expressed using the delta notation ($\delta^{13}\text{C}$) in per mil (‰)
231 relative to the V-PDB international standard.

232

233 **5. RESULTS**

234 **5.1 Petrography**

235 The suite of xenoliths exhibits the same mineralogy: $\text{Ol} > \text{Opx} > \text{Cpx} \gg \text{Sp}$. All samples are
236 plagioclase-free and are classified as spinel lherzolites and harzburgites (Figure 2). Peridotites show
237 protogranular to porphyroclastic textures, in which two generations of Ol, Opx and Cpx crystals are
238 observed (Figure 3): the first generation corresponds to large, elongated and deformed crystals of
239 sizes greater than 3 mm (porphyroclasts); the second generation corresponds to smaller crystals with
240 polygonal shapes (neoblasts $\leq 3\text{mm}$), which occur in the rock as a consequence of an intense
241 recrystallization process.

242 Olivines are present as translucent crystals without alteration. Ol porphyroclasts exhibit anhedral
243 forms (size <4.5 mm) with curved grain boundaries, kink bands and numerous fractures due to
244 deformation (Figure 3A); some crystals have Opx and Cpx inclusions ($<1\text{mm}$) with rounded shapes.
245 Most of the neoblasts are less than 2 mm long and are characterized by straight borders and subhedral
246 forms. Orthopyroxenes exhibit light brown colours without alteration; opx porphyroclasts are
247 characterized by anhedral and elongated forms with curved grain boundaries and diameters ≤ 4.5 mm

248 (Figure 3B, 3C and 3D). Neoblasts exhibit euhedral forms with well-developed straight boundaries
249 and sizes less than 2 mm; Opx tends to concentrate forming clusters of three or more crystals, where
250 vermicular spinel is commonly observed (Figure 3E and 3F); some Opx may contain small Cpx
251 inclusions (<0.2mm). Opx may exhibit a rough areas (especially over the rims) that resembles spongy
252 rims, which may expand over the entire crystal (Figure 3B, 3C and 3F). Cpx crystals are light green,
253 with subhedral to anhedral forms, sizes ≤ 2 mm (rare crystals with diameters greater than 4 mm are
254 present). Spongy textures along crystal rims in Cpx are very common and varies in thickness, this
255 texture sometimes develops as bands or affecting the entire crystal surface (Figure 3C and 3G).
256 Finally, spinel occurs as dark brown crystals with irregular shapes (anhedral forms with curved grain
257 borders), sizes ≤ 2 mm and develop as vermicular intergrowths in pyroxene clusters (Figure 3E and
258 3F).

259 Peridotites cut by glass veins that develop along the crystal borders, extending into single crystals as
260 micro-fractures. Veins have variable thicknesses, the largest being 0.3 mm thick (Figure 3D, 3F and
261 3H). Veins do not show a genetic relation with the host lava and are mainly formed by glass and may
262 contain relatively large (≤ 0.25 mm) crystals of Cpx, tiny crystals with high birefringence, identified
263 as carbonates; and rare opaque minerals.

264

265 **5.2 Fluid and melt inclusions**

266 Olivine crystals contain abundant dendritic trails of secondary inclusions consisting of glass, mineral
267 phases, and a fluid phase. Dendritic inclusion trails are intragranular and typically originate from the
268 glass/carbonate microveins permeating the rocks (Figure 4A). Figure 4 shows this peculiar texture
269 resulting from the association of large (15-30 μm) irregularly-shaped inclusions containing silicate
270 glass (melt) with subordinate crystals and a fluid phase in variable proportions, along with smaller
271 (<20 μm) inclusions dominated by glass (melt) or fluid, \pm crystals. Similar inclusion textures are
272 also observed in orthopyroxene and clinopyroxene, while fluid inclusions in the absence of glass,
273 generally observed in peridotites (Andersen and Neumann, 2001; Frezzotti and Touret, 2014), are
274 extremely rare. In inclusions, the silicate glass is colorless, isotropic, and does not show any
275 devitrification (Figure 4B). Mineral phases (< 30 μm) are high birefringent and texturally associated
276 with the glass (Figure 4C). The fluid is CO₂-rich, one or two phases (L, or L+V). Fluid-dominated
277 inclusions may contain tiny mineral grains, among which there is an opaque phase (Figure 4D).

278

279 **5.3 Raman microspectroscopy**

280 Raman microspectroscopy analyses of dendritic inclusions reveal that mineral phases texturally
281 associated with silicate glass are Mg-calcite (Figure 5A; vibrations at 1088, 714, 284, 158 cm^{-1}). The
282 fluid is pure CO₂ (Figure 5B; Fermi doublet at about 1282 -1387 cm^{-1}). Interestingly, in most CO₂
283 inclusions, Raman spectra also reveal the presence of dolomite (Figure 5C; vibrations at 1094-1096,
284 722-723, 299-300 cm^{-1}). Dolomite vibrations, however, are unexpectedly weak (likely linked to
285 disorder; Frezzotti et al., 2012a) and broad (full width at half maximum up to 15 cm^{-1}) (Figure 5C).
286 Also, the main vibration at 1098 cm^{-1} is downshifted from 2 to 4 cm^{-1} . These spectral characteristics
287 indicate a relevant order decrease in the crystalline structure as it occurs in decomposing carbonates
288 (Frezzotti and Peccerillo, 2007; Carteret et al., 2009; Frezzotti et al., 2012a).

289 The tiny mineral grains observed in a few CO₂ inclusions are magnesite (Figure 5D; vibrations at
290 1094, 723, 322, 202 cm⁻¹). An opaque mineral has been identified as pyrite (Figure 5D; vibrations at
291 342 and 377 cm⁻¹). The association of Mg-carbonate ± pyrite in CO₂-rich inclusions is suggestive of
292 fluid inclusion-host olivine reactions at low temperatures (Frezzotti et al., 2012b), probably during
293 host lava cooling at the surface.

294

295 **5.4 Elemental and Isotopic composition**

296 The elemental and isotopic composition of the crystal-hosted fluid inclusions in the JH mantle
297 xenoliths are reported in Table 2; reported errors are 1σ uncertainties, except for ²¹Ne/²²Ne_{ext} ratios
298 whose errors are 2σ uncertainties. ⁴He concentrations range between 8.56 x 10⁻¹⁴ and 1.29 x 10⁻¹¹
299 mol/g where the highest concentrations are observed in Cpx (~4.28 x 10⁻¹² mol/g) followed by Ol
300 (~2.21 x 10⁻¹² mol/g) and Opx (~2.06 x 10⁻¹² mol/g). ⁴He concentrations for the V-I crystals are
301 significantly lower than those measured in other nodules. ⁴⁰Ar* content ranges from 5.37 x 10⁻¹⁴ to
302 1.08 x 10⁻¹¹ mol/g; in general, both ⁴⁰Ar* and ⁴He values are similar to those previously reported in
303 mantle xenoliths from the European Subcontinental Lithospheric Mantle (European SCLM), the
304 West Antarctic Rift System (WARS), the Eastern Australia SCLM and some regions belonging to the
305 East African Rift (Northern/Southern Kenya rifts and the Ethiopia-Afar region; Figure 6A;
306 Matsumoto et al., 1998, 2000; Hopp et al., 2004, 2007a, 2007b; Buikin et al., 2005; Gautheron et al.,
307 2005a; Czuppon et al., 2009; Martelli et al., 2011; Halldórsson et al., 2014; Broadley et al., 2016;
308 Rizzo et al., 2018; Correale et al., 2019; Faccini et al., 2020). ²⁰Ne, ²¹Ne and ²²Ne values tend to be
309 high in Cpx and Opx; ²⁰Ne ranges from 1.42 x 10⁻¹⁶ to 5.08 x 10⁻¹⁴ mol/g, ²¹Ne from 5.22 x 10⁻¹⁹ to
310 1.21 x 10⁻¹⁶ mol/g and ²²Ne from 1.34 x 10⁻¹⁷ to 4.90 x 10⁻¹⁵ mol/g. CO₂ is the most abundant gas, on
311 average its contents are higher in Cpx and Opx (1.02 x 10⁻⁷ and 3.18 x 10⁻⁸ mol/g, respectively) than
312 in Ol (3.43 x 10⁻⁹ mol/g); CO₂ contents are positively correlated with ⁴He, ⁴⁰Ar*, ²⁰Ne, ²¹Ne and
313 ²²Ne, but are lower than those observed in European SCLM xenoliths (Figure 6B and 6C).

314 In detail, the Rc/Ra values vary as follows: Ol from 7.13 to 7.68 Ra, Opx from 6.15 to 7.54 Ra, and
315 Cpx from 5.40 to 7.59 Ra. The ⁴He/⁴⁰Ar* ratios vary between 0.14 and 3.11 (Figure 8), which
316 overlaps in part the typical production ratio of the mantle (⁴He/⁴⁰Ar* = 1 – 5; Yamamoto et al., 2009;
317 Marty, 2012); on average the highest values belong to Ol crystals (1.51 ± 0.76), compared to Opx
318 (0.72 ± 0.25) and Cpx (0.78 ± 0.40). ⁴He/²⁰Ne values range from 2.4 to 10483; the highest values are
319 recorded in Cpx and Ol (on average 2223.2 ± 3196.8 and 1498.6 ± 1306.1, respectively), while Opx
320 exhibits considerably lower ratios (<639). This tendency is also observed for ⁴⁰Ar/³⁶Ar ratios that
321 vary from 303 to 8231 in Cpx, from 392 to 2518 in Ol, and from 340 to 1436 in Opx. It should be
322 noted that those samples with the lowest values of Rc/Ra, also are depleted in ⁴He/Ar*, ⁴⁰Ar/³⁶Ar and
323 ⁴He/²⁰Ne. On average ²⁰Ne/²²Ne and ²¹Ne/²²Ne ratios are 10.2 ± 0.50 and 0.0332 ± 0.0058,
324 respectively; in both cases, the values are slightly higher in Cpx compared to Ol and Opx. Finally,
325 the isotope composition of CO₂ expressed as δ¹³C values (V-PDB) varies between -0.97 and -2.86‰
326 and does not exhibit a systematic variation between Ol, Opx and Cpx. The most negative value (-
327 2.86‰) was reported in IV-A Opx while the most positive values belong to two aliquots of the same
328 nodule: V-K Ol (-1.10) and V-K Opx (-0.97).

329

330

331 6. Discussion

332 Present textural and Raman spectroscopy observations indicate that the JH fluid inclusions are CO₂-
333 dominated (Figure 5) and, even more importantly, that they are strictly associated with the pervasive
334 infiltration of glass veins (Figures 3, 4). The inclusions typically exhibit the coexistence of glass,
335 mineral phases, and a fluid phase, and form dendritic trails of fluid inclusions originating from the
336 glass/carbonate microveins permeating the rocks (Figure 4A). The close association between glass
337 and fluid inclusions, and their originating from the glass microveins, are strongly suggestive of
338 trapping of fluids delivered by degassing of a carbonate-rich silicate melt at mantle depth. Textural
339 observations and preliminary compositional information (indicating that glass veins contain 59±3 wt
340 % SiO₂) clearly exclude that the glass veins are related to the basanitic to basaltic host magma.

341 In view of the above, and in line with previous work (Liang and Elthon, 1990; Luhr and Aranda-
342 Gómez, 1997), we relate the fluid inclusions trapped in JH xenoliths to a melt-related metasomatic
343 event deep in the source mantle. The overprinted textures in Cpx along crystal rims (named as spongy
344 rims by Luhr and Aranda-Gómez, 1997) (see Figure 3) have also been associated to this metasomatic
345 event (Liang and Elthon, 1990).

346 In the discussion below, we combined the above petrographic evidence and the isotopic signatures
347 (noble gases and CO₂) of the JH fluid inclusions to constrain volatile origin and mantle
348 characteristics. However, an initial screening of the dataset was necessary to filter out samples that
349 have suffered from secondary processes affecting fluid inclusion compositions (see Supplementary
350 information). The filtered dataset is used below to infer volatile sources and processes deep in the
351 mantle.

352

353 6.1 Inferences on the noble gas signature of the JH source mantle

354 6.1.1 Interaction with atmospheric fluids and evidence for a recycled atmospheric component

355 In order to correctly interpret the noble gas data obtained in fluid inclusions from the JH mantle
356 xenoliths, it is necessary to evaluate the interaction with atmospheric fluids. It is well known that Ar
357 and Ne are more susceptible (relative to He) to contamination, due to their higher abundances in
358 atmosphere relative to the mantle fluids. For this reason, tracers such as ⁴⁰Ar and ³⁶Ar, ⁴He/²⁰Ne,
359 ²⁰Ne/²²Ne, ²¹Ne/²²Ne, and ⁴⁰Ar/³⁶Ar are normally used to investigate the isotopic contribution from
360 the atmosphere (Matsumoto et al., 2001; Gurenko et al., 2006; Hopp et al., 2004, 2007a, 2007b;
361 Nuccio et al., 2008; Martelli et al., 2014; Oppenheimer et al., 2014; Rizzo et al., 2018).

362 He, Ne and Ar systematics suggest the existence of an atmospheric component in our samples
363 (especially in nodule V-I). In general, the measured R/Ra and ⁴He/²⁰Ne values fall along an air-
364 MORB mixing curve, and overlap with those measured in mantle xenoliths from the European
365 SCLM, the West Antarctic Rift System (WARS), Eastern Australia, Red sea region and N/S Kenya
366 rifts (Figure 7A). The existence of such an atmospheric component is corroborated by ⁴⁰Ar/³⁶Ar and
367 ²⁰Ne/²²Ne ratios significantly below the expected MORB values (44,000 and 12.5, respectively;
368 Burnard, 1997; Moreira, 1998; Sarda, 2004). As shown in Figure 7B, ⁴⁰Ar/³⁶Ar and ³He/³⁶Ar values
369 also fall along a two-component mixing between a MORB-like upper mantle and atmosphere
370 (He/Ar* ratios of 0.14 to 3.5 explain the whole data variability; see also Figure 9B). Likewise,
371 samples fit the binary mixing air-MORB when using the three-isotope neon plot (Figure 7C),
372 confirming the existence of atmospheric fluids in our inclusions. The atmospheric component is

373 especially notable in nodule V-I that exhibits an isotopic signature close to that of air with $^4\text{He}/^{20}\text{Ne}$
374 ratios below 10 (for Opx and Cpx) and $^{40}\text{Ar}/^{36}\text{Ar}$ values below 392. These compositions confirm that
375 this nodule likely suffered secondary processes that modified its pristine mantle signature. This
376 sample is therefore not considered representative of the local SCLM (and omitted from the following
377 discussion).

378 The atmospheric component identified in the fluid inclusions may derive from two main possible
379 processes, as summarized by Nuccio et al. (2008), Martelli et al. (2011), Correale et al. (2012), Rizzo
380 et al. (2018), and Faccini et al. (2020): a) air entrapment in crystal fractures during or after eruption
381 of transporting lava, and b) the interaction with subducted atmospheric fluids recycled in the upper
382 mantle.

383 Although air entrapment in crystals microcracks cannot be totally discarded due to surface exposure
384 of the xenoliths over the last 300 ky, the positive relation between ^3He and ^{36}Ar suggests a deep origin
385 (Figure 9A), i.e., a recycled atmospheric component in the lithospheric mantle likely inherited from
386 subduction (Matsumoto et al., 2001). In view of the above, and with the aim of constraining the
387 $^{40}\text{Ar}/^{36}\text{Ar}$ signature expected for the local mantle, we also evaluate the relationship between $^{20}\text{Ne}/^{22}\text{Ne}$
388 and $^{40}\text{Ar}/^{36}\text{Ar}$ ratios (Figure 9B), using the approach used by Langmuir et al. (1978) and Hopp et al.
389 (2007a). Considering an upper mantle $^{20}\text{Ne}/^{22}\text{Ne}$ equal to 12.5 (Sarda et al., 1988; Moreira et al.,
390 1998), $^{36}\text{Ar}/^{22}\text{Ne}$ ratios between 4.21 and 93.5, a maximum $^4\text{He}/^{20}\text{Ne}$ ratio of 11,000 and $^4\text{He}/^{40}\text{Ar}^*$
391 ratios between 0.14 and 3.11 (as observed in our samples; see Figures 7A and 8), we calculate a
392 $^{40}\text{Ar}/^{36}\text{Ar}$ signature of about 10,500 for the local upper mantle (see Figure 9B and Table 3). Assuming
393 a MORB-like $^{40}\text{Ar}/^{36}\text{Ar}$ signature of the pristine upper mantle (~44,000; Moreira et al., 1998), these
394 calculations further support the existence of an atmospheric component in the Mexican lithospheric
395 mantle, likely recycled during subduction events. Similar indications were observed in SCLM
396 xenoliths from European localities, West Antarctic Rift System (WARS), Eastern Australia, Red sea
397 region, N/S Kenya rifts and Ethiopia (Afar) (Matsumoto et al., 1998, 2000; Hopp et al., 2004, 2007a,
398 2007b; Buikin et al., 2005; Gautheron et al., 2005a; Czuppon et al., 2009; Martelli et al., 2011;
399 Halldórsson et al., 2014; Broadley et al., 2016; Rizzo et al., 2018; Correale et al., 2019; Faccini et
400 al., 2020).

401 Petrological evidence also highlights the interaction of the local upper mantle with metasomatic
402 fluids possibly coming from the subducted oceanic crust (Pier et al., 1989; Luhr and Aranda-Gómez,
403 1997; Dávalos-Elizondo et al., 2016). Even though the present-day plate geometry in central and
404 southern Mexico implies that the oceanic crust subduction terminates beneath the TMVB (Figure 1;
405 Pardo and Suárez, 1995; Ferrari et al., 2012) i.e. 200 km south JH, subduction of the Farallon plate
406 beneath the western part of North America during the Mesozoic and Paleogene could have potentially
407 modified the Mexican lithospheric mantle directly below la Mesa Central (Pier et al., 1989; Bunge
408 and Grand, 2000). Therefore, we consider realistic that the presence of an atmospheric component in
409 fluid inclusions from JH is mostly attributable to a local SCLM feature.

410

411 *6.1.2 Noble gas signature of the JH mantle source.*

412 Ne isotopes can additionally be used, in combination with He isotopes, to resolve any potential
413 influence of a mantle plume on the isotopic signature of the JH mantle xenoliths. To this aim, the
414 relationship between the extrapolated neon isotope ratio (i.e. the air-free mantle $^{21}\text{Ne}/^{22}\text{Ne}$ ratio

415 expressed as $^{21}\text{Ne}/^{22}\text{Ne}_{\text{EX}}$ and the $^3\text{He}/^4\text{He}$ values was evaluated (e.g., Hopp et al., 2004, 2007b;
416 Halldórsson et al., 2014). The $^{21}\text{Ne}/^{22}\text{Ne}_{\text{EX}}$ values were calculated by extrapolating the measured
417 $^{21}\text{Ne}/^{22}\text{Ne}$ ratios to Neon-B ($^{20}\text{Ne}/^{22}\text{Ne}=12.5$) using the methodology proposed by Graham (2002)
418 and Halldórsson et al. (2014). Only those samples with $^{40}\text{Ar}/^{36}\text{Ar}$ ratios > 500 and $^{20}\text{Ne}/^{22}\text{Ne}$ ratios
419 distinguishable from air were selected. For comparison, the same calculation was made using the Ne
420 isotopes previously reported for the European SCLM (Buikin et al., 2005; Gautheron et al., 2005a;
421 Martelli et al., 2011; Rizzo et al., 2018; Faccini et al., 2020), the WARS (Broadley et al., 2016;
422 Correale et al., 2019), Eastern Australia SCLM (Matsumoto et al., 1998, 2000), Red sea region (Hopp
423 et al., 2004; Halldórsson et al., 2014), Ethiopia (Afar) region (Halldórsson et al., 2014) and N/S
424 Kenya rifts (Hopp et al., 2007b; Halldórsson et al., 2014); as a result, the graph reported in the Figure
425 10A was obtained.

426 As evidenced in Figure 10A, samples V-K/VF Ol, VF Opx and V-E/V-H Cpx exhibit $(^{21}\text{Ne}/^{22}\text{Ne})_{\text{EX}}$
427 and $^4\text{He}/^3\text{He}$ ratios close to the theoretical value for a MORB-like upper mantle (as observed for some
428 mantle xenoliths from the Easter Australia SCLM and the Red sea region), the remaining values fall
429 along the MORB-Plume mixing line. When comparing our samples with other portions of SCLM on
430 Earth, we notice that JH nodules have similar $(^{21}\text{Ne}/^{22}\text{Ne})_{\text{EX}}$ but lower $^4\text{He}/^3\text{He}$ values, confirming
431 the presence of a dominating MORB component. Instead, the Ethiopian xenoliths more clearly
432 exhibit both $(^{21}\text{Ne}/^{22}\text{Ne})_{\text{EX}}$ and $^4\text{He}/^3\text{He}$ ratios close to the Plume endmember.

433 In the case of JH mantle xenoliths, $(^{21}\text{Ne}/^{22}\text{Ne})_{\text{EX}}$ ratios <0.05 would suggest a deep-mantle
434 contribution of Neon ($<10\%$). However, it must be taken into account that the samples less
435 contaminated by the atmospheric component fall within the AIR-MORB line when considering their
436 error bars (Figure 7C). In addition, the $^3\text{He}/^4\text{He}$ ratios reflect a homogeneous MORB-like signature.
437 Based on these evidences, we conclude that the upper mantle beneath JH is predominantly MORB-
438 like with a minimum contamination by a recycled crustal component, although we cannot totally
439 discard a deep-mantle contribution. This conclusion support the idea that the VESVF originates from
440 extension and melting of the lithospheric mantle under the Mesa Central province.

441 As discussed above, the relative invariance of the Rc/Ra values suggests that the upper mantle under
442 this portion of La Mesa Central is relatively homogeneous in terms of noble gases ($\text{Rc}/\text{Ra} = 7.39 \pm$
443 0.14 ; Figure 10B - D). This $^3\text{He}/^4\text{He}$ signature is similar to that measured at the WARS ($7.5 \pm 0.5 \text{ Ra}$
444 and $7.1 \pm 0.4 \text{ Ra}$; Broadley et al., 2016; Correale et al., 2019) and at the upper range of that inferred
445 at the N/S Kenya rifts and Red Sea region ($6.6 \pm 0.7 \text{ Ra}$ and $7.0 \pm 0.9 \text{ Ra}$, respectively; Hopp et al.,
446 2004, 2007b; Halldórsson et al., 2014), but manifestly less radiogenic than the European SCLM (6.1
447 ± 0.9 ; Gautheron and Moreira, 2002; Buikin et al., 2005; Gautheron et al., 2005a; Martelli et al.,
448 2011; Rizzo et al., 2018; Faccini et al., 2020).

449 The MORB-type $^3\text{He}/^4\text{He}$ signature at JH deserves some consideration in relation to the past
450 geodynamic history of the area. We envisage two possible scenarios.

451 In scenario 1, the relatively homogeneous (MORB-like) $^3\text{He}/^4\text{He}$ ratios for the JH mantle xenoliths
452 might be taken as indicative of a low-to-negligible recycling of crustal materials during the
453 subduction of Farallon plate (20-40 Ma). A limited input of U-Th-bearing crustal materials would in
454 fact explain well the low contribution of radiogenic ^4He in the local mantle. If this interpretation is
455 correct, then past subduction events would only have added a recycled atmospheric component into
456 the mantle (cfr 6.1.1). Alternatively, one may consider a scenario (scenario 2) in which any addition
457 of (subduction-related) materials during subduction of the Farallon plate was later (during the <20

458 Ma Basin and Range extensional phase) overprinted by an influx of MORB-like materials, rising
459 from deeper (asthenospheric to deep SCL) mantle domains. This latter scenario is supported by the
460 geodynamic reconstructions that indicate a metasomatism/refertilization of the lithospheric mantle
461 during the Basin and Range extensional phase. Paleo-subduction reconstructions indicate that the
462 Farallon plate subducted horizontally underneath Western North-America and Northern-Central
463 Mexico between 74 - 40Ma, producing the Laramide orogeny in the United States and the mountain
464 range known as the Sierra Madre Oriental (SMOr) east of the JH (Figure 1; Atwater, 1989; Cserna,
465 1989; Severinghaus and Atwater, 1990; Bunge and Grand, 2000; Eguiluz de Antuñano et al., 2000;
466 Lee, 2005). This tectonic configuration would have changed at ~40-20Ma, however, when the retreat
467 of the Farallon slab occurred, a commonly invoked cause for initiation of the Basin and Range
468 extension (Leeman and Harry, 1993; Nieto-Samaniego et al., 1999, 2005; Lee, 2005; Sedlock, 2003).
469 According to Nieto-Samaniego et al. (1999), retreating of the oceanic slab favored the influx of
470 younger and hotter asthenospheric material that ultimately led to melt generation and extension at
471 the base of the Mesa Central. Evidence of this process comes from the intense normal faulting in the
472 Mesa Central registered 30Ma, 23-24Ma 12-13Ma ago, and from the transition from calc-alkaline
473 volcanism (in the so-called Sierra Madre Occidental; SMO; Figure 1) to intraplate alkaline volcanism
474 (Henry and Aranda-Gomez, 1992; Nieto-Samaniego et al., 1999; Aranda Gómez et al., 2000).
475 Injection of ³He-rich (MORB-like) asthenospheric melts during the mid-Cenozoic could well have
476 caused re-fertilization/re-juvenation of the Mexican lithospheric mantle in a model similar to that
477 proposed for the lithospheric mantle beneath the Yangtze craton and the WARS (Correale et al.,
478 2016, 2019; Faccini et al., 2020). This scenario is possible if we assume that almost all ³He comes
479 from asthenospheric melts, as proposed by Gautheron and Moreira (2002) and Gautheron et al.
480 (2005a) to explain the noble gases systematics of the European SCLM (a steady-state model).

481 Irrespective of subduction is considered to have (scenario 2) or have not (scenario 1) impacted the
482 He mantle budget, there is unquestionable petrographic evidence (this study; Liang and Elthon, 1990;
483 Luhr and Aranda-Gómez, 1997) for a melt-related metasomatic event affecting the JH, potentially
484 during Basin and Range extensional phase (Nieto-Samaniego et al., 1999).

485

486 **6.2 ³He fluxes, ⁴He production and the helium residence time for the Mexican lithospheric** 487 **mantle**

488 The MORB-type He signature of JH xenoliths can quantitatively be interpreted in light of the SCLM
489 model of Gautheron and Moreira, (2002). According to the authors (see also (Griffin et al., 1999,
490 2009), the geochemical and isotopic characteristics of the SCLM are the ultimate result of any past
491 interaction with fluids and melts coming from (i) deeper mantle sources and/or (2) recycled slab
492 components that have alternated over geological time (Griffin et al., 1999). In terms of helium
493 isotopes, Gautheron and Moreira (2002) argued that the SCLM is globally homogeneous (6.1 ± 0.9
494 Ra). They based this inference on the study of suites of ultramafic xenoliths and alkali basalts
495 collected from different continental settings (Europe, USA, Antarctic, Australia, and West Africa).

496 In order to explain its helium isotopic homogeneity, Gautheron and Moreira (2002) proposed the
497 global lithospheric mantle is in steady state for helium. In their model, the global SCLM is
498 continuously metasomatized by melts and fluids with a MORB-like helium signature coming from
499 the asthenosphere (affecting the entire reservoir); eventually, this signature becomes more radiogenic
500 due to U and Th decay resulting in lower ³He/⁴He ratios (e.g. 6.1 ± 0.9 Ra). Thus, the steady-state

501 model is based on the balance between the He flux from the asthenosphere and the in-situ production
 502 in the lithosphere of radiogenic ⁴He. From this model, it is possible to estimate the helium residence
 503 time in the lithospheric mantle (Rt), the ³He flux (F) and the ⁴He production (P*). The model uses
 504 the dimensions of the SCLM (thickness, surface and density) assuming a constant U + Th
 505 concentration. These authors reported a Rt = ~200 Ma, F= 270 mol/yr and P* = 6.8x10⁶ mol/yr for
 506 the global SCLM, while Gautheron et al. (2005) obtained a Rt = 5-150 Ma, F= 3.5 x10⁴ at/m²/s (~ 1
 507 mol/yr) and P* ~ 3 x 10⁴ mol/yr for the European SCLM.

508 However, some studies on noble gas systematics (including our results) support a more fertile
 509 signature (³He/⁴He > 7.0 Ra) for some portions of the SCLM on Earth (e.g., Southern Australia and
 510 West Antarctic Rift; Matsumoto et al., 1998; Broadley et al., 2016; Correale et al., 2019). Therefore,
 511 we argue that the steady state model proposed by Gautheron and Moreira (2002) should be applied
 512 in local portions of SCLM to eventually detail their interactions with the asthenosphere. Using this
 513 steady-state model, and considering the ³He/⁴He signature of the JH mantle xenoliths, we estimated
 514 the helium residence time, the ³He flux and the ⁴He production for the lithospheric mantle located
 515 under the San Luis Potosí state (central Mexico):

$$516 \quad F = \frac{P^*}{\left(\frac{{}^4\text{He}}{{}^3\text{He}}\right)_{\text{SCLM}} - \left(\frac{{}^4\text{He}}{{}^3\text{He}}\right)_{\text{MORB}}} \quad \text{eq.3}$$

517 In eq. 3, F is the ³He flux (cc STP/yr) and P* is the ⁴He production (P*= 2.8 *10⁻¹⁴ * (4.35+Th/U) *
 518 U * M). U is the concentration of uranium in ppm and M is the mass of the subcontinental mantle.
 519 The helium residence time Rt is defined as:

$$520 \quad Rt = \frac{\text{Total } {}^3\text{He in the SCLM (cc STP)}}{F} \quad \text{eq.4}$$

521 The parameters used in the calculation are as follows: 1) the average of the ⁴He/³He ratios measured
 522 in JH mantle xenoliths equal to 97,500 (7.38 Ra) and a MORB endmember equal to 84,600 (8.5 Ra).
 523 The latter value is higher than that assumed by Gautheron and Moreira (2002) (8.0 Ra) because
 524 preliminary results for mantle xenoliths from other localities in central Mexico yield Rc/Ra values
 525 of ≤ 8.35 (unpublished data); 2) U contents between 0.01 and 0.03 ppm as previously reported for
 526 mantle xenoliths from central Mexico (Dávalos-Elizondo et al., 2016) and a Th/U = 3 as assumed by
 527 Gautheron and Moreira (2002); 3) A subcontinental mantle mass equal to 3.66x10²¹ g. This mass
 528 was estimated assuming a thickness of the local lithospheric mantle of ~150km (density of 3.3x10⁶
 529 g/m³; Gautheron and Moreira, 2002) and a surface of 7.4x10⁹ m² that includes all the Cenozoic
 530 intraplate monogenetic volcanic fields located in the San Luis Potosí state (VESVF, SDVF and Los
 531 Encinos volcanic field; see Figure 1; Aranda-Gómez et al., 2007); 5) A upper mantle ⁴He
 532 concentration equal to 1 x 10⁻⁶ ccSTP/g (4.5 x 10⁻¹¹ mol/g), which corresponds to the maximum value
 533 identified for continental mantle xenoliths (Gautheron and Moreira, 2002); this value is equivalent
 534 to a ³He concentration =1.0 x 10⁻¹¹ ccSTP/g (4.5 x 10⁻¹⁶ mol/g) assuming a Rc/Ra = 7.38; thus the
 535 total ³He estimated for the local SCLM is 1.64x10⁶ mol (3.66x10¹⁰ cc STP). The results obtained are
 536 reported in Table 4.

537 The calculated ³He fluxes for the Mexican lithospheric mantle vary from 0.027 to 0.080 mol/g
 538 (Figure 11A). These fluxes are very low if compared with the values reported for the global SCLM,
 539 the European SCLM or MORB values (800-1300 mol/g; Marty and Jambon, 1987; Javoy et al., 1989;
 540 Michael and Graham, 2015; Tucker et al., 2018). When scaled to the surface area (7.4x10⁹ m²) of
 541 volcanism in the San Luis Potosí state, our specific fluxes vary between 6.9 and 20.7 at/s/cm² (Figure

542 11B) which are well above the MORB and the global SCLM values (4.8 at/s/cm² and 3.5 at/s/cm²,
543 respectively; Craig et al., 1975; Gautheron and Moreira, 2002) confirming a high ³He contribution
544 from the asthenosphere under central Mexico.

545 The associated Rt values range from 20 to 60 Ma. These estimates are lower if compared to the global
546 SCLM and would explain the less radiogenic character of the Mexican lithospheric mantle. In this
547 model, the Rt values do not depend on the area but have a close relationship with the average of the
548 ³He/⁴He ratios measured in the mantle xenoliths. It is reasonable to think that the smaller the ³He/⁴He
549 ratio measured in the xenoliths (7.38 Ra for JH xenoliths and 6.1Ra for the SCLM), the longer the
550 helium residence time in the lithospheric mantle should be. Therefore, low Rt values implies low ⁴He
551 production and high ³He/⁴He ratios, as observed in JH mantle xenoliths. Moreover, our estimated Rt
552 range overlaps with the inferred age range for the retreating subduction of the Farallon slab (40-20
553 Ma ago) a processes, which may have triggered the injection of asthenospheric melts in the
554 lithospheric mantle and the generation of the Basin and Range province (Nieto-Samaniego et al.,
555 1999; Lee, 2005). If correct, our results would independently indicate that the last major geodynamic
556 modification in the lithospheric mantle underneath the JH occurred during the lower and mid-
557 Cenozoic. We argue that the refertilization event was able to increase the ³He/⁴He signature within
558 the MORB-like range, overprinting the pre-Cenozoic signature recorded by the Mexican lithospheric
559 mantle. Since then, the latter would have evolved in a similar way to that proposed by Gautheron and
560 Moreira (2002), i.e., in a steady state becoming slightly more radiogenic during the last ~20Ma down
561 to the measured ³He/⁴He values.

562 In conclusion, both the low production of ⁴He and the relative lower Rt (compared to other areas)
563 could explain the high ³He/⁴He ratios measured in JH mantle xenoliths. However, we caution these
564 are local estimates; therefore, in order to minimize the effect generated by the area and possible
565 mantle heterogeneities, future work will target obtaining isotopic data for mantle xenoliths from other
566 localities of the Basin and Range extension in Mexico. This will allow a more realistic reconstruction
567 of the evolution of the Mexican lithosphere in terms of noble gases.

568

569 *6.2.1 Mantle CO₂ fluxes*

570 We combine the ³He flux estimated above with the CO₂/³He ratios measured in the JH xenoliths (e.g.
571 Marty and Jambon, 1987; Tucker et al., 2018) to calculate the mantle-derived CO₂ fluxes in the area.
572 Taking U concentrations between 0.01 ppm and 0.03 ppm and a CO₂/³He_(avg) ~1.47 x 10⁹, the
573 calculated CO₂ fluxes range from 3.93 x 10⁷ mol/yr (1.02 x 10¹⁰ at/s/cm²) to 1.18 x 10⁸ mol/yr
574 (3.05x10¹⁰ at/s/cm²; Figure 11C-11D). Our estimated fluxes are lower than previously estimated for
575 other continental rift localities (such as the EAR), consistent with the small area of the San Luis
576 Potosí volcanic filed (considered in the model), and correspond to <0.1% of the MORB CO₂ fluxes;
577 similarly, our fluxes are lower than estimated for hot spot settings such as Hawaii or Canary Islands
578 (Hauri et al., 2019). Additional studies on noble gas and CO₂ isotopic data from other mantle
579 xenoliths locations in central and northwestern Mexico are required to further validate our results.

580

581

582 **6.3 Inferences on CO₂ origin.**

583 In JH peridotites, fluids are dominated by CO₂ (Figure 6), as typically recorded by other worldwide
584 mantle xenoliths (Andersen and Neumann, 2001; Deines, 2002; Frezzotti and Touret, 2014). Thus,
585 the CO₂ isotopic composition can be used to constrain carbon origin. Our samples exhibit δ¹³C ratios
586 between -0.97 and -2.86‰ (Figure 12A); they are therefore isotopically more positive (¹³C-rich)
587 than found in European mantle xenoliths in alkaline intra-plate and extensional contexts, such as in
588 the Hyblean plateau (southeast Sicily, Italy; ranging from -4 to -2‰; Correale et al., 2015) and Lower
589 Silesia (southwest Poland; ranging from -4.7 to -3.1‰; Rizzo et al., 2018).

590 The CO₂ isotopic composition in the JH peridotites is also well above the δ¹³C MORB mantle range
591 (-8‰ < δ¹³C < -4‰; Sano and Marty, 1995). When δ¹³C values are plotted against Rc/Ra and
592 CO₂/³He ratios (Figure 12B, 12C), our samples fall along a MORB-Limestone mixing line,
593 suggesting source mantle Carbon contamination by C-rich fluids with a crustal carbonate signature.

594 The crustal carbon component found in fluid inclusions of JH xenoliths may in principle derive from
595 two main distinct processes: (i) infiltration of CO₂ rich fluids derived by assimilation of carbonates
596 by host magmas during ascent through the continental crust, and (ii) mantle metasomatism by CO₂-
597 rich fluids and melts derived from subducted oceanic crust and sediments.

598 Infiltration of CO₂ fluids in mantle xenoliths outgassed during assimilation of carbonates in basanitic
599 magmas in the continental crust should be considered since JH maar formed on carbonate deposits
600 (the Valles-San Luis Potosí calcareous platform (PVSLP) and the Mesozoic Basin of central
601 Mexico). However, the relatively fast ascent rates of the host magma through the continental crust
602 (Luhr et al., 1989; Pier et al., 1989), and the lack of carbonate xenoliths in the host lava, argue against
603 a crustal component inherited during sin-eruptive magma ascent. Conversely, petrographic and
604 Raman evidence indicates pervasive infiltration of carbonate-bearing silicate melts and CO₂-fluids
605 in peridotites (Figure 4), strongly supporting deep carbon mobility during a metasomatic event in the
606 lithospheric mantle. We, therefore, conclude that the carbonate component identified in JH CO₂
607 fluids was trapped under mantle conditions and is related to CO₂ degassing of metasomatic
608 carbonate-rich silicate melts on reaction with mantle minerals. Metasomatic processes occurred well
609 before entrainment by the host magma and eruption (as proposed by Liang and Elthon, 1990).

610 As mentioned in the previous sections, northwestern Mexico's current tectonic configuration
611 indicates that the Cocos and Rivera plates do not directly affect the mantle under the Mesa Central,
612 making it difficult to consider involvement of present subduction (Figure 1). Moreover, some studies
613 suggest that the contribution of carbonate sediments from the subducting slab is minimal. The CO₂-
614 rich plume gases released by arc volcanoes (e.g., Popocatepetl) come from the assimilation of
615 limestone deposits, as evidenced by trace element analysis performed in mafic rocks and the presence
616 of carbonate xenoliths in volcanic deposits (Goff et al., 1998, 2001; Aiuppa et al., 2017). A low
617 contribution of subducted Carbon in fluids has also been proposed for other volcanic fields belonging
618 to the TMVB, such as the Sierra Chichinautzin Volcanic Field (SCVF; Verma, 2000) and the
619 Michoacan-Guanajuato Volcanic Field (MGVF; Verma and Hasenaka, 2004).

620 In contrast to present-day subduction being an unlikely driver, we emphasize a possible major role
621 played by older subduction of the Farallon underneath the northwestern margin of North America
622 during the Mesozoic and early Cenozoic (Atwater, 1989; Ferrari et al., 2012; Henry and Aranda-
623 Gomez, 1992; Sedlock, 2003). Several authors claim that the North American lithospheric mantle

624 could have been hydrated by fluids or melts released by flat subduction of the Farallon plate, as
625 evidenced by petrological studies of mantle xenoliths from the Sierra Nevada and the Colorado
626 Plateau (Smith et al., 1999; Lee, 2005; Li et al., 2008). “Farallon hydration” (Lee, 2005) is suggested
627 to have occurred during the late Cretaceous and early Cenozoic, and to have affected the lithospheric
628 mantle up to 800 km inboard of the trench (Li et al., 2008). This metasomatic event is also well
629 documented in Mexican xenoliths (Liang and Elthon, 1990; Dávalos-Elizondo et al., 2016; Levrèsse
630 et al., 2016). For example, Luhr and Aranda-Gómez (1997) interpreted the systematic east to west
631 oxygen fugacity increase in Cenozoic mantle xenoliths from central and northern Mexico as induced
632 by the progressive oxidation of the lithospheric mantle by fluids released by the Farallon oceanic
633 slab.

634 In light of the above, the interaction between subducted fluids delivered by the Farallon plate and the
635 Mexican lithospheric mantle could represent a feasible mechanism to explain the heavy $\delta^{13}\text{C}$
636 signatures of JH mantle fluids. We argue that the crustal carbon component identified in the fluid
637 inclusions would reflect a mantle feature induced by an old subduction-related carbonate component
638 inherited during the mid-Cenozoic before the Basin and Range extension (Middle Miocene; Henry
639 and Aranda-Gomez, 1992; Sedlock, 2003) and recycled in the local mantle.

640

641 7. CONCLUSIONS

642 We investigate the petrography and noble gas-CO₂ composition of fluid inclusions in ultramafic
643 mantle xenoliths collected from JH, in central Mexico. Peridotites are classified as spinel-lherzolites
644 and harzburgites. Petrographic observations and Raman microspectroscopy analyses of fluid and
645 melt inclusions reveal the coexistence of glass/carbonate microveins and a CO₂ fluid phase
646 permeating the rocks, suggesting interaction between peridotites and degassing carbonate-rich
647 silicate melts at mantle depth.

648 The $^4\text{He}/^{40}\text{Ar}^*$ range (0.14 - 3.11) partially overlaps that of fertile mantle (1-5), which could indicate
649 either a low degree of partial melting or the occurrence of a metasomatism/refertilization process by
650 melts degassing fluids ultimately entrapped in the mantle as secondary fluid inclusions.

651 Ne and Ar systematics reveal a mixing between atmospheric and MORB-like fluids, strongly
652 supporting the presence of an atmospheric component eventually recycled from the Farallon plate
653 subduction. Although, $(^{21}\text{Ne}/^{22}\text{Ne})_{\text{EX}}$ ratios suggest the existence of plume-derived Neon in our fluid
654 inclusions, JH mantle xenoliths exhibit homogeneous $^3\text{He}/^4\text{He}$ signature (7.39 ± 0.14 Ra) that is
655 comparable to that of the MORB-like mantle and similar to other worldwide SCLM localities (eg.,
656 Eastern Australia, N/S Kenya rifts and WARS). This isotopic signature results from a low recycling
657 of crustal components in the local mantle possibly overprinted by a metasomatism/refertilization
658 episode reasonably occurred after the retreat of the Farallon slab during the early and mid-Cenozoic.

659 Based on the “Steady-state” model proposed by Gautheron and Moreira (2002), we estimated a
660 helium residence time in the local SCLM between 20-60Ma, which overlaps the geodynamic
661 evolution of the area and the metasomatism/refertilization event. Since then, the lithospheric mantle
662 would have evolved in a steady state for helium (from a MORB signature ~ 8.5 Ra) becoming slightly
663 more radiogenic during the last ~ 20 Ma. We also calculated ^3He fluxes between 0.027 - 0.080 mol/g,

664 ⁴He production rates from 340 to 1000 mol/yr and mantle CO₂ fluxes from 3.93 x 10⁷ mol/yr to
665 1.18x10⁸ mol/yr represent less than the 0.1% of the MORB CO₂ fluxes.

666 The δ¹³C values measured in JH fluid inclusions reveal a binary mixing between a MORB-like upper
667 mantle and a crustal carbonate component (limestone). We propose that the crustal CO₂/carbonate
668 component identified in JH xenoliths was trapped under mantle conditions through metasomatic
669 reactions between peridotites and C-bearing silicate melts. These would have acted as carriers in the
670 local mantle of a recycled carbon component inherited from the Mesozoic to early Cenozoic Farallon
671 subduction.

672

673 **ACKNOWLEDGMENTS**

674 This work is part of the PhD (XXXIV cycle) of Andres Libardo Sandoval Velasquez at the University
675 of Palermo. This research was funded by the Italian Miur (Grant N. 2017LMNLAW) and from Deep
676 Carbon Observatory. We thank Mariagrazia Misseri and Mariano Tantillo for helping in sample
677 preparation and in the isotope analysis of noble gases carried out in the noble gas laboratory of INGV-
678 Palermo. We also thank Ygor Oliveri and Giorgio Capasso for their effort in the INGV-Palermo
679 stable-isotopes laboratory. Raman facilities were provided by DISAT at Università Milano Bicocca
680 within the frame of MIUR Progetti di Eccellenza 2018-2022. We are grateful to Dr. Jens Hopp and
681 Dr Michael Ward Broadley for their valuable comments that improved our manuscript.

682

683 **REFERENCES**

684

- 685 Aiuppa, A., Fischer, T.P., Plank, T., Robidoux, P., Di Napoli, R., 2017. Along-arc, inter-arc and arc-
686 to-arc variations in volcanic gas CO₂/ST ratios reveal dual source of carbon in arc volcanism.
687 *Earth-Science Reviews* 168, 24–47. <https://doi.org/10.1016/j.earscirev.2017.03.005>
- 688 Andersen, T., Neumann, E.-R., 2001. Fluid inclusions in mantle xenoliths. *Lithos* 55, 301–320.
689 [https://doi.org/10.1016/S0024-4937\(00\)00049-9](https://doi.org/10.1016/S0024-4937(00)00049-9)
- 690 Aranda-Gómez, J., Luhr, J.F., 1996. Origin of the Joya Honda maar, San Luis Potosí, México. *Journal*
691 *of Volcanology and Geothermal Research* 74, 1–18. [https://doi.org/10.1016/S0377-](https://doi.org/10.1016/S0377-0273(96)00044-3)
692 [0273\(96\)00044-3](https://doi.org/10.1016/S0377-0273(96)00044-3)
- 693 Aranda-Gómez, J.J., Henry, C.D., F. Luhr, J., 2000. Evolución tectonomagmática post-paleocénica
694 de la Sierra Madre Occidental y de la porción meridional de la provincia tectónica de
695 Cuencas y Sierras, México. *BSGM* 53, 59–71. <https://doi.org/10.18268/BSGM2000v53n1a3>
- 696 Aranda-Gómez, J.J., Luhr, J.F., Housh, T.B., Valdez-Moreno, G., Chávez-Cabello, G., 2007. Late
697 Cenozoic intraplate-type volcanism in central and northern México: A review, in: *Geology*
698 *of México: Celebrating the Centenary of the Geological Society of México*. Geological
699 Society of America. [https://doi.org/10.1130/2007.2422\(04\)](https://doi.org/10.1130/2007.2422(04))
- 700 Aranda-Gómez, J.J., Ortega-Gutiérrez, F., 1987. Mantle xenoliths in México, in: *Mantle Xenoliths*.
701 John Wiley, New York, pp. 75–84.
- 702 Atwater, T., 1989. Plate tectonic history of the northeast Pacific and western North America, in:
703 Winterer, E.L., Hussong, D.M., Decker, R.W. (Eds.), *The Eastern Pacific Ocean and Hawaii*.
704 Geological Society of America, North America, pp. 21–72. [https://doi.org/10.1130/DNAG-](https://doi.org/10.1130/DNAG-GNA-N.21)
705 [GNA-N.21](https://doi.org/10.1130/DNAG-GNA-N.21)
- 706 Barboza-Gudino, J.R., Tristán-González, M., Torres-Hernández, J.R., 1999. Tectonic setting of pre-
707 Oxfordian units from central and northeastern Mexico: A review, in: *Special Paper 340*:

708 Mesozoic Sedimentary and Tectonic History of North-Central Mexico. Geological Society
709 of America, pp. 197–210. <https://doi.org/10.1130/0-8137-2340-X.197>

710 Basu, A.R., 1977. Textures, microstructures and deformation of ultramafic xenoliths from San
711 Quintin, Baja California. *Tectonophysics* 43, 213–246. [https://doi.org/10.1016/0040-1951\(77\)90118-4](https://doi.org/10.1016/0040-1951(77)90118-4)

712

713 Boudoire, G., Rizzo, A.L., Arienzo, I., Di Muro, A., 2020. Paroxysmal eruptions tracked by
714 variations of helium isotopes: inferences from Piton de la Fournaise (La Réunion island). *Sci*
715 *Rep* 10, 9809. <https://doi.org/10.1038/s41598-020-66260-x>

716 Boudoire, G., Rizzo, A.L., Di Muro, A., Grassa, F., Liuzzo, M., 2018. Extensive CO₂ degassing in
717 the upper mantle beneath oceanic basaltic volcanoes: First insights from Piton de la
718 Fournaise volcano (La Réunion Island). *Geochimica et Cosmochimica Acta* 235, 376–401.
719 <https://doi.org/10.1016/j.gca.2018.06.004>

720 Broadley, M.W., Ballentine, C.J., Chavrit, D., Dallai, L., Burgess, R., 2016. Sedimentary halogens
721 and noble gases within Western Antarctic xenoliths: Implications of extensive volatile
722 recycling to the sub continental lithospheric mantle. *Geochimica et Cosmochimica Acta* 176,
723 139–156. <https://doi.org/10.1016/j.gca.2015.12.013>

724 Buikin, A., Trieloff, M., Hopp, J., Althaus, T., Korochantseva, E., Schwarz, W.H., Altherr, R., 2005.
725 Noble gas isotopes suggest deep mantle plume source of late Cenozoic mafic alkaline
726 volcanism in Europe. *Earth and Planetary Science Letters* 230, 143–162.
727 <https://doi.org/10.1016/j.epsl.2004.11.001>

728 Bunge, H.-P., Grand, S.P., 2000. Mesozoic plate-motion history below the northeast Pacific Ocean
729 from seismic images of the subducted Farallon slab. *Nature* 405, 337–340.
730 <https://doi.org/10.1038/35012586>

731 Burnard, P., 2004. Diffusive fractionation of noble gases and helium isotopes during mantle melting.
732 *Earth and Planetary Science Letters* 220, 287–295. [https://doi.org/10.1016/S0012-821X\(04\)00060-3](https://doi.org/10.1016/S0012-821X(04)00060-3)

733

734 Burnard, P., 1997. Vesicle-Specific Noble Gas Analyses of “Popping Rock”: Implications for
735 Primordial Noble Gases in Earth. *Science* 276, 568–571.
736 <https://doi.org/10.1126/science.276.5312.568>

737 Carrillo-Bravo, J., 1971. La plataforma de Valles-San Luis Potosí. *Boletín de la Asociación*
738 *Mexicana de Geólogos Petroleros*. *Boletín de la Asociación Mexicana de Geólogos*
739 *Petroleros* 23, 100.

740 Carteret, C., Dandeu, A., Moussaoui, S., Muhr, H., Humbert, B., Plasari, E., 2009. Polymorphism
741 Studied by Lattice Phonon Raman Spectroscopy and Statistical Mixture Analysis Method.
742 Application to Calcium Carbonate Polymorphs during Batch Crystallization. *Crystal Growth*
743 *& Design* 9, 807–812. <https://doi.org/10.1021/cg800368u>

744 Correale, A., Martelli, M., Paonita, A., Rizzo, A., Brusca, L., Scribano, V., 2012. New evidence of
745 mantle heterogeneity beneath the Hyblean Plateau (southeast Sicily, Italy) as inferred from
746 noble gases and geochemistry of ultramafic xenoliths. *Lithos* 132–133, 70–81.
747 <https://doi.org/10.1016/j.lithos.2011.11.007>

748 Correale, A., Paonita, A., Rizzo, A., Grassa, F., Martelli, M., 2015. The carbon-isotope signature of
749 ultramafic xenoliths from the Hyblean Plateau (southeast Sicily, Italy): Evidence of mantle
750 heterogeneity. *Geochem. Geophys. Geosyst.* 16, 600–611.
751 <https://doi.org/10.1002/2014GC005656>

752 Correale, A., Pelorosso, B., Rizzo, A.L., Coltorti, M., Italiano, F., Bonadiman, C., Giacomoni, P.P.,
753 2019. The nature of the West Antarctic Rift System as revealed by noble gases in mantle
754 minerals. *Chemical Geology* 524, 104–118. <https://doi.org/10.1016/j.chemgeo.2019.06.020>

755 Correale, A., Rizzo, A.L., Barry, P.H., Lu, J., Zheng, J., 2016. Refertilization of lithospheric mantle
756 beneath the Yangtze craton in south-east China: Evidence from noble gases geochemistry.
757 *Gondwana Research* 38, 289–303. <https://doi.org/10.1016/j.gr.2016.01.003>

758 Craig, H., Clarke, W.B., Beg, M.A., 1975. Excess ^3He in deep water on the East Pacific Rise. *Earth*
759 *and Planetary Science Letters* 26, 125–132. [https://doi.org/10.1016/0012-821X\(75\)90079-5](https://doi.org/10.1016/0012-821X(75)90079-5)

760 Cserna, Z. de, 1989. An outline of the geology of Mexico, in: Bally, A.W., Palmer, A.R. (Eds.), *The*
761 *Geology of North America—An Overview*. Geological Society of America, pp. 233–264.
762 <https://doi.org/10.1130/DNAG-GNA-A.233>

763 Czuppon, G., Matsumoto, T., Handler, M.R., Matsuda, J., 2009. Noble gases in spinel peridotite
764 xenoliths from Mt Quincan, North Queensland, Australia: Undisturbed MORB-type noble
765 gases in the subcontinental lithospheric mantle. *Chemical Geology* 266, 19–28.
766 <https://doi.org/10.1016/j.chemgeo.2009.03.029>

767 Dávalos-Elizondo, M.G., Aranda Gómez, J.J., Levresse, G., Cervantes-de la Cruz, K.E., 2016.
768 *Química mineral y geoquímica de xenolitos del manto del campo volcánico Santo Domingo,*
769 *San Luis Potosí: evidencias de procesos metasomáticos del manto bajo porciones de la Mesa*
770 *Central, México. Revista Mexicana de Ciencias Geológicas* 33, 81–104.

771 Day, J.M.D., Barry, P.H., Hilton, D.R., Burgess, R., Pearson, D.G., Taylor, L.A., 2015. The helium
772 flux from the continents and ubiquity of low- $^3\text{He}/^4\text{He}$ recycled crust and lithosphere.
773 *Geochimica et Cosmochimica Acta* 153, 116–133. <https://doi.org/10.1016/j.gca.2015.01.008>

774 Deines, P., 2002. The carbon isotope geochemistry of mantle xenoliths. *Earth-Science Reviews* 58,
775 247–278. [https://doi.org/10.1016/S0012-8252\(02\)00064-8](https://doi.org/10.1016/S0012-8252(02)00064-8)

776 Eguiluz de Antuñano, S., Aranda García, M., Marrett, R., 2000. Tectónica de la Sierra Madre
777 Oriental, México. *BSGM* 53, 1–26. <https://doi.org/10.18268/BSGM2000v53n1a1>

778 Faccini, B., Rizzo, A.L., Bonadiman, C., Ntaflos, T., Seghedi, I., Grégoire, M., Ferretti, G., Coltorti,
779 M., 2020. Subduction-related melt refertilisation and alkaline metasomatism in the Eastern
780 Transylvanian Basin lithospheric mantle: Evidence from mineral chemistry and noble gases
781 in fluid inclusions. *Lithos* 364–365, 105516. <https://doi.org/10.1016/j.lithos.2020.105516>

782 Ferrari, L., Orozco-Esquivel, T., Manea, V., Manea, M., 2012. The dynamic history of the Trans-
783 Mexican Volcanic Belt and the Mexico subduction zone. *Tectonophysics* 522–523, 122–
784 149. <https://doi.org/10.1016/j.tecto.2011.09.018>

785 Fix, J.E., 1975. The Crust and Upper Mantle of Central Mexico. *Geophysical Journal International*
786 43, 453–499. <https://doi.org/10.1111/j.1365-246X.1975.tb00643.x>

787 Foley, S.F., Fischer, T.P., 2017. An essential role for continental rifts and lithosphere in the deep
788 carbon cycle. *Nature Geosci* 10, 897–902. <https://doi.org/10.1038/s41561-017-0002-7>

789 Frezzotti, M., Peccerillo, A., 2007. Diamond-bearing COHS fluids in the mantle beneath Hawaii.
790 *Earth and Planetary Science Letters* 262, 273–283.
791 <https://doi.org/10.1016/j.epsl.2007.08.001>

792 Frezzotti, M.L., Andersen, T., Neumann, E.-R., Simonsen, S.L., 2002a. Carbonatite melt–CO₂ fluid
793 inclusions in mantle xenoliths from Tenerife, Canary Islands: a story of trapping,
794 immiscibility and fluid–rock interaction in the upper mantle. *Lithos* 64, 77–96.
795 [https://doi.org/10.1016/S0024-4937\(02\)00178-0](https://doi.org/10.1016/S0024-4937(02)00178-0)

796 Frezzotti, M.L., Ferrando, S., Tecce, F., Castelli, D., 2012b. Water content and nature of solutes in
797 shallow-mantle fluids from fluid inclusions. *Earth and Planetary Science Letters* 351–352,
798 70–83. <https://doi.org/10.1016/j.epsl.2012.07.023>

799 Frezzotti, M.L., Tecce, F., Casagli, A., 2012a. Raman spectroscopy for fluid inclusion analysis.
800 *Journal of Geochemical Exploration* 112, 1–20.
801 <https://doi.org/10.1016/j.gexplo.2011.09.009>

802 Frezzotti, M.-L., Touret, J.L.R., 2014. CO₂, carbonate-rich melts, and brines in the mantle.
803 *Geoscience Frontiers* 5, 697–710. <https://doi.org/10.1016/j.gsf.2014.03.014>

804 Gautheron, C., Moreira, M., 2002. Helium signature of the subcontinental lithospheric mantle. *Earth*
805 *and Planetary Science Letters* 199, 39–47. [https://doi.org/10.1016/S0012-821X\(02\)00563-0](https://doi.org/10.1016/S0012-821X(02)00563-0)

806 Gautheron, C., Moreira, M., Allègre, C., 2005a. He, Ne and Ar composition of the European
807 lithospheric mantle. *Chemical Geology* 217, 97–112.
808 <https://doi.org/10.1016/j.chemgeo.2004.12.009>

809 Gennaro, M.E., Grassa, F., Martelli, M., Renzulli, A., Rizzo, A.L., 2017. Carbon isotope composition
810 of CO₂-rich inclusions in cumulate-forming mantle minerals from Stromboli volcano
811 (Italy). *Journal of Volcanology and Geothermal Research* 346, 95–103.
812 <https://doi.org/10.1016/j.jvolgeores.2017.04.001>

813 Goff, F., Janik, C.J., Werner, C., Counce, D., Stimac, J.A., Siebe, C., Love, S.P., Williams, S.N.,
814 Fischer, T.P., Johnson, L., 1998. Geochemical surveillance of magmatic volatiles at
815 Popocatepetl volcano, Mexico. *GSA Bulletin* 110, 695–710. [https://doi.org/10.1130/0016-7606\(1998\)110<0695:GSOMVA>2.3.CO;2](https://doi.org/10.1130/0016-7606(1998)110<0695:GSOMVA>2.3.CO;2)

817 Goff, F., Love, S.P., Warren, R.G., Counce, D., Obenholzner, J., Siebe, C., Schmidt, S.C., 2001.
818 Passive infrared remote sensing evidence for large, intermittent CO₂ emissions at
819 Popocatepetl volcano, Mexico. *Chemical Geology* 177, 133–156.
820 [https://doi.org/10.1016/S0009-2541\(00\)00387-9](https://doi.org/10.1016/S0009-2541(00)00387-9)

821 Gómez-Tuena, A., Orozco-Esquivel, M.A., Ferrari, L., 2007. Igneous petrogenesis of the Trans-
822 Mexican Volcanic Belt, in: *Geology of México: Celebrating the Centenary of the*
823 *Geological Society of México*. Geological Society of America.
824 [https://doi.org/10.1130/2007.2422\(05\)](https://doi.org/10.1130/2007.2422(05))

825 Graham, D.W., 2002. Noble Gas Isotope Geochemistry of Mid-Ocean Ridge and Ocean Island
826 Basalts: Characterization of Mantle Source Reservoirs. *Reviews in Mineralogy and*
827 *Geochemistry* 47, 247–317. <https://doi.org/10.2138/rmg.2002.47.8>

828 Griffin, W.L., O'Reilly, S., Ryan, C.G., 1999. The composition and origin of sub-continental
829 lithospheric mantle, in: *Mantle Petrology: Field Observations and High Pressure*
830 *Experimentation: A Tribute to Francis F. (Joe) Boyd*. The Geochemical Society, pp. 13–45.

831 Griffin, W.L., O'Reilly, S.Y., Afonso, J.C., Begg, G.C., 2009. The Composition and Evolution of
832 Lithospheric Mantle: a Re-evaluation and its Tectonic Implications. *Journal of Petrology* 50,
833 1185–1204. <https://doi.org/10.1093/petrology/egn033>

834 Gurenko, A.A., Hoernle, K.A., Hauff, F., Schmincke, H.-U., Han, D., Miura, Y.N., Kaneoka, I.,
835 2006. Major, trace element and Nd–Sr–Pb–O–He–Ar isotope signatures of shield stage lavas
836 from the central and western Canary Islands: Insights into mantle and crustal processes.
837 *Chemical Geology* 233, 75–112. <https://doi.org/10.1016/j.chemgeo.2006.02.016>

838 Gutmann, J.T., 1986. Origin of four and five-phase ultramafic xenoliths from Sonora, Mexico.
839 *American Mineralogist* 71, 1079–1084.

840 Halldórsson, S.A., Hilton, D.R., Scarsi, P., Abebe, T., Hopp, J., 2014. A common mantle plume
841 source beneath the entire East African Rift System revealed by coupled helium-neon
842 systematics: HELIUM-NEON ISOTOPES IN THE EARS. *Geophys. Res. Lett.* 41, 2304–
843 2311. <https://doi.org/10.1002/2014GL059424>

844 Hauri, E.H., Cottrell, E., Kelley, K.A., Tucker, J.M., Shimizu, K., Voyer, M.L., Marske, J., Saal,
845 A.E., 2019. Carbon in the Convecting Mantle, in: Orcutt, B.N., Daniel, I., Dasgupta, R.
846 (Eds.), *Deep Carbon*. Cambridge University Press, pp. 237–275.
847 <https://doi.org/10.1017/9781108677950.009>

848 Heber, V.S., Wieler, R., Baur, H., Olinger, C., Friedmann, T.A., Burnett, D.S., 2009. Noble gas
849 composition of the solar wind as collected by the Genesis mission. *Geochimica et*
850 *Cosmochimica Acta* 73, 7414–7432. <https://doi.org/10.1016/j.gca.2009.09.013>

851 Henry, C.D., Aranda-Gómez, J.J., 1992. The real southern Basin and Range: Mid- to late Cenozoic
852 extension in Mexico. *Geology* 20, 701–704. [https://doi.org/10.1130/0091-7613\(1992\)020<0701:TRSBAR>2.3.CO;2](https://doi.org/10.1130/0091-7613(1992)020<0701:TRSBAR>2.3.CO;2)

854 Hopp, J., Ionov, D.A., 2011. Tracing partial melting and subduction-related metasomatism in the
855 Kamchatkan mantle wedge using noble gas compositions. *Earth and Planetary Science*
856 *Letters* 302, 121–131. <https://doi.org/10.1016/j.epsl.2010.12.001>

857 Hopp, J., Trierloff, M., Altherr, R., 2004. Neon isotopes in mantle rocks from the Red Sea region
858 reveal large-scale plume–lithosphere interaction. *Earth and Planetary Science Letters* 219,
859 61–76. [https://doi.org/10.1016/S0012-821X\(03\)00691-5](https://doi.org/10.1016/S0012-821X(03)00691-5)

- 860 Hopp, J., Trieloff, M., Altherr, R., 2007b. Noble gas compositions of the lithospheric mantle below
861 the Chyulu Hills volcanic field, Kenya. *Earth and Planetary Science Letters* 261, 635–648.
862 <https://doi.org/10.1016/j.epsl.2007.07.027>
- 863 Hopp, J., Trieloff, M., Buikin, A., Korochantseva, E., Schwarz, W., Althaus, T., Altherr, R., 2007a.
864 Heterogeneous mantle argon isotope composition in the subcontinental lithospheric mantle
865 beneath the Red Sea region. *Chemical Geology* 240, 36–53.
866 <https://doi.org/10.1016/j.chemgeo.2007.01.004>
- 867 Housh, T.B., Aranda-Gómez, J.J., Luhr, J.F., 2010. Isla Isabel (Nayarit, México): Quaternary alkalic
868 basalts with mantle xenoliths erupted in the mouth of the Gulf of California. *Journal of*
869 *Volcanology and Geothermal Research* 197, 85–107.
870 <https://doi.org/10.1016/j.jvolgeores.2009.06.011>
- 871 Javoy, M., Pineau, F., Agrinier, P., 1989. Volatiles and Stable Isotopes in Recycling, in: Hart, S.R.,
872 Gülen, L. (Eds.), *Crust/Mantle Recycling at Convergence Zones*. Springer Netherlands,
873 Dordrecht, pp. 121–138. https://doi.org/10.1007/978-94-009-0895-6_13
- 874 Kennedy, B.M., Hiyagon, H., Reynolds, J.H., 1990. Crustal neon: a striking uniformity. *Earth and*
875 *Planetary Science Letters* 98, 277–286. [https://doi.org/10.1016/0012-821X\(90\)90030-2](https://doi.org/10.1016/0012-821X(90)90030-2)
- 876 Kurz, M.D., 1986. Cosmogenic helium in a terrestrial igneous rock. *Nature* 320, 435–439.
877 <https://doi.org/10.1038/320435a0>
- 878 Langmuir, C.H., Vocke, R.D., Hanson, G.N., Hart, S.R., 1978. A general mixing equation with
879 applications to Icelandic basalts. *Earth and Planetary Science Letters* 37, 380–392.
880 [https://doi.org/10.1016/0012-821X\(78\)90053-5](https://doi.org/10.1016/0012-821X(78)90053-5)
- 881 Lee, C.A., 2005. Trace Element Evidence for Hydrous Metasomatism at the Base of the North
882 American Lithosphere and Possible Association with Laramide Low- Angle Subduction.
883 *The Journal of Geology* 113, 673–685. <https://doi.org/10.1086/449327>
- 884 Lee, H., Muirhead, J.D., Fischer, T.P., Ebinger, C.J., Kattenhorn, S.A., Sharp, Z.D., Kianji, G., 2016.
885 Massive and prolonged deep carbon emissions associated with continental rifting. *Nature*
886 *Geosci* 9, 145–149. <https://doi.org/10.1038/ngeo2622>
- 887 Leeman, W.P., Harry, D.L., 1993. A Binary Source Model for Extension-Related Magmatism in the
888 Great Basin, Western North America. *Science* 262, 1550–1554.
889 <https://doi.org/10.1126/science.262.5139.1550>
- 890 Levresse, G., Cervantes-de la Cruz, K.E., Aranda-Gómez, J.J., Dávalos-Elizondo, M.G., Jiménez-
891 Sandoval, S., Rodríguez-Melgarejo, F., Alba-Aldave, L.A., 2016. CO₂ fluid inclusion
892 barometry in mantle xenoliths from central Mexico: A detailed record of magma ascent.
893 *Journal of Volcanology and Geothermal Research* 310, 72–88.
894 <https://doi.org/10.1016/j.jvolgeores.2015.11.012>
- 895 Li, Z.-X.A., Lee, C.-T.A., Peslier, A.H., Lenardic, A., Mackwell, S.J., 2008. Water contents in mantle
896 xenoliths from the Colorado Plateau and vicinity: Implications for the mantle rheology and
897 hydration-induced thinning of continental lithosphere. *J. Geophys. Res.* 113, B09210.
898 <https://doi.org/10.1029/2007JB005540>
- 899 Liang, Y., Elthon, D., 1990. Geochemistry and petrology of spinel lherzolite xenoliths from
900 Xalapasco de La Joya, San Luis Potosi, Mexico: Partial melting and mantle metasomatism.
901 *J. Geophys. Res.* 95, 15859. <https://doi.org/10.1029/JB095iB10p15859>
- 902 López-Doncel, R., 2003. La Formación Tamabá del Cretácico medio en la porción central del
903 margen occidental de la Plataforma Valles. *Revista Mexicana de Ciencias Geológicas* 20, 1–
904 19.
- 905 Luhr, J.F., Aranda-Gomez, J.J., 1997. Mexican Peridotite Xenoliths and Tectonic Terranes:
906 Correlations among Vent Location, Texture, Temperature, Pressure, and Oxygen Fugacity.
907 *Journal of Petrology* 38, 1075–1112. <https://doi.org/10.1093/etroj/38.8.1075>
- 908 Luhr, J.F., Aranda-Gomez, J.J., Pier, J.G., 1989. Spinel-lherzolite-bearing quaternary volcanic
909 centers in San Luis Potosí, Mexico: 1. Geology, mineralogy, and petrology. *J. Geophys.*
910 *Res.* 94, 7916. <https://doi.org/10.1029/JB094iB06p07916>

911 Martelli, M., Bianchini, G., Beccaluva, L., Rizzo, A., 2011. Helium and argon isotopic compositions
912 of mantle xenoliths from Tallante and Calatrava, Spain. *Journal of Volcanology and*
913 *Geothermal Research* 200, 18–26. <https://doi.org/10.1016/j.jvolgeores.2010.11.015>

914 Martelli, M., Rizzo, A.L., Renzulli, A., Ridolfi, F., Arienzo, I., Rosciglione, A., 2014. Noble-gas
915 signature of magmas from a heterogeneous mantle wedge: The case of Stromboli volcano
916 (Aeolian Islands, Italy). *Chemical Geology* 368, 39–53.
917 <https://doi.org/10.1016/j.chemgeo.2014.01.003>

918 Marty, B., 2012. The origins and concentrations of water, carbon, nitrogen and noble gases on Earth.
919 *Earth and Planetary Science Letters* 313–314, 56–66.
920 <https://doi.org/10.1016/j.epsl.2011.10.040>

921 Marty, B., Jambon, A., 1987. C3He in volatile fluxes from the solid Earth: implications for carbon
922 geodynamics. *Earth and Planetary Science Letters* 83, 16–26. [https://doi.org/10.1016/0012-](https://doi.org/10.1016/0012-821X(87)90047-1)
923 [821X\(87\)90047-1](https://doi.org/10.1016/0012-821X(87)90047-1)

924 Marty, B., Tolstikhin, I.N., 1998. CO2 fluxes from mid-ocean ridges, arcs and plumes. *Chemical*
925 *Geology* 145, 233–248. [https://doi.org/10.1016/S0009-2541\(97\)00145-9](https://doi.org/10.1016/S0009-2541(97)00145-9)

926 Matsumoto, T., Chen, Y., Matsuda, J.-I., 2001. Concomitant occurrence of primordial and recycled
927 noble gases in the Earth's mantle. *Earth and Planetary Science Letters* 185, 35–47.
928 [https://doi.org/10.1016/S0012-821X\(00\)00375-7](https://doi.org/10.1016/S0012-821X(00)00375-7)

929 Matsumoto, T., Honda, M., McDougall, I., O'Reilly, S.Y., 1998. Noble gases in anhydrous lherzolites
930 from the newer volcanics, southeastern Australia: a MORB-like reservoir in the
931 subcontinental mantle. *Geochimica et Cosmochimica Acta* 62, 2521–2533.
932 [https://doi.org/10.1016/S0016-7037\(98\)00173-2](https://doi.org/10.1016/S0016-7037(98)00173-2)

933 Matsumoto, T., Honda, M., McDougall, I., O'Reilly, S.Y., Norman, M., Yaxley, G., 2000. Noble
934 gases in pyroxenites and metasomatised peridotites from the Newer Volcanics, southeastern
935 Australia: Implications for mantle metasomatism. *Chemical Geology* 168, 49–73.
936 [https://doi.org/10.1016/S0009-2541\(00\)00181-9](https://doi.org/10.1016/S0009-2541(00)00181-9)

937 Mercier, J.-C.C., Nicolas, A., 1975. Textures and Fabrics of Upper-Mantle Peridotites as Illustrated
938 by Xenoliths from Basalts. *Journal of Petrology* 16, 454–487.
939 <https://doi.org/10.1093/petrology/16.1.454>

940 Michael, P.J., Graham, D.W., 2015. The behavior and concentration of CO2 in the suboceanic
941 mantle: Inferences from undegassed ocean ridge and ocean island basalts. *Lithos* 236–237,
942 338–351. <https://doi.org/10.1016/j.lithos.2015.08.020>

943 Morán-Zenteno, D.J., Cerca, M., Keppie, J.D., 2005. La evolución tectónica y magmática cenozoica
944 del suroeste de México: avances y problemas de interpretación. *BSGM* 57, 319–341.
945 <https://doi.org/10.18268/BSGM2005v57n3a4>

946 Moreira, M., 1998. Rare Gas Systematics in Popping Rock: Isotopic and Elemental Compositions in
947 the Upper Mantle. *Science* 279, 1178–1181. <https://doi.org/10.1126/science.279.5354.1178>

948 Nieto-Samaniego, Á.F., Alaniz-Álvarez, S.A., Camprubí í Cano, A., 2005. La Mesa Central de
949 México: estratigrafía, estructura y evolución tectónica cenozoica. *BSGM* 57, 285–318.
950 <https://doi.org/10.18268/BSGM2005v57n3a3>

951 Nieto-Samaniego, Á.F., Ferrari, L., Alaniz-Alvarez, S.A., Labarthe-Hernández, G., Rosas-Elguera,
952 J., 1999. Variation of Cenozoic extension and volcanism across the southern Sierra Madre
953 Occidental volcanic province, Mexico. *GSA Bulletin* 111, 347–363.
954 [https://doi.org/10.1130/0016-7606\(1999\)111<0347:VOCEAV>2.3.CO;2](https://doi.org/10.1130/0016-7606(1999)111<0347:VOCEAV>2.3.CO;2)

955 Nuccio, P.M., Paonita, A., Rizzo, A., Rosciglione, A., 2008. Elemental and isotope covariation of
956 noble gases in mineral phases from Etnean volcanics erupted during 2001–2005, and genetic
957 relation with peripheral gas discharges. *Earth and Planetary Science Letters* 272, 683–690.
958 <https://doi.org/10.1016/j.epsl.2008.06.007>

959 Oppenheimer, C., Fischer, T.P., Scaillet, B., 2014. Volcanic Degassing: Process and Impact, in:
960 *Treatise on Geochemistry*. Elsevier, pp. 111–179. [https://doi.org/10.1016/B978-0-08-](https://doi.org/10.1016/B978-0-08-095975-7.00304-1)
961 [095975-7.00304-1](https://doi.org/10.1016/B978-0-08-095975-7.00304-1)

962 Ozima, M., Podosek, F.A., 2002. Noble Gas Geochemistry. Cambridge University Press.
963 Pardo, M., Suárez, G., 1995. Shape of the subducted Rivera and Cocos plates in southern Mexico:
964 Seismic and tectonic implications. *J. Geophys. Res.* 100, 12357–12373.
965 <https://doi.org/10.1029/95JB00919>
966 Pier, J.G., Luhr, J.F., Podosek, F.A., Aranda-Gómez, J.J., 1992. The La Breña-El Jagüey Maar
967 Complex, Durango, Mexico: II. Petrology and geochemistry. *Bull Volcanol* 54, 405–428.
968 <https://doi.org/10.1007/BF00312322>
969 Pier, J.G., Podosek, F.A., Luhr, J.F., Brannon, J.C., Aranda-Gómez, J.J., 1989. Spinel-lherzolite-
970 bearing quaternary volcanic centers in San Luis Potosí, Mexico: 2. SR and ND Isotopic
971 Systematics. *J. Geophys. Res.* 94, 7941. <https://doi.org/10.1029/JB094iB06p07941>
972 Plank, T., Manning, C.E., 2019. Subducting carbon. *Nature* 574, 343–352.
973 <https://doi.org/10.1038/s41586-019-1643-z>
974 Raisz, E., 1959. Landforms of Mexico.
975 Rizzo, A.L., Pelorosso, B., Coltorti, M., Ntaflos, T., Bonadiman, C., Matusiak-Malek, M., Italiano,
976 F., Bergonzoni, G., 2018. Geochemistry of Noble Gases and CO₂ in Fluid Inclusions From
977 Lithospheric Mantle Beneath Wilcza Góra (Lower Silesia, Southwest Poland). *Front. Earth*
978 *Sci.* 6, 215. <https://doi.org/10.3389/feart.2018.00215>
979 Roedder, E., 1984. Fluid Inclusions: An Introduction to Studies of All Types of Fluid Inclusions,
980 Gas, Liquid, Or Melt, Trapped in Materials from Earth and Space, and Their Application to
981 the Understanding of Geologic Processes. Mineralogical Society of America.
982 Sano, Y., Marty, B., 1995. Origin of carbon in Fumarolic gas from island arcs. *Chemical Geology*
983 119, 265–274. [https://doi.org/10.1016/0009-2541\(94\)00097-R](https://doi.org/10.1016/0009-2541(94)00097-R)
984 Sarda, P., 2004. Surface noble gas recycling to the terrestrial mantle. *Earth and Planetary Science*
985 *Letters* 228, 49–63. <https://doi.org/10.1016/j.epsl.2004.09.026>
986 Sarda, P., Staudacher, T., Allegre, C., 1988. Neon isotopes in submarine basalts. *Earth and Planetary*
987 *Science Letters* 91, 73–88. [https://doi.org/10.1016/0012-821X\(88\)90152-5](https://doi.org/10.1016/0012-821X(88)90152-5)
988 Saucedo, R., Macías, J.L., Ocampo-Díaz, Y.Z.E., Gómez-Villa, W., Rivera-Olguín, E., Castro-
989 Govea, R., Sánchez-Núñez, J.M., Layer, P.W., Torres Hernández, J.R., Carrasco-Núñez, G.,
990 2017. Mixed magmatic–phreatomagmatic explosions during the formation of the Joya
991 Honda maar, San Luis Potosí, Mexico. *Geological Society, London, Special Publications*
992 446, 255–279. <https://doi.org/10.1144/SP446.11>
993 Sedlock, R.L., 2003. Geology and tectonics of the Baja California Peninsula and adjacent areas, in:
994 Tectonic Evolution of Northwestern Mexico and the Southwestern USA. *Geological Society*
995 *of America*. <https://doi.org/10.1130/0-8137-2374-4.1>
996 Severinghaus, J., Atwater, T., 1990. Chapter 1: Cenozoic geometry and thermal state of the
997 subducting slabs beneath western North America, in: *Geological Society of America*
998 *Memoirs*. Geological Society of America, pp. 1–22. <https://doi.org/10.1130/MEM176-p1>
999 Smith, D., Alexis Riter, J.C., Mertzman, S.A., 1999. Water–rock interactions, orthopyroxene growth,
1000 and Si-enrichment in the mantle: evidence in xenoliths from the Colorado Plateau,
1001 southwestern United States. *Earth and Planetary Science Letters* 165, 45–54.
1002 [https://doi.org/10.1016/S0012-821X\(98\)00251-9](https://doi.org/10.1016/S0012-821X(98)00251-9)
1003 Steiger, R.H., Jäger, E., 1977. Subcommittee on geochronology: Convention on the use of decay
1004 constants in geo- and cosmochemistry. *Earth and Planetary Science Letters* 36, 359–362.
1005 [https://doi.org/10.1016/0012-821X\(77\)90060-7](https://doi.org/10.1016/0012-821X(77)90060-7)
1006 Streckeisen, A., 1976. To each plutonic rock its proper name. *Earth-Science Reviews* 12, 1–33.
1007 [https://doi.org/10.1016/0012-8252\(76\)90052-0](https://doi.org/10.1016/0012-8252(76)90052-0)
1008 Tucker, J.M., Mukhopadhyay, S., Gonnermann, H.M., 2018. Reconstructing mantle carbon and
1009 noble gas contents from degassed mid-ocean ridge basalts. *Earth and Planetary Science*
1010 *Letters* 496, 108–119. <https://doi.org/10.1016/j.epsl.2018.05.024>
1011 Verma, S.P., 2000. Geochemistry of the subducting Cocos plate and the origin of subduction-
1012 unrelated mafic volcanism at the volcanic front of the central Mexican Volcanic Belt, in:

1013 Cenozoic Tectonics and Volcanism of Mexico. Geological Society of America.
1014 <https://doi.org/10.1130/0-8137-2334-5.195>
1015 Verma, S.P., Hasenaka, T., 2004. Sr, Nd, and Pb isotopic and trace element geochemical constraints
1016 for a veined-mantle source of magmas in the Michoacan-Guanajuato Volcanic Field, west-
1017 central Mexican Volcanic Belt. *Geochem. J.* 38, 43–65.
1018 <https://doi.org/10.2343/geochemj.38.43>
1019 Wojdyr, M., 2010. Fityk: a general-purpose peak fitting program. *J Appl Cryst* 43, 1126–1128.
1020 <https://doi.org/10.1107/S0021889810030499>
1021 Yamamoto, J., Nishimura, K., Sugimoto, T., Takemura, K., Takahata, N., Sano, Y., 2009. Diffusive
1022 fractionation of noble gases in mantle with magma channels: Origin of low He/Ar in mantle-
1023 derived rocks. *Earth and Planetary Science Letters* 280, 167–174.
1024 <https://doi.org/10.1016/j.epsl.2009.01.029>
1025
1026
1027
1028
1029
1030
1031
1032
1033
1034
1035
1036
1037
1038
1039
1040
1041
1042
1043
1044
1045

1046 Figure Captions

1047 **Figure 1.** Location of the Joya Honda maar (JH) and geodynamic setting. The map shows the Mexican part
1048 of the Basin and Range Province which has an extension of $9.4 \times 10^5 \text{ km}^2$ (Henry and Aranda-Gomez, 1992);
1049 the image was adapted from Aranda-Gómez et al. (2000). The green area is the area used to estimate the ^4He
1050 production, the helium residence time and $^3\text{He}\text{-CO}_2$ fluxes for the lithospheric mantle located under San Luis
1051 Potosí state (see subsections 6.5 and 6.5.1). The pink square represents the location of the Los Encinos Volcanic
1052 Field (LE); although this is a monogenetic volcanic field associated with the Basin and Range extension, this
1053 lacks mantle xenoliths. Contours of Sierra Madre Occidental, Sierra Madre Oriental, the Transmexican
1054 Volcanic Belt and Mesa Central provinces were build based on Gómez-Tuena et al. (2007). VESVF: Ventura
1055 Espiritu Santo Volcanic Field, SDVF: Santo Domingo Volcanic Field, PiVF: Pinacate Volcanic Field, PaVF:
1056 Las Palomas Volcanic Field, Po: Potrillo maar, CVF: the Camargo Volcanic Field, DVF: Durango Volcanic
1057 Field, SQVF: San Quintin Volcanic Field, II: Isla Isabel. Upper right image: Google Earth image (February
1058 20th, 2020) showing the Joya Honda maar morphology and sampling area.

1059 **Figure 2.** Ternary classification for ultramafic and mafic rocks, from Streckeisen (1976).

1060 **Figure 3.** Microphotographs of the JH mantle xenoliths in cross-polarized light (A, B, C, D, E, G, H) and
1061 transmitted plane-polarized light (F). Ol: olivine, Opx: orthopyroxene, Cpx: clinopyroxene, Sp: spinel. A) Ol
1062 porphyroclast with well-developed kink bands and glass-rich veins. B) Spongy rims developed in Opx crystals;
1063 C) Cpx and Opx crystals are almost and totally replaced by the spongy rim. D) Porphyroclastic texture; Opx
1064 crystal being cut by a glass-rich vein. E) Opx cluster. F) Opx cluster cut by a vein composed of light brown
1065 glass and some opaque minerals, note the presence of spongy rims in Opx. G) Cpx porphyroclast with
1066 development of spongy bands. H) Glass-rich veins around Opx porphyroclast.

1067 **Figure 4.** Microphotographs of inclusions identified in olivine. A) Melt and fluid inclusions originating from
1068 microveins. B) Intragranular trail of dendritic inclusions. C) Inclusions composed by glass and high
1069 birefringent mineral phases (cross-polarized light illumination). D) Opaque phases associated to fluid
1070 inclusions.

1071 **Figure 5:** Raman spectroscopy applied in olivine inclusions. A) Raman spectra of birefringent mineral phases
1072 (Mg-calcite) observed in Figure 4C. B) Raman spectra of pure CO_2 fluid inclusions identified in Figure 4D. C)
1073 Raman spectra of dolomite contained in some inclusions of Figure 4B. D) Raman spectra of magnesite and
1074 pyrite contained in olivine inclusions.

1075 **Figure 6.** ^4He , $^{40}\text{Ar}^*$ and CO_2 contents measured in fluid inclusions hosted in JH mantle xenoliths. SCLM:
1076 Subcontinental Lithospheric Mantle. The West Antarctic Rift System (WARS) SCLM compositional range
1077 was built using fluid inclusions data measured by Broadley et al. (2016) and Correale et al. (2019). European
1078 SCLM range includes fluid inclusions values measured in mantle xenoliths from the Rhenish Massif
1079 (Germany), Pannonian basin, Massif Central (Central France), Tallante - Calatrava (Spain), Lower Silesia
1080 (Poland) and the Eastern Transylvanian Basin; data was taken from Buikin et al. (2005), Gautheron et al.,
1081 (2005a), Martelli et al. (2011), Rizzo et al. (2018) and Faccini et al. (2020). Eastern Australia SCLM data was
1082 taken from Matsumoto et al. (1998, 2000) and Czuppon et al. (2009). Red sea region data from Hopp et al.
1083 (2004), Hopp et al. (2007a) and Halldórsson et al. (2014). Northern/Southern Kenya rifts data was taken from
1084 Hopp et al. (2007b) and Halldórsson et al. (2014). The Ethiopia (afar) field was designed after Halldórsson et
1085 al. (2014).

1086 **Figure 7.** A) $^4\text{He}/^{20}\text{Ne}$ vs R/Ra diagram, the solid lines represent the binary mixing between air and an upper
1087 mantle source with R/Ra values between 7 and 8, B) $^3\text{He}/^{40}\text{Ar}$ vs $^{40}\text{Ar}/^{36}\text{Ar}$ diagram. C) $^{21}\text{Ne}/^{22}\text{Ne}$ vs. $^{20}\text{Ne}/^{22}\text{Ne}$
1088 diagram in which the green line represents the binary mixing air-MORB mantle as defined by Sarda et al.
1089 (1988) and Moreira et al. (1998) at $^{21}\text{Ne}/^{22}\text{Ne}_{\text{air}} = 0.029$ and $^{20}\text{Ne}/^{22}\text{Ne}_{\text{air}} = 9.8$ and $^{21}\text{Ne}/^{22}\text{Ne} = 0.06$ and
1090 $^{20}\text{Ne}/^{22}\text{Ne} = 12.5$; the primordial neon composition is reported as Solar wind at $^{21}\text{Ne}/^{22}\text{Ne} = 0.0328$ and
1091 $^{20}\text{Ne}/^{22}\text{Ne} = 13.8$ (Heber et al., 2009); the crust endmember was plotted at $^{21}\text{Ne}/^{22}\text{Ne} = 0.6145$ and $^{20}\text{Ne}/^{22}\text{Ne} =$

1092 0.3 (Kennedy et al., 1990). The WARS SCLM, European SCLM, Ethiopia (Afar), N/S Kenya rifts, Eastern
1093 Australia SCLM and Red sea compositional ranges were built using fluid inclusions data cited in Figure 6.

1094 **Figure 8.** $^4\text{He}/^{40}\text{Ar}^*$ vs $^3\text{He}/^4\text{He}$ corrected for air contamination (Rc/Ra) ratios of fluid inclusions from JH
1095 mantle xenoliths. MORB range is reported at Rc/Ra = 8 + 1 (Graham, 2002) and $^4\text{He}/^{40}\text{Ar}^*$ from 1 to 5
1096 (Yamamoto et al., 2009). The WARS SCLM, European SCLM, Ethiopia (Afar), N/S Kenya rifts, Eastern
1097 Australia SCLM and Red sea compositional ranges were built using fluid inclusions data cited in Figure 6. The
1098 diffusive fractionation path is modeled using the diffusion coefficient (D) of ^3He , ^4He , and $^{40}\text{Ar}^*$
1099 ($D^3\text{He}/D^4\text{He}=1.15$ and $D^4\text{He}/D^{40}\text{Ar}=3.16$ in solid mantle; Burnard, 2004; Yamamoto et al., 2009) (see
1100 supplementary material). Partial melting (see arrow) can lead to decreasing $^4\text{He}/^{40}\text{Ar}^*$ (see supplementary
1101 materials).

1102 **Figure 9.** A) ^{36}Ar vs ^3He concentration. Plotted values correspond to samples with $^{40}\text{Ar}/^{36}\text{Ar} > 500$. B)
1103 $^{20}\text{Ne}/^{22}\text{Ne}$ vs $^{40}\text{Ar}/^{36}\text{Ar}$. Mixing curves are the result of mass-balance and isotopic mass balance equations using
1104 the parameters reported in Table 3.

1105 **Figure 10.** A) $^{21}\text{Ne}/^{22}\text{Ne}_{\text{EX}}$ ratios vs $^4\text{He}/^3\text{He}$ ratios, adapted from Hopp et al. (2004) and Halldórsson et al.
1106 (2014). Values with 2σ uncertainties $<10\%$ are plotted. Dotted lines are binary mixing between three
1107 endmembers: 1) Plume, at 20Ra and $^{21}\text{Ne}/^{22}\text{Ne}_{\text{EX}} = 0.034 \pm 0.001$, 2) MORB-like upper mantle at 8 Ra , 7 Ra
1108 and $^{21}\text{Ne}/^{22}\text{Ne}_{\text{EX}} = 0.06 \pm 0.001$ and SCLM at $6.1 \pm 0.9\text{ Ra}$ and $^{21}\text{Ne}/^{22}\text{Ne}_{\text{EX}} = 0.07 \pm 0.001$. B) ^3He , C) ^4He
1109 and D) $^{40}\text{Ar}^*$ vs $^3\text{He}/^4\text{He}$ corrected for air contamination (Rc/Ra). MORB range is report ed at Rc/Ra = 8 ± 1
1110 (Graham, 2002).

1111 **Figure 11.** A) Comparison between ^3He fluxes measured in central Mexico based on JH mantle xenoliths
1112 analysis (at $U=0.01$ and 0.03 ppm) and other localities. MORB value was estimated using data from Michael
1113 and Graham (2015) and based on $\text{CO}_2/^3\text{He}$ ratio $=2.2 \times 10^9$ (Marty and Tolstikhin, 1998); SCLM value was
1114 taken from Gautheron and Moreira (2002); the European SCLM flux was calculated based on Gautheron et al.
1115 (2005a). B) ^3He fluxes scaled to the surface area. See the text for more details. C) Associated CO_2 fluxes
1116 (mol/yr) for central Mexico compared with other tectonic localities. MORB CO_2 flux was calculated after
1117 Michael and Graham (2015); EAR1 and EAR2 values were taken from Lee et al. (2016) and Foley and Fischer
1118 (2017), respectively; Hawaii and Canary fluxes were obtained from Hauri et al. (2019). D) CO_2 fluxes scaled
1119 to the surface area.

1120 **Figure 12.** A) CO_2 vs $\delta^{13}\text{C}$. Hyblean, Stromboli and European SCLM data from Correale et al. (2015), Gennaro
1121 et al. (2017) and Rizzo et al. (2018), respectively. B) $\delta^{13}\text{C}$ vs $^3\text{He}/^4\text{He}$ corrected for air contamination (Rc/Ra).
1122 Dotted lines are binary mixing between two endmembers: 1) Limestone at $\delta^{13}\text{C} = -1, 1$ and Rc/Ra= 0.01 and 2)
1123 MORB-like upper mantle at $\delta^{13}\text{C} = -4$ and Rc/Ra = 7.38. C) $\delta^{13}\text{C}$ vs $\text{CO}_2/^3\text{He}$. Dotted lines are binary mixing
1124 between two endmembers: 1) Limestone at $\delta^{13}\text{C} = -1, 1$ and $\text{CO}_2/^3\text{He} = 10^{-13}$ and 2) MORB-like upper mantle
1125 at $\delta^{13}\text{C} = -4$ and $\text{CO}_2/^3\text{He} = 1.00 \times 10^{-9}, 2.00 \times 10^{-9}$.

1126

1127
1128
1129
1130
1131
1132

TABLES

Table 1. Modal composition of JH mantle xenoliths.

Sample	Rock type	Ol (%)	Opx (%)	Cpx (%)	Sp (%)
VE	Lherzolite	54.47	28.96	14.37	2.2
VJ	Lherzolite	52.01	32.31	13.39	2.29
IVA	Lherzolite	72.48	15.86	10.45	1.21
VF	Lherzolite	52.08	33.97	11.93	2.02
VI	Lherzolite	53.41	23.48	19.79	3.32
VG	Harzburgite	68.14	30.04	1.26	0.56
VK	Lherzolite	61.27	24.59	13.69	0.44
VH	Harzburgite	62.08	31.26	4.47	2.18

1133
1134
1135
1136
1137
1138
1139
1140
1141
1142

Table 2. Fluid inclusions compositions from JH mantle xenoliths. Concentrations are reported in mol/g. r*: reply made in sample V-I.

Sample	Phase	Weight (g)	³ He	⁴ He	²⁰ Ne	²¹ Ne	²² Ne	CO ₂ ^a	⁴⁰ Ar	³⁶ Ar	⁴⁰ *Ar	⁴ He/ ²⁰ Ne	⁴ He/ ⁴⁰ Ar*	⁴ He/CO ₂	R/Ra	Rc/Ra	error +/- (1σ)
V-A	OI	0.95855	1.67E-17	1.65E-12	9.11E-16	2.72E-18	9.26E-17	2.80E-11	2.09E-12	1.50E-15	1.65E-12	1814.0	1.00	0.05901	7.26	7.26	0.06
V-A	Opx	0.26388	4.74E-18	4.91E-13	8.90E-15	2.59E-17	9.00E-16	3.91E-10	3.61E-12	5.45E-15	2.00E-12	55.2	0.25	0.00126	6.91	6.94	0.13
V-A	Cpx	0.21991	6.45E-18	6.57E-13	5.81E-16	2.62E-18	5.41E-17	6.23E-09	5.16E-12	1.55E-15	4.70E-12	1131.4	0.14	0.00011	7.06	7.06	0.13
V-B	OI	0.99706	2.53E-17	2.48E-12	1.84E-15	5.52E-18	1.88E-16	2.26E-10	3.70E-12	6.01E-15	1.92E-12	1349.7	1.29	0.01100	7.32	7.33	0.06
V-B	Opx	0.4776	3.43E-17	3.36E-12	6.75E-15	1.97E-17	6.61E-16	4.88E-08	7.67E-12	7.95E-15	5.32E-12	497.5	0.63	0.00007	7.34	7.35	0.06
V-B	Cpx	0.48584	4.67E-17	4.62E-12	4.41E-16	2.00E-18	3.61E-17	9.70E-08	1.12E-11	1.36E-15	1.08E-11	10483.3	0.43	0.00005	7.27	7.27	0.06
V-C	OI	0.59294	3.71E-18	3.74E-13	2.35E-16	n.a	2.61E-17	2.38E-10	8.96E-13	3.56E-16	7.91E-13	1593.9	0.47	0.00157	7.13	7.13	0.10
V-C	Cpx	0.5587	8.55E-18	8.40E-13	5.73E-16	1.82E-18	5.87E-17	7.61E-10	2.57E-12	1.02E-15	2.27E-12	1466.6	0.37	0.00110	7.32	7.33	0.07
V-D	OI	1.02241	2.08E-17	2.08E-12	3.76E-16	1.25E-18	3.67E-17	9.18E-10	2.76E-12	1.27E-15	2.38E-12	5534.0	0.87	0.00227	7.19	7.19	0.06
V-D	Opx	0.49922	9.46E-18	9.43E-13	2.33E-15	7.04E-18	2.39E-16	4.39E-09	2.07E-12	3.30E-15	1.09E-12	404.4	0.86	0.00021	7.21	7.22	0.08
V-D	Cpx	0.47389	2.66E-17	2.59E-12	3.02E-16	1.23E-18	2.73E-17	3.25E-08	6.01E-12	7.58E-16	5.78E-12	8576.0	0.45	0.00008	7.37	7.37	0.07
V-E	OI	1.02916	2.51E-17	2.42E-12	1.22E-15	3.90E-18	1.19E-16	4.11E-09	8.79E-13	3.38E-16	7.79E-13	1982.0	3.11	0.00059	7.47	7.47	0.07
V-E	Opx	0.51352	1.98E-17	1.90E-12	5.12E-15	1.56E-17	5.16E-16	2.74E-08	3.03E-12	2.11E-15	2.41E-12	371.6	0.79	0.00007	7.49	7.50	0.07
V-E	Cpx	0.32954	3.96E-17	3.81E-12	3.93E-15	1.27E-17	3.81E-16	1.25E-07	7.06E-12	1.50E-15	6.62E-12	970.0	0.58	0.00003	7.48	7.48	0.07
V-F	OI	1.01203	2.57E-17	2.44E-12	3.49E-15	1.05E-17	3.55E-16	2.81E-09	2.50E-12	2.81E-15	1.67E-12	700.6	1.46	0.00087	7.57	7.57	0.07
V-F	Opx	0.52681	1.66E-17	1.61E-12	4.91E-15	1.51E-17	4.98E-16	1.85E-08	2.37E-12	2.11E-15	1.75E-12	328.5	0.92	0.00009	7.41	7.42	0.08
V-F	Cpx	0.31734	5.58E-17	5.29E-12	2.01E-14	6.07E-17	1.99E-15	1.78E-07	1.06E-11	1.24E-14	6.98E-12	262.9	0.76	0.00003	7.58	7.59	0.07
V-G	OI	1.00336	1.94E-17	1.81E-12	7.91E-16	2.44E-18	7.78E-17	3.91E-11	1.19E-12	1.72E-15	6.81E-13	2292.1	2.66	0.04634	7.68	7.68	0.07
V-G	Opx	0.50526	1.29E-17	1.23E-12	3.20E-15	9.62E-18	3.26E-16	4.54E-09	1.47E-12	1.69E-15	9.68E-13	384.5	1.27	0.00027	7.53	7.53	0.08
V-G	Cpx	0.32136	3.21E-17	3.15E-12	1.57E-15	5.55E-18	1.52E-16	2.24E-08	3.17E-12	9.41E-16	2.89E-12	2003.4	1.09	0.00014	7.32	7.32	0.07
V-H	OI	1.0181	4.21E-17	4.03E-12	4.72E-15	1.47E-17	4.66E-16	4.72E-09	6.44E-12	6.29E-15	4.58E-12	853.7	0.88	0.00085	7.51	7.52	0.08
V-H	Opx	0.53853	1.95E-17	1.86E-12	4.01E-14	1.16E-16	3.94E-15	1.23E-08	1.52E-11	4.14E-14	2.93E-12	46.5	0.64	0.00015	7.47	7.52	0.08
V-H	Cpx	0.30754	3.92E-17	3.73E-12	3.52E-15	1.13E-17	3.46E-16	5.09E-08	4.74E-12	1.93E-15	4.17E-12	1062.1	0.90	0.00007	7.56	7.56	0.07
V-I	OI	1.0437	8.62E-19	8.56E-14	1.42E-16	5.22E-19	1.39E-17	4.74E-11	2.25E-13	5.78E-16	5.37E-14	604.6	1.59	0.00181	7.24	7.25	0.13
V-I	Opx	0.5057	9.92E-19	9.93E-14	1.55E-16	6.59E-19	1.34E-17	2.26E-10	3.77E-13	8.58E-16	1.23E-13	639.0	0.8	0.00044	7.18	7.19	0.15
V-I	Cpx	0.49525	9.34E-19	1.23E-13	5.08E-14	1.46E-16	4.90E-15	n.a	1.13E-11	3.72E-14	2.97E-13	2.4	0.41	n.a	4.84	5.46	0.14
V-I r*	OI	1.01139	9.47E-19	9.25E-14	4.09E-16	1.32E-18	4.07E-17	7.54E-10	1.75E-13	4.48E-16	4.32E-14	226.0	2.14	0.00012	7.36	7.37	0.17
V-I r*	Opx	0.50086	9.81E-19	1.15E-13	1.13E-14	3.37E-17	1.14E-15	1.31E-09	2.02E-12	5.94E-15	2.63E-13	10.1	0.44	0.00009	5.98	6.15	0.08
V-I r*	Cpx	0.57112	7.37E-19	9.81E-14	9.68E-15	2.89E-17	9.72E-16	4.07E-10	5.64E-13	1.62E-15	8.59E-14	10.1	1.14	0.00024	5.26	5.40	0.14
V-J	OI	1.0333	3.63E-17	3.53E-12	3.77E-15	1.15E-17	3.76E-16	4.55E-09	5.30E-12	6.20E-15	3.47E-12	937.0	1.02	0.00078	7.38	7.38	0.07
V-J	Opx	0.5061	5.02E-17	4.93E-12	7.60E-15	2.36E-17	7.58E-16	1.08E-07	1.02E-11	7.88E-15	7.87E-12	649.1	0.63	0.00005	7.32	7.33	0.08
V-J	Cpx	0.30875	1.11E-16	1.07E-11	6.19E-15	2.02E-17	6.07E-16	3.23E-07	8.59E-12	2.87E-15	7.75E-12	1726.7	1.38	0.00003	7.50	7.50	0.07
V-K	OI	1.0225	5.42E-17	5.24E-12	4.99E-15	1.58E-17	4.99E-16	2.46E-08	7.72E-12	6.93E-15	5.67E-12	1049.9	0.92	0.00021	7.45	7.45	0.08
V-K	Opx	0.52687	5.37E-17	5.13E-12	2.48E-14	7.37E-17	2.38E-15	1.05E-07	1.54E-11	2.07E-14	9.25E-12	206.6	0.55	0.00005	7.53	7.54	0.08
V-K	Cpx	0.30567	7.40E-17	7.07E-12	4.08E-14	1.21E-16	4.11E-15	1.16E-07	1.06E-11	1.40E-14	6.47E-12	173.4	1.09	0.00006	7.52	7.53	0.07
IV A	OI	1.03046	2.52E-17	2.43E-12	4.47E-15	1.29E-17	4.34E-16	1.47E-09	2.09E-12	3.40E-15	1.08E-12	543.9	2.24	0.00165	7.45	7.45	0.08
IV A	Opx	0.49715	3.04E-17	3.02E-12	1.05E-14	3.07E-17	1.03E-15	4.49E-08	5.48E-12	6.38E-15	3.59E-12	286.9	0.84	0.00007	7.23	7.23	0.10
IV A	Cpx	0.47966	1.29E-16	1.29E-11	1.25E-14	3.82E-17	1.22E-15	2.73E-07	1.20E-11	9.65E-15	9.11E-12	1033.2	1.42	0.00005	7.21	7.21	0.06

Table 2. Continued. ^a First estimation of CO₂ during noble gases analysis; ^b CO₂ measured from glass line.

Sample	Phase	⁴⁰ Ar/ ³⁶ Ar	error +/- (1σ)	³⁸ Ar/ ³⁶ Ar	error +/- (1σ)	²⁰ Ne/ ²² Ne	error +/- (1σ)	²¹ Ne/ ²² Ne	error +/- (1σ)	(²¹ Ne/ ²² Ne) EX to 12.5	error +/- (2σ)	CO ₂ / ³ He	³ He/ ³⁶ Ar	CO ₂ / ³ He	CO ₂ ^b	δ ¹³ C
V-A	Ol	1391.46	1.24	0.19251	0.00037	9.93	0.06	0.0297	0.00135	0.043	0.003	1.68E+06	0.0111	n.a	n.a	n.a
V-A	Opx	662.11	0.93	0.18892	0.00036	9.87	0.04	0.0288	0.00050	n.a	n.a	8.24E+07	0.0009	n.a	n.a	n.a
V-A	Cpx	3320.08	9.83	0.20543	0.00042	n.a	n.a	n.a	n.a	n.a	n.a	9.66E+08	0.0041	n.a	n.a	n.a
V-B	Ol	614.85	0.37	0.18772	0.00035	9.87	0.04	0.0296	0.00082	0.053	0.003	8.93E+06	0.0042	n.a	n.a	n.a
V-B	Opx	964.58	0.65	0.18291	0.00033	9.97	0.03	0.0298	0.00045	0.041	0.001	1.42E+09	0.0043	2.58E+09	1.17E-07	-2.30
V-B	Cpx	8231.50	13.81	0.20717	0.00043	12.18	0.26	0.0553	0.00431	n.a	n.a	2.07E+09	0.0343	n.a	n.a	n.a
V-C	Ol	2518.41	13.00	0.22231	0.00049	n.a	n.a	n.a	n.a	n.a	n.a	6.43E+07	0.0104	n.a	n.a	n.a
V-C	Cpx	2511.64	5.81	0.19747	0.00039	n.a	n.a	n.a	n.a	n.a	n.a	8.90E+07	0.0084	n.a	n.a	n.a
V-D	Ol	2177.87	2.53	0.19317	0.00037	10.57	0.16	0.0354	0.00227	n.a	n.a	4.41E+07	0.0164	n.a	n.a	n.a
V-D	Opx	626.23	0.62	0.18834	0.00035	n.a	n.a	n.a	n.a	n.a	n.a	4.64E+08	0.0029	n.a	n.a	n.a
V-D	Cpx	7926.55	24.39	0.20644	0.00043	11.03	0.39	0.0452	0.00659	n.a	n.a	1.22E+09	0.0350	1.61E+09	4.27E-08	-1.55
V-E	Ol	2598.15	11.14	0.19010	0.00036	10.37	0.07	0.0332	0.00107	0.049	0.003	1.64E+08	0.0743	n.a	n.a	n.a
V-E	Opx	1436.20	1.91	0.18305	0.00033	10.00	0.04	0.0306	0.00046	0.050	0.002	1.39E+09	0.0094	n.a	n.a	n.a
V-E	Cpx	4719.85	15.56	0.18136	0.00033	10.25	0.05	0.0338	0.00115	0.058	0.004	3.16E+09	0.0265	9.17E+08	3.63E-08	-2.66
V-F	Ol	889.63	0.69	0.18730	0.00035	9.87	0.04	0.0297	0.00064	n.a	0.003	1.09E+08	0.0091	n.a	n.a	n.a
V-F	Opx	1123.07	1.53	0.19054	0.00036	9.93	0.04	0.0307	0.00072	0.063	0.003	1.11E+09	0.0079	1.15E+09	1.91E-08	-1.34
V-F	Cpx	856.84	0.53	0.18382	0.00034	10.12	0.03	0.0306	0.00045	0.042	0.001	3.18E+09	0.0045	1.12E+09	6.22E-08	-1.66
V-G	Ol	690.44	0.68	0.18565	0.00034	10.23	0.06	0.0316	0.00117	0.045	0.003	2.02E+06	0.0112	n.a	n.a	n.a
V-G	Opx	866.39	1.50	0.18036	0.00032	9.85	0.04	0.0296	0.00062	n.a	n.a	3.52E+08	0.0076	n.a	n.a	n.a
V-G	Cpx	3371.87	14.57	0.18281	0.00033	11.06	0.11	0.0390	0.00227	n.a	n.a	6.97E+08	0.0341	n.a	n.a	n.a
V-H	Ol	1023.71	0.63	0.18503	0.00034	10.18	0.03	0.0317	0.00041	0.048	0.001	1.12E+08	0.0067	n.a	n.a	n.a
V-H	Opx	366.42	0.00	0.18303	0.00033	10.11	0.02	0.0301	0.00027	0.039	0.001	6.33E+08	0.0005	n.a	n.a	n.a
V-H	Cpx	2457.00	6.70	0.19215	0.00037	10.15	0.05	0.0326	0.00104	0.056	0.004	1.30E+09	0.0203	n.a	n.a	n.a
V-I	Ol	388.43	0.86	0.19569	0.00038	n.a	n.a	n.a	n.a	n.a	n.a	5.50E+07	0.0015	n.a	n.a	n.a
V-I	Opx	439.10	1.49	0.19092	0.00036	11.59	0.73	0.0492	0.01944	n.a	n.a	2.28E+08	0.0586	n.a	n.a	n.a
V-I	Cpx	303.48	0.16	0.18009	0.00032	10.24	0.01	0.0323	0.00025	n.a	n.a	0.00E+00	0.0000	n.a	n.a	n.a
V-I r*	Ol	391.97	1.17	0.19246	0.00038	10.39	0.16	0.0336	0.00251	n.a	n.a	7.95E+08	0.0021	n.a	n.a	n.a
V-I r*	Opx	339.74	0.26	0.18402	0.00035	9.91	0.03	0.0296	0.00029	n.a	n.a	1.33E+09	0.0002	n.a	n.a	n.a
V-I r*	Cpx	348.57	0.56	0.18113	0.00034	9.98	0.03	0.0298	0.00034	n.a	n.a	5.52E+08	0.0005	n.a	n.a	n.a
V-J	Ol	854.91	0.48	0.18694	0.00035	10.05	0.03	0.0307	0.00053	0.047	0.002	1.25E+08	0.0058	n.a	n.a	n.a
V-J	Opx	1294.25	0.87	0.18590	0.00035	10.08	0.03	0.0313	0.00056	0.051	0.002	2.15E+09	0.0064	3.82E+09	1.92E-07	-2.13
V-J	Cpx	2993.26	5.58	0.19053	0.00036	10.24	0.03	0.0335	0.00071	0.056	0.002	2.90E+09	0.0388	2.10E+09	2.34E-07	-1.30
V-K	Ol	1114.13	0.00	0.18660	0.00035	10.07	0.03	0.0319	0.00049	0.058	0.002	4.54E+08	0.0078	3.82E+08	2.07E-08	-1.10
V-K	Opx	741.96	0.00	0.18186	0.00033	10.32	0.02	0.0316	0.00031	0.042	0.001	1.95E+09	0.0026	1.88E+09	1.01E-07	-2.08
V-K	Cpx	756.34	0.50	0.18796	0.00035	9.92	0.02	0.0296	0.00029	0.041	0.001	1.57E+09	0.0053	3.38E+08	2.50E-08	-0.97
IV A	Ol	614.05	0.43	0.18144	0.00034	10.14	0.04	0.0303	0.00050	0.039	0.001	5.84E+07	0.0074	n.a	n.a	n.a
IV A	Opx	858.77	0.49	0.18068	0.00033	10.10	0.03	0.0298	0.00045	n.a	n.a	1.48E+09	0.0048	2.22E+09	6.76E-08	-2.86
IV A	Cpx	1238.93	24.70	0.18113	0.00034	10.25	0.03	0.0314	0.00047	0.043	0.001	2.11E+09	0.0134	1.18E+09	1.52E-07	-1.25

1144

1145

1146

Table 3. Expected noble gas isotopic ratios for the Mexican lithospheric mantle. $^{20}\text{Ne}/^{22}\text{Ne}_{\text{air}}$ $^{40}\text{Ar}/^{36}\text{Ar}_{\text{air}}$ ratios after Steiger and Jäger (1977) and Ozima and Podosek (2002).

R/Ra	$^4\text{He}/^{40}\text{Ar}^*$	$^4\text{He}/^{20}\text{Ne}$	$^{36}\text{Ar}/^{22}\text{Ne}$	$^{40}\text{Ar}/^{36}\text{Ar}$	$^{20}\text{Ne}/^{22}\text{Ne}$	$^{20}\text{Ne}/^{22}\text{Ne}_{\text{air}}$	$^{40}\text{Ar}/^{36}\text{Ar}_{\text{air}}$
7.39 ± 0.14	0.14 - 3.11	11000	4.21 - 93.5	10500	12.5	9.8	295.5

1147

1148

1149

1150

Table 4. ^4He production rates, ^3He fluxes, helium residence time and CO_2 fluxes calculated for the lithospheric mantle beneath central Mexico. P*, F and Rt values were calculated based on mathematical formulations proposed by Gautheron and Moreira (2002). P*: ^4He production, F: ^3He flux, Rt: Helium residence time.

U (ppm)	P* (ccSTP/g)	P* (mol/yr)	F (ccSTP/year)	F (mol/yr)	Rt (Ma)	CO_2 flux (mol/yr)	CO_2 flux (g/yr)
0.01	7.69E+06	3.43E+02	5.99E+02	0.027	61.17	3.93E+07	1.73E+09
0.012	9.23E+06	4.12E+02	7.19E+02	0.032	50.97	4.72E+07	2.08E+09
0.014	1.08E+07	4.81E+02	8.38E+02	0.037	43.69	5.50E+07	2.42E+09
0.016	1.23E+07	5.49E+02	9.58E+02	0.043	38.23	6.29E+07	2.77E+09
0.018	1.38E+07	6.18E+02	1.08E+03	0.048	33.98	7.07E+07	3.11E+09
0.02	1.54E+07	6.87E+02	1.20E+03	0.053	30.58	7.86E+07	3.46E+09
0.022	1.69E+07	7.55E+02	1.32E+03	0.059	27.80	8.65E+07	3.80E+09
0.024	1.85E+07	8.24E+02	1.44E+03	0.064	25.49	9.43E+07	4.15E+09
0.026	2.00E+07	8.93E+02	1.56E+03	0.070	23.53	1.02E+08	4.50E+09
0.028	2.15E+07	9.62E+02	1.68E+03	0.075	21.84	1.10E+08	4.84E+09
0.03	2.31E+07	1.03E+03	1.80E+03	0.080	20.39	1.18E+08	5.19E+09

1151

SUPPLEMENTARY MATERIAL

THE COMPOSITION OF FLUIDS STORED IN THE CENTRAL MEXICAN LITHOSPHERIC MANTLE: INFERENCES FROM NOBLE GASES AND CO₂ IN MANTLE XENOLITHS

A. Sandoval-Velasquez¹, A.L. Rizzo², M. Frezzotti³, R. Saucedo⁴ and A. Aiuppa^{1,2}.

Author's affiliations

¹*DiSTeM, Università di Palermo, Via Archirafi 36, 90123 Palermo, Italy.*

²*Istituto Nazionale di Geofisica e Vulcanologia (INGV), Sezione di Palermo, Via Ugo La Malfa 153, 90146 Palermo, Italy,*

³*Dipartimento di Scienze dell'Ambiente e della Terra, Università di Milano Bicocca, Piazza della Scienza 4, 20126 Milano, Italy,*

⁴*Instituto de Geología, Universidad Autónoma de San Luis Potosí, Dr M. Nava no. 5, Zona Universitaria, 78240 San Luis Potosí, México*

Corresponding author e-mail: andreslibardo.sandovalvelasquez@unipa.it

1. Premise

We discuss here the possible role played by secondary processes that may have concurred to determine the noble gas isotope composition of the fluid inclusions. Our attempt is to show that these secondary processes have overall played little role (with a few exceptions noted), and that therefore the fluid inclusions are well representative of the source mantle. The few samples that have to some extent suffered from secondary processes are filtered out from further discussion (see main text) on volatile origin and processing in the mantle source.

2. Exposure to cosmic rays

Several studies have shown that rocks exposed to cosmic rays (i.e. after eruption) favor the accumulation of ³He in the crystal lattices shifting the original ³He/⁴He ratios to higher values (Kurz, 1986; Lal, 1987; Dunai and Baur, 1995; Dunai, 2010; Broadley et al., 2016; Nesterenok and Yakubovich, 2016; Correale et al., 2019). According to e.g. Dunai and Baur (1995) and Correale et al. (2019 and references therein), crystals with low He concentrations are more prone to changes due to the diffusion of ³He from lattices into the fluid inclusions. However, in the case of the JH mantle xenoliths, the aliquots with the lowest He contents (³He < 10⁻¹⁷ and ⁴He < 10⁻¹²; Figure 9A, 9B) generally show an opposite effect, that is a decrease in ³He/⁴He compared to the samples with the highest helium concentrations that we interpreted as the result of diffusive fractionation. The eruption time of JH xenoliths (311 ± 19 ka; Saucedo et al., 2017) limits the exposure time to cosmic rays. Finally, the single step crushing method prevents the contribution of secondary He accumulated in the crystal lattice (cosmogenic ³He and radiogenic ⁴He), as evidenced by other authors (Kurz, 1986; Graham, 2002; Rizzo et al., 2018; Correale et al., 2019; Faccini et al., 2020). We therefore conclude that the effect of cosmogenic ³He in our samples is negligible.

40

41 **3. Diffusive Fractionation**

42 As shown in Figure 6, the lowest noble gas concentrations (especially helium) were measured in V-I crystals
43 and, to a minor extent, in V-A and V-C ($^4\text{He} < 10^{-12}$ mol/g). Some CO_2 depletion is also evident in sample V-I
44 (Figure 6C). When plotting ^3He , ^4He , $^{40}\text{Ar}^*$, and $^4\text{He}/^{40}\text{Ar}^*$ vs. R_c/R_a (Figures 8 and 10B-10D), we find that
45 in sample V-I the He and Ar depletion is also accompanied by $^3\text{He}/^4\text{He} < 6.15$ Ra, which are sensibly lower
46 than the dataset average (7.39 ± 0.14 Ra). In samples V-A and V-C, the $^3\text{He}/^4\text{He}$ decrease is less important. It
47 is worth noting that the lower R_c/R_a values mostly correspond to pyroxenes (Opx and Cpx) from the same
48 nodule, while Ol crystals are less or not modified. Indeed, Ol from V-I show $^3\text{He}/^4\text{He}$ values ($7.25 - 7.37$ Ra)
49 that are within the above reported average of the dataset.

50 Following Burnard et al. (1998), Burnard (2004), and Yamamoto et al. (2009), this data variability can be
51 interpreted as due to preferential loss of He (relative to Ar and CO_2) due to diffusive fractionation. In fact, in
52 case of radiogenic ^4He in-growth or addition to fluid inclusions, an increase of ^4He concentration with
53 decreasing $^3\text{He}/^4\text{He}$ values should be expected, without any relative decrease of ^3He , $^{40}\text{Ar}^*$, and $^4\text{He}/^{40}\text{Ar}^*$. We
54 highlight that He diffusion into the fast flowing melt-filled dissolution channels cutting the mantle is commonly
55 invoked during partial melting (Burnard, 2004; Yamamoto et al., 2009; Faccini et al., 2020) and/or
56 metasomatism of solid mantle that prevalently affects pyroxene crystals. Previous studies suggest that the ^4He
57 diffusion coefficient is considerably higher than that of ^{40}Ar ($D_{^4\text{He}}/D_{^{40}\text{Ar}} = 3.16$ in solid mantle; Burnard, 2004;
58 Yamamoto et al., 2009); this is fundamentally based on the assumption that the difference in the atomic masses
59 of the two elements are the key controls of their different diffusion coefficients. Likewise, the difference in
60 mass between ^3He and ^4He implies important differences in their diffusivities ($D_{^3\text{He}}/D_{^4\text{He}} = 1.15$; Trull and
61 Kurz, 1993; Burnard, 2004; Yamamoto et al., 2009). Hence, in case of diffusive loss of He, a decrease in
62 $^3\text{He}/^4\text{He}$ and $^4\text{He}/^{40}\text{Ar}^*$ is expected, as observed in V-A and V-I pyroxenes. Because the clearest evidence of
63 diffusive fractionation is observed in pyroxenes, we exclude V-C because Ol from this sample show $^3\text{He}/^4\text{He}$
64 values (7.13 Ra) comparable to Opx (7.33 Ra) from the same nodule (although Ol have lower He
65 concentrations). In any case, in order to properly interpret the origin of the He in the following sections of the
66 discussion, pyroxenes from V-I and V-A nodules will not be discussed further.

67 To support the hypothesis of a diffusive fractionation, in Figures 8 and 10B-C-D we model this process based
68 on the approach proposed by Burnard et al. (1998), Burnard (2004), Yamamoto et al. (2009), and already
69 applied in Boudoire et al. (2020) and Faccini et al. (2020). We consider a starting mantle composition of ^3He
70 $= 1.56 \times 10^{-17}$ mol/g, $^4\text{He} = 1.5 \times 10^{-12}$ mol/g, and $^{40}\text{Ar}^* = 6 \times 10^{-13}$ mol/g, which corresponds to the lowest
71 concentrations of these species in nodules not evidently modified by diffusion. We additionally use a starting
72 $^4\text{He}/^{40}\text{Ar}^* = 2.5$ (the average mantle production ratio), and a $^3\text{He}/^4\text{He} = 7.5$ Ra, which is within the R_c/R_a
73 variability of the dataset. According to our modeling, diffusive fractionation is able to justify the data
74 variability observed in pyroxene from V-A and V-I samples, which will not be discussed anymore.

75

76 **4. Effects on fluid inclusions by mantle melting and/or fluid-melt partitioning**

77 It has been previously inferred that the noble gas signature of mantle xenoliths can depend to some extent on
78 the melting history of the mantle source, and that the $^4\text{He}/^{40}\text{Ar}^*$ ratio is a useful tracer to recognize relative
79 variations of partial melting degree in mantle xenoliths (Graham, 2002; Burnard, 2004; Yamamoto et al., 2009;
80 Correale et al., 2012, 2016, 2019; Rizzo et al., 2018; Faccini et al., 2020). The utility of $^4\text{He}/^{40}\text{Ar}^*$ stands on
81 the different mineral/melt partition coefficients of the two elements (e.g., olivine, $D_{\text{He}} = 0.00017$ and $D_{\text{Ar}} = 0.0011$;
82 Herber et al., 2007). In detail, it is suggested that, even considering the wide uncertainties in the
83 derived partition coefficients (Heber et al., 2007), He is more incompatible than Ar, and can thus escape the
84 mantle more effectively during partial melting, ultimately causing a $^4\text{He}/^{40}\text{Ar}^*$ decrease in the mantle residuum

85 (Burnard, 2004; Heber et al., 2007; Yamamoto et al., 2009). This possible mantle partial melting trend is
86 indicated in Figure 8.

87 In the JH nodules, the majority of Ol crystals have $^4\text{He}/^{40}\text{Ar}^*$ values within the typical production ratio of a
88 fertile mantle ($^4\text{He}/^{40}\text{Ar}^* = 1\text{--}5$; Marty, 2012), while Opx and Cpx crystals exhibit slightly lower $^4\text{He}/^{40}\text{Ar}^*$
89 ratios, from 0.4 to 1.4. In general, the $^4\text{He}/^{40}\text{Ar}^*$ population of our samples could imply that mantle melting
90 may have to some extent impacted the Opx and Cpx noble gas signature, but not that of Ol, ultimately
91 suggesting a low degree of partial melting. However, any detailed consideration on this process is prevented
92 by the lack of mineral chemistry in our samples to be compared to the composition of fluid inclusions. In
93 addition, we stress that the degrees of partial melting are not well constrained on petrological basis for the JH
94 spinel lherzolites, as a wide range (7–22%) has been proposed in previous work (Liang and Elthon, 1990).

95 The mentioned behavior of $^4\text{He}/^{40}\text{Ar}^*$ in relation to partial melting is valid if fluid inclusions trapped in mantle
96 minerals represent a residuum rather than inclusions degassed from melt(s) percolating and metasomatizing
97 the local mantle. Nevertheless, our suite of samples exhibits textural evidence of interstitial glass veins bearing
98 dendritic trails of secondary melt and fluid inclusions related to pervasive mantle metasomatism driven by
99 carbonate-rich silicate melt. This suggests that the composition of fluid inclusions (e.g., $^4\text{He}/^{40}\text{Ar}^*$) could also,
100 or alternatively (to mantle melting), be influenced by fluid-melt partitioning from the metasomatizing melt. In
101 fact, assuming a mantle with $^4\text{He}/^{40}\text{Ar}^*=1$, and considering the olivine/melt partition coefficient proposed by
102 Heber et al. (2007), the first melt should have $^4\text{He}/^{40}\text{Ar}^*=6.5$ while the first gas exsolved from the melt should
103 have $^4\text{He}/^{40}\text{Ar}^*=0.92$ (assuming a solubility ratio $S_{\text{He}}/S_{\text{Ar}}\sim 7$; Lux, 1987). This implies, that a metasomatizing
104 melt poorly or slightly degassed would equally fit most of the dataset. According to the petrographic evidence,
105 metasomatic melt degassing seems the most reasonable process to explain most of our fluid inclusions
106 compositional variability.

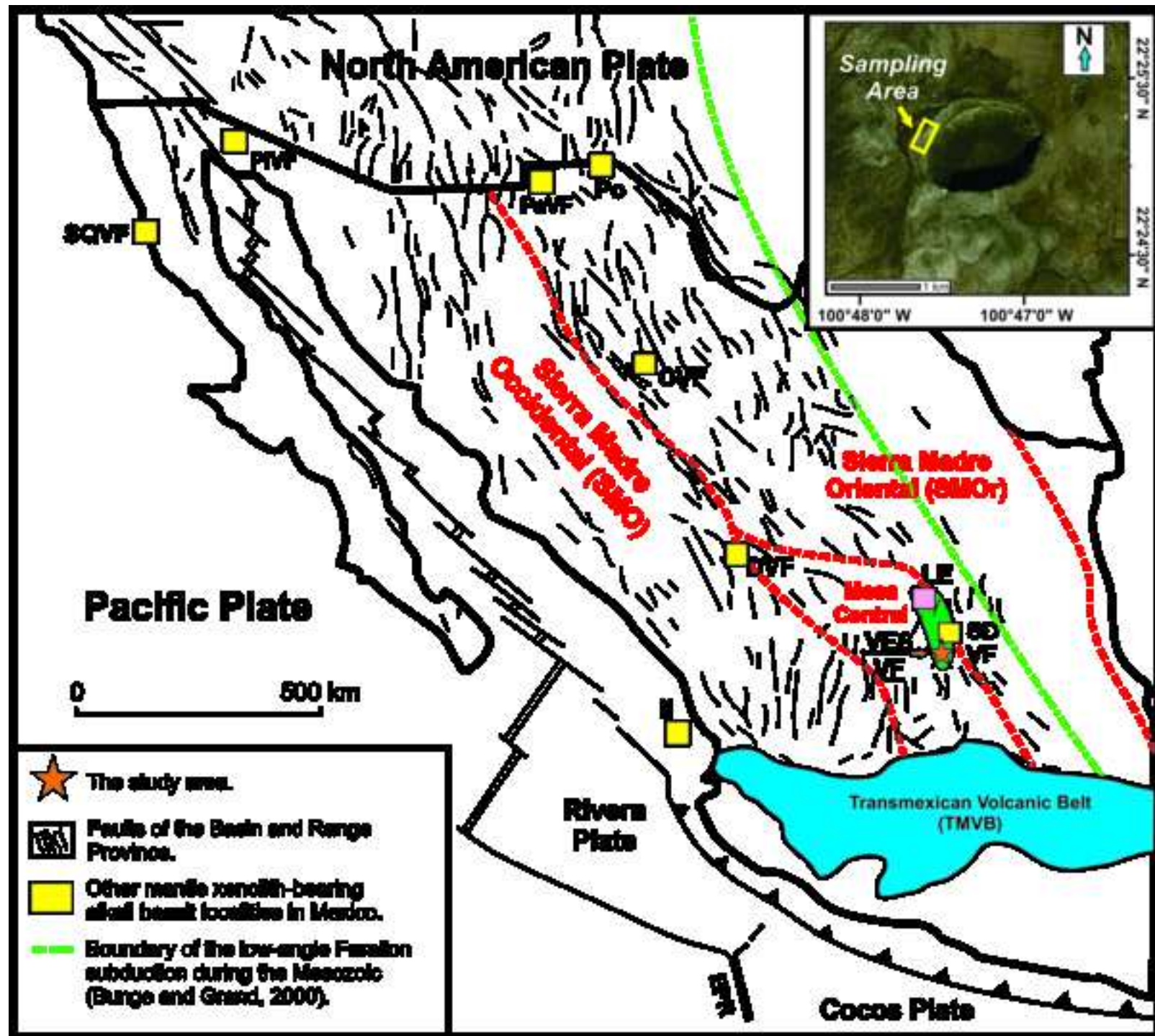
107

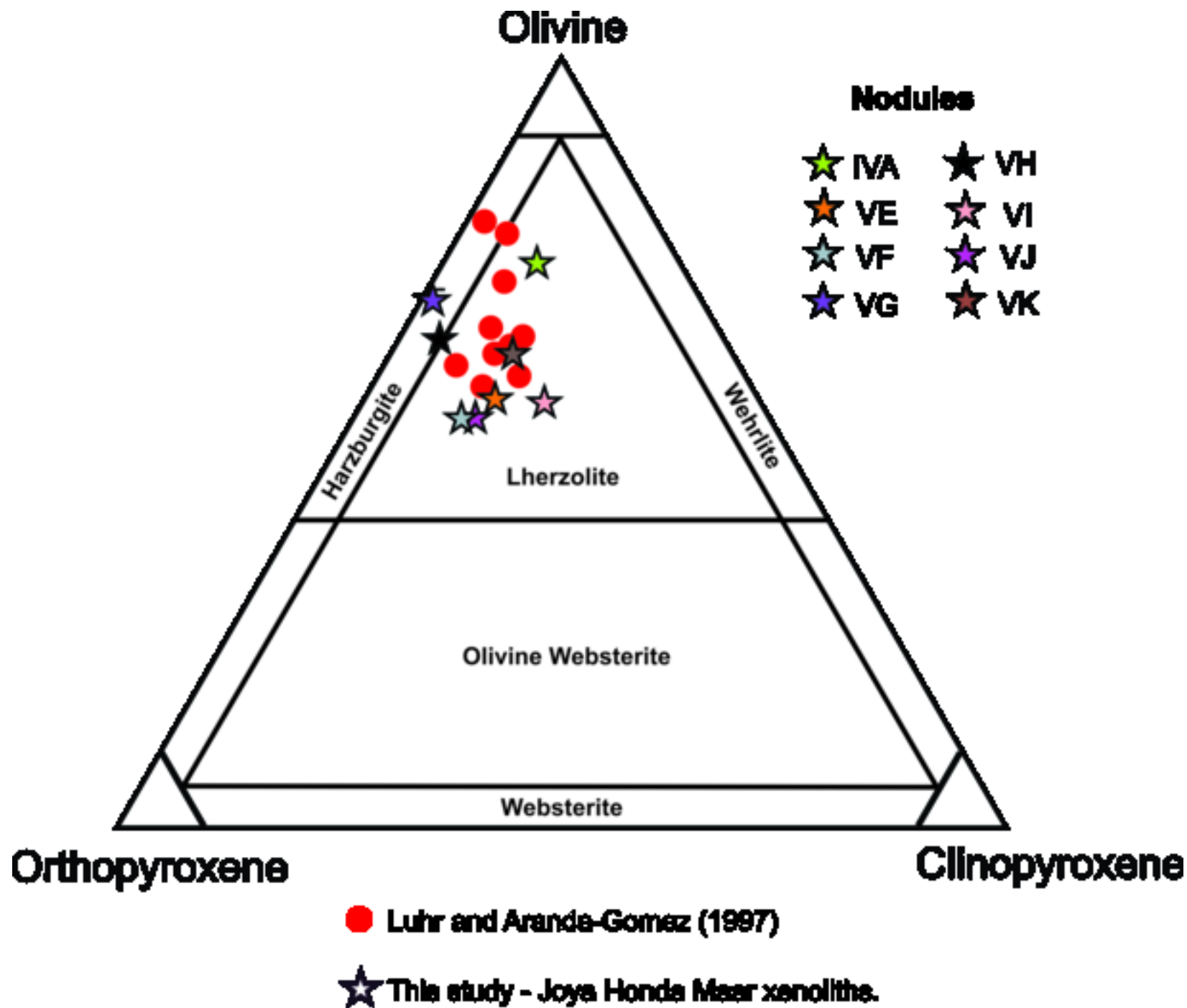
108 **References:**

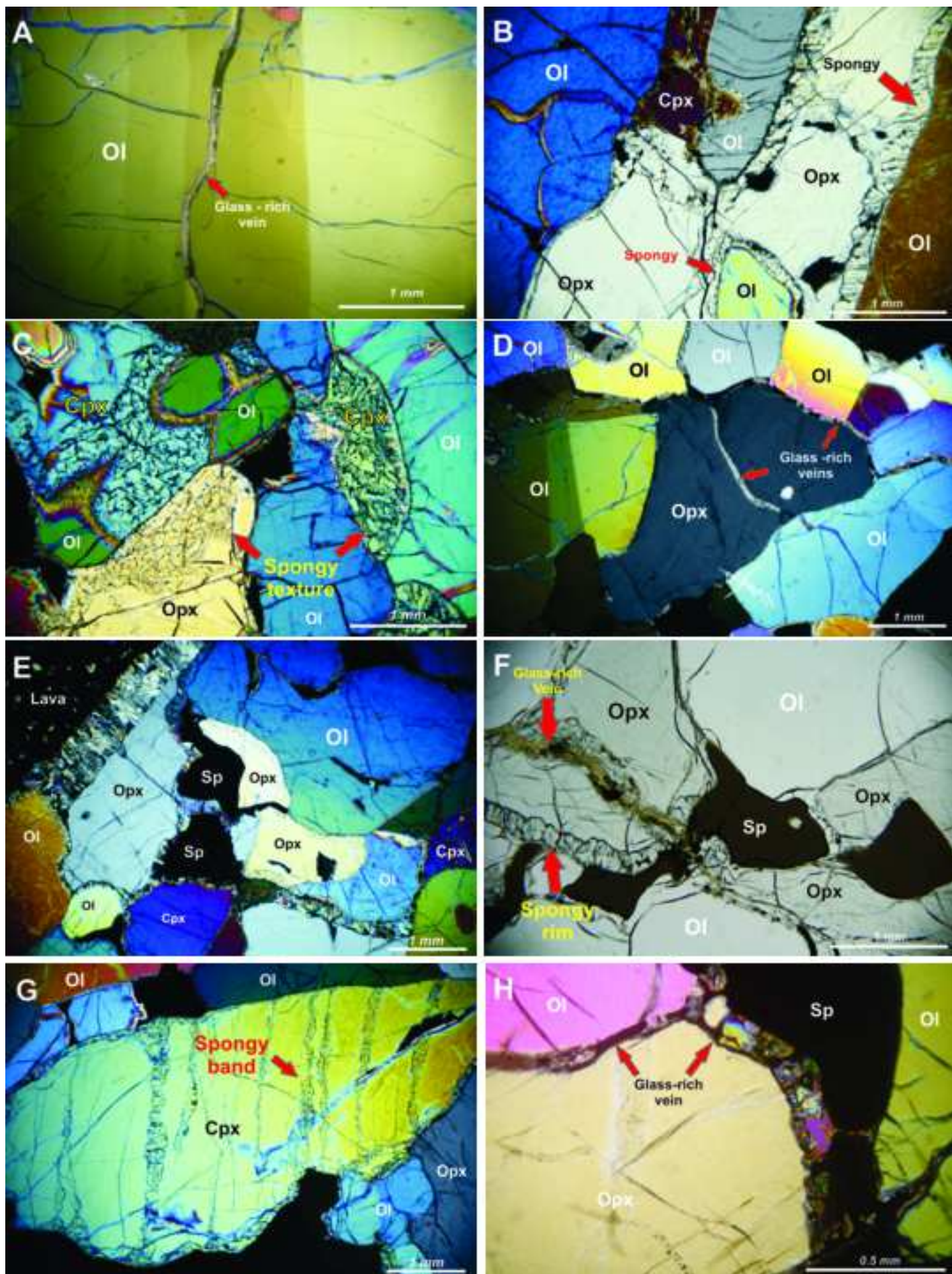
- 109 Boudoire, G., Rizzo, A.L., Arienzo, I., Di Muro, A., 2020. Paroxysmal eruptions tracked by variations of
110 helium isotopes: inferences from Piton de la Fournaise (La Réunion island). *Sci Rep* 10, 9809.
111 <https://doi.org/10.1038/s41598-020-66260-x>
112
- 113 Broadley, M.W., Ballentine, C.J., Chavrit, D., Dallai, L., Burgess, R., 2016. Sedimentary halogens and noble
114 gases within Western Antarctic xenoliths: Implications of extensive volatile recycling to the sub
115 continental lithospheric mantle. *Geochimica et Cosmochimica Acta* 176, 139–156.
116 <https://doi.org/10.1016/j.gca.2015.12.013>
117
- 118 Burnard, P., 2004. Diffusive fractionation of noble gases and helium isotopes during mantle melting. *Earth
119 and Planetary Science Letters* 220, 287–295. [https://doi.org/10.1016/S0012-821X\(04\)00060-3](https://doi.org/10.1016/S0012-821X(04)00060-3)
- 120 Burnard, P.G., Farley, K.A., Turner, G., 1998. Multiple fluid pulses in a Samoan harzburgite. *Chemical
121 Geology* 147, 99–114. [https://doi.org/10.1016/S0009-2541\(97\)00175-7](https://doi.org/10.1016/S0009-2541(97)00175-7)
122
- 123 Correale, A., Martelli, M., Paonita, A., Rizzo, A., Brusca, L., Scribano, V., 2012. New evidence of mantle
124 heterogeneity beneath the Hyblean Plateau (southeast Sicily, Italy) as inferred from noble gases and
125 geochemistry of ultramafic xenoliths. *Lithos* 132–133, 70–81.
126 <https://doi.org/10.1016/j.lithos.2011.11.007>
127
- 128 Correale, A., Pelorosso, B., Rizzo, A.L., Coltorti, M., Italiano, F., Bonadiman, C., Giacomoni, P.P., 2019. The
129 nature of the West Antarctic Rift System as revealed by noble gases in mantle minerals. *Chemical
130 Geology* 524, 104–118. <https://doi.org/10.1016/j.chemgeo.2019.06.020>

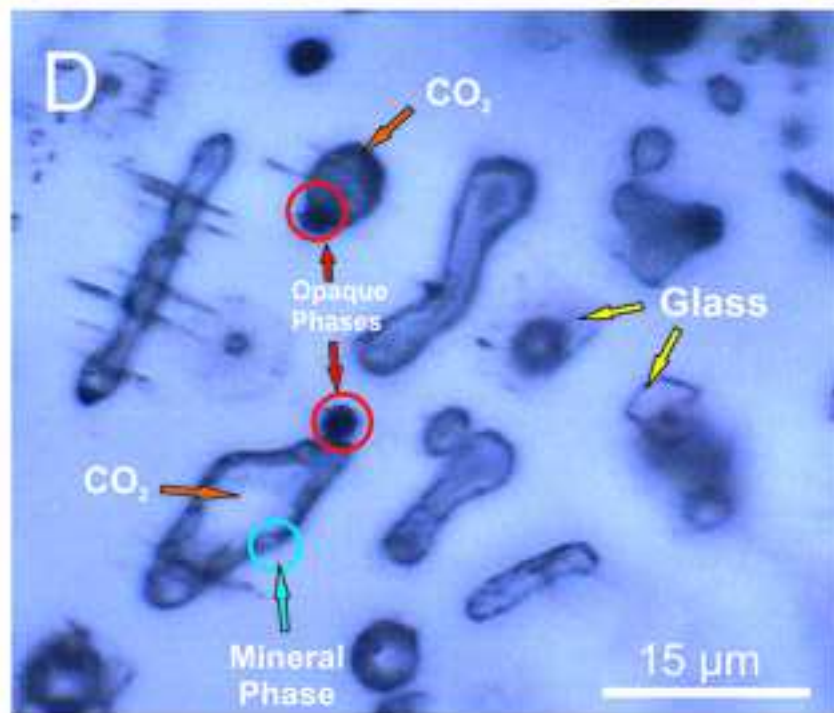
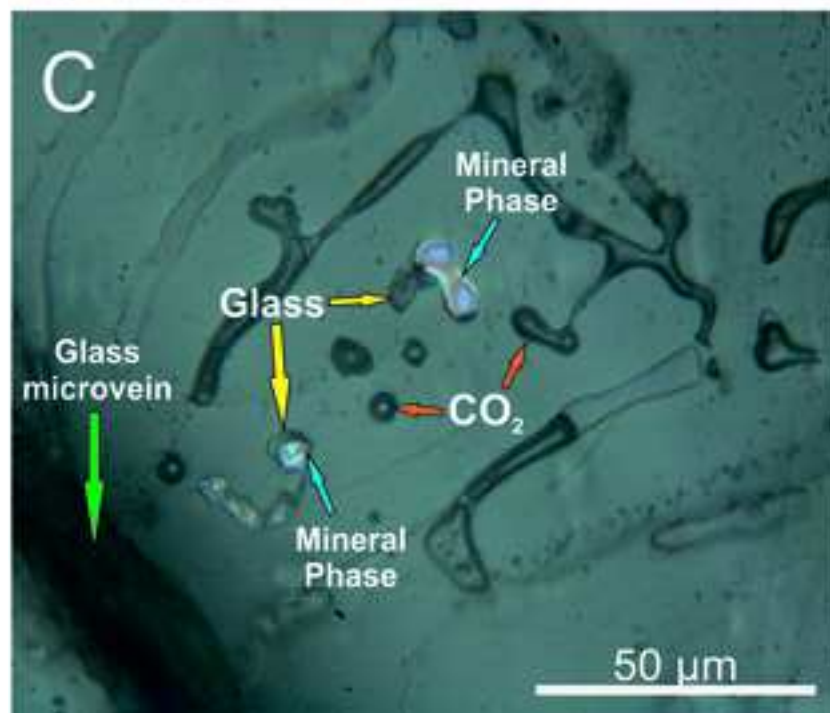
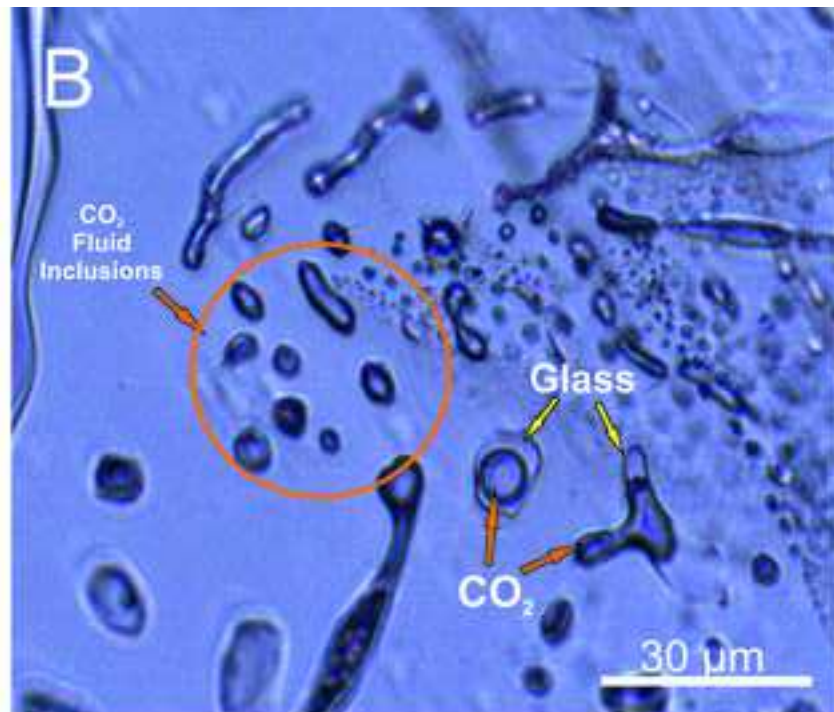
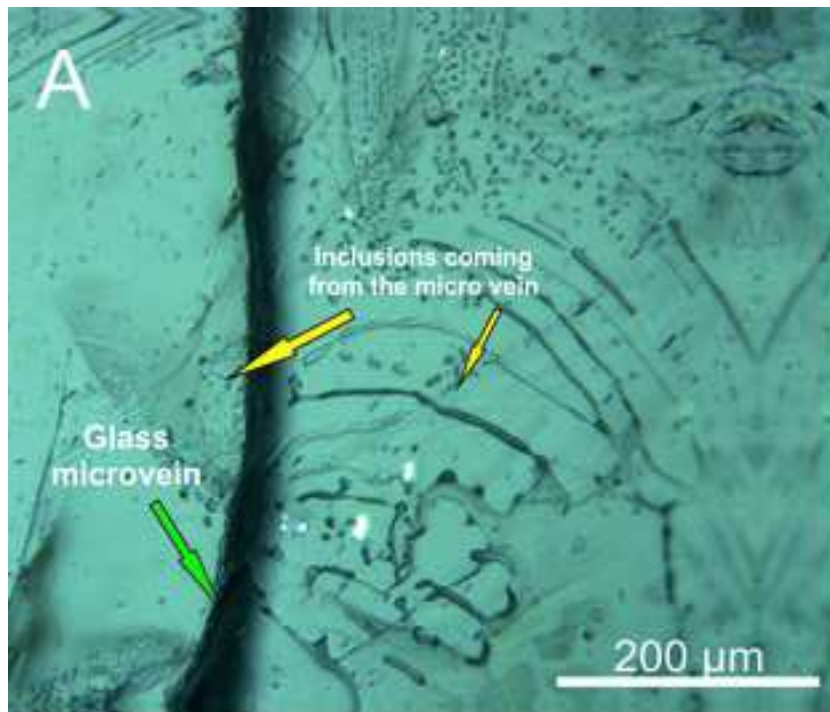
- 131 Correale, A., Rizzo, A.L., Barry, P.H., Lu, J., Zheng, J., 2016. Refertilization of lithospheric mantle beneath
132 the Yangtze craton in south-east China: Evidence from noble gases geochemistry. *Gondwana Research*
133 38, 289–303. <https://doi.org/10.1016/j.gr.2016.01.003>
134
- 135 Dunai, T.J., 2010. *Cosmogenic Nuclides: Principles, Concepts and Applications in the Earth Surface Sciences*.
136 Cambridge University Press, Cambridge. <https://doi.org/10.1017/CBO9780511804519>
137 Dunai, T.J., Baur, H., 1995. Helium, neon, and argon systematics of the European subcontinental mantle:
138 Implications for its geochemical evolution. *Geochimica et Cosmochimica Acta* 59, 2767–2783.
139 [https://doi.org/10.1016/0016-7037\(95\)00172-V](https://doi.org/10.1016/0016-7037(95)00172-V)
140
- 141 Faccini, B., Rizzo, A.L., Bonadiman, C., Ntaflos, T., Seghedi, I., Grégoire, M., Ferretti, G., Coltorti, M., 2020.
142 Subduction-related melt refertilisation and alkaline metasomatism in the Eastern Transylvanian Basin
143 lithospheric mantle: Evidence from mineral chemistry and noble gases in fluid inclusions. *Lithos* 364–
144 365, 105516. <https://doi.org/10.1016/j.lithos.2020.105516>
145
- 146 Graham, D.W., 2002. Noble Gas Isotope Geochemistry of Mid-Ocean Ridge and Ocean Island Basalts:
147 Characterization of Mantle Source Reservoirs. *Reviews in Mineralogy and Geochemistry* 47, 247–
148 317. <https://doi.org/10.2138/rmg.2002.47.8>
149
- 150 Heber, V.S., Brooker, R.A., Kelley, S.P., Wood, B.J., 2007. Crystal–melt partitioning of noble gases (helium,
151 neon, argon, krypton, and xenon) for olivine and clinopyroxene. *Geochimica et Cosmochimica Acta*
152 71, 1041–1061. <https://doi.org/10.1016/j.gca.2006.11.010>
153
- 154 Kurz, M.D., 1986. Cosmogenic helium in a terrestrial igneous rock. *Nature* 320, 435–439.
155 <https://doi.org/10.1038/320435a0>
156
- 157 Lal, D., 1987. Production of ^3He in terrestrial rocks. *Chemical Geology: Isotope Geoscience section* 66, 89–
158 98. [https://doi.org/10.1016/0168-9622\(87\)90031-5](https://doi.org/10.1016/0168-9622(87)90031-5)
159
- 160 Liang, Y., Elthon, D., 1990. Geochemistry and petrology of spinel lherzolite xenoliths from Xalapasco de La
161 Joya, San Luis Potosi, Mexico: Partial melting and mantle metasomatism. *J. Geophys. Res.* 95, 15859.
162 <https://doi.org/10.1029/JB095iB10p15859>
163
- 164 Lux, G., 1987. The behavior of noble gases in silicate liquids: Solution, diffusion, bubbles and surface effects,
165 with applications to natural samples. *Geochimica et Cosmochimica Acta* 51, 1549–1560.
166 [https://doi.org/10.1016/0016-7037\(87\)90336-X](https://doi.org/10.1016/0016-7037(87)90336-X)
167
- 168 Marty, B., 2012. The origins and concentrations of water, carbon, nitrogen and noble gases on Earth. *Earth*
169 *and Planetary Science Letters* 313–314, 56–66. <https://doi.org/10.1016/j.epsl.2011.10.040>
170
- 171 Nesterenok, A.V., Yakubovich, O.V., 2016. Production of ^3He in rocks by reactions induced by particles of
172 the nuclear-active and muon components of cosmic rays: Geological and petrological implications.
173 *Petrology* 24, 21–34. <https://doi.org/10.1134/S0869591116010057>
174
- 175 Rizzo, A.L., Pelorosso, B., Coltorti, M., Ntaflos, T., Bonadiman, C., Matusiak-Małek, M., Italiano, F.,
176 Bergonzoni, G., 2018. Geochemistry of Noble Gases and CO_2 in Fluid Inclusions From Lithospheric

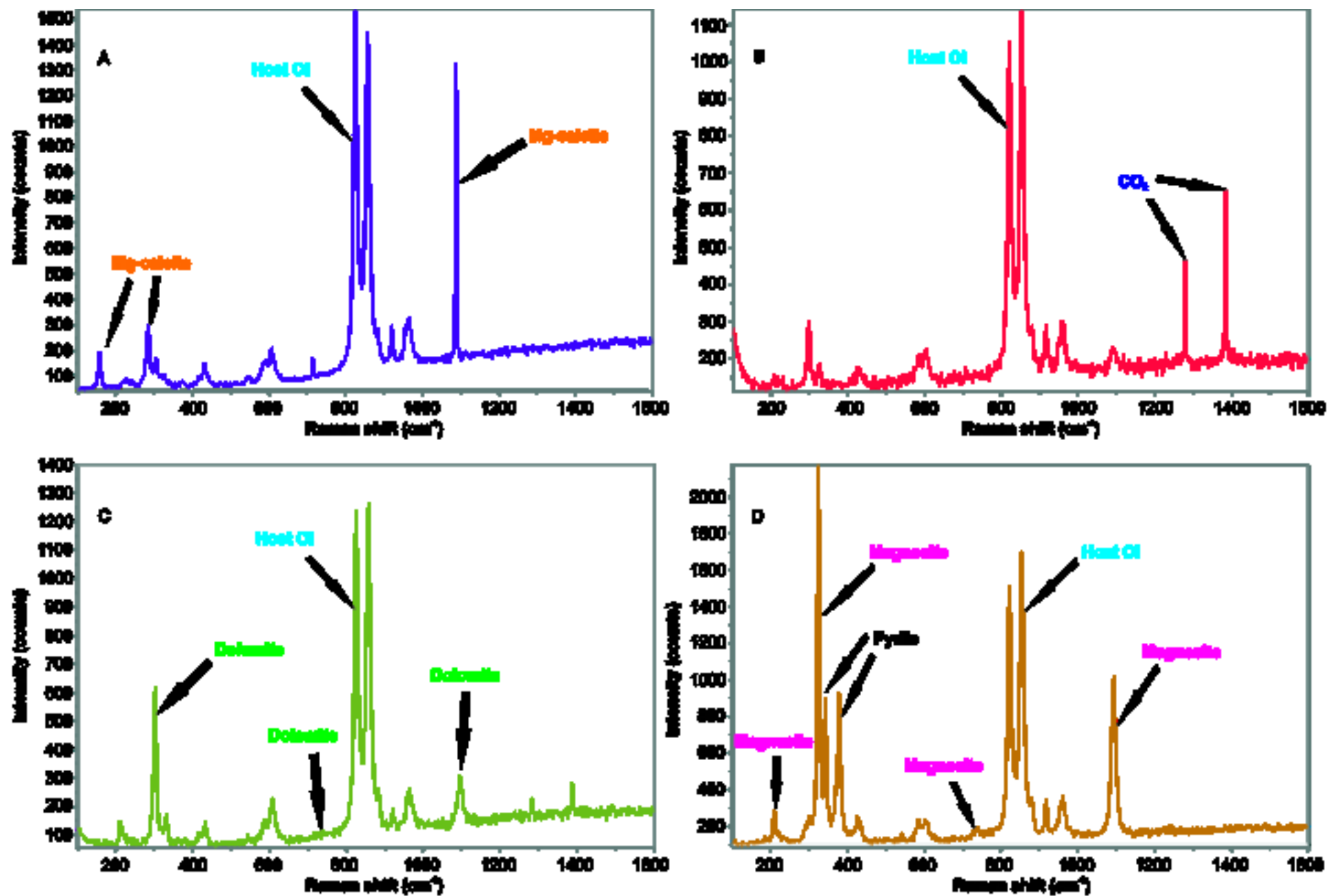
- 177 Mantle Beneath Wilcza Góra (Lower Silesia, Southwest Poland). *Front. Earth Sci.* 6, 215.
178 <https://doi.org/10.3389/feart.2018.00215>
179
- 180 Saucedo, R., Macías, J.L., Ocampo-Díaz, Y.Z.E., Gómez-Villa, W., Rivera-Olgúin, E., Castro-Govea, R.,
181 Sánchez-Núñez, J.M., Layer, P.W., Torres Hernández, J.R., Carrasco-Núñez, G., 2017. Mixed
182 magmatic–phreatomagmatic explosions during the formation of the Joya Honda maar, San Luis Potosí,
183 Mexico. *Geological Society, London, Special Publications* 446, 255–279.
184 <https://doi.org/10.1144/SP446.11>
185
- 186 Trull, T.W., Kurz, M.D., 1993. Experimental measurements of ³He and ⁴He mobility in olivine and
187 clinopyroxene at magmatic temperatures. *Geochimica et Cosmochimica Acta* 57, 1313–1324.
188 [https://doi.org/10.1016/0016-7037\(93\)90068-8](https://doi.org/10.1016/0016-7037(93)90068-8)
189
- 190 Yamamoto, J., Nishimura, K., Sugimoto, T., Takemura, K., Takahata, N., Sano, Y., 2009. Diffusive
191 fractionation of noble gases in mantle with magma channels: Origin of low He/Ar in mantle-derived
192 rocks. *Earth and Planetary Science Letters* 280, 167–174. <https://doi.org/10.1016/j.epsl.2009.01.029>
193

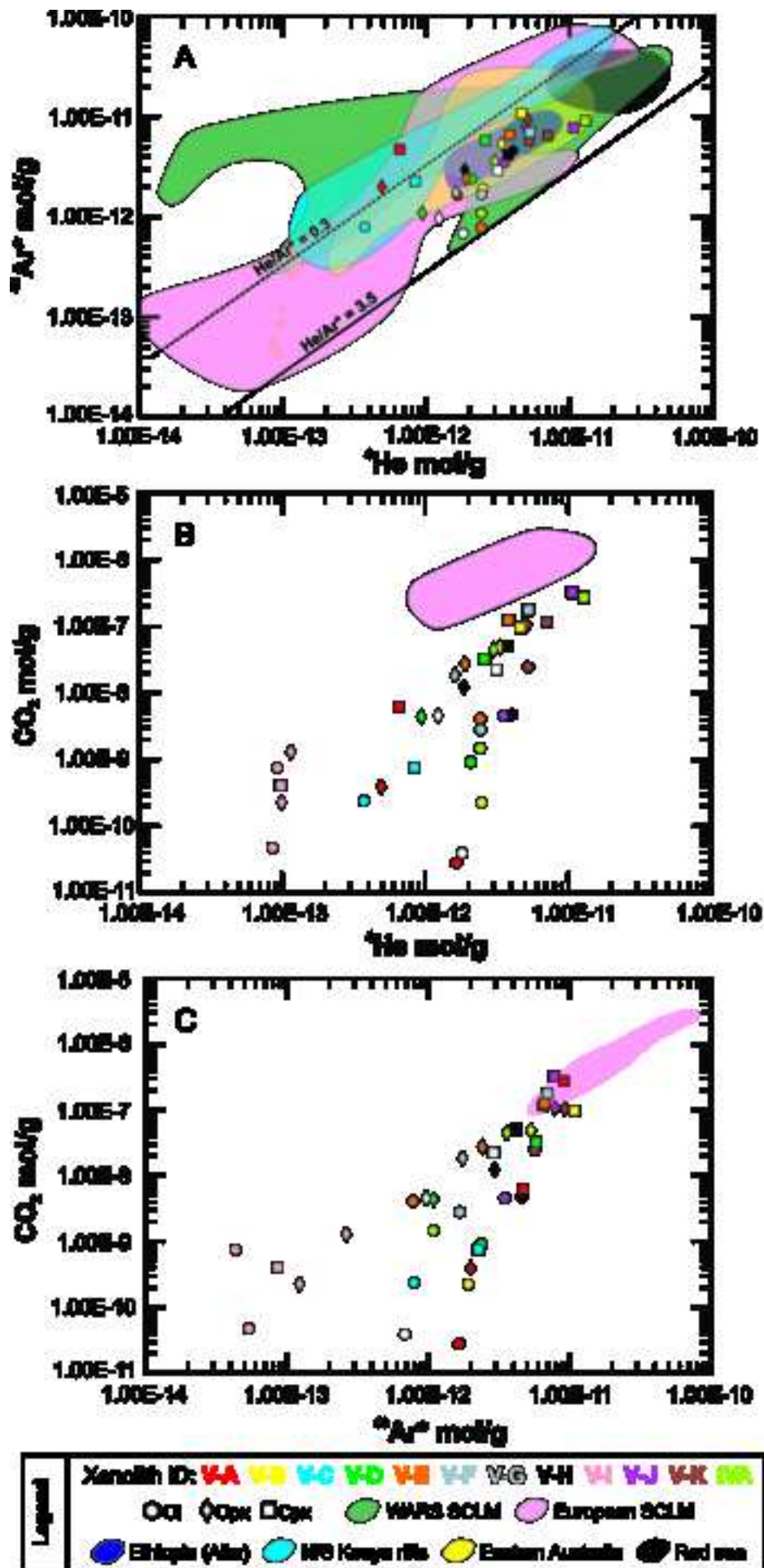


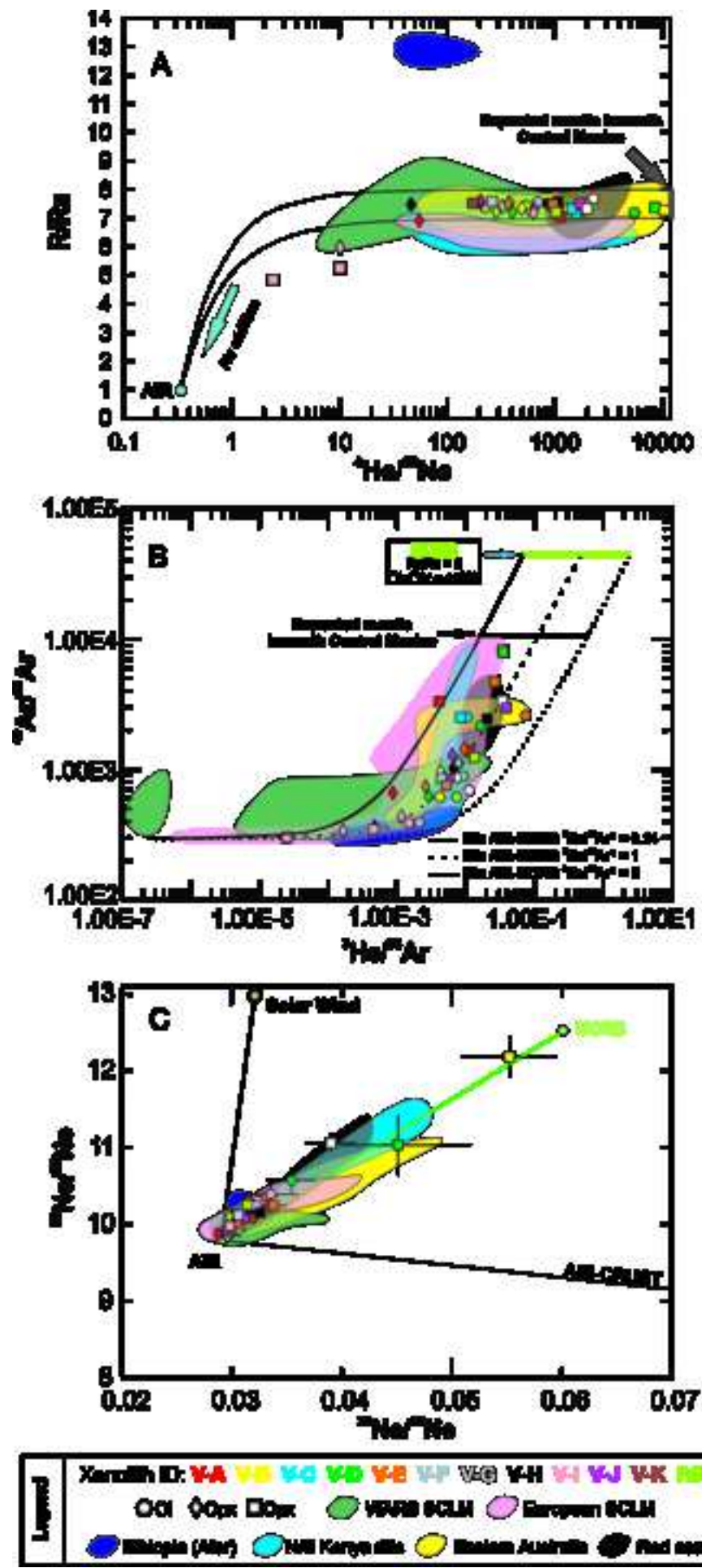


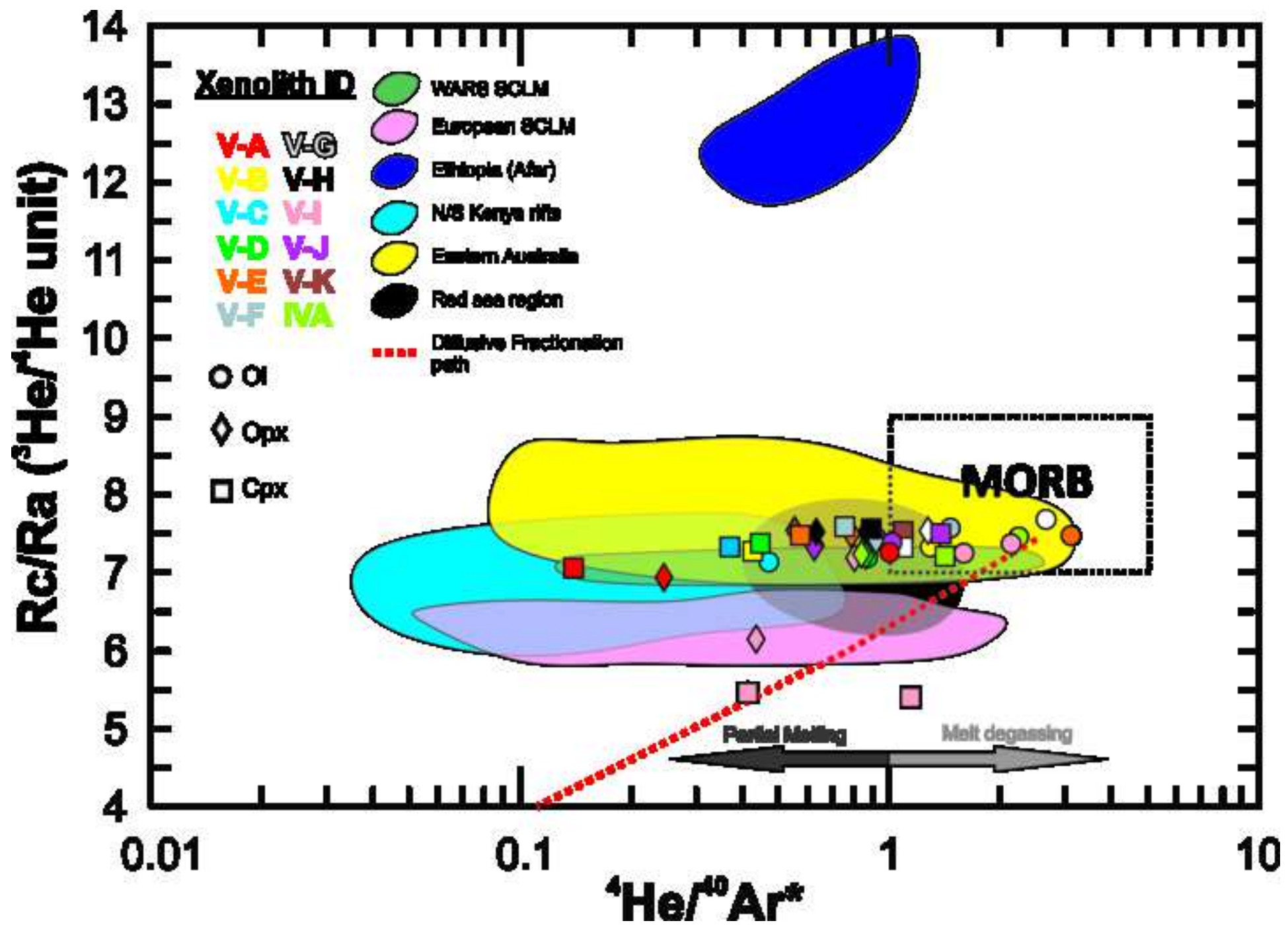


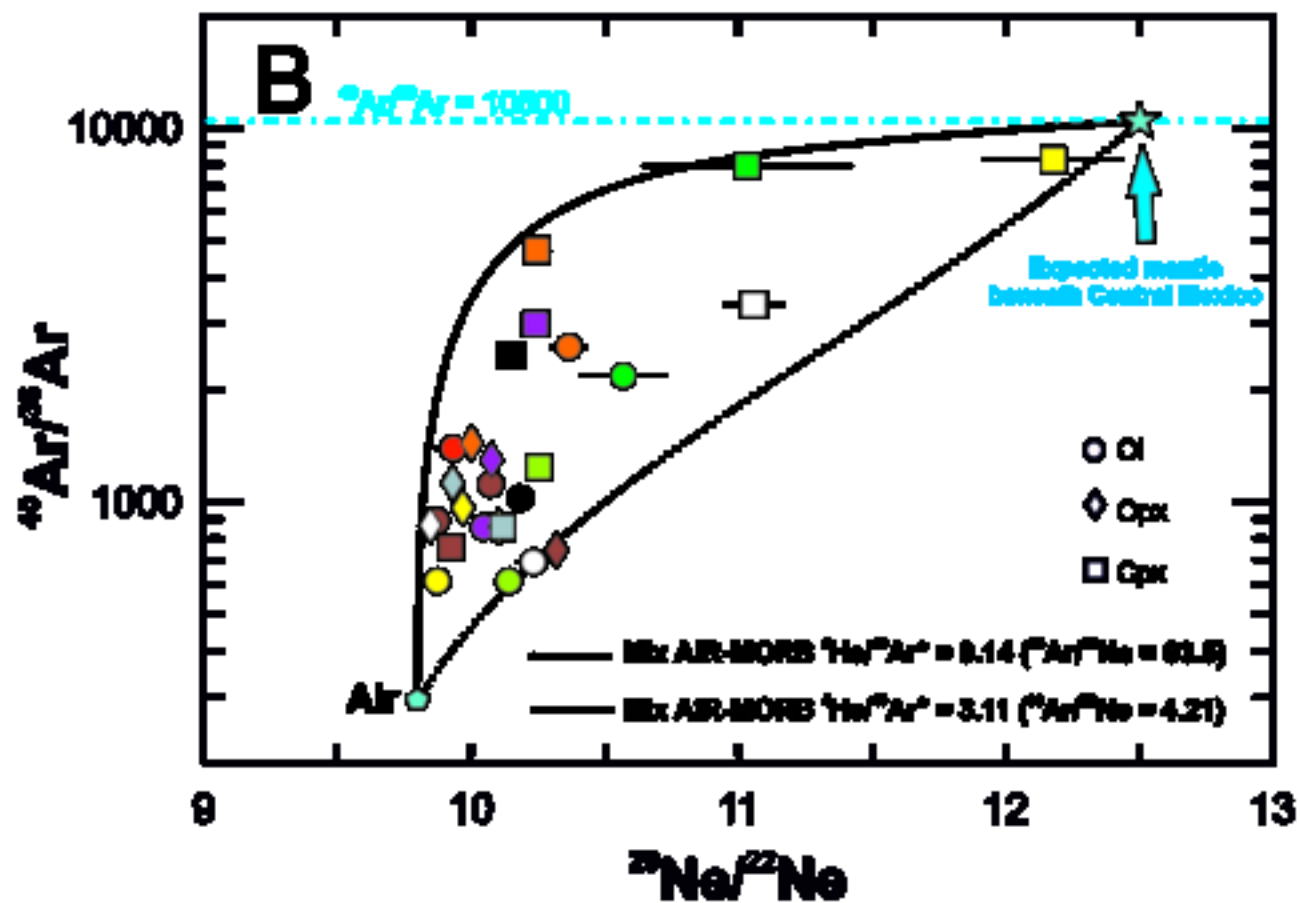
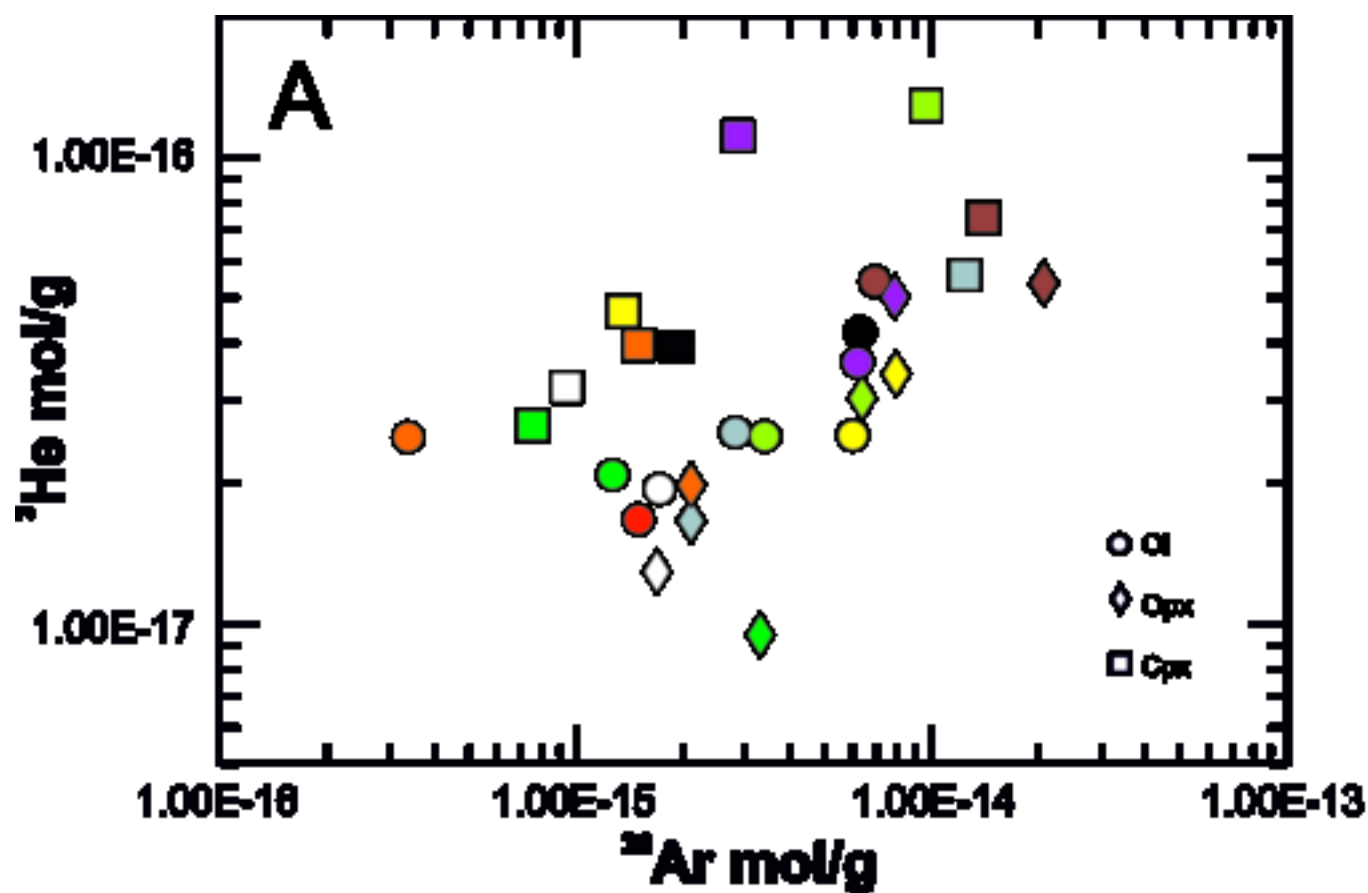




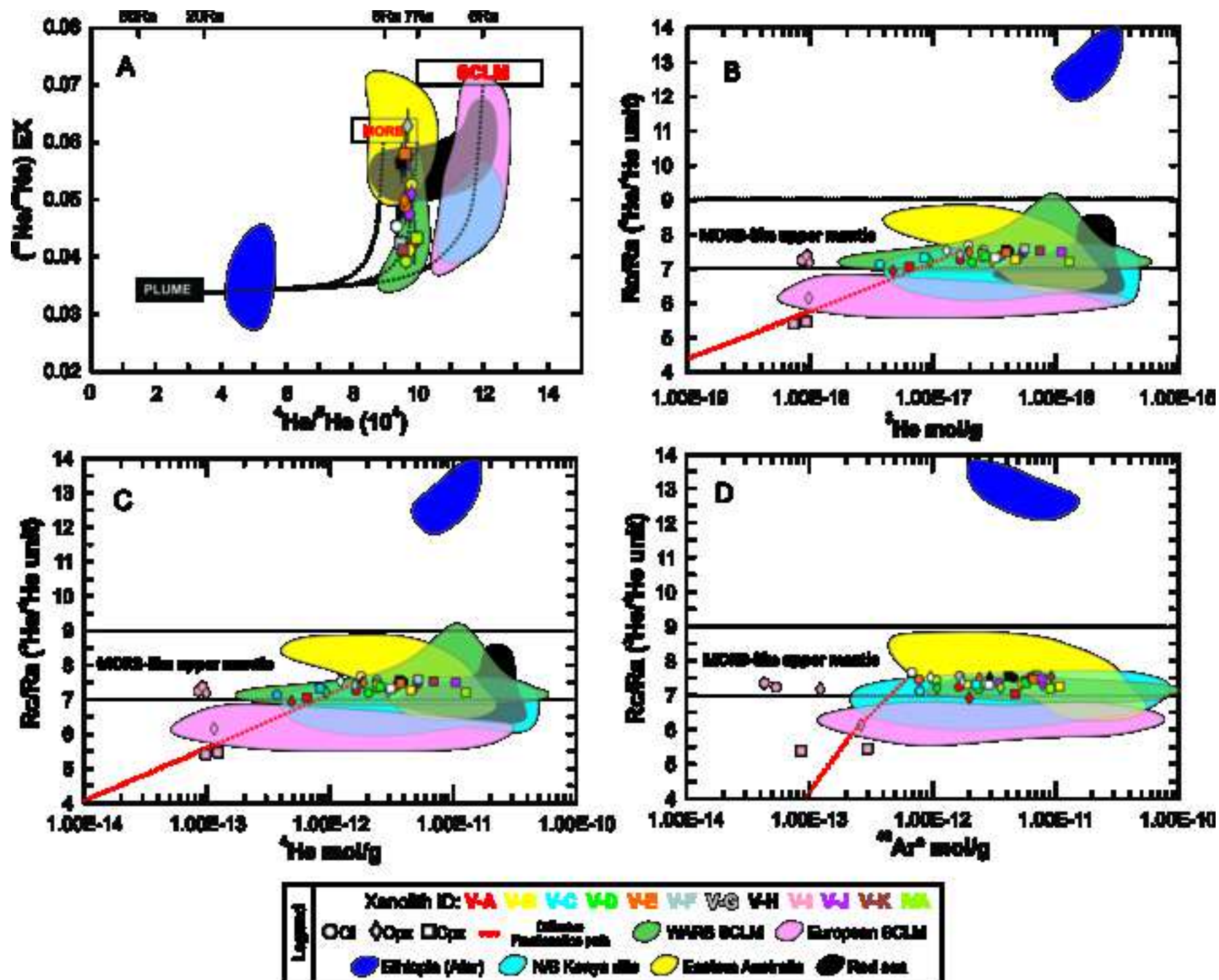


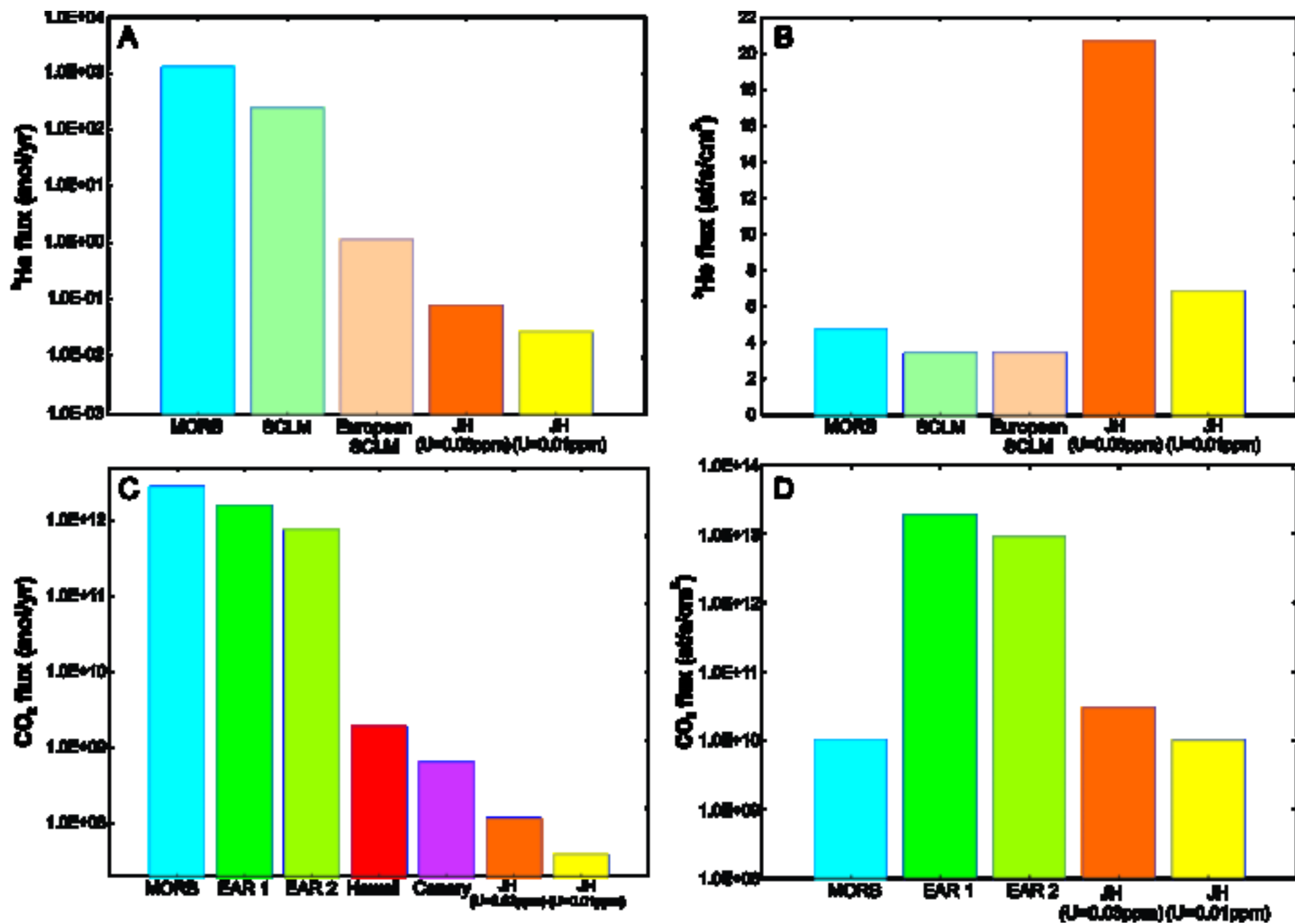


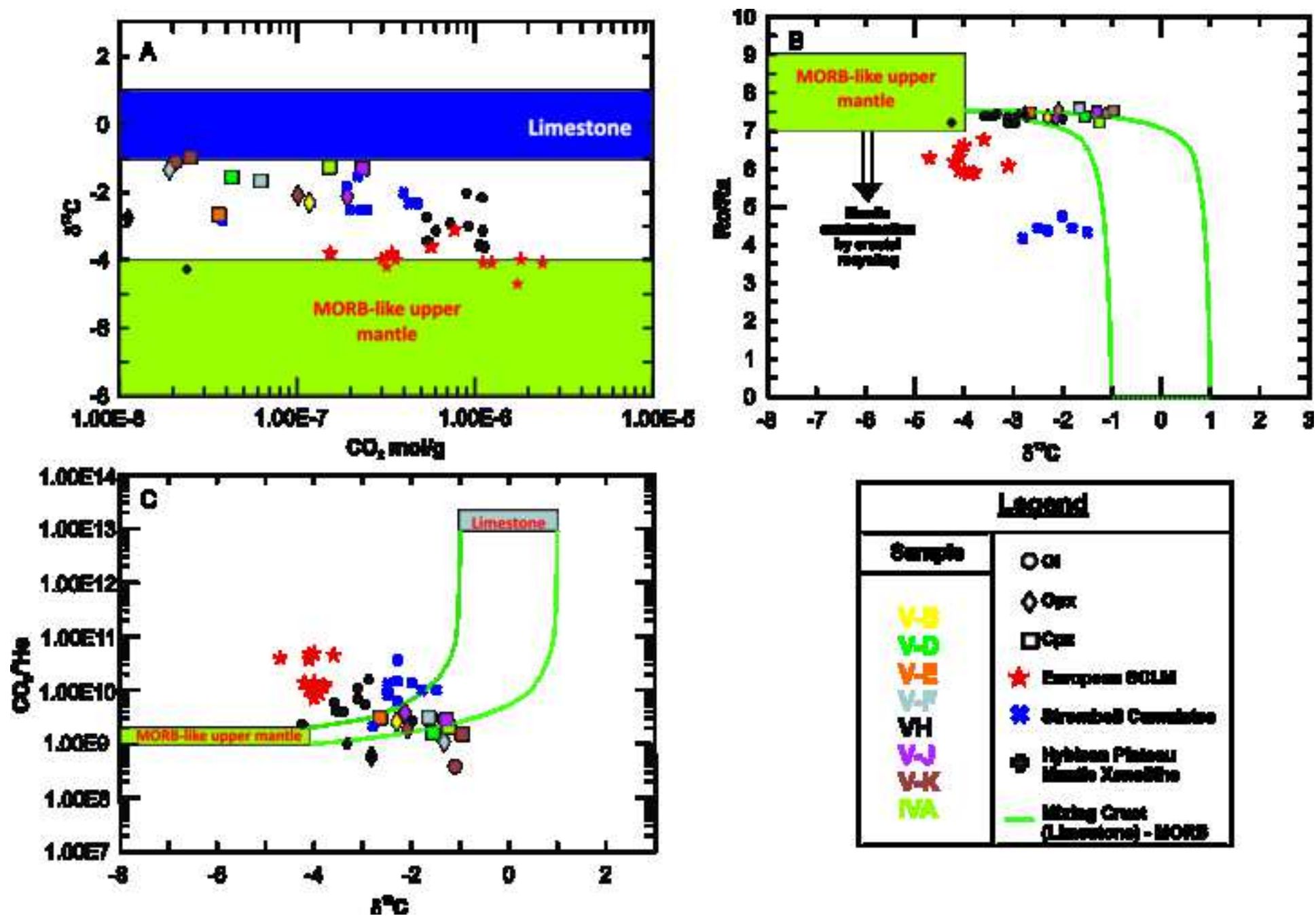




Xenolith ID: V-A V-B V-D V-E V-F V-G V-H V-I V-J V-K VA







Declaration of interests

The authors declare that they have no known competing financial interests or personal relationships that could have appeared to influence the work reported in this paper.

The authors declare the following financial interests/personal relationships which may be considered as potential competing interests: